IMPERIAL COLLEGE LONDON

DEPARTMENT OF CHEMICAL ENGINEERING

Non-Newtonian Effects on Richtmyer-Meshkov Instabilities and Shock-Driven Nuclear Fusion Target

Author:
Usman Rana Mohammad

CID:
01840724

1. Supervisor:
Prof. Omar K. Matar

2. Supervisor:
Dr. Thomas Abadie

3. Supervisor:
Dr. Nathan Joiner

Submitted in partial fulfillment of the requirements of the PhD degree in chemical engineering at Imperial College London

April 2024

Abstract

This PhD project aims to develop computational methods for studying non-Newtonian effects in highly compressible flows. The research is conducted within the context of clean energy applications that exploit fusion technology, which involves the rapid collapse of bubbles culminating in energy generation through nuclear fusion. The study examines interface-capturing methods: algebraic volume-of-fluid and a hybrid interface-tracking method called front-tracking. Several validation simulations involving shock-tube, bubble collapse, Richtmyer-Meshkov instabilities, and Kelvin-Helmholtz instabilities are conducted to determine the relative merits of these methods. The focus of this comparison is on interface resolution, performance, and the robustness of each technique. Additionally, the project explores non-Newtonian effects. The aim is to investigate how the non-Newtonian effects influence the evolution of vorticity, Richtmyer-Meshkov instabilities, and Kelvin-Helmholtz instabilities, as well as how the RMI and KHI impact the average density, pressure, and temperature in a Fusion Target.

Statement of Originality

I hereby declare that this thesis is my own work. All work that is not my own has been appropriately referenced. All the results presented in this thesis are the outcome of my own research, conducted under the supervision of my supervisors, Prof. Omar K. Matar, Dr. Thomas Abadie, and Dr. Nathan Joiner. This work has not been submitted to any other institution for any academic qualification

Copyright Declaration

The copyright of this thesis rests with the author. Unless otherwise indicated, its contents are licensed under a Creative Commons Attribution-NonCommercial 4.0 International Licence (CC BY-NC). Under this licence, you may copy and redistribute the material in any medium or format. You may also create and distribute modified versions of the work. This is on the condition that: you credit the author and do not use it, or any derivative works, for a commercial purpose. When reusing or sharing this work, ensure you make the licence terms clear to others by naming the licence and linking to the licence text. Where a work has been adapted, you should indicate that the work has been changed and describe those changes. Please seek permission from the copyright holder for uses of this work that are not included in this licence or permitted under UK Copyright Law.

Contents

List of Figures **xxi**

List of Tables **xxii**

Nomenclature **xxiii**

Acknowledgments **xxvii**

1 Introduction **1**

2 Literature Review **4**
2.1 Nuclear Fusion 4
2.1.1 Inertial Confinement Fusion 5
2.1.2 Inertial Confinement Fusion in a Collapsing Bubble 6
2.2 Hydrodynamic Instabilities 8
2.2.1 Richtmyer-Meshkov Instabilities 8
2.2.2 Rayleigh-Taylor Instabilities 9
2.2.3 Kelvin-Helmholtz Instabilities 10
2.3 Fundamentals of Compressible Flows 11
2.3.1 Compressible Flows 11
2.3.2 Rankine-Hugoniot Relations and Shock Waves 13
2.3.3 Riemann Problem 14
2.4 Governing equations 21
2.4.1 Multiphase Flows 23

3 Numerical Codes **33**
3.1 BlastFOAM vs OpenFOAM 33
3.1.1 Shock-Tube Validation Cases 33
3.1.2 Shock-Induced Bubble Collapse 54
3.2 BlastFOAM vs Hytrac 58
3.2.1 Multi-material 1D Shock-Tube 58
3.2.2 RMI Trilab 66

3.2.3 Kelvin-Helmholtz Instabilities 72
3.2.4 RMI: Jacobs-Krivets Case and Mesh Independence 73
3.3 Impact of Initial Wavelength 78
3.4 Limitations of Models 79

4 RMI:Non-Newtonian Effects 81
4.1 Code Development 81
4.1.1 Code Validation 83
4.2 Evolution of RMI 84
4.2.1 Shear-Thinning Effects 92
4.2.2 Shear Thinning Effects with lower flow index 110
4.2.3 Shear Thinning Effects and Temperature Effects 113
4.2.4 Summary and Implications 117
4.3 Limitations of Models 118

5 Fusion Target 120
5.1 Viscosity Effects on Shock Dynamics 120
5.1.1 1-D shock-tube 120
5.1.2 Shock-driven nuclear fusion 129
5.2 Effect of material properties 141
5.3 Impact of Coverslip on RMI 149
5.4 Limitations of Models 156

6 Conclusion and Future Work 158
6.1 Conclusion and Summary 158
6.2 Future Work 160

7 Appendices 162
7.1 Tri-Lab case with Hytrac 162
7.1.1 AMR level Study 162
7.1.2 Smoothening Factor Study 164
7.1.3 Redistribuation Factor Study 165

Bibliography 166

List of Figures

2.1 An illustration of a nuclear fusion reaction: Deuterium + Tritium → Helium + neutron [1]. 4
2.2 A schematic of inertial confinement fusion process at the National Ignition Facility at the Lawrence Livermore Laboratory, USA [2]. . . . 6
2.3 Sonoluminescence in a collapsing bubble: a bubble is excited with sound waves; (a) at low pressure, the bubble starts expanding; (b) as the pressure increases the bubble contracts and collapses; (c) the bubble collapse leads to light emission as a result of energy cascade: from the ions to electrons, and then to photons [3]. 7
2.4 A schematic showing the development of a Richtmyer-Meshkov instability: (a) a shock wave travelling towards an interface separating two fluids of different density; (b) the generation of vorticity after the impact; (c) deformation of the interface following shock impact [4]. 9
2.5 An illustration of the development of Rayleigh-Taylor instabilities as well as Kelvin-Helmholtz instabilities in the last three snapshots [5]. 10
2.6 An illustration of the development of Kelvin-Helmholtz instabilities [6] 11
2.7 Solution structure of the Riemann problem [7]. 16
2.8 Wave patterns that can occur in a Riemann problem Case (a): left rarefaction wave right shock wave Case (b): left shock wave right rarefaction wave Case (c) left and right rarefaction waves Case (d) left and right shock wave [7]. 16
2.9 left shock wave in case (a) and left rarefaction wave in case (b) [7]. . 19
2.10 right shock wave in case (a) and right rarefaction wave in case (b) [7]. 20
2.11 Classification of computational multiphase flow methods [8]. 24
2.12 The volume fraction function in volume-of-fluid [9]. 26
2.13 The interface reconstruction using the SLIC method in VOF [10]. . . 27
2.14 The interface reconstruction using the PLIC method in VOF [10]. . . 28
2.15 An illustration of front-tracking method [11]. 30
2.16 Grid communication between the eulerian and the lagrangian grid in front-tracking [10]. 31

2.17 Interface reconstruction by level contours in hybrid front-tracking/level set method by Shin et al. [11]. 31

3.1 1-D shock-tube domain as used in 5 Toro tests. 34

3.2 Pressure results for Toro test 1 at $t = 0.2$. The comparison includes BlastFOAM (solid red line), OpenFOAM (dashed black line), and the exact solution (solid blue line) of the Riemann problem using the SFCD numerical scheme with a 1000-cell mesh and ideal gas equation of state. 36

3.3 Density results for Toro test 1 at $t = 0.2$. The comparison includes BlastFOAM (solid red line), OpenFOAM (dashed black line), and the exact solution (solid blue line) of the Riemann problem using the SFCD numerical scheme with a 1000-cell mesh and ideal gas equation of state. 36

3.4 Temperature results for Toro test 1 at $t = 0.2$. The comparison includes BlastFOAM (solid red line), OpenFOAM (dashed black line), and the exact solution (solid blue line) of the Riemann problem using the SFCD numerical scheme with a 1000-cell mesh and ideal gas equation of state. 37

3.5 Velocity results for Toro test 1 at $t = 0.2$. The comparison includes BlastFOAM (solid red line), OpenFOAM (dashed black line), and the exact solution (solid blue line) of the Riemann problem using the SFCD numerical scheme with a 1000-cell mesh and ideal gas equation of state. 37

3.6 Pressure results for Toro test 1 at $t = 0.2$. The comparison includes different numerical schemes: Minmod, SFCD, SuperBee, Upwind, and VanLeer as implemented in BlastFOAM, with the exact solution (solid blue line) of the Riemann problem using a 1000-cell mesh and ideal gas equation of state. 39

3.7 Pressure results for Toro test 1 at $t = 0.2$. The comparison includes different numerical schemes: Minmod, SFCD, SuperBee, Upwind, and VanLeer as implemented in OpenFOAM, with the exact solution (solid blue line) of the Riemann problem using a 1000-cell mesh and ideal gas equation of state. 39

3.8 Density results for Toro test 1 at $t = 0.2$. The comparison includes different numerical schemes: Minmod, SFCD, SuperBee, Upwind, and VanLeer as implemented in BlastFOAM, with the exact solution (solid blue line) of the Riemann problem using a 1000-cell mesh and ideal gas equation of state. 40

3.9 Density results for Toro test 1 at $t = 0.2$. The comparison includes different numerical schemes: Minmod, SFCD, SuperBee, Upwind, and VanLeer as implemented in OpenFOAM, with the exact solution (solid blue line) of the Riemann problem using a 1000-cell mesh and ideal gas equation of state. 40

3.10 Temperature results for Toro test 1 at $t = 0.2$. The comparison includes different numerical schemes: Minmod, SFCD, SuperBee, Upwind, and VanLeer as implemented in BlastFOAM, with the exact solution (solid blue line) of the Riemann problem using a 1000-cell mesh and ideal gas equation of state. 41

3.11 Temperature results for Toro test 1 at $t = 0.2$. The comparison includes different numerical schemes: Minmod, SFCD, SuperBee, Upwind, and VanLeer as implemented in OpenFOAM, with the exact solution (solid blue line) of the Riemann problem using a 1000-cell mesh and ideal gas equation of state. 41

3.12 Velocity results for Toro test 1 at $t = 0.2$. The comparison includes different numerical schemes: Minmod, SFCD, SuperBee, Upwind, and VanLeer as implemented in BlastFOAM, with the exact solution (solid blue line) of the Riemann problem using a 1000-cell mesh and ideal gas equation of state. 42

3.13 Velocity results for Toro test 1 at $t = 0.2$. The comparison includes different numerical schemes: Minmod, SFCD, SuperBee, Upwind, and VanLeer as implemented in OpenFOAM, with the exact solution (solid blue line) of the Riemann problem using a 1000-cell mesh and ideal gas equation of state. 42

3.14 Pressure results for Toro test 2 at $t = 0.15$. The comparison includes simulation results with BlastFOAM using the second-order numerical scheme SFCD and the exact solution (solid blue line) of the Riemann problem with a 1000-cell mesh and ideal gas equation of state. . . . 44

3.15 Density results for Toro test 2 at $t = 0.15$. The comparison includes simulation results with BlastFOAM using the second-order numerical scheme SFCD and the exact solution (solid blue line) of the Riemann problem with a 1000-cell mesh and ideal gas equation of state. . . . 44

3.16 Temperature results for Toro test 2 at $t = 0.15$. The comparison includes simulation results with BlastFOAM using the second-order numerical scheme SFCD and the exact solution (solid blue line) of the Riemann problem with a 1000-cell mesh and ideal gas equation of state. 45

3.17 Velocity results for Toro test 2 at $t = 0.15$. The comparison includes simulation results with BlastFOAM using the second-order numerical scheme SFCD and the exact solution (solid blue line) of the Riemann problem with a 1000-cell mesh and ideal gas equation of state. . . . 45

3.18 Pressure results for Toro test 3 at $t = 0.12$. The comparison includes simulation results with BlastFOAM (solid red line) and OpenFOAM (dash-dot black line) using the second-order numerical scheme SFCD, and the exact solution (solid blue line) of the Riemann problem with a 1000-cell mesh and ideal gas equation of state. 46

3.19 Density results for Toro test 3 at $t = 0.12$. The comparison includes simulation results with BlastFOAM (solid red line) and OpenFOAM (dash-dot black line) using the second-order numerical scheme SFCD, and the exact solution (solid blue line) of the Riemann problem with a 1000-cell mesh and ideal gas equation of state. 47
3.20 Temperature results for Toro test 3 at $t = 0.12$. The comparison includes simulation results with BlastFOAM (solid red line) and OpenFOAM (dash-dot black line) using the second-order numerical scheme SFCD, and the exact solution (solid blue line) of the Riemann problem with a 1000-cell mesh and ideal gas equation of state. 47
3.21 Velocity results for Toro test 3 at $t = 0.12$. The comparison includes simulation results with BlastFOAM (solid red line) and OpenFOAM (dash-dot black line) using the second-order numerical scheme SFCD, and the exact solution (solid blue line) of the Riemann problem with a 1000-cell mesh and ideal gas equation of state. 48
3.22 Pressure results for Toro test 4 at $t = 0.35$. The comparison includes simulation results with BlastFOAM (solid red line) and OpenFOAM (dash-dot black line) using the second-order numerical scheme SFCD, and the exact solution (solid blue line) of the Riemann problem with a 1000-cell mesh and ideal gas equation of state. 49
3.23 Density results for Toro test 4 at $t = 0.35$. The comparison includes simulation results with BlastFOAM (solid red line) and OpenFOAM (dash-dot black line) using the second-order numerical scheme SFCD, and the exact solution (solid blue line) of the Riemann problem with a 1000-cell mesh and ideal gas equation of state. 49
3.24 Temperature results for Toro test 4 at $t = 0.35$. The comparison includes simulation results with BlastFOAM (solid red line) and OpenFOAM (dash-dot black line) using the second-order numerical scheme SFCD, and the exact solution (solid blue line) of the Riemann problem with a 1000-cell mesh and ideal gas equation of state. 50
3.25 Velocity results for Toro test 4 at $t = 0.35$. The comparison includes simulation results with BlastFOAM (solid red line) and OpenFOAM (dash-dot black line) using the second-order numerical scheme SFCD, and the exact solution (solid blue line) of the Riemann problem with a 1000-cell mesh and ideal gas equation of state. 50
3.26 Pressure results for Toro test 5 at $t = 0.08$. The comparison includes simulation results with BlastFOAM (solid red line) using the second-order numerical scheme SFCD, and the exact solution (solid blue line) of the Riemann problem with a 1000-cell mesh and ideal gas equation of state. 51
3.27 Density results for Toro test 5 at $t = 0.08$. The comparison includes simulation results with BlastFOAM (solid red line) using the second-order numerical scheme SFCD, and the exact solution (solid blue line) of the Riemann problem with a 1000-cell mesh and ideal gas equation of state. 52

3.28 Temperature results for Toro test 5 at $t = 0.08$. The comparison includes simulation results with BlastFOAM (solid red line) using the second-order numerical scheme SFCD, and the exact solution (solid blue line) of the Riemann problem with a 1000-cell mesh and ideal gas equation of state. 52
3.29 Velocity results for Toro test 5 at $t = 0.08$. The comparison includes simulation results with BlastFOAM (solid red line) using the second-order numerical scheme SFCD, and the exact solution (solid blue line) of the Riemann problem with a 1000-cell mesh and ideal gas equation of state. 53
3.30 A schematic of the shock-induced bubble collapse simulation domain as used in OpenFoam and BlastFOAM. 54
3.31 Comparison of BlastFOAM and OpenFOAM shock-induced bubble collapse density plots with the experimental schlieren images of Haas et al. using ideal gas for air and helium and a Mach 1.22 shock wave. at $52\mu s$ (a) and $60\mu s$ (b) after the impact of the shock wave upon helium. 55
3.32 Comparison of BlastFOAM and OpenFOAM shock-induced bubble collapse density plots with the experimental schlieren images of Haas et al. using ideal gas for air and helium and a Mach 1.22 shock wave. at $80\mu s$ (c) and $245\mu s$ (d) after the impact of the shock wave upon helium. 56
3.33 Comparison of BlastFOAM and OpenFOAM shock-induced bubble collapse density plots with the experimental schlieren images of Haas et al. using ideal gas for air and helium and a Mach 1.22 shock wave. at $427\mu s$ (e) and $983\mu s$ (f) after the impact of the shock wave upon helium. 56
3.34 1-D domain of the multi-material shock-tube. 58
3.35 Pressure predictions by BlastFOAM and Hytrac at 4×10^{-9} seconds, utilizing the stiffened gas equation of state for copper and plastic, and the ideal gas equation of state for deuterium ($\rho = 0.16$ kg/m^3). . 60
3.36 Temperature predictions by BlastFOAM and Hytrac at 4×10^{-9} seconds, utilizing the stiffened gas equation of state for copper and plastic, and the ideal gas equation of state for deuterium ($\rho = 0.16$ kg/m^3). 60
3.37 Density predictions by BlastFOAM and Hytrac at 4×10^{-9} seconds, utilizing the stiffened gas equation of state for copper and plastic, and the ideal gas equation of state for deuterium ($\rho = 0.16$ kg/m^3). . 61
3.38 Velocity predictions by BlastFOAM and Hytrac at 4×10^{-9} seconds, utilizing the stiffened gas equation of state for copper and plastic, and the ideal gas equation of state for deuterium ($\rho = 0.16$ kg/m^3). . 61
3.39 Pressure predictions by BlastFOAM and Hytrac at 5×10^{-8} seconds, using the stiffened gas equation of state for copper and plastic, and the ideal gas equation of state for deuterium ($\rho = 0.16$ kg/m^3). . . . 62
3.40 Temperature predictions by BlastFOAM and Hytrac at 5×10^{-8} seconds, using the stiffened gas equation of state for copper and plastic, and the ideal gas equation of state for deuterium ($\rho = 0.16$ kg/m^3). . 62

3.41 Density predictions by BlastFOAM and Hytrac at 5×10^{-8} seconds, using the stiffened gas equation of state for copper and plastic, and the ideal gas equation of state for deuterium ($\rho = 0.16$ kg/m^3). . . . 63

3.42 Velocity predictions by BlastFOAM and Hytrac at 5×10^{-8} seconds, using the stiffened gas equation of state for copper and plastic, and the ideal gas equation of state for deuterium ($\rho = 0.16$ kg/m^3). . . . 63

3.43 Pressure predictions by BlastFOAM and Hytrac at 5×10^{-9} seconds, using the stiffened gas equation of state for copper and plastic, and the ideal gas equation of state for deuterium ($\rho = 100.0$ kg/m^3). . . . 64

3.44 Temperature predictions by BlastFOAM and Hytrac at 5×10^{-9} seconds, using the stiffened gas equation of state for copper and plastic, and the ideal gas equation of state for deuterium ($\rho = 100.0$ kg/m^3). 65

3.45 Density predictions by BlastFOAM and Hytrac at 5×10^{-9} seconds, using the stiffened gas equation of state for copper and plastic, and the ideal gas equation of state for deuterium ($\rho = 100.0$ kg/m^3). . . . 65

3.46 Velocity predictions by BlastFOAM and Hytrac at 5×10^{-9} seconds, using the stiffened gas equation of state for copper and plastic, and the ideal gas equation of state for deuterium ($\rho = 100.0$ kg/m^3). . . . 66

3.47 Schematic of the flow configuration in which a perturbation of wavelength λ is applied to an interface separating two phases at pressure p_0 of initial densities $\rho_{air,0}$ and $\rho_{SF6,0}$ shown by the light grey and white regions, respectively, where $\rho_{air,0} > \rho_{SF6,0}$. A shock is initiated in the air phase (dark grey region) with density $\rho_{air,s}$ and pressure $p_{air,s}$, which travels in the direction of the lighter phase at constant speed U_s 66

3.48 Temporal variation of the perturbation amplitude for At = 0.635 and Ma = 1.3, the red solid and dashed lines represent the predictions of the Richtmyer Model and Dimonte Schneider Model (DS Late Stage Model), and black solid and green dashed lines represent the numerical predictions obtained for the BlastFOAM and Hytrac using ideal gas equation of state. 68

3.49 Evolution of the Richtmyer-Meshkov instability at $AT = 0.635$, $Ma = 1.3$, using the ideal gas equation of state for air and SF6. This showcases different AMR levels (1-3) in BlastFOAM (BF) and Hytrac (HT) at three time intervals: $t = 1 \times 10^{-3}$ s, 1.8×10^{-3} s, and 3×10^{-3} s. . 70

3.50 Evolution of the Richtmyer-Meshkov instability at $AT = 0.635$, $Ma = 1.3$, using the ideal gas equation of state for air and SF6, AMR 4 in Hytrac (HT) at three time intervals: $t = 8 \times 10^{-4}$ s, 1.8×10^{-3} s, and 3×10^{-3} s. 70

3.51 Evolution of the Richtmyer-Meshkov instability in BlastFOAM: The red line represents the volume fraction 0.5 using AMR level 1, the black line corresponds to AMR level 2, and the green line indicates AMR level 3 at $AT = 0.635$ and $Ma = 1.3$, employing the ideal gas equation of state at 3×10^{-3} s. 71

3.52 Evolution of the Richtmyer-Meshkov instability in BlastFOAM: a, b , c and represent the volume fraction 0.4, 0.5 , 0.6 and 0.7 using adaptive mesh refinement (AMR) level 2 at $AT = 0.635$ and $Ma = 1.3$, employing the ideal gas equation of state at 3×10^{-3} s. 71

3.53 Schematic of a flow configuration, where the upper flow region containing air and the lower flow region containing SF6 are separated by an interface. the dark gray area is initialized with a velocity of $U_1 = 400$ m/s, while the light gray area is initialized with a velocity of $U_2 = 700$ m/s. 72

3.54 Temporal Evolution of Kelvin-Helmholtz instability in air and SF6 fluids using the ideal gas equation of state: a comparative analysis with BlastFOAM and Hytrac simulations. Panel (a) displays BlastFOAM simulations at $t = 5.2 \times 10^{-3}$, where the upper part is generated with adaptive mesh refinement (AMR) level 4 and the lower part with AMR level 5. Panel (b) presents BlastFOAM simulations at $t = 1 \times 10^{-2}$, with the upper part employing AMR level 4 and the lower part AMR level 5. Panel (c) showcases Hytrac simulations at $t = 5.2 \times 10^{-3}$, with the upper and lower parts generated with AMR levels 4 and 5, respectively. Panel (d) illustrates Hytrac results at $t = 1 \times 10^{-2}$, also utilizing AMR level 4 for the upper part and AMR level 5 for the lower part. . 73

3.55 Schematic of a fully-developed mushroom-like structure formed following the passage of a shock. The features that characterise the structure are shown together with their defined dimensions. 74

3.56 Temporal variation of the perturbation amplitude for $At = 0.635$ and $Ma = 1.3$, (a), where the red solid and dashed lines represent the predictions of the Richtmyer (1960) and Dimonte Schneider (2000) models, and black solid and red dashed lines represent to the numerical predictions obtained for the BlastFOAM and Jacobs and Krivets. . 74

3.57 Comparison of experimental results for amplitude (black dots) from Jacobs and Krievets [12], theoretical models by Richtmyer [13] and the Late Stage model [14] (red line), with BlastFOAM simulations using the ideal gas equation of state for air and SF_6, where purple line represents AMR level 2, blue AMR level 3, and green AMR level 4 respectively. 75

3.58 Comparison of experimental results for span (black dots) from Jacobs and Krivets [12], with BlastFOAM simulations using the ideal gas equation of state for air and SF_6, where red represents AMR level 2, blue AMR level 3, and green AMR level 4 respectively. 76

3.59 Comparison of experimental results for stream (black dots) from Jacobs and Krivets [12], with BlastFOAM simulations using the ideal gas equation of state for air and SF_6, where red represents AMR level 2, blue AMR level 3, and green AMR level 4 respectively. 76

3.60 Comparison of experimental results for neck (black dots) from Jacobs and Krivets [12], with BlastFOAM simulations using the ideal gas equation of state for air and SF_6, where red represents AMR level 2, blue AMR level 3, and green AMR level 4 respectively. 77
3.61 Comparison of the development of Richtmyer-Meshkov instability (RMI) using different initial wavelengths: (a) corresponds to 1.5 mm, (b) to 3 mm, and (c) to 4.5 mm at $t_1 = 0.00045$ s and $t_2 = 0.0009$ s. Simulations are performed using BlastFOAM with the ideal gas equation of state for air and SF_6 an intial shock at Mach 1.3. 79

4.1 A sketch of the domain as used in BlastFOAM for the shear-thinning flow simulation in a pipe. 84
4.2 Comparison of BlastFOAM predicted using stiffened gas equation of state and theoretical velocity [15] profile for a shear-thinning power-law fluid in a pipe with n = 0.75, K=1.47 $Pa\ s^n$, ρ=1000 kg/m^3 84
4.3 Schematic of the flow configuration in which a perturbation of wavelength λ is applied to an interface separating two phases at pressure p_0 of initial densities $\rho_{h,0}$ and $\rho_{l,0}$ shown by the light grey and white regions, respectively, where $\rho_{h,0} > \rho_{l,0}$. A shock is initiated in the heavier phase (dark grey region) with density $\rho_{h,s}$ and pressure $p_{h,s}$, which travels in the direction of the lighter phase at constant speed U_s. 87
4.4 Projections of the density field in the $x - y$ plane depicting the development of a RMI in inviscid case, and a subsequent KHI, driven by the left-to-right propagation of a shock wave from the heavier towards the lighter phase for t = 0, 0.06, 0.67,1.35,1.43,1.89 shown in (a)-(f), respectively. The parameter values are $At = -0.66$, $Ma = 5$, and $Fr = 48571$; the remaining parameters are in table 4.1. 93
4.5 Temporal variation of the perturbation amplitude for $At = -0.66$ and $Ma = 5$, (a), where the black solid and dashed curves represent the predictions of the Richtmyer [13] and Dimonte and Schneider [16] models, the blue curves represent the inviscid case, while the red dashed and solid lines represent the numerical predictions obtained for the Newtonian-Newtonian and BCY cases, respectively; in the latter case, the light and heavy fluids correspond to Newtonian and BCY fluids, respectively; here, $T_1 - T_4$ correspond to t = 0.075, 0.18,1.41, and 1.48, respectively. Snapshots of the $x - y$ projections of the density field at $t = T_1 - T_4$ depicting the interface shape superimposed on vorticity contours shown in (b)-(e), respectively; in each panel the predictions associated with the BCY and inviscid cases are shown on the left and right, respectively. Variation of the z-component of the vorticity with arc length for the inviscid and viscous cases represented by blue and red lines for $t = T_1 - T_4$ shown in (f)-(i), respectively, plotted on the heavy- (with $\alpha = 0.9$) and light-side (with $\alpha = 0.1$) of the interface using solid and dashed lines, respectively. The rest of the parameters remain unchanged from the previous figure. 94

4.6 Temporal variation of the perturbation amplitude for $At = -0.66$ and $Ma = 10$, (a), where the black solid and dashed lines represent the predictions of the [13] and Dimonte and Schneider [16] models, the blue curves represent the inviscid case, while the red dashed and solid lines represent the numerical predictions obtained for the Newtonian-Newtonian and BCY cases, respectively; in the latter case, the light and heavy fluids correspond to Newtonian and BCY fluids, respectively; here, $T_1 - T_4$ correspond to $t =$ 0.037, 0.085, 0.815, and 1.175, respectively. Snapshots of the $x - y$ projections of the density field at $t = T_1 - T_4$ depicting the interface shape superimposed on vorticity contours shown in (b)-(e), respectively; in each panel the predictions associated with the BCY and inviscid cases are shown on the left and right, respectively. Variation of the z-component of the vorticity with arc length for the inviscid and viscous cases represented by blue and red lines for $t = T_1 - T_4$ shown in (f)-(i), respectively, plotted on the heavy- (with $\alpha = 0.9$) and light-side (with $\alpha = 0.1$) of the interface using solid and dashed lines, respectively. The rest of the parameters remain unchanged from the previous figure. 96

4.7 Temporal evolution of the length of the stream, span, and neck (see figure 4.7 for the definitions of these features) $At = -0.66$ shown in (a)-(c), respectively. In each panel, the red and blue solid lines designate the inviscid and BCY cases for $Ma = 10$, and their dashed counterparts the $Ma = 5$ case, respectively. The solid and dashed vertical lines at $t =$ 0.71 and $t =$ 0.95, and $t = 1.41$ and $t = 1.89$ highlight the times at which the interface is impacted by the first and second reflected shocks for $Ma = 10$ and $Ma = 5$, respectively. The rest of the parameters are unchanged from previous figures. 98

4.8 Fully-developed $x - y$ projections of the density field for the inviscid case in the (At, Ma) space for $At = (-0.048, -0.230, -0.66)$ and $Ma = (5, 7.5, 10)$; the rest of the parameters remain unchanged from previous figures. 104

4.9 Fully-developed $x - y$ projections of the density field for the case wherein the lighter and heavier phases correspond to Newtonian and BCY fluids, respectively, in the (At, Ma) space for $At = (-0.048, -0.230, -0.66)$ and $Ma = (5, 7.5, 10)$; the rest of the parameters remain unchanged from previous figures. 105

4.10 Orientation of the pressure, density, and viscosity gradients following shock impact and protrusion of the heavier phase into the lighter one. 106

4.11 Temporal evolution of the spatial integrals of Terms 3, 4, 8, and 11, I_3, I_4, I_8, and I_{11} shown between $t = 0.06-0.16$ and $t = 1.4-1.5$ in (a) and (b), respectively, highlighting the effect of impact by the primary shock at $t \approx 0.7$ in (a), and reflected shock at $t \approx 1.415$ in (b), for $At = -0.66$ and $Ma = 5$. The green solid and dotted lines represent I_4 and I_{11}, the solid and dashed khaki lines represent I_3 and I_8 for there case wherein the heavier and lighter phases correspond to BCY and Newtonian fluids, respectively. The dashed black line represents I_4 for the case wherein both fluids are treated as inviscid. The insets in panel (b) represent $x - y$ projections of the density field for the inviscid and BCY cases following the impact of the reflected shock. All other parameters mirror those from preceding figures. 106

4.12 Temporal evolution of the spatial integrals of Terms 5, 6, 9, and 10, I_5, I_6, I_9, and I_{10} shown between $t = 0.06 - 0.16$ and $t = 1.4 - 1.5$ in (a) and (b), respectively, highlighting the effect of impact by the primary shock at $t \approx 0.7$ in (a), and reflected shock at $t \approx 1.415$ in (b), for $At = -0.66$ and $Ma = 5$. The blue solid and dashed lines represent I_5 and I_6, and the gray solid and dashed lines represent I_{10} and I_9, respectively. All other parameters mirror those from preceding figures. 107

4.13 Temporal evolution of the spatial integrals of Terms 1, 2, 7, and 12, I_1, I_2, I_7, and I_{12} shown between $t = 0.06-0.16$ and $t = 1.4-1.5$ in (a) and (b), respectively, highlighting the effect of impact by the primary shock at $t \approx 0.7$ in (a), and reflected shock at $t \approx 1.415$ in (b), for $At = -0.66$ and $Ma = 5$. The red solid and dashed lines represent I_1 and I_{12}, and the orange solid and dashed lines represent I_2 and I_7, respectively. The black dashed lines represent I_1 for the inviscid case. All other parameters mirror those from preceding figures. 108

4.14 Variation of the arc length integrals of Terms 4 and 11 of equation 4.33, $I_4^{(s)}$ and $I_{11}^{(s)}$, respectively, when the primary shock impacts the interface with AT = 0.66 for $Ma = 2.5$, $Ma = 5$, and $Ma = 10$ shown in (a) and (b), (c) and (d), and (e) and (f), respectively. The blue and red lines represent the inviscid case and that wherein the heavier and lighter phases correspond to BCY and Newtonian fluids, respectively. The solid and dashed lines represent the results associated with $\alpha = 0.9$ and $\alpha = 0.1$, respectively. 109

4.15 Temporal variation of the perturbation amplitude for $At = -0.66$ and $Ma = 5$, (a), where the black solid and dashed curves represent the predictions of the Richtmyer [13] and Dimonte and Schneider [16] models, the blue curves represent the inviscid case, while the red dotted, solid and dashed lines represent the numerical predictions obtained for the BCY with $n = 0.55$, BCY (n=0.25) and Newtonian-Newtonian cases, respectively; in the latter case, the light and heavy fluids correspond to Newtonian and BCY fluids, respectively; here, $T_1 - T_4$ correspond to t = 0.075, 0.18,1.41, and 1.48, respectively. . 110

4.16 Fully-developed $x - y$ projections of the density field at $Ma = 6$, $At = 0.66$ for the cases inviscid in (a), BCY ($n = 0.25$) in (b) and BCY ($n = 0.55$) in (c), wherein the lighter and heavier phases correspond to Newtonian and BCY fluids, respectively, the rest of the parameters remain unchanged from previous figures. 111

4.17 Temporal evolution of the spatial integrals of Terms 3, 8, and 11, I_3, I_8, and I_{11}, showcased between $t = 0.06 - 0.16$ and $t = 1.4 - 1.5$ in panels (a) and (b), respectively. These segments highlight the impacts of the primary shock at $t \approx 0.7$ in (a), and the reflected shock at $t \approx 1.415$ in (b), for $At = -0.66$ and $Ma = 5$. The green lines (solid for $n = 0.55$, dashed for $n = 0.25$) illustrate I_{11} within the BCY model, while I_3 and I_8 are depicted by khaki (solid for $n = 0.55$, dashed for $n = 0.25$) and yellow lines (solid for $n = 0.55$, dashed for $n = 0.25$), respectively. This convention allows for a direct comparison between different flow indices. Consistency with previous figures is maintained for all other parameters. 112

4.18 Temporal evolution of the spatial integrals of Terms 5, 6, 9, and 10, I_5, I_6, I_9, and I_{10} shown between $t = 0.06 - 0.16$ and $t = 1.4 - 1.5$ in (a) and (b), respectively, highlighting the effect of impact by the primary shock at $t \approx 0.7$ in (a), and reflected shock at $t \approx 1.415$ in (b), for $At = -0.66$ and $Ma = 5$.The dark blue lines (solid for $n = 0.55$, dashed for $n = 0.25$) illustrate I_5. The light blue lines (solid for $n = 0.55$, dashed for $n = 0.25$) illustrate I_6. The gray lines (solid for $n = 0.55$, dashed for $n = 0.25$) illustrate I_{10}. The black lines (solid for $n = 0.55$, dashed for $n = 0.25$) illustrate I_9. This convention allows for a direct comparison between different flow indices. Consistency with previous figures is maintained for all other parameters. 112

4.19 Temporal evolution of the spatial integrals of Terms 2, 7, and 12, I_2, I_7, and I_{12} shown between $t = 0.06 - 0.16$ and $t = 1.4 - 1.5$ in (a) and (b), respectively, highlighting the effect of impact by the primary shock at $t \approx 0.7$ in (a), and reflected shock at $t \approx 1.415$ in (b), for $At = -0.66$ and $Ma = 5$. The dark red lines (solid for $n = 0.55$, dashed for $n = 0.25$) illustrate I_{12}.The light red lines (solid for $n = 0.55$, dashed for $n = 0.25$) illustrate I_7. The orange lines (solid for $n = 0.55$, dashed for $n = 0.25$) illustrate I_2. This convention allows for a direct comparison between different flow indices. Consistency with previous figures is maintained for all other parameters 113

4.20 Temporal variation of the perturbation amplitude for $At = -0.66$ and $Ma = 5$, (a), where the black solid and dashed curves represent the predictions of th e Richtmyer [13] and Dimonte and Schneider [16] models, the blue curves represent the inviscid case, while the red dotted, solid and dashed lines represent the numerical predictions obtained for the BCY with $n = 0.55$, BCYT and Newtonian-Newtonian cases, respectively; in the latter case, the light and heavy fluids correspond to Newtonian and BCY fluids, respectively; here, $T_1 - T_4$ correspond to $t =$ 0.075, 0.18,1.41, and 1.48, respectively. 114

4.21 Fully-developed $x - y$ projections of the density field at $Ma = 6$, $At = 0.66$ for the cases inviscid in (a), BCYT in (b) and BCY ($n = 0.55$) in (c), wherein the lighter and heavier phases correspond to Newtonian and BCY fluids, respectively, the rest of the parameters remain unchanged from previous figures. 115

4.22 Temporal evolution of the spatial integrals of Terms 3, 8, and 11, I_3, I_8, and I_{11}, showcased between $t = 0.06 - 0.16$ and $t = 1.4 - 1.5$ in panels (a) and (b), respectively. These segments highlight the impacts of the primary shock at $t \approx 0.7$ in (a), and the reflected shock at $t \approx 1.415$ in (b), for $At = -0.66$ and $Ma = 5$. The green lines (solid for BCY $n = 0.55$, dotted for BCYT) illustrate I_{11} within the BCY model, while I_3 and I_8 are depicted by khaki (solid for BCY $n = 0.55$, dotted for BCYT) and yellow lines (solid for BCY $n = 0.55$, dotted for BCYT), respectively. This convention allows for a direct comparison between different flow indices. Consistency with previous figures is maintained for all other parameters. 116

4.23 Temporal evolution of the spatial integrals of Terms 5, 6, 9, and 10, I_5, I_6, I_9, and I_{10} shown between $t = 0.06-0.16$ and $t = 1.4-1.5$ in (a) and (b), respectively, highlighting the effect of impact by the primary shock at $t \approx 0.7$ in (a), and reflected shock at $t \approx 1.415$ in (b), for $At = -0.66$ and $Ma = 5$.The dark blue lines (solid for $n = 0.55$, dotted for $n = 0.25$) illustrate I_5. The light blue lines (solid for BCY $n = 0.55$, dotted for BCYT) illustrate I_6. The gray lines (solid for BCY $n = 0.55$, dotted for BCYT) illustrate I_{10}. The black lines (solid for BCY $n = 0.55$, dotted for BCYT) illustrate I_9. This convention allows for a direct comparison between different flow indices. Consistency with previous figures is maintained for all other parameters. 116

4.24 Temporal evolution of the spatial integrals of Terms 2, 7, and 12, I_2, I_7, and I_{12} shown between $t = 0.06 - 0.16$ and $t = 1.4 - 1.5$ in (a) and (b), respectively, highlighting the effect of impact by the primary shock at $t \approx 0.7$ in (a), and reflected shock at $t \approx 1.415$ in (b), for $At = -0.66$ and $Ma = 5$. The dark red lines (solid for $n = 0.55$, dashed for $n = 0.25$) illustrate I_{12}.The light red lines (solid for BCY $n = 0.55$, dotted for BCYT) illustrate I_7. The orange lines (solid for BCY $n = 0.55$, dashed for BCYT) illustrate I_2. This convention allows for a direct comparison between different flow indices. Consistency with previous figures is maintained for all other parameters 117

5.1 Schematic of a flow configuration, where the right gray region contains PMMA (of density ρ_p) and the white region contains deuterium (of density ρ_d). The dark gray area is initialized with a shock, which travels towards the deuterium. 121

5.2 Density (a) and velocity (b) predictions at $t = 0.03$ using the BlastFOAM solver, with the ideal gas equation of state for deuterium and the stiffened gas equation of state for PMMA, under inviscid and viscous conditions. The study evaluates three viscous scenarios based on non-dimensionalised viscosity values: μ_{low} with deuterium at a viscosity of 5×10^{-5} and PMMA at 1, μ_{medium} with deuterium's viscosity unchanged and PMMA's increased to 2, and μ_{high}, where deuterium remains at 5×10^{-5} but PMMA's viscosity is raised to 4. 123

5.3 Pressure (a) and temperature (b) predictions at $t = 0.03$ using the BlastFOAM solver, with the ideal gas equation of state for deuterium and the stiffened gas equation of state for PMMA, under inviscid and viscous conditions. The study evaluates three viscous scenarios based on non-dimensionalised viscosity values: μ_{low} with deuterium at a viscosity of 5×10^{-5} and PMMA at 1, μ_{medium} with deuterium's viscosity unchanged and PMMA's increased to 2, and μ_{high}, where deuterium remains at 5×10^{-5} but PMMA's viscosity is raised to 4. 124

5.4 Density (a) and velocity (b) predictions at $t = 0.03$ using the BlastFOAM solver, with the ideal gas equation of state for deuterium and the stiffened gas equation of state for PMMA, under inviscid and viscous conditions. The study evaluates three viscous scenarios based on non-dimensionalised viscosity values: μ_{low} with deuterium at a viscosity of 5×10^{-5} and PMMA at 1, μ_{medium} with deuterium's viscosity unchanged and PMMA's increased to 2, and μ_{high}, where deuterium remains at 5×10^{-5} but PMMA's viscosity is raised to 4. The density of deuterium is increased by a factor of 6.25 as compared to the base case shown in figures 5.2 and 5.3. 125

5.5 Pressure (a) and temperature (b) predictions at $t = 0.03$ using the BlastFOAM solver, with the ideal gas equation of state for deuterium and the stiffened gas equation of state for PMMA, under inviscid and viscous conditions. The study evaluates three viscous scenarios based on non-dimensionalised viscosity values: μ_{low} with deuterium at a viscosity of 5×10^{-5} and PMMA at 1, μ_{medium} with deuterium's viscosity unchanged and PMMA's increased to 2, and μ_{high}, where deuterium remains at 5×10^{-5} but PMMA's viscosity is raised to 4. The density of deuterium is increased by a factor of 6.25 as compared to the base case shown in figures 5.2 and 5.3. 126

5.6 Density (a) and velocity (b) predictions $t = 1.21$using the BlastFOAM solver, with the ideal gas equation of state for deuterium and the stiffened gas equation of state for PMMA, under inviscid and viscous conditions. The study evaluates three viscous scenarios based on non-dimensionalised viscosity values: μ_{low} with deuterium at a viscosity of 5×10^{-5} and PMMA at 1, μ_{medium} with deuterium's viscosity unchanged and PMMA's increased to 2, and μ_{high}, where deuterium remains at 5×10^{-5} but PMMA's viscosity is raised to 4. The density of deuterium is increased by a factor of 625 as compared to the base case shown in Figures 5.2 and 5.3. 127

5.7 Pressure (a) and temperature (b) predictions at $t = 1.21$ using the BlastFOAM solver, with the ideal gas equation of state for deuterium and the stiffened gas equation of state for PMMA, under inviscid and viscous conditions. The study evaluates three viscous scenarios based on non-dimensionalised viscosity values: μ_{low} with deuterium at a viscosity of 5×10^{-5} and PMMA at 1, μ_{medium} with deuterium's viscosity unchanged and PMMA's increased to 2, and μ_{high}, where deuterium remains at 5×10^{-5} but PMMA's viscosity is raised to 4. The density of deuterium is increased by a factor of 625 as compared to the base case shown in Figures 5.2 and 5.3. 128

5.8 Experimental setup as used in explosion-driven thermonuclear fusion experiment by Derentowicz et al. [17]. A Mach wave is generated through explosion. This Mach wave shots the polyethylene foil into the conical region filled with deuterium. The deuterium gas is compressed to achieve neutrons through thermonuclear fusion. 130

5.9 Simulation domain as used in BlastFOAM to simulate the Derentowicz et al. [17] experiment. 132

5.10 Comparison of inviscid and viscous cases, where a constant viscosity is applied to deuterium and PMMA. figures (a), (b), and (c) display pressure at 0.13, 0.152, and 0.19, respectively. This scenario is considered the base case; the densities for deuterium and PMMA align with the original base case, as demonstrated in figures 5.2 and 5.3. . 133

5.11 Comparison of inviscid and viscous cases, with a constant dynamic viscosity for PMMA and temperature-dependent viscosity for deuterium, as described by equation 5.1. figures (a), (b), and (c) display densities at 0.3, 0.32, and 0.34. This scenario is considered the base case; the densities for deuterium and PMMA align with the original base case, as shown in figures 5.2 and 5.3. 134

5.12 Comparison of inviscid and viscous case at, with a constant dynamic viscosity for PMMA and temperature-dependent viscosity for deuterium, as described by equation 5.1. figures (a), (b), (c) and (d) display densities at 0.2, 0.25, 0.28 and 0.3. This scenario is considered the base case; the densities for deuterium and PMMA align with the original base case, as shown in figures 5.2 and 5.3. 136

5.13 Comparison of inviscid and viscous cases, with a constant dynamic viscosity for deuterium and PMMA. figures (a), (b), and (c) display densities at 0.3, 0.32, and 0.34. This scenario is considered the base case; the densities for deuterium and PMMA align with the original base case, as shown in figures 5.2 and 5.3. 137

5.14 Comparison of two viscous scenarios: one with a constant dynamic viscosity for both deuterium and PMMA, denoted as *viscous_const*, and another where a constant dynamic viscosity is used for deuterium while a temperature-dependent viscosity is applied for PMMA. figures (a), (b), and (c) display densities at 0.3, 0.32, and 0.34, respectively. This scenario is considered the base case; the densities for deuterium and PMMA align with the original base case, as demonstrated in figures 5.2 and 5.3. 138

5.15 Comparison of inviscid and viscous cases at, where a constant viscosity is applied to deuterium and PMMA . figures (a), (b), and (c) display pressure at 0.13, 0.152, and 0.19, respectively. In this case the density of deuterium is increased by a factor of 625 compared to the base case as shown in the 1D simulation in figures 5.2 and 5.3 and 2-D simulation in 5.10. 139

5.16 Comparison of the inviscid case with two viscous scenarios at $t = 0.5$: In (a), a constant non-dimensional dynamic viscosity of 5×10^{-6} is applied to deuterium, and a non-dimensional dynamic viscosity of 2 is applied to PMMA. In figure (b), a non-dimensional dynamic viscosity of 5×10^{-6} is used for deuterium, and a non-dimensional dynamic viscosity of 4 is used for PMMA. 140

5.17 Comparison of amplitude predictins by Richtmyer model [13] and the RMI growth in BlastFOAM's simulation using ideal gas equation of state for deuterium and stiffened gas equation of state for copper and PMMA. 141

5.18 Comparison of an inviscid case with two viscous cases at $t = 0.241$ displaying the volume fraction of deuterium. figure (a) represents the inviscid case, (b) the low viscosity case, and (c) the high viscosity case. The ideal gas equation of state is used for deuterium, and the stiffened gas equation of state is used for PMMA and copper. Copper is treated as inviscid in all cases, and PMMA is modelled with the BCY model 4.18. 143

5.19 Zoomed-in comparison of an inviscid case with two viscous cases from figure 5.18. 143

5.20 Comparison of an inviscid case with two viscous cases $t = 0.63$ displaying the volume fraction of deuterium. figure (a) represents the inviscid case, (b) the low viscosity case, and (c) the high viscosity case. The ideal gas equation of state is used for deuterium, and the stiffened gas equation of state is used for PMMA and copper. Copper is treated as inviscid in all cases, and PMMA is modelled with the BCY model 4.18. 144

5.21 Zoomed-in comparison of an inviscid case with two viscous cases from figure 5.20 144

5.22 Comparison of an inviscid case with two viscous cases at $t = 0.664$ displaying the volume fraction of deuterium. figure (a) represents the inviscid case, (b) the low viscosity case, and (c) the high viscosity case. The ideal gas equation of state is used for deuterium, and the stiffened gas equation of state is used for PMMA and copper. Copper is treated as inviscid in all cases, and PMMA is modelled with the BCY model 4.18. 145

5.23 Zoomed-in comparison of an inviscid case with two viscous cases from figure 5.22 145

5.24 Comparison of an inviscid case with two viscous cases $t = 0.772$ displaying the volume fraction of deuterium. figure (a) represents the inviscid case, (b) the low viscosity case, and (c) the high viscosity case. The ideal gas equation of state is used for deuterium, and the stiffened gas equation of state is used for PMMA and copper. Copper is treated as inviscid in all cases, and PMMA is modelled with the BCY model 4.18. 146

5.25 Zoomed-in comparison of an inviscid case with two viscous cases from figure 146

5.26 Comparison of area-averaged deuterium density predictions using the ideal gas equation of state for deuterium and the stiffened gas equation of state for copper and PMMA. Predictions are categorized by the viscosity models: inviscid, low viscosity (denoted as $\mu_{\infty,\text{low}}$), and high viscosity (denoted as $\mu_{\infty,\text{high}}$). Copper is treated as inviscid in all scenarios. For viscous cases, the BCY model (see equation 4.18) is applied to PMMA. 147

5.27 Comparison of area-averaged deuterium pressure predictions using the ideal gas equation of state for deuterium and the stiffened gas equation of state for copper and PMMA. Predictions are categorized by the viscosity models: inviscid, low viscosity (denoted as $\mu_{\infty,\text{low}}$), and high viscosity (denoted as $\mu_{\infty,\text{high}}$). Copper is treated as inviscid in all scenarios. For viscous cases, the BCY model (see equation 4.18) is applied to PMMA. 147

5.28 Comparison of area-averaged temperature pressure predictions using the ideal gas equation of state for deuterium and the stiffened gas equation of state for copper and PMMA. Predictions are categorized by the viscosity models: inviscid, low viscosity (denoted as $\mu_{\infty,\text{low}}$), and high viscosity (denoted as $\mu_{\infty,\text{high}}$). Copper is treated as inviscid in all scenarios. For viscous cases, the BCY model (see equation 4.18) is applied to PMMA. 148

5.29 Domain of 5 different case with different configurations of coverslips as used in BlastFOAM 149

5.30 Comparison of cases a, b, c, d, and e at $t = 0.16$, displaying the volume fraction of deuterium. case a represents the original scenario. In case b, the coverslip is substituted with deuterium. In case c, the thickness of deuterium is reduced by half. In case d, the coverslip is composed of a different configuration, made up of PMMA/PVC. In case e, the coverslip is made from a different configuration, specifically PMMA/PVC. All cases are treated as inviscid, using the ideal gas equation of state for deuterium, and the stiffened gas equation of state is applied to PMMA, PVC, and copper. 151

5.31 Zoomed-in comparison of cases a, b, c, and d at $t = 0.16$ from figure 5.30. 151

5.32 Comparison of cases a, b, c, d, and e at $t = 0.338$, displaying the volume fraction of deuterium. Case a represents the original scenario. In case b, the coverslip is substituted with deuterium. In case c, the thickness of deuterium is reduced by half. In case d, the coverslip is composed of a different configuration, made up of PMMA/PVC. In case e, the coverslip is made from a different configuration, specifically PMMA/PVC. All cases are treated as inviscid, using the ideal gas equation of state for deuterium, and the stiffened gas equation of state is applied to PMMA, PVC, and copper. 152

5.33 Zoomed-in comparison of cases a, b, c, and d at $t = 0.338$ from Figure 5.32. 152

5.34 Comparison of cases a, b, c, d, and e at $t = 0.48$, displaying the volume fraction of deuterium. Case a represents the original scenario. In case b, the coverslip is substituted with deuterium. In sase c, the thickness of deuterium is reduced by half. In case d, the coverslip is composed of a different configuration, made up of PMMA/PVC. In case e, the coverslip is made from a different configuration, specifically PMMA/PVC. All cases are treated as inviscid, using the ideal gas equation of state for deuterium, and the stiffened gas equation of state is applied to PMMA, PVC, and copper. 153
5.35 Zoomed-in comparison of cases a, b, c, and d at $t = 0.48$ from Figure 5.32. 153
5.36 Comparison of cases a, c, d, and e at $t = 0.664$, displaying the volume fraction of deuterium. Case a represents the original scenario. In case c, the thickness of deuterium is reduced by half. In case d, the coverslip is composed of a different configuration, made up of PMMA/PVC. In case e, the coverslip is made from a different configuration, specifically PMMA/PVC. All cases are treated as inviscid, using the ideal gas equation of state for deuterium, and the stiffened gas equation of state is applied to PMMA, PVC, and copper. 154
5.37 Zoomed-in comparison of cases a, c, and d at $t = 0.664$ from Figure 5.32. 154
5.38 Comparison of predicted deuterium area-averaged density using BlastFOAM across different cases: a) original coverslip, c) halved-thickness coverslip, d and e) PMMA/PVC coverslips in various configurations (see figure 5.29). Ideal gas state equations used for deuterium; stiffened gas equations for PMMA, PVC, and copper. 155
5.39 Comparison of predicted deuterium area-averaged pressure using BlastFOAM across different cases: a) original coverslip, c) halved-thickness coverslip, d and e) PMMA/PVC coverslips in various configurations (see figure 5.29). Ideal gas state equations used for deuterium; stiffened gas equations for PMMA, PVC, and copper. 155
5.40 Comparison of predicted deuterium area-averaged temperature using BlastFOAM across different cases: a) original coverslip, c) halved-thickness coverslip, d and e) PMMA/PVC coverslips in various configurations (see figure 5.29). Ideal gas state equations used for deuterium; stiffened gas equations for PMMA, PVC, and copper. 156

7.1 Evolution of the Richtmyer-Meshkov instability at $AT = 0.635$, $Ma = 1.3$, using the ideal gas equation of state for air and SF6. This showcases different AMR levels (0-3) in Hytrac (HT) at three time intervals: $t = 1 \times 10^{-3}$ s. 162
7.2 Evolution of the Richtmyer-Meshkov instability at $AT = 0.635$, $Ma = 1.3$, using the ideal gas equation of state for air and SF6. This showcases different AMR levels (0-3) in Hytrac (HT) at three time intervals: $t = 1.3 \times 1.0^{-3}$ s. 162

7.3 Evolution of the Richtmyer-Meshkov instability at $AT = 0.635$, $Ma = 1.3$, using the ideal gas equation of state for air and SF6. This showcases different AMR levels (0-3) in Hytrac (HT) at three time intervals: $t = 1.8 \times 10^{-3}$ s. 163
7.4 Evolution of the Richtmyer-Meshkov instability at $AT = 0.635$, $Ma = 1.3$, using the ideal gas equation of state for air and SF6. This showcases different AMR levels (0-3) in Hytrac (HT) at three time intervals: $t = 2.8 \times 10^{-3}$ s. 163
7.5 Evolution of the Richtmyer-Meshkov instability at $AT = 0.635$, $Ma = 1.3$, using the ideal gas equation of state for air and SF6. This showcases different AMR levels (0-3) in Hytrac (HT) at three time intervals: $t = 3.0 \times 10^{-3}$ s. 163
7.6 Evolution of the Richtmyer-Meshkov instability at $AT = 0.635$, $Ma = 1.3$, using the ideal gas equation of state for air and SF6. This showcases different smoothening factors (SF) $SF = 15$ in (a), $SF = 1000$ in (b), and $SF = 50000$ in (c) in Hytrac (HT) at three time intervals: $t = 1.3 \times 10^{-3}$ s. 164
7.7 Evolution of the Richtmyer-Meshkov instability at $AT = 0.635$, $Ma = 1.3$, using the ideal gas equation of state for air and SF6. This showcases different smoothening factors (SF) $SF = 15$ in (a), $SF = 1000$ in (b), and $SF = 50000$ in (c) in Hytrac (HT) at three time intervals: $t = 1.8 \times 10^{-3}$ s. 164
7.8 Evolution of the Richtmyer-Meshkov instability at $AT = 0.635$, $Ma = 1.3$, using the ideal gas equation of state for air and SF6. This showcases different redistribution factors (RF) $RF = 10$ in (a), $RF = 20$ in (b), and $RF = 200$ in (c) in Hytrac (HT) at three time intervals: $t = 1.3 \times 10^{-3}$ s. 165
7.9 Evolution of the Richtmyer-Meshkov instability at $AT = 0.635$, $Ma = 1.3$, using the ideal gas equation of state for air and SF6. This showcases different redistribution factors (RF) $RF = 10$ in (a), $RF = 20$ in (b), and $RF = 200$ in (c) in Hytrac (HT) at three time intervals: $t = 1.8 \times 10^{-3}$ s. 165

List of Tables

3.1 Toro tests data [7] 34
3.2 Comparison of BlastFOAM and OpenFOAM for various tests 53
3.3 Initial conditions of multi-material Shock-Tube. 58
3.4 Initial conditions of Trilab RMI case. 66
3.5 Initial condition of KHI case. 72
3.6 Initial condition of Jacobs and Krivets case. 73
3.7 Initial conditions 78

4.1 Dimensionless stiffened gas equation of state parameters which appear in equation (4.16). The initial densities are scaled on $\rho_{h,0}$. Rheological parameters for the light and heavy phases which appear in equations (4.18). 92
4.2 A breakdown of the rate of change of vorticity into the terms that appear on the right-hand-side of equation 4.33. The terms are characterised as 'Stabilising' or 'Destabilising' depending on their time-averaged contribution to this equation, and are ranked according to the magnitude of their respective contributions, e.g, 'S1' and 'D1' correspond to the terms with the largest stabilising and destabilising contributions, respectively. 102

Nomenclature

α	compressibility constant
γ	ratio of specific heat capacity cp/cv
Γ_{KHI}	growth rate of KHI
μ	dynamic viscosity
ψ	compressibility
ρ	density
σ	surface tension
τ	viscous stress
a	speed of sound in Riemann problem
A_t	Atwood number
c	speed of sound
C_k	volume fraction function
D	deuterium
E	energy
e	specific internal energy
e_∞	reference energy constant
F	force
G	shear modulus of the elastic materials
g	gravitational acceleration

H	indicator function
h	enthalpy or amplitude
He	helium
K	bulk modulus of the elastic materials
K_s	coefficient of stiffness
m	mass
m	relative Mach number of two streams in direction of perturbation in KHI
Ma	Mach number
n	neutron
n	polytropic exponent
p	pressure
p_∞	pressure at the bubble level, including the hydrostatic pressure
p_{g0}	initial bubble pressure
p_v	vapour pressure
R	gas constant
R	radius
r	radius
T	temperature
T	tritium
t	time
u	velocity component in x direction
V	volume
v	velocity component in y direction
v	volume
w	velocity component in z direction
x	spatial direction
x_{KHI}	ratio of complex frequency of the pertubation Γ_{KHI}
y	spatial direction

z	spatial direction
$\boldsymbol{\omega}$	vorticity vector
F_{body}	body forces vector
$\mathrm{F}_{surface}$	surface forces vector
F	vector of fluxes
q	heatflux vector
u	velocity vector
W	vector of primitive variables
BF	BlastFOAM
CFD	computational fluid dynamics
e.g.	exempli gratia
EOS	equation of state
FDM	finite difference method
FEM	finite element method
FLF	First Light Fusion
ICF	inertial confinement fusion
KHI	Kelvin-Helmholtz instability
LS	level set methods
Ltd.	limited company
MCF	magnetic confinement fusion
MFG	Matar Fluid Group
NIF	National Ignition Facility
OF	OpenFOAM
RMI	Richtmyer-Meshkov instability
RTI	Rayleigh-Taylor instability
VOF	volume-of-fluid methods

Acknowledgments

First, I would like to thank Almighty Allah for blessing me with this opportunity. I would also like to thank my supervisors, Prof. Omar Matar and Dr. Thomas Abadie at Imperial College London. I am very thankful for all their support during the last four years. I cannot imagine having better supervisors than Prof. Matar and Dr. Abadie. Their continuous support in matters beyond academia has greatly helped me. I was able to learn how to be productive, how to solve problems, and how to present. Prof. Matar and Dr. Abadie were always available to discuss research and all other matters of life, even on weekends. These four years have been the best journey of my life, working with some of the best people in their fields at one of the best universities in the world. I am also grateful for all the support I received from the Matar Fluids Group at Imperial College London, especially from Dr. Lyes Kahouadji and Ricardo, now Dr. Ricardo Constante. I was able to make amazing friendships at Imperial. I loved the time I spent in London and Oxford. I felt at home. I have never experienced such tolerance as I did in London and Oxford. London will always be my home, and I hope I can come back soon.

I am also grateful to First Light Fusion for providing the financial support for my PhD. I enjoyed working at First Light Fusion. In the beginning, the weekly travel from London to Oxford was very trying, but I got used to it. Dr. Nathan Joiner and Dr. David Chapman helped me with their expertise at First Light Fusion. I am very thankful for their support.

Finally, I would like to thank my family, my father, my sisters, my brother, and my wife who provided all the emotional support. I would like to thank my mother for all the hard work she put into me. I remember when I was at school and had difficulties, my mother always helped however she could. She could not read or write or solve any math problems, but she always sat down for hours and tried her best to help me. Even during my PhD, whenever I got stuck, she was there to support me. My mother may not know what a PhD is, or in which field I will earn it, but she knows it is something good.

Chapter 1

Introduction

Global warming is considered to be one of the greatest challenges of the 21^{st} century. On the one hand, increasing atmospheric temperature results in droughts. On the other, it causes the melting of glaciers, which then leads to flooding and increasing sea levels. For this reason, global warming could make several parts of our planet uninhabitable. As a result, there is an urgent need to act on global warming. Greenhouse gas emissions are considered to be the main cause of global warming. A solution for this societal challenge could be clean energy production through nuclear fusion technology. This technology is considered to be more cost-effective, reliable, scalable, and, importantly, inherently safer than nuclear fission technology.

Nuclear fission involves the splitting of a heavy atomic nucleus into two lighter nuclei, along with a few neutrons and a large amount of energy. This process is typically initiated by bombarding a heavy nucleus (such as uranium-235 or plutonium-239) with a neutron. The energy released during fission is harnessed in nuclear power plants to generate electricity. However, fission produces radioactive waste that remains hazardous for thousands of years and poses significant challenges for disposal and environmental safety. Additionally, the potential for catastrophic accidents, as seen in Chernobyl and Fukushima, raises concerns about the safety of nuclear fission technology.

Nuclear fusion, on the other hand, involves the combination of two light atomic nuclei to form a heavier nucleus, accompanied by the release of a significant amount of energy. Fusion reactions power the sun and other stars, where hydrogen nuclei fuse to form helium under extreme temperatures and pressures. Fusion has several advantages over fission: it produces much less radioactive waste, the fuel sources (such as deuterium and tritium) are more abundant, and there is no risk of a runaway chain reaction leading to a meltdown. However, achieving and maintaining the

conditions necessary for sustained nuclear fusion on Earth is extremely challenging and is the focus of ongoing research and development. Nuclear fusion is explored worldwide using different methods such as inertial confinement fusion (ICF) and magnetic confinement fusion (MCF). Recently, novel approaches to inertial confinement fusion have been introduced involving rapid bubble collapse culminating in energy generation via nuclear fusion. The energy produced by the nuclear fusion reaction can be used for clean electricity generation.

A nuclear fusion reaction is initiated under extreme conditions. Achieving and maintaining extremely high temperatures and densities to initiate thermonuclear burn is a major challenge of ICF. Hydrodynamic instabilities such as Kelvin-Helmholtz, Rayleigh-Taylor, and Richtmyer-Meshkov occur in ICF and lead to mixing of hotter and cooler layers, ultimately inhibiting ignition in ICF As a result, understanding the mixing induced by these instabilities is key to achieving sustainable ICF. Recent research in ICF, however, has primarily focused on experiments even though a detailed understanding of the mixing that controls flow dynamics and, indirectly, the thermonuclear burn in ICF, cannot be obtained solely from experiments. Therefore, there is an urgent need to use computational methods to gain insight into the mixing and the flow dynamics to optimise the design parameters of an ICF reactors.

Analysis of flows related to ICF require the development of multiphase computational methods for highly compressible flows. Interface-capturing and tracking approaches such as the volume-of-fluid and front-tracking methods could be suitable for simulation of the high-energy flows associated with ICF. Both computational methods have their advantages and disadvantages: the volume-of-fluid methods conserve mass readily, but front-tracking methods predict interfacial dynamics with superior accuracy. Furthermore, both methods need to be tested and applied for high-energy, compressible flows, and this will be the main subject of the present thesis.

The first stage of this research will involve the assessment and validation of the volume-of-fluid and front-tracking methods using a series of tests involving shock-tube flows, bubble collapse, and the development of Kelvin-Helmholtz and Richtmyer-Meshkov instabilities. In these tests, simulations will be carried out to ascertain whether the front-tracking and volume-of-fluid methods can determine the interface region accurately and conserve mass, momentum, and energy. The validated methods will be used to simulate models of ICF for parameter ranges relevant to fusion energy generation and the design of ICF reactors.

The rest of this thesis is organized as follows: Chapter 2 provides a literature review of relevant topics such as Inertial Confinement Fusion (ICF), hydrodynamic instabilities, shock waves, and interface modeling methods. Chapter 3 assesses different numerical codes, including OpenFOAM, BlastFOAM, and Hytrac. Chapter 4 conducts a detailed study to investigate the influence of non-Newtonian viscosity on the evolution of vorticity, as well as the Richtmyer-Meshkov instabilities (RMI) and Kelvin-Helmholtz instabilities (KHI). Chapter 5 explores how viscosity affects shock dynamics, the RMI/KHI, and average pressure, temperature, and density in a Fusion Target. chapter 6 concludes this work and outlines future research directions.

Novel Contributions

This thesis introduces several innovative contributions to the understanding of Richtmyer-Meshkov instabilities in non-Newtonian fluids, with a focus on their implications for inertial confinement fusion (ICF). The primary novel aspects include:

1. Validation of a hybrid front-tracking and volume-of-fluid method for highly-compressible, multiphase flows. This involves the assessment of whether these methods can capture highly compressible flows accurately and determine interface regions with precision.

2. Further development of the BlastFOAM code to model non-Newtonian shear-thinning flows, enhancing its capability to handle complex fluid dynamics scenarios relevant to ICF.

3. Formulation and investigation of a vorticity equation for non-Newtonian fluids. This includes breaking down each term to identify which terms generate and which terms dampen the vorticity.

4. Investigation of non-Newtonian effects on the evolution of hydrodynamic instabilities, such as the Richtmyer-Meshkov instabilities (RMI) and Kelvin-Helmholtz instabilities (KHI), through numerical simulations. This includes detailed analysis of how non-Newtonian viscosity impacts the growth of instabilities.

5. Investigation into the Influence of coverslip material on flow dynamics within ICF targets: This study explores how different coverslip materials affect the shock dynamics and post-compression properties average pressure, temperature, and density within inertial confinement fusion (ICF) targets. The findings provide valuable insights into optimizing coverslip material choice to enhance the efficiency and effectiveness of ICF processes.

Chapter 2

Literature Review

2.1 Nuclear Fusion

In a nuclear fusion reaction, two or more atomic nuclei are fused to form a single nucleus and subatomic particles, such as neutrons. The final mass of the products is less than the total mass of the reactants. This difference in the final mass can be explained with Einstein's equation $E = mc^2$, which is converted into energy that is released in a fusion reaction if the produced nuclei are lighter than iron-56 or nickel-62, where E represents energy, m represents mass, and c is the speed of light in a vacuum. The equation shows that mass can be converted into energy. Otherwise, the energy is absorbed in the case of fusion of heavier nuclei. This implies that lighter elements like hydrogen are more suitable for a nuclear fusion reaction in which hydrogen isotopes, deuterium, and tritium are fused to produce helium. An extremely large amount of energy plus a neutron is released during this process. An illustration of a fusion reaction is shown in figure 2.1.

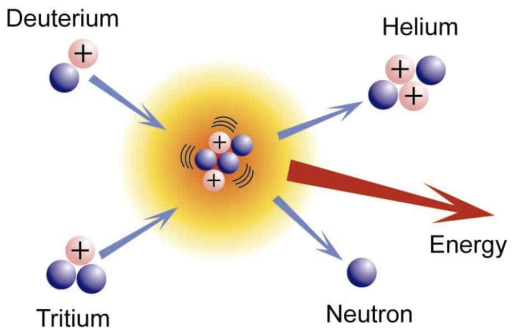


Figure 2.1: An illustration of a nuclear fusion reaction: Deuterium + Tritium → Helium + neutron [1].

Nuclear fusion is also the process by which energy is produced in stars by burning hydrogen. There is an almost unlimited resource available for nuclear fusion, considering that hydrogen is the most abundant element in the universe. The hydrogen isotopes deuterium and tritium needed for a fusion reaction can be produced from water (deuterium), and lithium (tritium). Although tritium is radioactive, it does not produce any serious danger, and its half-life is approximately 12 years.

Nuclear fusion technology is considered the holy grail of energy, which can help meet the exponential rise in energy demand without producing undesired carbon products or nuclear waste that is radioactive for millions of years. However, three main conditions are necessary for achieving nuclear fusion. First, extremely high temperatures (hotter than the surface of the sun) are required so that the ions can overcome the Coulomb barrier and combine. The Coulomb barrier refers to the electrostatic force that repels positively charged atomic nuclei from each other. Second, the ions must be confined to initiate collision and fusion. An ion density of 2-3$\times 10^{20}$ ions/m^3 is considered to be suitable. Third, the plasma must be kept hot long enough for the fusion reaction to commence.

Several methods, such as magnetic confinement fusion (MCF) and inertial confinement fusion (ICF), are currently being explored worldwide to achieve sustainable nuclear fusion. The MCF method uses strong magnetic fields to confine the plasma. The goal is to keep the extremely hot plasma away from the reactor walls and keep a large number of particles in confinement through magnetic forces to initiate a fusion reaction. Notable examples of MCF reactors are Tokamak and Stellarator reactor designs. ICF will be the main subject of this PhD, and a detailed description of it is provided below. The interested reader is referred to [18] for a more detailed description of MCF.

2.1.1 Inertial Confinement Fusion

The invention of powerful lasers in the 1960s facilitated the exploration of ICF technology. The idea behind this is that fusion fuel is heated rapidly by the lasers and the created plasma is compressed so immensely that it will not have enough time to escape. The plasma is trapped by its own inertial forces before it is burned in a fusion reaction. The National Ignition Facility (NIF) in Lawrence Livermore National Laboratory in the USA is an example of a facility conducting research with applications to ICF technology. A schematic illustration of ICF (at NIF) is given in figure 2.2.

A small spherical capsule about a 5 mm in diameter filled with deuterium and tritium gas is placed inside a gold canister called a hohlraum (German for cavity). The inner hohlraum is beamed with lasers. Since the hohlraum consists of gold, the laser light is converted into X-rays by the inner hohlraum walls. The X-rays are uniformly aimed at the capsule. The intense radiation of X-rays ablates the outer portion of the capsule shell and leads to the implosion of the outer shell. The internal energy increases immensely as the spherical capsule is compressed. The compression of the capsule leads to very high temperatures and densities and a fusion reaction is initi-

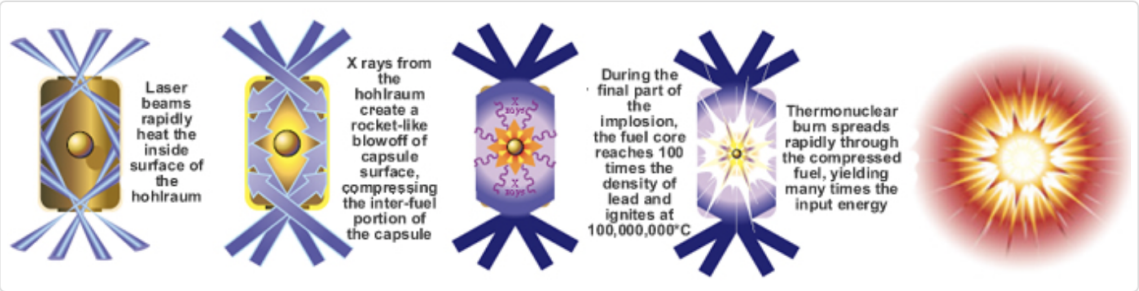


Figure 2.2: A schematic of inertial confinement fusion process at the National Ignition Facility at the Lawrence Livermore Laboratory, USA [2].

ated at these extreme conditions. This reaction releases energy and produces helium and very energetic neutrons.

Achieving and maintaining extremely high temperatures and densities to initiate thermonuclear burn is a major challenge of ICF which requires a uniform compression of the spherical capsule. A non-uniform/non-spherical compression will not heat the core of the capsule, called the 'hotspot', to the required temperatures. Flow phenomena such as Rayleigh-Taylor, Kelvin-Helmholtz, and Richtmyer-Meshkov instabilities, lead to the mixing of hot fuel and cold outer shell of the capsule. This perturbs the compression process that is no longer uniform. The perturbation by hydrodynamic instabilities reduces the temperature at the core of the capsule and inhibits ignition. As a result, understanding the mixing induced by the hydrodynamic instabilities is key to achieving sustainable ICF.

2.1.2 Inertial Confinement Fusion in a Collapsing Bubble

In 1934, Frenzel and Schultes [19] discovered the *sonoluminescence* effect during their research on sonar at the University of Cologne. They placed an ultrasound transducer in a tank of photographic developer fluid. After developing the film, the researchers found small dots on it. The occurrence of these dots was unexpected. Further experiments led to the conclusion that these dots were small bubbles that occurred, burst, and emitted light whenever the ultrasound transducer is switched on. The sonoluminescence phenomenon remained unexplained until Jarman [20] from Imperial College London in 1960 suggested a theory that this phenomenon could result from microshocks within the bursting bubble. Support for this theory comes from numerical simulations [21] that showed a sudden pressure and temperature rise after the bubble collapse. This theory is supported by experimental research as well. Matula et al. [22] measured an acoustic pulse near the bubble after the light emission. This acoustic pulse could be the rebound of the shock inside the bubble after the collapse. Sonoluminescence occurs when a gas bubble in a liquid is excited by acoustic waves. This excitation of the bubble leads to expansion and contraction of the bubble and it ends with a sudden collapse of the bubble. This sudden collapse results in light emission, as shown, in figure 2.3. Moss et al. [23] suggest that the

flash after the collapse could result from the energy cascade from the ions to the electrons, to the photons. It is assumed that the occurring shock becomes stronger as it reaches the bubble's centre. The shock compresses and heats the bubble's centre so much that light is emitted because of thermal emission from a radiating plasma consisting of ions and electrons. Strong experimental evidence for plasma generation was obtained in 2005 by Flannigan and Suslick [24]. The authors reported extreme conditions (temperature $>$ 15000 K and pressure $>$ 4000 atm [25], [26]) and a correlation between the driving pressure and the plasma electron density in bubble collapse. The temperature, plasma electron density, and degree of ionization increase with the rising pressure. The plasma electron density in these experiments was reported to be similar to that obtained at the Lawrence Livermore National Laboratory ICF experiments.

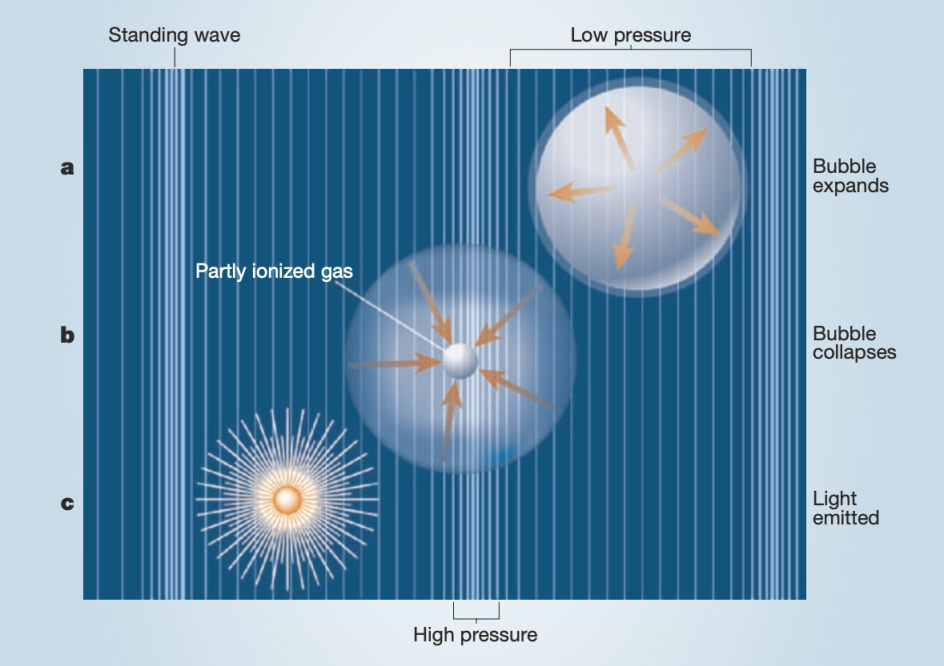


Figure 2.3: Sonoluminescence in a collapsing bubble: a bubble is excited with sound waves; (a) at low pressure, the bubble starts expanding; (b) as the pressure increases the bubble contracts and collapses; (c) the bubble collapse leads to light emission as a result of energy cascade: from the ions to electrons, and then to photons [3].

The work of Hawker and Ventikos [27] [28] [29] indicated that extreme conditions could be achieved in controlled shock-induced bubble collapse; these extreme conditions could facilitate a thermonuclear fusion reaction. The technology enabled by these findings involves rapid bubble collapse and shock-induced compression culminating in energy generation via nuclear fusion. However, it is crucial to determine the effect of hydrodynamic instabilities and the mixing they engender on the degree of inertial confinement associated with these fusion processes. This thesis, particularly in chapter 5, emphasizes how the choice of coverslip material influences these dynamics and contributes to optimizing fusion processes.

2.2 Hydrodynamic Instabilities

Small perturbations at the interface between two fluids of different densities can grow exponentially, resulting in the development of hydrodynamic instabilities under certain conditions; these instabilities could, in turn, lead to secondary flows, and possibly turbulence. A turbulent regime promotes an increase in mixing, and a rise in the rates of heat and mass transfer, as a result of strong interfacial deformation. Instability-induced mixing in ICF can take place between the hot fuel and the cold outer shell of the capsule, which reduces the temperature at the core of the capsule and inhibits ignition. For this reason, understanding the mixing and flow dynamics associated with phenomena such as Rayleigh-Taylor, Kelvin-Helmholtz, and Richtmyer-Meshkov instabilities is key to achieving sustainable ICF. The following is a review of the literature relevant to each of these instabilities within the context of mixing in relation to ICF.

2.2.1 Richtmyer-Meshkov Instabilities

In 1960, R. Richtmyer [30] proposed a theoretical and numerical analysis of shock-induced interface perturbations. Richtmyer's theoretical model for instability growth is based on the following equation:

$$\frac{dh}{dt} = A_t h_0 k \Delta u \tag{2.1}$$

where h is the perturbation amplitude, h_0 is the initial perturbation amplitude, A_t is the Atwood number, k is the wavenumber, Δu is the velocity difference across the interface, and t is time. This theory was qualitatively confirmed by the shock-tube experiments of E. Meshkov [31] in 1969. The Richtmyer-Meshkov instabilities develop due to the perturbation growth at the interface between two fluids of different densities initiated by a shock wave interaction with the interface. The Richtmyer-Meshkov instability incorporates compressibility, such as shock and rarefaction waves with hydrodynamic instabilities that lead to a transition to the turbulent regime. When a shock wave traverses an interface, it amplifies the perturbations, which are initially present at the interface. The amplification and growth of the perturbation result from the generation of vorticity. This vorticity develops due to the several mechanisms such as the misalignment of the pressure gradient of the shock and the density gradient across the interface, called the *baroclinic vorticity*. The development of the Richtmyer-Meshkov instability is illustrated in figure 2.4. In figure 2.4(a), an interface between a heavier fluid (ρ_2) and a lighter one (ρ_1) is impacted by a shock wave. The shock wave interaction with the interface produces vorticity of varying strength at the interface. This vorticity gradient along the interface results in variations in the velocity along the interface, as shown in figure 2.4(b), which leads to further stretching and deformation of the interface, see figure 2.4(c). The deformation of the interface caused by the Richtmyer-Meshkov instability can lead to secondary

flows driven by the Kelvin-Helmholtz instability. A detailed discussion of Richtmyer-Meshkov instabilities and the research in this field is given in chapter 4.1. In this thesis, the non-Newtonian effects on the evolution of hydrodynamic instabilities, such as the Richtmyer-Meshkov instability (RMI) and Kelvin-Helmholtz instability (KHI), are investigated. This includes a detailed analysis of how non-Newtonian viscosity impacts the growth of instabilities. Additionally, the formulation and investigation of a vorticity equation for non-Newtonian fluids are presented. This includes breaking down each term to identify which terms generate and which terms dampen the vorticity. The vorticity-driven RMI is studied in detail in chapter 4.1 to understand how non-Newtonian effects impact the vorticity evolution.

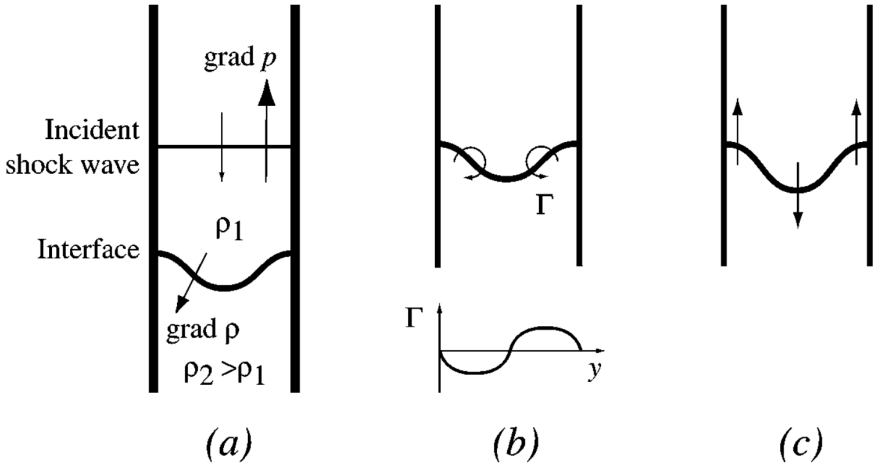


Figure 2.4: A schematic showing the development of a Richtmyer-Meshkov instability: (a) a shock wave travelling towards an interface separating two fluids of different density; (b) the generation of vorticity after the impact; (c) deformation of the interface following shock impact [4].

2.2.2 Rayleigh-Taylor Instabilities

Lord Rayleigh [32] described the development of instabilities, which occur when a heavier fluid overlies a lighter one. If these fluids are subjected to gravitational acceleration, the interface separating the fluids is distorted and mixing is initiated through so-called Rayleigh-Taylor instabilities. These instabilities can grow without bound, giving rise to complex structures due to the mixing of the two fluids, though viscosity and surface tension act to mitigate large wavenumber perturbations. The following equation can be used to estimate the growth of the RTI:

$$h^2 = -k\Delta g \frac{(\rho_2 - \rho_1)}{(\rho_2 + \rho_1)} \tag{2.2}$$

where h is the perturbation amplitude, k is the wavenumber, Δg is the gravitational acceleration difference, ρ_1 is the density of the lighter fluid, and ρ_2 is the density of the heavier fluid. The experimental work by Lewis [33] confirmed the theoretical predictions of Lord Rayleigh and G. I. Taylor during the early stages of the flow, where the perturbation growth can still be predicted by linear models. During the latter stages, in the nonlinear regime of perturbation development, buoyancy-drag models are used to investigate the perturbation growth due to complex behaviour of the Rayleigh-Taylor instability. The complexity and richness of the patterns generated by this instability has made it a popular subject for numerical simulations [5], as shown in figure 2.5.

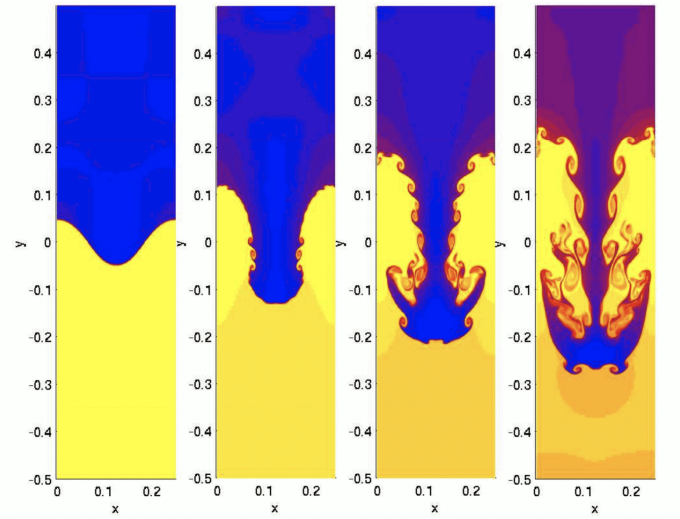


Figure 2.5: An illustration of the development of Rayleigh-Taylor instabilities as well as Kelvin-Helmholtz instabilities in the last three snapshots [5].

2.2.3 Kelvin-Helmholtz Instabilities

The Kelvin-Helmholtz instabilities [34, 35] develop due to the presence of a velocity gradient in a single fluid or across an interface of multiphase fluids. Several factors such as gravity, viscosity, surface tension, perturbation wavenumber, tangential velocity difference, and density ratio, influence the perturbation growth in this instability. Gravity, viscosity, and surface tension damp the perturbation growth, whereas higher perturbation wavenumber, velocity, and density gradient increase the instability growth. In compressible flows, the Kelvin-Helmholtz instabilities can be described using the following equation:

$$\frac{x_{KHI}^2 - 1}{x_{KHI}^4} = \frac{\gamma_1^2 c_2^2}{\gamma_2^2 c_1^2} \left[\frac{(x_{KHI} - Ma_{relative})^2 - \frac{c_2^2}{c_1^2}}{(x_{KHI} - Ma_{relative})^4} \right] \tag{2.3}$$

where x_{KHI} represents the ratio of the complex frequency of the perturbation Γ_{KHI} to the product of the wavenumber k and the velocity difference ΔU. γ_1 and γ_2 are the specific heat ratios of the first and second fluids, respectively, and c_1 and c_2 are the speeds of sound in the first and second fluids, respectively. $Ma_{relative}$ is the relative Mach number of the flow.

$$x_{KHI} = \frac{\Gamma_{KHI}}{k\Delta U} \tag{2.4}$$

The instability growth rate can be calculated by obtaining the imaginary part of the frequency Γ_{KHI} and using equation 2.4. The Kelvin-Helmholtz instabilities can be found in several natural and man-made processes such as clouds, the Great Red Spot in the atmosphere of Jupiter, supernova explosions, and ICF. An illustration of Kelvin-Helmholtz instability is given in figure 2.6.



Figure 2.6: An illustration of the development of Kelvin-Helmholtz instabilities [6]

As previously mentioned, hydrodynamic instabilities such as RMI, RTI and KHI occur in ICF. These instabilities initiate mixing between the hot fuel and the cold outer shell of the capsule. The mixing between these regions reduces the temperature required for ignition. For this reason, it is crucial to understand and control the mixing process in conventional ICF.

2.3 Fundamentals of Compressible Flows

2.3.1 Compressible Flows

If the density of a fluid varies with the change of pressure and temperature, it is defined as *compressible*. On the contrary, flows with constant density assumption are categorised as *incompressible*. However, in real life, all flows are compressible to some extent, but some e.g., liquids are considered incompressible, as a result of negligible density changes in case of compression. Gases, on the other hand, show higher density variation with the changes in pressure and temperature. For this reason, gases are mostly considered as compressible. The compressibility of a fluid, ψ, can be defined as follows:

$$\psi = -\frac{1}{v}\frac{\partial v}{\partial p} \tag{2.5}$$

where ψ is the compressibility, v is the specific volume, and p is the pressure. The negative sign indicates that an increase in pressure leads to a decrease in volume. Gases tend to have higher compressibility e.g. air's compressibility is around 10^{-5} m^2/N at 1 atm. Liquids like water, on the other hand, have lower ψ, which is approximately 10^{-10} m^2/N at 1 atm for water. Equation 2.5 can be expressed in terms of density instead of volume. Assuming that the fluid element has a unit mass, this leads to $\rho = 1/v$; as a result, equation 2.5 can be written in terms of the density:

$$\psi = \frac{1}{\rho}\frac{\partial \rho}{\partial p} \tag{2.6}$$

Speed of Sound

The speed of sound c describes the transmission of small disturbances through a medium. These disturbances are transmitted by the collisions of randomly moving molecules. The speed of sound depends on the properties of a medium e.g. stiffness. Gases have a significantly lower speed of sound compared to that in liquids and solids as a result of lower stiffness, e.g., c in air is around $343m/s$, in water $1481m/s$, and in iron $5120m/s$. The following equations can be used to determine the speed of sound in gases c_g, liquids c_l, and solids c_s, respectively:

$$c_g = \sqrt{\gamma R T} \tag{2.7a}$$

$$c_l = \sqrt{\frac{K_s}{\rho}} \tag{2.7b}$$

$$c_s = \sqrt{\frac{K + \frac{4}{3}G}{\rho}} \tag{2.7c}$$

In these equations, c_g is the speed of sound in gases, which is influenced by the heat capacity ratio γ, the specific gas constant R, and the temperature T. The speed of sound in liquids, c_l, depends on the isentropic bulk modulus K_s and the density ρ. For solids, the speed of sound c_s is determined by both the bulk modulus K and the shear modulus G, as well as the density ρ. When an object travels through a medium, it creates disturbances. If the object travels slower than the actual speed of sound of the medium (gas, liquid, solid or plasma) then this is regarded as subsonic travel and accordingly, the compressibility effects are considered to be negligible. In case of approximately the same speed as the traveling object and the speed of sound of the medium, it is said to be transonic travel. In the transonic regime, compressibility effects become important.

If the speed of the travelling object is higher than the speed of sound of the medium then it is considered as supersonic travel and the compressibility effects become very important and they cannot be neglected as a result of the occurrence of shock waves and significant density changes. The Mach number Ma is used to categorise the fluid flow in subsonic, transonic, or supersonic regime. The Mach number Ma can be calculated with equation as follows:

$$Ma = \frac{v_o}{c} \tag{2.8}$$

where v_0 is the speed of the travelling object and c is the speed of the sound in the medium. The flow regimes can then be categorised in terms of Mach number:

subsonic regime	$M < 1$
transonic regime	$M \approx 1$
supersonic regime	$M > 1$

2.3.2 Rankine-Hugoniot Relations and Shock Waves

The study of compressible flow is closely intertwined with the study of shock waves. In a shock wave, fluid properties such as density, temperature, velocity, and pressure experience a rapid change over a small region. These drastic changes across a shock wave can be studied mathematically with the Rankine-Hugoniot relations. Shock waves occur at supersonic flow conditions. These supersonic flow conditions trigger changes in the flow field, which are generally nonlinear and involve intricate interactions. The Rankine-Hugoniot relations offer the essential mathematical framework to tackle these challenges and to obtain insightful solutions.

The conservation laws of mass, momentum, and energy are applied to derive the Rankine-Hugoniot relations. The conservation laws establish a way of relating the fluid properties across a shock wave. In a 1-D steady flow, the Rankine-Hugoniot relations can be written in the following form:

$$\rho_2 u_2 = \rho_1 u_1 \tag{2.9a}$$

$$p_2 + \rho_2 u_2^2 = p_1 + \rho_1 u_1^2 \tag{2.9b}$$

$$\frac{1}{2}u_2^2 + \frac{\gamma}{\gamma - 1}\frac{p_2}{\rho_2} = \frac{1}{2}u_1^2 + \frac{\gamma}{\gamma - 1}\frac{p_1}{\rho_1} \tag{2.9c}$$

.

In these equations, ρ_1 is the density of the fluid in the pre-shock state, and ρ_2 is the density of the fluid in the post-shock state. The term u_1 represents the velocity of the fluid in the pre-shock state, and u_2 represents the velocity of the fluid in the post-shock state. The pressure of the fluid in the pre-shock state is denoted by p_1, and the pressure of the fluid in the post-shock state is denoted by p_2. The adiabatic index, γ, is the ratio of specific heats. The subscripts 1 and 2 are used to distinguish the state of the fluid upstream (before) and downstream (after) the shock wave, respectively. In the field of compressible flows, shocks are essential phenomena that affect fluid behaviour. As a result, understanding shock waves and their effect on the flow field has important implications for several practical applications. This includes ICF, supersonic combustion, aerodynamics, etc. Shock waves interact with physical phenomena for example, other shock waves, boundaries etc. These interactions increase the complexity of the flow. Comprehensive study of these processes requires a detailed understanding of complex flow configurations. A method for solving the Riemann problem is a valuable tool for providing a good understanding of impact of the shock waves on the flow behaviour and their interactions, particular relevant in compressible flows. A detailed description of the Riemann problem is given in the following section.

2.3.3 Riemann Problem

The Riemann problem, named after mathematician Bernhard Riemann, is one of the fundamental problems in the area of hyperbolic conservation laws theory. The Riemann problem gives valuable insights into the complex behavior of shock waves. Abrupt changes in fluid properties such as pressure, density, velocity, and temperature lead to a Riemann problem. One of the most notable examples of a Riemann problem, is which arises in shock-tubes.

The classic shock-tube problem consists of two stationary fluids. One fluid is usually highly pressurized, while the other is at low pressure. There exist several other theoretical shock-tube problems as well, where the fluids are at the same pressure but they differ in their other thermophysical or flow properties such as density, temperature, or velocity. In a classic shock-tube problem, the fluids are separated by a diaphragm. The sudden removal of the diaphragm produces a rarefaction wave, a contact discontinuity, and a shock wave. The shock wave compresses the fluid in the lower-pressure region. This leads to a sudden increase in temperature, pressure, density, and velocity. The Riemann problem will be used in chapter 3 as a reference solution to assess the ability of the volume-of-fluid method as implemented in OpenFOAM/BlastFOAM and front-tracking method in Hytrac to capture shocks.

Methodology for Solving 1-D Riemann Problem:

A detailed description of the solution methodology for the one-dimensional (1-D) Riemann problem is given below. Since the shock-tube cases will be used to assess the accuracy of the multiphase interface capturing method in BlastFOAM/OpenFOAM

and interface tracking method in Hytrac for highly compressible flows. Unsteady 1-D Euler equations and the ideal gas equation of state are used in this solution technique. This solution assumes that no vacuum is present. The interested reader is referred to [7] for a solution of Riemann problem within a vacuum.

The Riemann problem for 1-D unsteady Euler equations is the initial value problem (IVP) for conservation laws:

$$\mathbf{U}_t + \mathbf{F}(\mathbf{U})_x = \mathbf{0} \tag{2.10}$$

where $\mathbf{U}$ and $\mathbf{F}$ are expressed by

$$\mathbf{U} = \begin{bmatrix} \rho \\ \rho u \\ E \end{bmatrix}, \quad \mathbf{F} = \begin{bmatrix} \rho u \\ \rho u^2 + p \\ u(E+p) \end{bmatrix} \tag{2.11}$$

The initial conditions for this Riemann problem are as follows:

$$\mathbf{U}(\mathbf{x}, \mathbf{0}) = \begin{cases} \mathbf{U}_L & \text{if x} < 0 \\ \mathbf{U}_R & \text{if x} > 0 \end{cases}$$

where $\mathbf{W}$ is the vector of primitive variables (density, velocity, and pressure) and $\mathbf{U}_L$ is the velocity in the left region and $\mathbf{U}_R$ is the velocity in the right region:

$$\mathbf{W}_L = \begin{bmatrix} \rho_L \\ u_L \\ p_L \end{bmatrix}, \mathbf{W}_R = \begin{bmatrix} \rho_R \\ u_R \\ p_R \end{bmatrix} \tag{2.12}$$

In these equations, ρ_L and ρ_R represent the densities of the fluid in the left and right regions, respectively. The terms u_L and u_R represent the velocities of the fluid in the left and right regions, respectively. The terms p_L and p_R represent the pressures of the fluid in the left and right regions, respectively. The structure of the Riemann problem consists of three waves: a shock wave, a contact discontinuity, and a rarefaction wave. These waves have the eigenvalue of $\lambda_1 = u-a$, $\lambda_2 = u$, and $\lambda_3 = u+a$. The three waves divide the solution region into four constant states: $\mathbf{W}_L$, $\mathbf{W}_{*L}$,$\mathbf{W}_{*R}$ and $\mathbf{W}_R$ as shown in figure 2.7.

The solution for $\mathbf{W}_L$ and $\mathbf{W}_R$ is known from the initial conditions, while $\mathbf{W}_{*L}$ and $\mathbf{W}_{*L}$ are unknown. This unknown region is referred to as the star region. The unknown region is divided by the contact discontinuity (λ_2=u), whereas the left

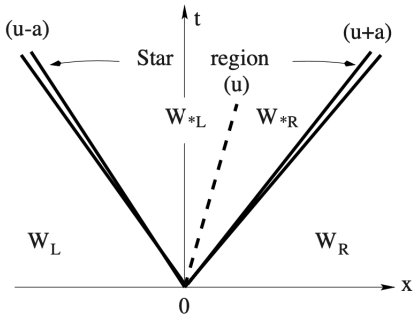


Figure 2.7: Solution structure of the Riemann problem [7].

(λ_1=u-a) and the right waves(λ_2=u+a) are either a shock wave or a rarefaction wave. There can be four different wave patterns in the solution of the Riemann problem as illustrated in figure 2.8.

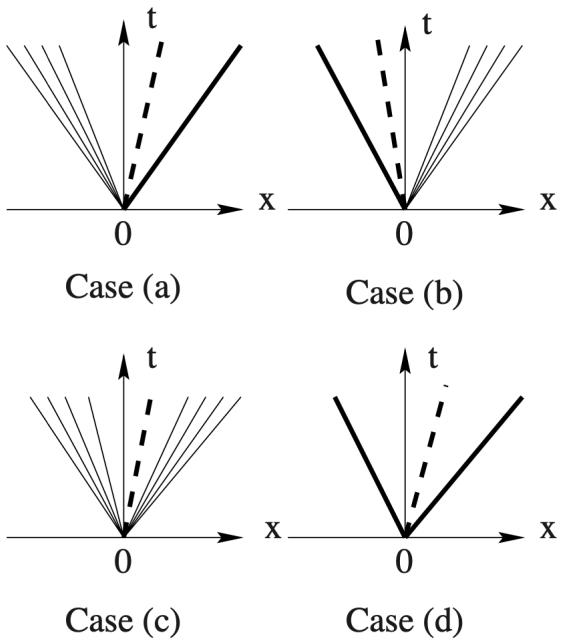


Figure 2.8: Wave patterns that can occur in a Riemann problem Case (a): left rarefaction wave right shock wave Case (b): left shock wave right rarefaction wave Case (c) left and right rarefaction waves Case (d) left and right shock wave [7].

An eigenstructure analysis of the Euler equations shows that the pressure p_* and the velocity u_* in the star region are constant, whereas the density is ρ_{*L} in the $\mathbf{W}_{*L}$ region and ρ_{*R} in the $\mathbf{W}_{*R}$ region. Interested reader is referred to [7] for a detailed description of the eigenstructure analysis of Euler equations. The solution for p_* can be found with equation 2.13. The definition of the variables used in equation 2.13 is given below.

$$f(p, \mathbf{W}_L, \mathbf{W}_R) \equiv f_L(p, \mathbf{W}_L) + f_R(p, \mathbf{W}_R) + \Delta u = 0, \Delta u \equiv u_R - u_L, \qquad (2.13)$$

with f_L given by

$$f_L(p, \mathbf{W_L}) = \begin{cases} (p - p_L)\left[\frac{A_L}{p+B_L}\right]^{1/2} & \text{if } p > p_L \text{ (shock)}, \\ \frac{2a_L}{(\gamma-1)}\left[\left(\frac{p}{p_L}\right)^{\frac{\gamma-1}{2\gamma}} - 1\right] & \text{if } p \leq p_L \text{ (rarefaction)} \end{cases} \tag{2.14}$$

and with f_R

$$f_R(p, \mathbf{W_R}) = \begin{cases} (p - p_R)\left[\frac{A_R}{p+B_R}\right]^{1/2} & \text{if } p > p_R \text{ (shock)}, \\ \frac{2a_R}{(\gamma-1)}\left[\left(\frac{p}{p_R}\right)^{\frac{\gamma-1}{2\gamma}} - 1\right] & \text{if } p \leq p_R \text{ (rarefaction)} \end{cases} \tag{2.15}$$

The data-dependent constants A_R, A_L, B_R and B_L can be determined with the following equations.

$$\left.\begin{aligned} A_L &= \frac{2}{(\gamma+1)\rho_L}, \\ B_L &= \frac{(\gamma-1)}{(\gamma+1)p_L}, \\ A_R &= \frac{2}{(\gamma+1)\rho_R}, \\ B_R &= \frac{(\gamma-1)}{(\gamma+1)p_R}, \end{aligned}\right\} \tag{2.16}$$

The pressure p_* is calculated by solving the equation 2.13 along with equations 2.14 -2.16 numerically. The obtained pressure is used in equation 2.14 to compute the velocity u_* in the star region.

$$u_* = \frac{1}{2}(u_L + u_R) + \frac{1}{2}[f_R(p_*) - f_L(p_*)] \tag{2.17}$$

The unknown densities ρ_{*L} and ρ_{*R} are obtained by identifying the types of waves. The wave can be identified as a shock or a rarefaction wave by comparing the pressure p_* to the pressures p_L and p_R. By obtaining the values of u_*, p_*, ρ_{*L} and ρ_{*R} in the regions $\mathbf{W}_L$, $\mathbf{W}_{*L}$,$\mathbf{W}_{*R}$ and $\mathbf{W}_R$ and identifying the type of the waves the solution of the Riemann problem is completed.

Left Shock Wave

A left shock wave is identified by the condition $p_* > p_L$. For a shock wave, only the density behind the shock and the shock speed has to be calculated. The pressure p_* and u_* are known from the equation 2.13 and 2.17. The density ρ_{*L} can be calculated using the following relation:

$$\rho_{*L} = \rho_L \left[\frac{\frac{p_*}{p_L} + \frac{\gamma-1}{\gamma+1}}{\frac{\gamma-1}{\gamma+1}\frac{p_*}{p_L} + 1} \right] \tag{2.18}$$

The shock speed is determined with the following equation:

$$S_L = u_L - a_L \left[\frac{\gamma+1}{2\gamma}\frac{p_*}{p_L} + \frac{\gamma-1}{2\gamma} \right]^{1/2} \tag{2.19}$$

Left Rarefaction Wave

A left rarefaction wave is identified by the condition $p_* \leq p_L$. The pressure p_* and u_* are known from the equation 2.13 and 2.17. For a rarefaction the density behind the wave, Head and Tail of the wave and the fan enclosed by the Head of the Tail have to be calculated as shown in figure 2.9

$$\rho_{*L} = \rho_L \left(\frac{p_*}{p_L} \right)^{\frac{1}{\gamma}} \tag{2.20}$$

The sound speed behind the rarefaction wave is:

$$a_{*L} = a_L \left(\frac{p_*}{p_L} \right)^{\frac{\gamma-1}{2\gamma}} \tag{2.21}$$

The rarefaction wave is enclosed by the Head S_{HL} and the Tail S_{TL}.

$$S_{HL} = u_L - a_L \tag{2.22}$$

$$S_{TL} = u_* - a_{*L} \tag{2.23}$$

The solution inside the fan is determined with the following equations:

$$\mathbf{W}_{Lfan} = \begin{cases} \rho & = \rho_L \left[2\frac{\gamma+1}{\gamma-1} + \left(\frac{\gamma-1}{\gamma+1}\right) a_L \left(u_L - \frac{x}{t}\right) \right]^{\frac{2}{\gamma-1}}, \\ u & = \frac{2}{\gamma+1} \left[a_L + \frac{\gamma-1}{2} u_L + \frac{x}{t} \right], \\ p & = p_L \left[2\frac{\gamma+1}{\gamma-1} + \left(\frac{\gamma-1}{\gamma+1}\right) a_L \left(u_L - \frac{x}{t}\right) \right]^{\frac{2\gamma}{\gamma-1}} \end{cases}$$

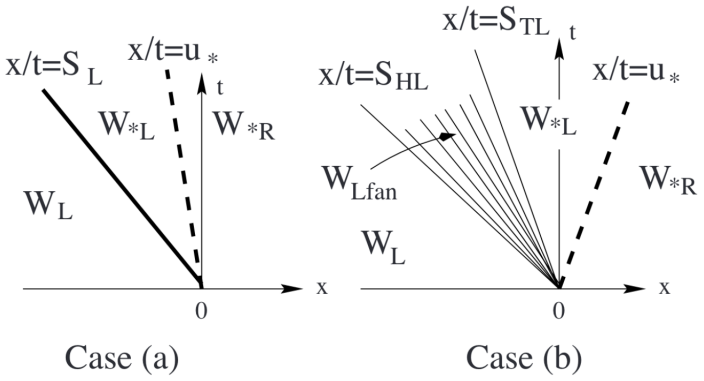


Figure 2.9: left shock wave in case (a) and left rarefaction wave in case (b) [7].

Right Shock Wave

A right shock wave as shown in 2.10 is identified by the condition $p_* > p_R$. For a shock wave, only the density behind the shock and the shock speed have to be calculated. The pressure p_* and u_* are known from the equation 2.13 and 2.17. The density ρ_{*R} can be calculated using the following relation

$$\rho_{*R} = \rho_R \left[\frac{\frac{p_*}{p_R} + \frac{\gamma-1}{\gamma+1}}{\frac{\gamma-1}{\gamma+1}\frac{p_*}{p_R} + 1} \right] \tag{2.24}$$

The shock speed is determined with the following equation:

$$S_R = u_R + a_R \left[\frac{\gamma+1}{2\gamma}\frac{p_*}{p_R} + \frac{\gamma-1}{2\gamma} \right]^{1/2} \tag{2.25}$$

Right Rarefaction Wave

A right rarefaction wave is identified by the condition $p_* \leq p_R$. The pressure p_* and u_* are known from the equation 2.13 and 2.17. For a rarefaction the density behind the wave, Head and Tail of the wave and the fan enclosed by the Head of the Tail

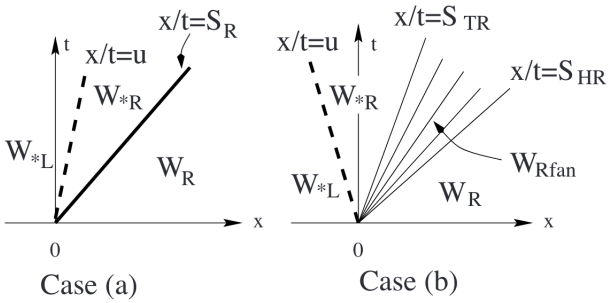


Figure 2.10: right shock wave in case (a) and right rarefaction wave in case (b) [7].

have to be calculated as shown in figure 2.10:

$$\rho_{*R} = \rho_R \left(\frac{p_*}{p_R} \right)^{\frac{1}{\gamma}} \tag{2.26}$$

The sound speed behind the rarefaction wave is:

$$a_{*R} = a_R \left(\frac{p_*}{p_R} \right)^{\frac{\gamma-1}{2\gamma}} \tag{2.27}$$

The rarefaction wave is enclosed by the Head S_{HR} and the Tail S_{TR}.

$$S_{HR} = u_R - a_R \tag{2.28}$$

$$S_{TR} = u_* - a_{*R} \tag{2.29}$$

The solution inside the fan is determined with the following equations:

$$\mathbf{W}_{Rfan} = \begin{cases} \rho & = \rho_R \left[2\frac{\gamma+1}{\gamma-1} + \left(\frac{\gamma-1}{\gamma+1} \right) a_L \left(u_L - \frac{x}{t} \right) \right]^{\frac{2}{\gamma-1}}, \\ u & = \frac{2}{\gamma+1} \left[a_R + \frac{\gamma-1}{2} u_R + \frac{x}{t} \right], \\ p & = p_R \left[2\frac{\gamma+1}{\gamma-1} + \left(\frac{\gamma-1}{\gamma+1} \right) a_R \left(u_R - \frac{x}{t} \right) \right]^{\frac{2\gamma}{\gamma-1}}. \end{cases}$$

The validation of a hybrid front-tracking and volume-of-fluid method for highly compressible flows is performed in chapter 3 using the shock-tube Toro tests, which are examples of the Riemann problem. This involves the assessment of whether these methods can capture highly compressible flows accurately and determine interface with precision

2.4 Governing equations

The governing equations are obtained by applying the following three laws of conservation.

1. Conservation of mass
2. Conservation of momentum
3. Conservation of energy

A brief description of the governing equations is given in this chapter. The interested reader is referred to [10] for a detailed description.

Continuity equation

The mass balance: "The rate of increase of mass in a fluid element is equal to the net rate of flow of mass into the fluid element" is applied to an infinitesimal, fixed control volume to obtain the mass continuity equation (mass conservation equation):

$$\frac{\partial \rho}{\partial t} + \boldsymbol{\nabla} \cdot (\rho \mathbf{u}) = 0 \tag{2.30}$$

In incompressible flows, the first term in the continuity equation is considered to be zero because of constant density assumption.

$$\boldsymbol{\nabla} \cdot \mathbf{u} = 0 \tag{2.31}$$

Momentum equation

The momentum equation is obtained from Newton's Second Law, which describes the conservation of momentum, and states that the rate of change of momentum of fluid-particle equals the sum of the forces on the particle. A fixed infinitesimal control volume is used to derive the momentum equation:

$$\frac{\partial \rho \mathbf{u}}{\partial t} + \boldsymbol{\nabla} (\rho \mathbf{u}\mathbf{u}) = -\boldsymbol{\nabla} p + \boldsymbol{\nabla} \cdot \left(\mu \left[\boldsymbol{\nabla} \mathbf{u} + (\boldsymbol{\nabla} \mathbf{u})^T - \frac{2}{3} (\boldsymbol{\nabla} \cdot \mathbf{u}) \mathbf{I} \right] \right) + \rho \mathbf{g} \tag{2.32}$$

Energy equation

The energy equation is obtained by applying the First Law of Thermodynamics to a fixed infinitesimal control volume, which states that the rate of change of energy of a fluid particle is equal to the rate of heat addition to the fluid particle plus the rate of work done on the particle:

$$\frac{\partial (\rho e)}{\partial t} + \boldsymbol{\nabla} \cdot [(\rho e + p)\mathbf{u}] = \boldsymbol{\nabla} \cdot (\mu \boldsymbol{\nabla} \cdot \mathbf{u}\mathbf{u}) - \rho \mathbf{g} \cdot \mathbf{u} \tag{2.33}$$

where, t, ρ, μ, $\mathbf{u}$, p, $\mathbf{g}$ correspond to the time, local density and viscosity, velocity, pressure, and acceleration due to gravity. Using the wavelength of the interface perturbation λ (see chapter 4 for a detailed explanation), the shock velocity U_S, the corresponding time scale $t_S = \lambda/U_S$, and dynamic pressure $\rho_h U_S^2$, the equations are written in dimensionless form:

$$\tilde{\boldsymbol{\nabla}} \cdot \tilde{\mathbf{u}} = -\frac{1}{\tilde{\rho}} \frac{D\tilde{\rho}}{D\tilde{t}} = -\frac{Ma^2}{\tilde{\rho}} \frac{D\tilde{p}}{D\tilde{t}} \tag{2.34}$$

$$\frac{\partial \tilde{\rho}\tilde{\mathbf{u}}}{\partial \tilde{t}} + \tilde{\boldsymbol{\nabla}} \left(\tilde{\rho}\tilde{\mathbf{u}}\tilde{\mathbf{u}}\right) = -\tilde{\boldsymbol{\nabla}}\tilde{p} + \frac{1}{Re}\tilde{\boldsymbol{\nabla}} \cdot \left(\tilde{\mu}\left[\tilde{\boldsymbol{\nabla}}\tilde{\mathbf{u}} + \left(\tilde{\boldsymbol{\nabla}}\tilde{\mathbf{u}}\right)^T - \frac{2}{3}\left(\tilde{\boldsymbol{\nabla}} \cdot \tilde{\mathbf{u}}\right)\mathbf{I}\right]\right) + \frac{1}{Fr^2}\tilde{\rho}\tilde{\mathbf{g}} \tag{2.35}$$

$$\frac{\partial(\tilde{\rho}\tilde{e})}{\partial \tilde{t}} + \tilde{\boldsymbol{\nabla}} \cdot [(\tilde{\rho}\tilde{e} + \tilde{p})\tilde{\mathbf{u}}] = \frac{1}{Re}\tilde{\boldsymbol{\nabla}} \cdot (\tilde{\mu}\tilde{\boldsymbol{\nabla}} \cdot \tilde{\mathbf{u}}\tilde{\mathbf{u}}) - \frac{1}{Fr^2}\tilde{\rho}\tilde{\mathbf{g}} \cdot \tilde{\mathbf{u}} \tag{2.36}$$

where $Ma =$, $Re =$ and $Fr =$ stand for the Mach, Reynolds, and Froude numbers, respectively.

Equation of State

The equation of state relates the state variable such as density ρ, pressure p, temperature T or specific internal energy e under a given condition. In incompressible flows, the density is considered to be constant. For this reason, the mass conservation equation and the momentum equation are sufficient to describe the flow field if no heat transfer is involved in the physical system. However, in case of heat addition, the energy equation is needed as well to describe incompressible flows. On the other hand, in compressible flows the density changes due to pressure and temperature variation. As a result, a linkage between the mass and momentum equation on the one hand and the energy equation on the other is required. Ideal gas equation is used for gases and is defined below:

The stiffened gas equation of state is employed to describe solids and liquids.

$$\tilde{p} = (\gamma - 1)\tilde{\rho}\tilde{e} - \gamma\tilde{p_0} \tag{2.37}$$

where $\tilde{p}$ is the dimensionless pressure, γ is the adiabatic index, $\tilde{\rho}$ is the dimensionless density, $\tilde{e}$ is the dimensionless specific internal energy, and $\tilde{p_0}$ is the dimensionless stiffening pressure. The gases are modelled with the ideal gas equation of state. The ideal gas law can be reformulated to involve the density of the gas, ρ, by substituting

the volume V with the mass and density relationship. From the standard form $PV = nRT$, and knowing that $V = \frac{m}{\rho} = \frac{nM}{\rho}$, the equation can be derived as follows:

$$p\left(\frac{nM}{\rho}\right) = nRT \tag{2.38}$$

where p is the pressure, n is the number of moles, M is the molar mass, ρ is the density, R is the universal gas constant, and T is the temperature.

Rheological Model

The non-Newtonian fluid behaviour is modeled using the Bird-Carreau-Yasuda model. Both shear-thinning and temperature dependence are taken into account when modeling the viscosity:

$$\tilde{\mu}(\dot{\gamma}, \tilde{T}) = \tilde{\mu}_\infty + \frac{\tilde{\mu_0}\tilde{E}_T - \tilde{\mu}_\infty}{[1 + (\tilde{\kappa}\tilde{E}_T)^2(\dot{\gamma}^2)]^{(1-n)/2}} \tag{2.39}$$

$$\tilde{E_T} = \exp[a(\frac{\tilde{T}_{ref}}{\tilde{T} - b} - c)] \tag{2.40}$$

where μ_∞ and μ_0 represent the infinite and zero shear-rate viscosities, respectively. The flow index is denoted by n, while κ represents the relaxation time. The constants a, b, and c are included to account for the temperature dependence of the viscosity, with a being set to zero in simulation cases where the viscosity is only considered as a function of shear rate. This choice of setting $a = 0$ eliminates the influence of temperature on the viscosity in such cases and enables a more focused investigation of the shear-rate-dependent viscosity behavior. Note that equations (4.16) and (4.18) are dimensionless.

2.4.1 Multiphase Flows

Multiphase flows refer to flows, consisting of at least two immiscible fluids with different thermophysical properties, e.g. liquid-gas, gas-gas, or liquid-plasma. These flows have found application in research and industrial fields such as energy generation, automotive, aviation and robotics. Multiphase flows play a crucial role in the development process of different technologies, for instance, enhancing the combustion efficiency of internal combustion engines or understanding the dynamics and mixing of materials in inertial confinement fusion. Obtaining a detailed understanding of the mixing in inertial confinement fusion (ICF) from experiments alone is difficult. For this reason, there is heavy reliance on computational multiphase methods for predicting design parameters. Computational methods for multiphase flows needs to be designed to work well in extreme conditions such as high pressures, high temperatures, and high-density variations between the different phases. Furthermore, they should be able to operate accurately in opposite extremes of strongly

surface tension-dominant flows versus strongly deforming flows. Some of the most important challenges of numerical methods for multiphase flows include:

1. Mass, momentum, and energy conservation,
2. Accurate calculation of discontinuities across the interface,
3. Modelling of complex topologies,
4. Simulation stability,
5. Accurate calculation of surface tension forces.

Several computational methods exist for multiphase/two-phase flows. An overview of these methods is given in figure 2.11. A detailed description of all the two-phase flow methods is beyond the scope of this thesis. The interested reader is referred to [10] and [36]. The Lattice-Boltzmann-Method (LBM), Smoothed-Particle Hydrodynamics (SPH), two-fluid methods like the Eulerian-Eulerian or Eulerian-Lagrangian approach are considered not suitable for the requirements of this PhD project due to higher computational costs and excessive development work required.

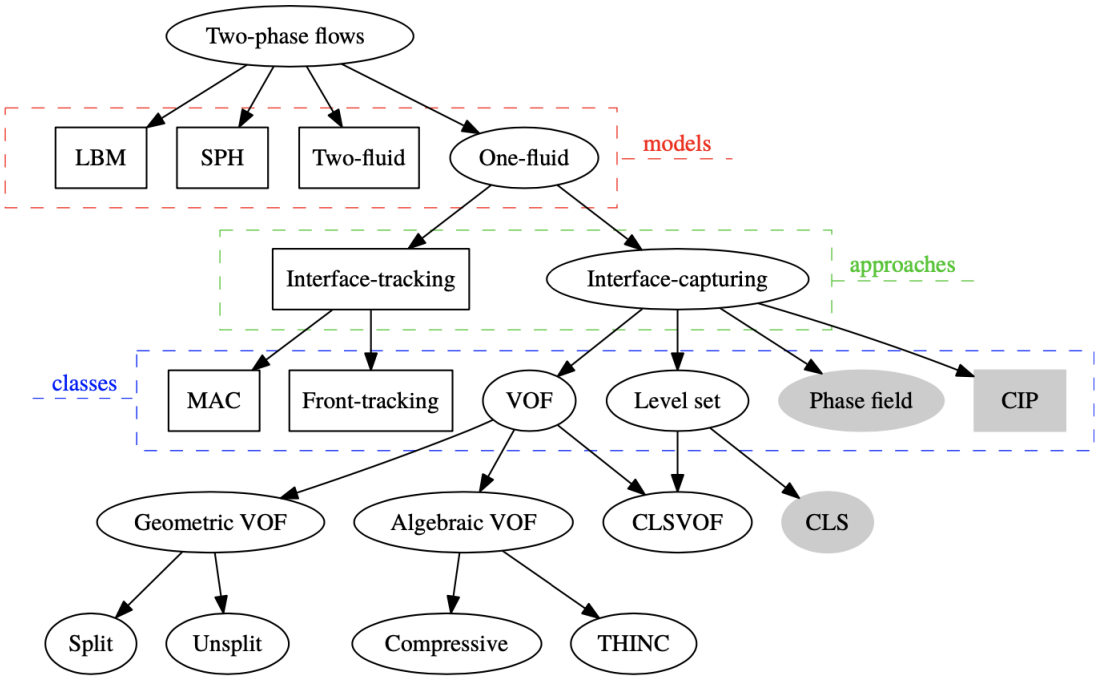


Figure 2.11: Classification of computational multiphase flow methods [8].

The focus of this PhD project will be one-fluid multiphase methods: the volume-of-fluid and front-tracking. Both computational methods have their advantages and disadvantages. The volume-of-fluid methods are considered to conserve mass, momentum, and energy better. However, the accurate prediction of the interface region

remains a challenge (especially with algebraic VOF) which is critical for understanding the dynamics and mixing of multi-materials in inertial confinement fusion. On the other hand, front-tracking can precisely predict the interface, but conservation of mass, momentum, and energy is a challenge in front-tracking (especially hybrid front-tracking). Furthermore, both methods need to be tested for high-energy flows. There is a lack of understanding of whether these methods can simulate highly compressible flows. This gap in understanding will be addressed in this PhD project.

The volume-of-fluid methods are categorised as interface-capturing and the front-tracking methods as interface-tracking. The interface refers to the region which separates the two fluids. Therefore, an accurate calculation of the interface is crucial to achieve accurate results in multiphase simulations especially in the research field of inertial confinement fusion, where the interface is essential for the understanding of dynamics and the mixing of the materials. A description of the other one-fluid methods such as marker and cell (MAC), phase field and constraint interpolation profile (CIP) can be found in [36] and [8].

Interface Capturing Methods

In Interface capturing methods, the interface is captured by a scalar function such as volume fraction in VOF or the distance function in Level Set Method. The volume-of-fluid (VOF) and the Level Set (LS) methods are well-known interface-capturing methods for multiphase modelling but both methods have their advantages and disadvantages and varying degrees of success in the modelling of multiphase flows over wide regimes (high temperature, pressure and density gradients).

Volume-of-Fluid Methods

A phase indicator function $H(\mathbf{x}, t)$ is used in VOF to identify the two different fluids:

$$H(\mathbf{x}, t) = \begin{cases} 1 & \text{if x is in the reference fluid} \\ 0 & \text{if x is in the other fluid} \end{cases}$$

The indicator function does not change in each fluid parcel unless phase change is taking place. As a result, the material derivative of the indicator function H becomes zero:

$$\frac{DH}{Dt} = \frac{\partial H}{\partial t} + \nabla \cdot (\mathbf{u}H) - H\nabla \cdot \mathbf{u} = 0 \tag{2.41}$$

This equation states that the material derivative of the phase indicator function H is zero, meaning H remains constant along a fluid parcel's path unless a phase change occurs. Here, $\frac{DH}{Dt}$ is the material derivative of H, $\frac{\partial H}{\partial t}$ is the partial derivative of H with respect to time, $\nabla \cdot (\mathbf{u}H)$ represents the divergence of the product of velocity $\mathbf{u}$ and H, and $H\nabla \cdot \mathbf{u}$ is the product of H and the divergence of the velocity field $\mathbf{u}$.

The spatial average of the H in each computational cell is used to calculate the volume fraction: The spatial average of the H in each computational cell is used to calculate the volume fraction:

$$C_k(t) = \frac{1}{V}\int_{\Omega} H(\mathbf{x}, t)dV \tag{2.42}$$

Here, $C_k(t)$ is the volume fraction, V is the volume of the computational cell, and $\int_{\Omega} H(\mathbf{x}, t)dV$ represents the integral of H over the cell volume Ω. Integrating equation 2.42 over a computational cell and substituting H in 2.42 by equation 2.41 leads to the following equation for volume fraction:

$$V\frac{\partial C_k(t)}{\partial t} + \int_{\partial\Omega} (\mathbf{u}\cdot\mathbf{n})H(x,t)dS = \int_{\Omega} H\nabla\cdot\mathbf{u}dV \tag{2.43}$$

Figure 2.12 illustrates how the different fluids and the location of the interface is determined in VOF by using the volume fraction function (C_k). The volume fraction function C_k varies between 1 and 0. The cells with $C_k = 1$ are occupied by only the reference fluid, and the cells with $C_k = 0$ are only filled with the other fluid. The interface is located in those cells where the value of the volume fraction is $0 < C_k < 1$.

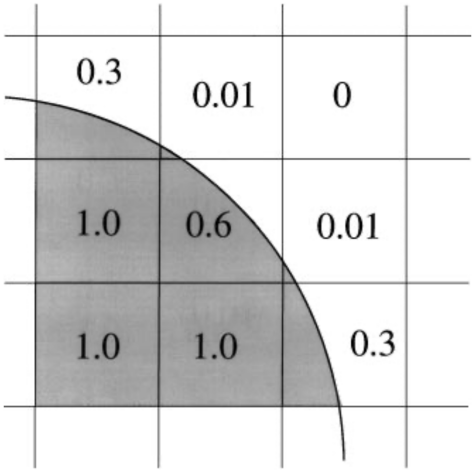


Figure 2.12: The volume fraction function in volume-of-fluid [9].

The volume-of-fluid method proceeds in two steps: the determination of the interface and the advection of the interface. Two different methods are available to determine the interface and its advection. One method reconstructs the interface and advects the interface with geometric methods. This method is called geometric VOF. The other method, called the algebraic VOF does not reconstruct the interface.

In this method, the interface is determined with equation 2.42 with a numerical approximation (volume-averaged, polynomial or hyperbolic-tangent representation) for the indicator function. The advection of the calculated interface is performed using numerical schemes such as compressive or THINC (tangent of hyperbola for interface capturing). A detailed description of the flux computing schemes compressive and THINC can be found in [8].

The geometric VOF method proceeds in two steps as aforementioned. The first is the reconstruction of the interface based on the known volume fraction C_k and the normal to the interface. After reconstructing the interface, volume fraction fluxes are computed for the advection. The simple line interface calculation (SLIC) was one of the first methods used for the reconstruction of the interface. SLIC is first order with lower accuracy. In this method, the Interface is reconstructed out of segments aligned with the mesh. An illustration of the SLIC method is given in figure 2.13. Although easy to implement, this interface reconstruction is not smooth and inaccurate. Therefore, the advection of this coarse interface generates flotsam [9].

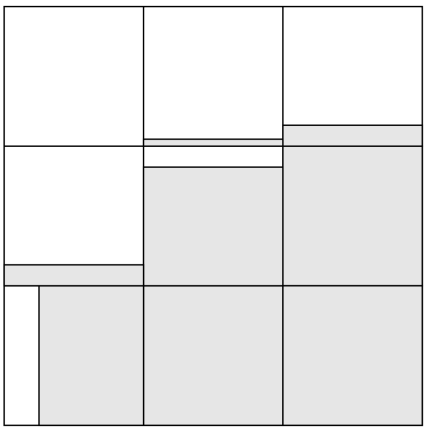


Figure 2.13: The interface reconstruction using the SLIC method in VOF [10].

The piecewise linear interface reconstruction (PLIC) is another method used to reconstruct the interface in geometric VOF. An illustration of PLIC is given in figure 2.14. This method can reconstruct a smooth and more accurate interface as compared to SLIC. In PLIC, the interface is reconstructed as a line (2D) or as a plane (3D). The equation 2.44 is used to approximate the interface:

$$\mathbf{m} \cdot \mathbf{x} + a = 0 \tag{2.44}$$

Equation 2.44 approximates the interface in the PLIC method. Here, $\mathbf{m}$ is the interface normal vector, $\mathbf{x}$ is the position vector, and a is a constant used to approximate the volume fraction C_k in each computational cell. Different authors have developed various approaches to calculate the interface normal m. Some of the most

well-known methods will be described briefly in this chapter. The interested reader is referred to [8] for a detailed description of the methods briefly described in this chapter and as well as the other available methods. One of well-known methods is the Young's method. Youngs' method calculates m in 2.44 as an approximation to a normalized gradient of the volume fraction. It is considered to be fast and accurate at low resolutions. Unfortunately, this method does not converge with increasing mesh refinement and even becomes less accurate at high resolutions. The centered-columns method is another method used to estimate the interface normal m. This method yields accurate results at high resolutions. Further development of the Youngs' method is the mixed Youngs-centered method (MYC) that combines the advantages of the Youngs's method (accurate results at low resolution) and the centred-columns method (accurate results at high resolution). The efficient least-squares volume-of-fluid interface reconstruction algorithm (ELVIRA) is a second-order accurate method developed for unstructured Cartesian meshes. ELVIRA has higher computational cost as compared to MYC. As a result, the MYC method has been widely used in the two-phase flow community. Although ELVIRA delivers better results on unstructured meshes as compared to MYC.

After the reconstruction of the interface, the next step in geometric VOF is the advection of the interface. Two different types of methods have been developed to advect the interface: the split method and the unsplit method. The unsplit method advects the computed interface in one step. The unsplit method is computationally more expensive and more complicated to implement as compared to the split method. The split method calculates one-dimensional advection in every spatial direction. Split method is easier to implement but it is considered to be less accurate than the unsplit method that can perform better in resolving non-smooth interfaces [8].

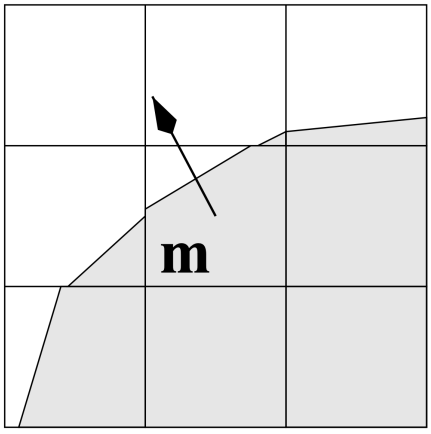


Figure 2.14: The interface reconstruction using the PLIC method in VOF [10].

Level Set Methods

The level set method is another interface-capturing computational method for multiphase simulations. This method uses a smooth signed distance function $\phi(x,t)$ to identify the different fluids and the interface. The distance function is negative in one fluid and positive in the other, and at the interface, it is equal to 0:

$$\phi(\mathbf{x},t) = \begin{cases} \phi(\mathbf{x}) & \text{if x is in the reference fluid} \\ 0 & \text{if at the interface} \\ -\phi(\mathbf{x}) & \text{if x is in the other fluid} \end{cases}$$

The distance function evolves according to the equation 2.45. The level set method can calculate interface properties (normal, curvature) accurately due to its smooth distance function. However, the function ϕ loses its signed distance characteristics after solving the advection equation. As a result, a re-initialization step is required to identify the fluids and the interface. This is the major drawback of the level set method that makes it a non-conservative method.

Several authors have tried to develop a mass-conservative level set method. The study from Enright et al. [8] is worth mentioning in this regard. Enright et al. developed a hybrid particle level set method. In this method, the interface is seeded with particles and an algorithm is employed to attract the particles towards the interface and update the distance function after the advection step. The author claims that the mass loss could be reduced from 80% to 2.6%. Furthermore, it is reported that the mass loss error reduces with higher resolution. This hybrid level set method can reduce the mass loss error as claimed by the authors. However, it makes the level method much more complicated and the simplicity is lost, which is one of the most important reasons for using the level set method.

$$\frac{\partial \phi}{\partial t} + \mathbf{u} \cdot \nabla \phi = 0 \tag{2.45}$$

Equation 2.45 describes the evolution of the distance function ϕ, where $\frac{\partial \phi}{\partial t}$ is the partial derivative of ϕ with respect to time, $\mathbf{u}$ is the velocity vector, and $\nabla \phi$ represents the gradient of ϕ.

Coupled Volume-of-Fluid Level Set Method

The level set and the volume-of-fluid methods have complementary advantages and disadvantages. The level set method can resolve the interface very accurately. However, it is not mass-conservative and the hybrid version of the level set method with mass loss correction by Enright et al. makes its algorithm very complicated. The volume-of-fluid method is mass conservative but the accurate computation of interface properties is not straightforward. Therefore, Sussman and Pucket [37] developed a coupled LS/VOF method, which takes advantage of mass conservation of the volume-of-fluid method and the accurate interface resolution of the level set method. The resulting method can resolve the interface accurately but some new problems

appear with this hybrid method such as lower accuracy in under-resolved regions and scalability.

Interface Tracking Methods

Interface tracking methods apply a different approach to identify the interface between the fluids than the interface capturing methods. While these methods use a marker function such as the volume fraction or the distance function to identify the different fluids and the boundary between them, interface tracking methods use connected marker points to represent explicitly the interface. Those marker points are then advected using the computed fluid velocity. Front-tracking is an interface tracking method that employs two different grids: a fixed one (Eulerian grid), where the governing equations are solved and a moving grid (Lagrangian grid), which contain the marker points that represent the interface.

Front-Tracking Methods

The basic idea of front-tracking is shown in figure 2.15. The elements (marker points) representing the interface are logically connected. The idea behind the logical connection of the elements is to determine the interface geometry by fitting a curve/surface through the elements. Furthermore, the logical connection of the elements is used for bookkeeping as well, so that in case of topology changes the elements can be deleted or added. The bookkeeping of the elements is straightforward in 2D, where the elements can be structured by connected lists. However, in 3D the implementation of a bookkeeping algorithm becomes very complicated considering the frequent topology changes. The governing equations are solved on the fixed grid as aforementioned and the location, where the material properties change are determined by the lagrangian grid. Therefore, both grids have to communicate with each other. A simplified overview of the grid communication is given is figure 2.16. The interface is advected using the interpolated fluid velocity that is computed on the fixed grid. Most of the interfacial physics such as surface tension is computed on the lagrangian grid. The surface tension term in the governing equation (solved on the fixed grid) is updated through the grid communication.

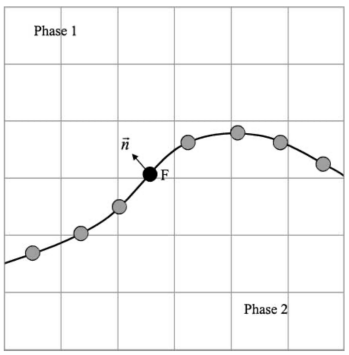


Figure 2.15: An illustration of front-tracking method [11].

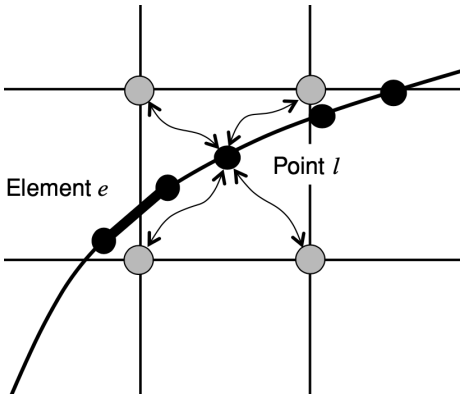


Figure 2.16: Grid communication between the eulerian and the lagrangian grid in front-tracking [10].

Hybrid Front-Tracking Methods

Front-tracking can maintain a sharp interface and conserve mass. However, the logical connectivity of the elements and the bookkeeping algorithm makes this method very complicated and computationally expensive. Therefore, this is one of the most important disadvantages of the front-tracking method. 3D front-tracking methods have been developed by Tryggvason et al. [38] and Glimm et al. [39] and [40]. The authors were able to achieve accurate simulations with their front-tracking methods. Further development of the front-tracking method is the hybrid front-tracking/level set method. Several authors have developed this method in different ways. The basic idea behind this hybrid method is to mitigate the complexity resulting from the logical connectivity of the elements and the bookkeeping algorithm.

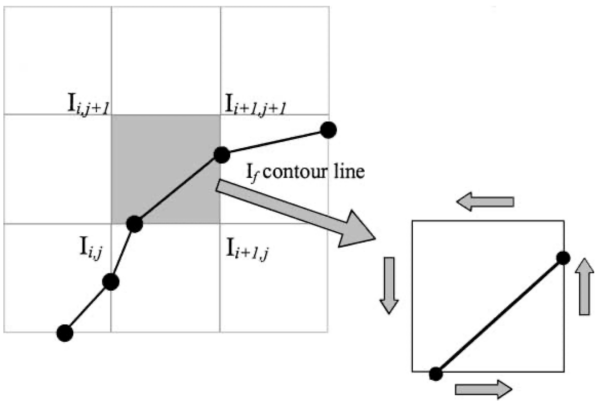


Figure 2.17: Interface reconstruction by level contours in hybrid front-tracking/level set method by Shin et al. [11].

One of the well-known hybrid front-tracking/level set methods is the Level Contour Reconstruction Method developed by Shin et al. [11]. In this method, the authors focused on a simple and robust algorithm. Their algorithm does not keep track of element connectivity, which makes its implementation much easier than the pure

front-tracking method. A brief description of Shin et al. method is given here. The interested reader is encouraged to read the prime source [11] for a detailed description. The existing approach in MFG front-tracking corresponds to that of the hybrid method developed by Shin et al. [11]. In this hybrid front-tracking/level set method Shin et al. use an interface reconstruction procedure to eliminate the need for bookkeeping for deleting/adding of the interfacial elements in case of topology changes. This procedure simplifies the algorithm significantly. Two different methods are used to represent the interface: an indicator function with a value of 0.5 at the interface and the tracked interface elements. The algorithm can either start with the indicator function and interface elements can be deposited on the 0.5 contours of the indicator function or the indicator function can be determined from the tracked interface elements. If the latter procedure (calculation of the indicator function from the tracked interface elements) is used, then at the end of a time step the tracked interface elements will be discarded and the interface will be reconstructed based on the 0.5 contour value in each computational cell using linear interpolation. An illustration of this procedure is shown in figure 2.17.

The neighbouring elements from the adjacent computational cell will have the same endpoint location. As a result, these adjacent interface elements will move with the same velocity. Although these elements do not have a logical connection as in the pure front-tracking method, they are physically connected. As a result of the simplification of the algorithm (no need for logical connection) hybrid front-tracking method has a significant advantage over the pure front-tracking method. However, mass conservation errors resulting from the reconstruction algorithm need to be mitigated with the use of high order interpolation methods [41], which makes the implementation challenging on unstructured grids.

The interface-capturing methods algebraic/geometric volume-of-fluid and the interface-tracking method hybrid front-tracking MFG front-tracking will be further developed in this PhD project to model highly compressible multiphase flows. First validations of the algebraic volume-of-fluid method are carried out against shock-tube flows and shock-induced bubble collapse case in the following chapter 3. In this thesis, the volume-of-fluid and front-tracking methods are assessed to determine their capability in capturing strong shocks and accurately capturing the interface. The evaluation is focused on their performance in various scenarios, including shock-tube tests and hydrodynamic instabilities.

Chapter 3

Numerical Codes

Validation of a hybrid front-tracking and volume-of-fluid method for highly compressible flows is performed in this chapter using the Toro shock-tube tests, which are examples of the Riemann problem. This involves the assessment of whether these methods can capture highly compressible flows accurately and determine interface regions precisely. Two codes based on the volume-of-fluid method, OpenFOAM and BlastFOAM, and one hybrid front-tracking code are assessed. The assessments include Toro shock-tube tests, 1-D Kalsiki shock-tube, bubble collapse, Richtmyer-Meshkov instability, and Kelvin-Helmholtz instability to evaluate their ability to capture strong shocks, accurately capture the interface, and represent the underlying flow dynamics and physics.

3.1 BlastFOAM vs OpenFOAM

3.1.1 Shock-Tube Validation Cases

Five different 1-D Riemann problems known as Toro tests [7] are used to investigate whether the VOF codes BlastFOAM and OpenFOAM can capture shocks accurately. Typically, these tests are conducted using a shock-tube divided into two regions by a diaphragm. These regions may consist of fluids with different velocities, pressures, or densities. Upon the removal of the diaphragm, three waves are initiated: 1) a shock wave that travels from the higher-pressure region to the low-pressure region; 2) a rarefaction wave that expands from the low-pressure region to the high-pressure region; and 3) a contact discontinuity, which is the middle wave between the shock wave and the rarefaction wave. These five Riemann problems (Toro tests) provide a benchmark for assessing the shock-capturing capability of a numerical code. The five Toro shock-tube tests are given in table 3.1.

Table 3.1: Toro tests data [7]

Test	ρ_L	u_L	p_L	ρ_R	u_R	p_R
1	1.0	0.75	1.0	0.125	0.0	0.1
2	1.0	-2.0	0.4	1.0	2.0	0.4
3	1.0	0.0	1000.0	1.0	0.0	0.01
4	5.99924	19.5975	460.894	5.99242	-6.19633	46.0950
5	1.0	-19.59745	1000.0	1.0	-19.59745	0.01

A 1-D shock-tube domain as illustrated in figure 3.1 is utilized. The mesh is composed of 1000×1 cells. The 2nd-order numerical scheme SFCD is employed in both OpenFOAM and BlastFOAM. OpenFOAM and BlastFOAM utilize the algebraic volume-of-fluid method to model multiphase flows.

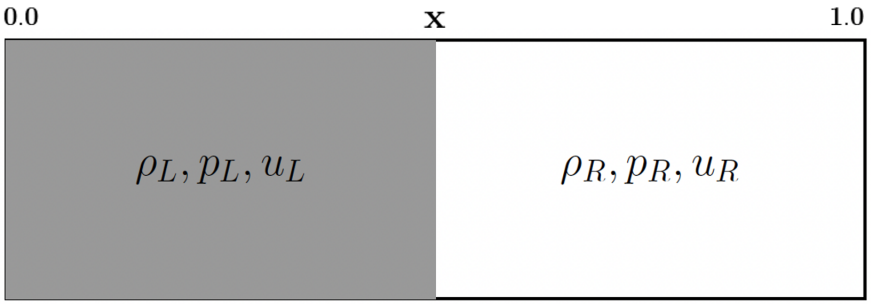


Figure 3.1: 1-D shock-tube domain as used in 5 Toro tests.

Test 1:

The shock-tube is initialized with one fluid in both regions (left and right). The left region is highly pressurized, whereas the right region is at low pressure. These regions are separated by an artificial interface at $x = 0.5$. The pressurized fluid is released into the low-pressure region at $t = 0$. The high-pressure fluid expands and drives a shock wave that compresses the fluid in the right region, leading to a sudden increase in temperature, pressure, density, and velocity. An analytical solution exists for this Riemann problem. Test 1 of the Riemann problem is simulated with OpenFOAM and BlastFOAM, and the simulation results are compared with the analytical results (exact solution). OpenFOAM and BlastFOAM can capture shocks, as shown in figures 3.2, 3.3, 3.4 and 3.5. However, the results from OpenFOAM are slightly more diffusive at the discontinuity compared to BlastFOAM in terms of temperature and density predictions. There is a discrepancy regarding the temperature and density predictions between the exact solution and OpenFOAM. A question occurs: What is the reason for the excessive diffusion in OpenFOAM. Does it come from the algebraic volume-of-fluid method that is considered to be very diffusive, or does this diffusion result from the numerical schemes? The algebraic volume-of-fluid as implemented in OpenFOAM and BlastFOAM uses an indicator function H to identify the fluids; its spatial average in a computational cell is used to calculate the volume fraction function based on a color function. The thermophysical properties of

each fluid are calculated according to this volume fraction function (equation 2.42). The volume fraction is considered to be equal to its spatial average everywhere in a computational cell. This leads to a smearing of the interface since an interface is not reconstructed in each computational cell. However, a smearing of the results as shown in 3.3, 3.4 cannot result from the diffusive algebraic volume-of-fluid method. Since this simulation is conducted with the same fluid in both regions. This leads to unity volume fraction function in each computational cell. Therefore, there is no real interface and the used numerical scheme (SFCD) has to be taken into consideration to investigate the reason for the diffusive results.

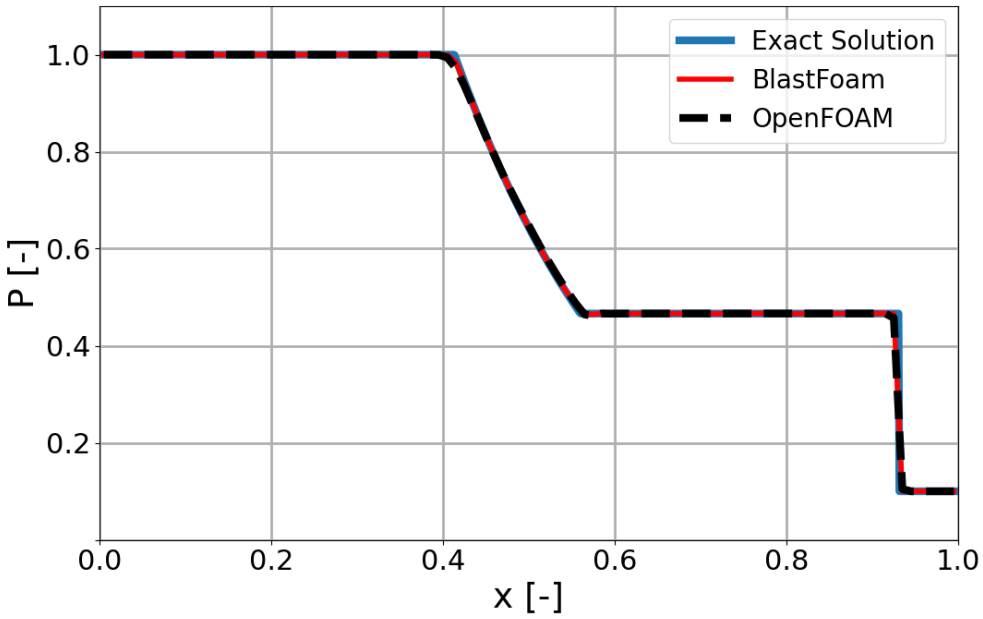


Figure 3.2: Pressure results for Toro test 1 at $t = 0.2$. The comparison includes BlastFOAM (solid red line), OpenFOAM (dashed black line), and the exact solution (solid blue line) of the Riemann problem using the SFCD numerical scheme with a 1000-cell mesh and ideal gas equation of state.

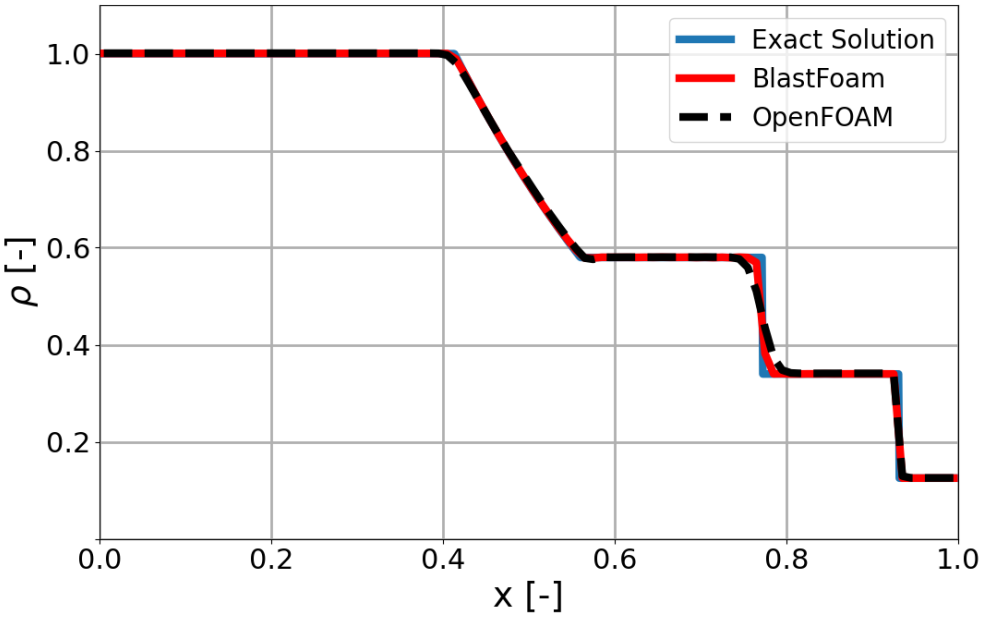


Figure 3.3: Density results for Toro test 1 at $t = 0.2$. The comparison includes BlastFOAM (solid red line), OpenFOAM (dashed black line), and the exact solution (solid blue line) of the Riemann problem using the SFCD numerical scheme with a 1000-cell mesh and ideal gas equation of state.

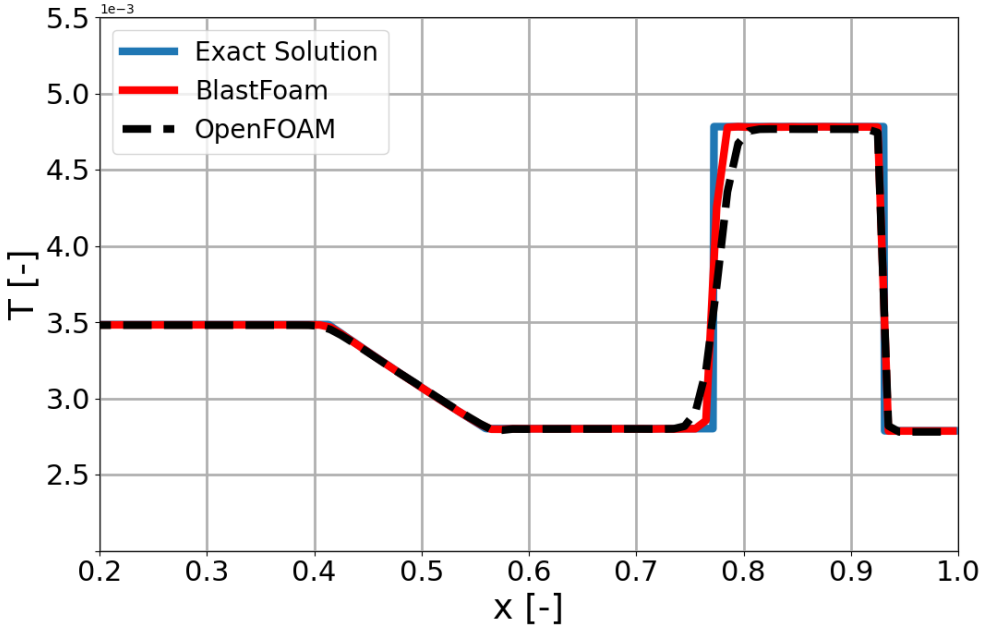


Figure 3.4: Temperature results for Toro test 1 at $t = 0.2$. The comparison includes BlastFOAM (solid red line), OpenFOAM (dashed black line), and the exact solution (solid blue line) of the Riemann problem using the SFCD numerical scheme with a 1000-cell mesh and ideal gas equation of state.

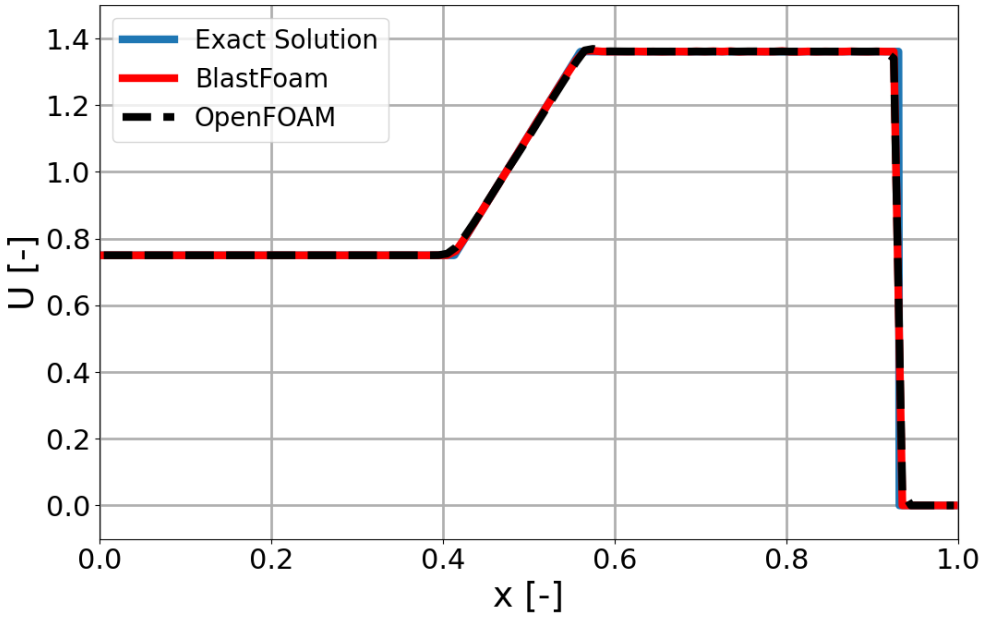


Figure 3.5: Velocity results for Toro test 1 at $t = 0.2$. The comparison includes BlastFOAM (solid red line), OpenFOAM (dashed black line), and the exact solution (solid blue line) of the Riemann problem using the SFCD numerical scheme with a 1000-cell mesh and ideal gas equation of state.

Numerical Scheme Study

Numerical schemes play a major role in computational fluid dynamics. Numerical schemes are essential in solving partial differential equations that govern the fluid behaviour. For this reason, it is of great importance to choose a suitable numerical scheme for the given conditions. A study using Toro test 1 is performed to assess the efficiency and accuracy of several numerical schemes such as Upwind, Minmod, SuperBee, VanLeer and SFCD. The second-order unbounded numerical scheme Central Differencing is not included in this study due to its known oscillatory nature.

Upwind: Upwind is a first order numerical scheme. This numerical scheme is known for its stability but it is also very diffusive. Upwind uses the upstream values for the flux computations.

SFCD: SFCD is a second order bounded numerical scheme. This numerical scheme utilizes a filtering procedure to ensure stability and avoid non-physical oscillations around the discontinuity.

VanLeer: VanLeer is a second-order flux limiter scheme that falls under the category of Total Variation Diminishing (TVD) schemes. It achieves high resolution at discontinuities and avoids introducing non-physical oscillations, making it particularly useful for problems involving shock waves.

Minmod: Minmod is a second-order flux limiter scheme as well like VanLeer. Minmod avoids non-physical oscillations by being more diffusive at the discontinuity.

SuperBee: Superbee is a high-resolution TVD flux limiter scheme like VanLeer and Minmod. Superbee is known to be very sharp compared to other TVD numerical schemes. However, this sharpness comes at a cost. This numerical scheme can produce non-physical oscillations near the discontinuity.

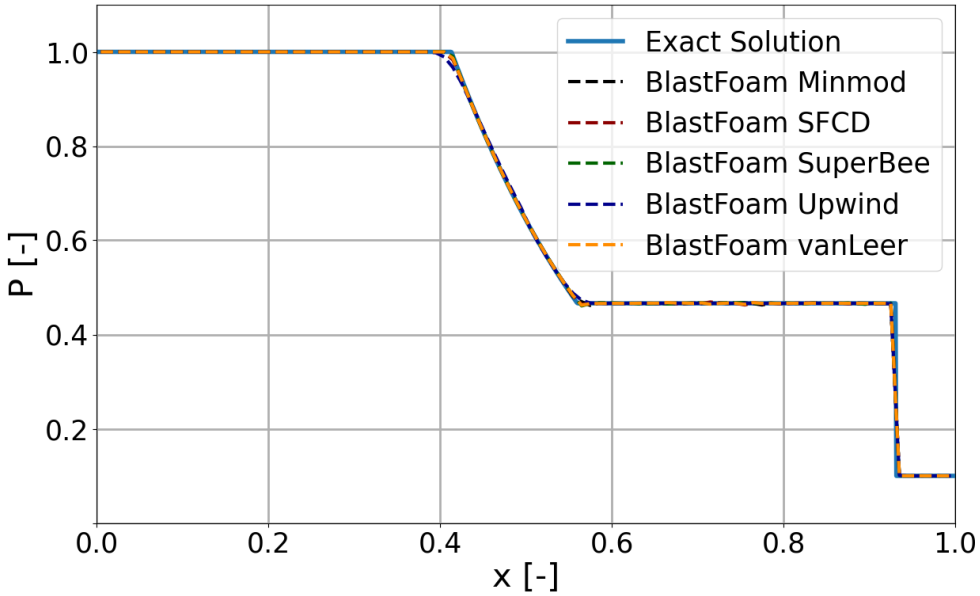


Figure 3.6: Pressure results for Toro test 1 at $t = 0.2$. The comparison includes different numerical schemes: Minmod, SFCD, SuperBee, Upwind, and VanLeer as implemented in BlastFOAM, with the exact solution (solid blue line) of the Riemann problem using a 1000-cell mesh and ideal gas equation of state.

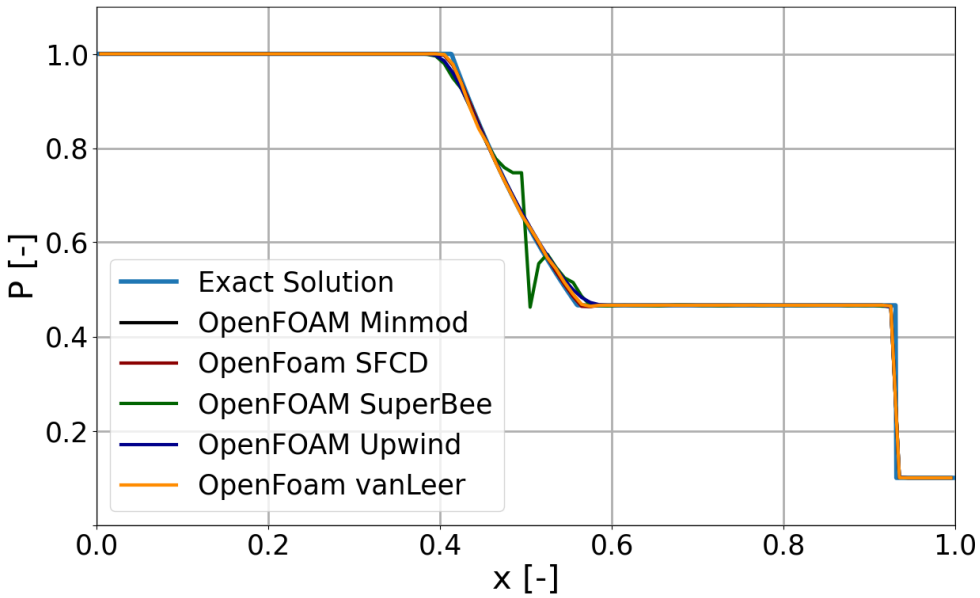


Figure 3.7: Pressure results for Toro test 1 at $t = 0.2$. The comparison includes different numerical schemes: Minmod, SFCD, SuperBee, Upwind, and VanLeer as implemented in OpenFOAM, with the exact solution (solid blue line) of the Riemann problem using a 1000-cell mesh and ideal gas equation of state.

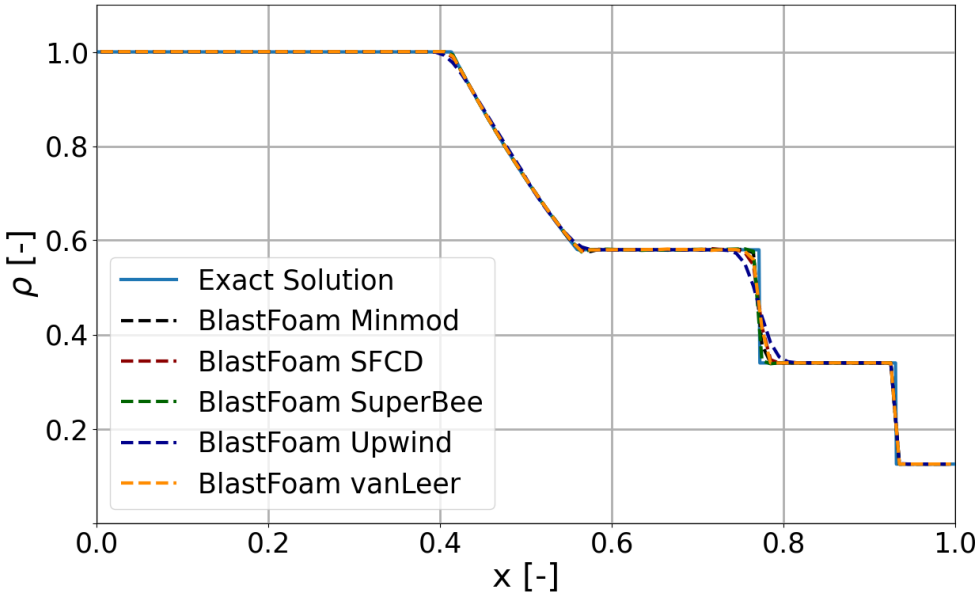


Figure 3.8: Density results for Toro test 1 at $t = 0.2$. The comparison includes different numerical schemes: Minmod, SFCD, SuperBee, Upwind, and VanLeer as implemented in BlastFOAM, with the exact solution (solid blue line) of the Riemann problem using a 1000-cell mesh and ideal gas equation of state.

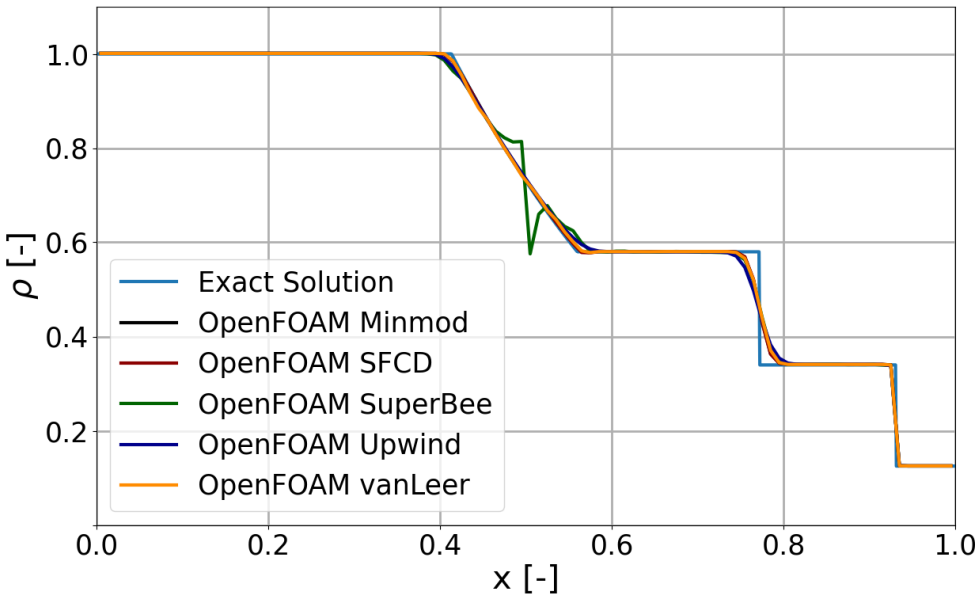


Figure 3.9: Density results for Toro test 1 at $t = 0.2$. The comparison includes different numerical schemes: Minmod, SFCD, SuperBee, Upwind, and VanLeer as implemented in OpenFOAM, with the exact solution (solid blue line) of the Riemann problem using a 1000-cell mesh and ideal gas equation of state.

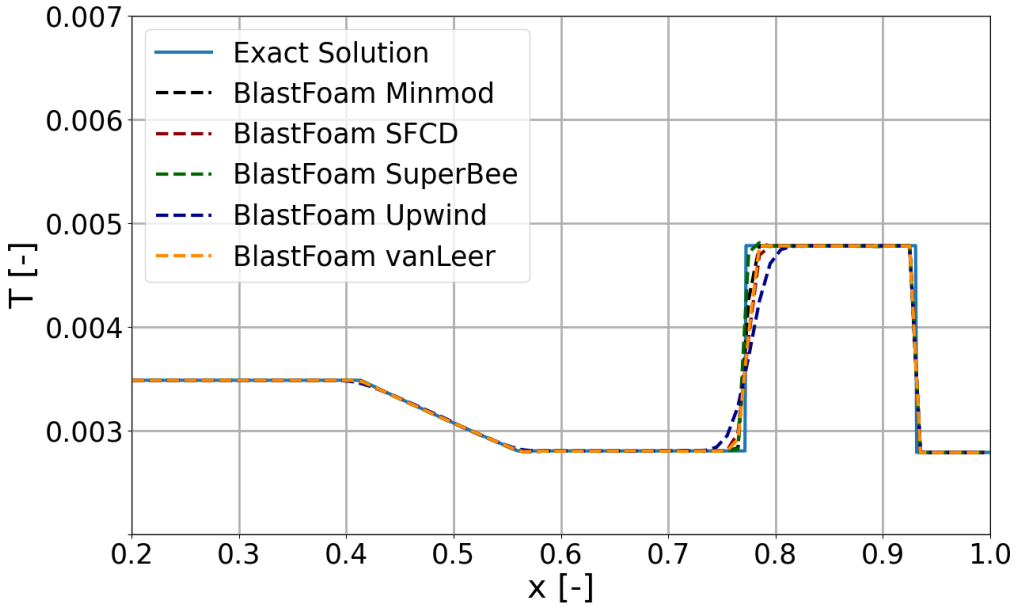


Figure 3.10: Temperature results for Toro test 1 at $t = 0.2$. The comparison includes different numerical schemes: Minmod, SFCD, SuperBee, Upwind, and VanLeer as implemented in BlastFOAM, with the exact solution (solid blue line) of the Riemann problem using a 1000-cell mesh and ideal gas equation of state.

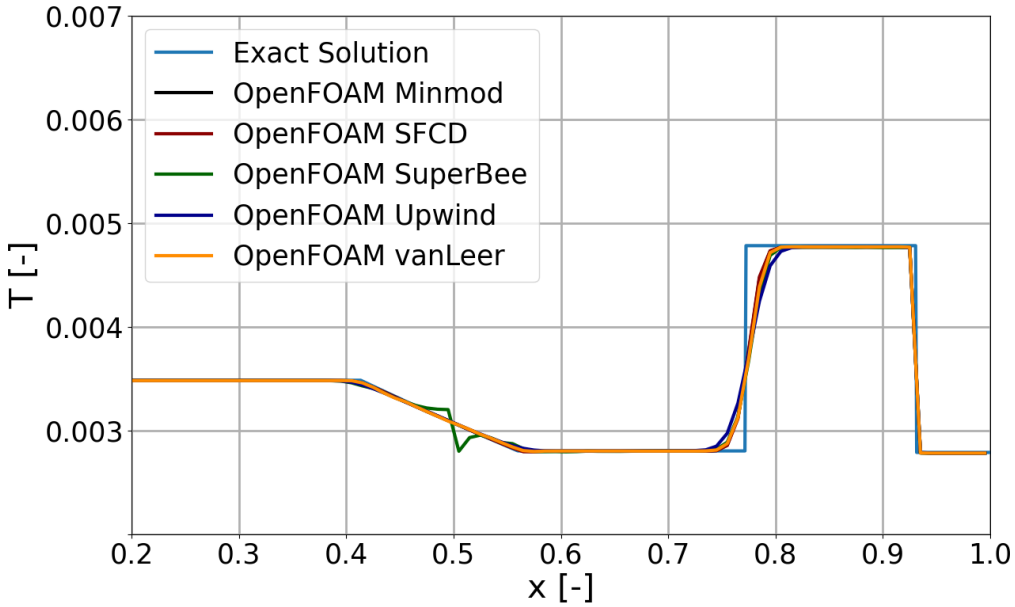


Figure 3.11: Temperature results for Toro test 1 at $t = 0.2$. The comparison includes different numerical schemes: Minmod, SFCD, SuperBee, Upwind, and VanLeer as implemented in OpenFOAM, with the exact solution (solid blue line) of the Riemann problem using a 1000-cell mesh and ideal gas equation of state.

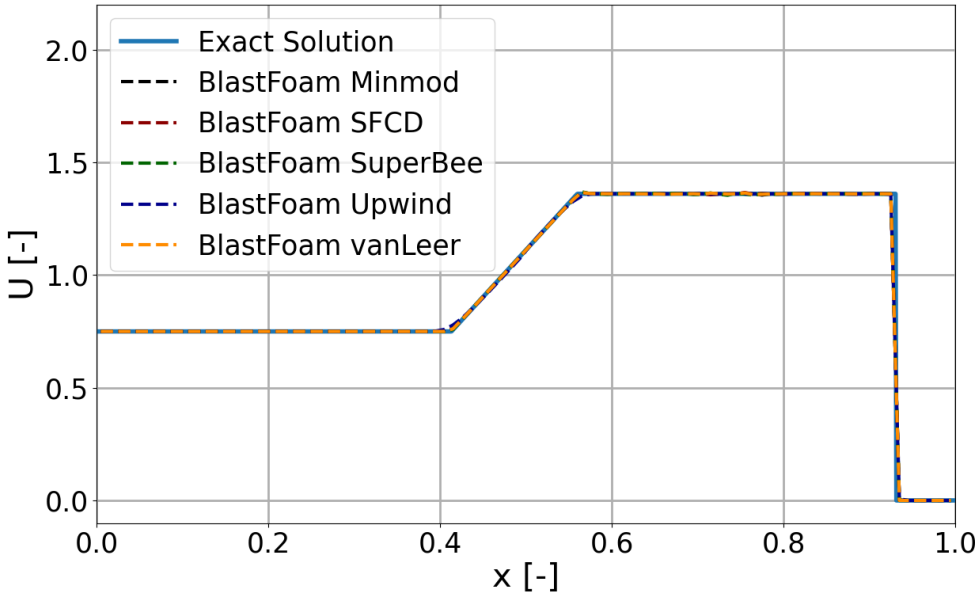


Figure 3.12: Velocity results for Toro test 1 at $t = 0.2$. The comparison includes different numerical schemes: Minmod, SFCD, SuperBee, Upwind, and VanLeer as implemented in BlastFOAM, with the exact solution (solid blue line) of the Riemann problem using a 1000-cell mesh and ideal gas equation of state.

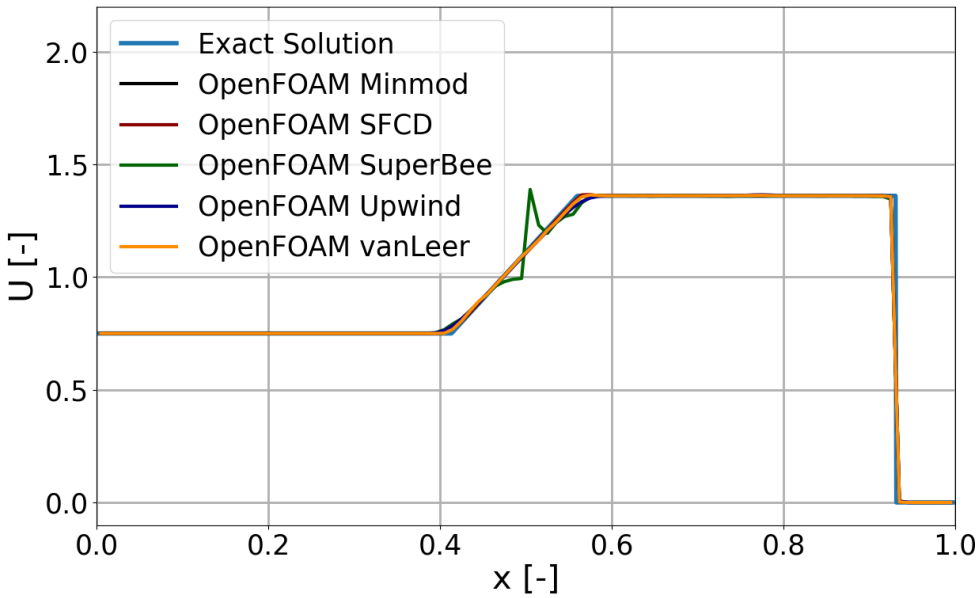


Figure 3.13: Velocity results for Toro test 1 at $t = 0.2$. The comparison includes different numerical schemes: Minmod, SFCD, SuperBee, Upwind, and VanLeer as implemented in OpenFOAM, with the exact solution (solid blue line) of the Riemann problem using a 1000-cell mesh and ideal gas equation of state.

In BlastFOAM, the fourth-order Runge-Kutta method is chosen for its stability benefits when using the SuperBee scheme. However, for all other numerical schemes within BlastFOAM, the Euler numerical method is preferred for its computational efficiency. In contrast, in OpenFOAM Euler time integration method is applied for all numerical schemes due to unavailability of Runge-Kutta method in OpenFOAM. This limitation becomes particularly evident with the SuperBee numerical scheme in OpenFOAM, which tends to produce significant oscillations. Regarding the diffusivity of numerical schemes, Upwind, a first-order numerical scheme, is identified as the most diffusive in both OpenFOAM and BlastFOAM. The TVD numerical schemes Minmod and VanLeer are more accurate in OpenFOAM and BlastFOAM as compared to Upwind. In BlastFOAM, on the other hand there is a significant difference between Upwind and the TVD numerical schemes Minmod and VanLeer. Minmod and VanLeer agree far better with the exact solution as compared to Upwind which is very diffusive. Interestingly, OpenFOAM solutions are more diffusive compared to those from BlastFOAM, especially when using the TVD numerical schemes. SFCD is the most accurate numerical scheme in OpenFOAM, although the difference between the SFCD and other numerical schemes is small in OpenFOAM. This study provides valuable knowledge. The results indicate that numerical schemes such as SFCD, Minmod and VanLeer are the most suitable ones. The numerical scheme SFCD will be used in the following Toro tests since SFCD is the most accurate numerical scheme in OpenFOAM. In BlastFOAM SFCD is also in close agreement with the exact solution.

Test 2

Toro test 2 is the so-called 123 problem. This problem consists of two symmetric rarefaction waves and a trivial contact wave of zero speed. The star region of this Riemann problem is close to a vacuum. This makes this Riemann problem suitable for testing the capability of numerical codes for low-density fluids. Moreover, this test case allows us to test whether the numerical code can capture complex wave interactions without generating any non-physical oscillations or numerical artifacts. BlastFOAM's simulation results are very close to the exact solution, whereas OpenFOAM fails this test. Using different numerical schemes in OpenFOAM, e.g., Upwind, Minmod, VanLeer, or changing the time step or mesh, did not yield any positive results for this test. One of the reasons could be the inherent design of the compressibleInterFoam solver in OpenFOAM, which might not be optimal for handling the sharp discontinuities and complex wave interactions present in low-density fluids.

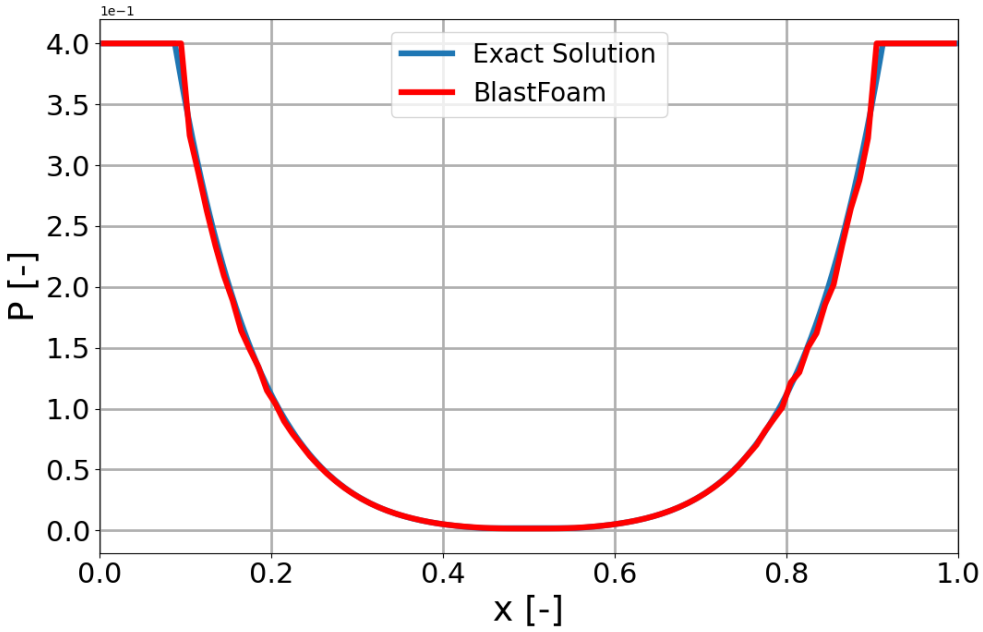


Figure 3.14: Pressure results for Toro test 2 at $t = 0.15$. The comparison includes simulation results with BlastFOAM using the second-order numerical scheme SFCD and the exact solution (solid blue line) of the Riemann problem with a 1000-cell mesh and ideal gas equation of state.

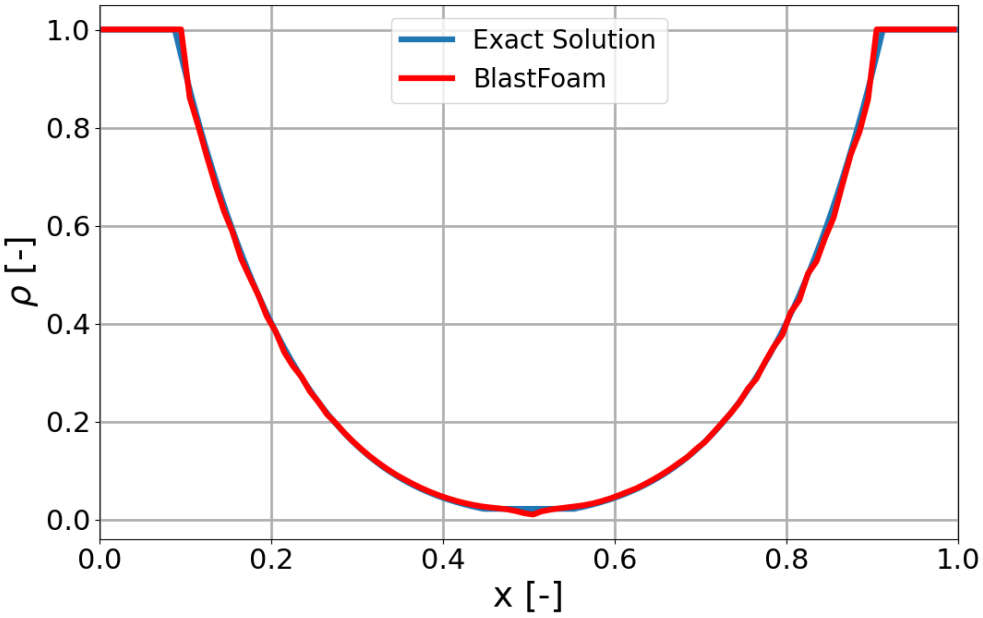


Figure 3.15: Density results for Toro test 2 at $t = 0.15$. The comparison includes simulation results with BlastFOAM using the second-order numerical scheme SFCD and the exact solution (solid blue line) of the Riemann problem with a 1000-cell mesh and ideal gas equation of state.

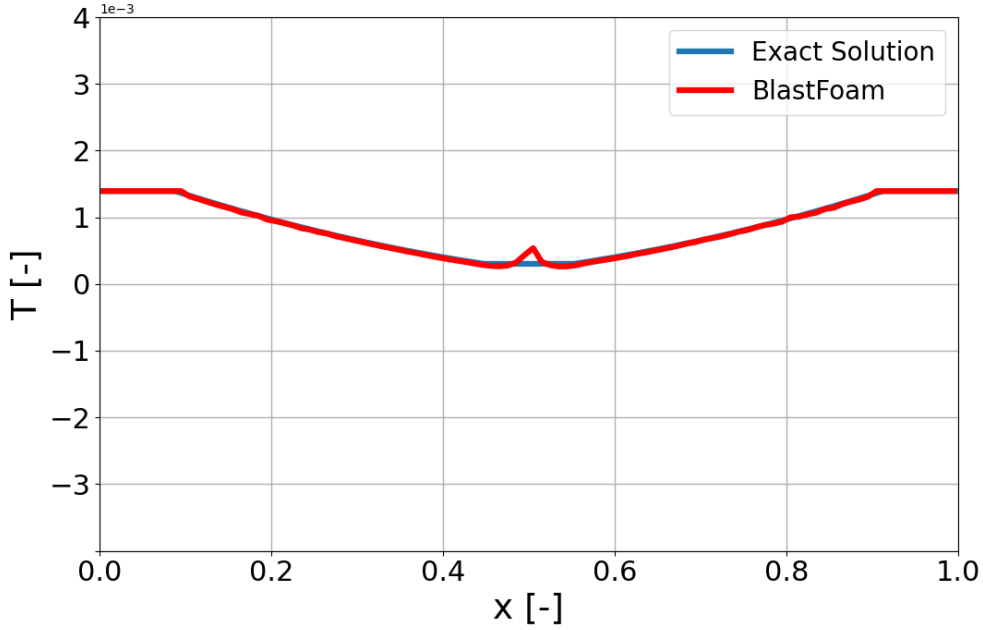


Figure 3.16: Temperature results for Toro test 2 at $t = 0.15$. The comparison includes simulation results with BlastFOAM using the second-order numerical scheme SFCD and the exact solution (solid blue line) of the Riemann problem with a 1000-cell mesh and ideal gas equation of state.

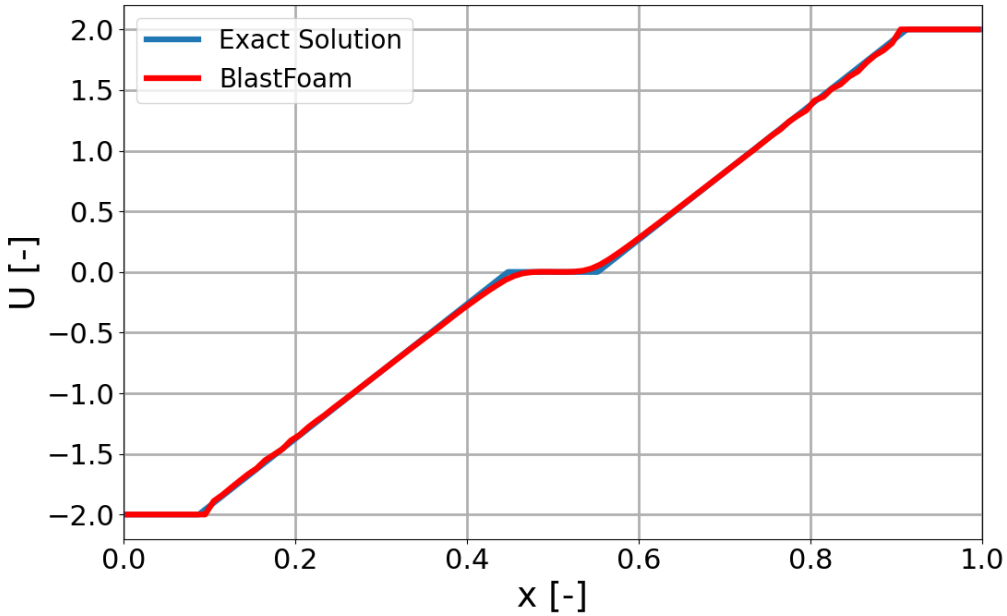


Figure 3.17: Velocity results for Toro test 2 at $t = 0.15$. The comparison includes simulation results with BlastFOAM using the second-order numerical scheme SFCD and the exact solution (solid blue line) of the Riemann problem with a 1000-cell mesh and ideal gas equation of state.

Test 3

Toro test 3 is a very challenging test case to simulate due to its extreme conditions. This test case produces a shock wave with a Mach number of 198. The pressure in the left region is 100,000 times higher than in the right region. This creates an extremely strong blast wave. Therefore, this case is suitable for assessing the robustness and accuracy of a numerical code. Both codes, OpenFOAM and BlastFOAM, pass this test. The predicted pressure, temperature, density, and velocity by OpenFOAM and BlastFOAM are very close to the exact solution. OpenFOAM is slightly more diffusive at the contact discontinuity for temperature and density predictions compared to BlastFOAM. Toro test 3 is a very important test case for benchmarking computational methods developed for highly compressible flows. This problem tests if a numerical code can handle complex shock interactions, which occur in many engineering applications, such as supersonic combustion, supernovae, or inertial confinement fusion. This Riemann problem drives the numerical code to its limits and assists in detecting any weaknesses in the shock-capturing capabilities of the numerical code.

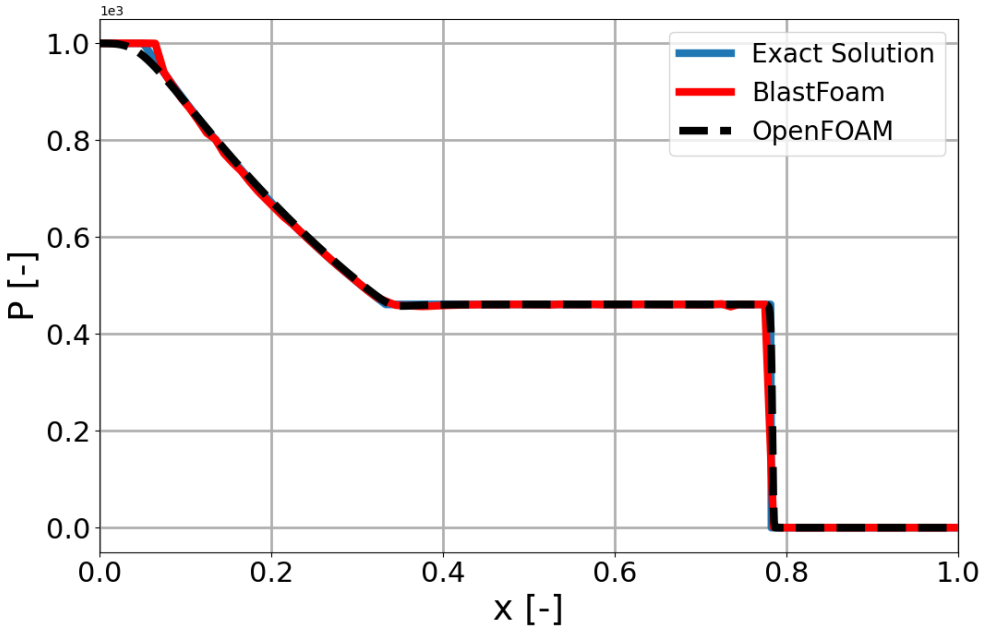


Figure 3.18: Pressure results for Toro test 3 at $t = 0.12$. The comparison includes simulation results with BlastFOAM (solid red line) and OpenFOAM (dash-dot black line) using the second-order numerical scheme SFCD, and the exact solution (solid blue line) of the Riemann problem with a 1000-cell mesh and ideal gas equation of state.

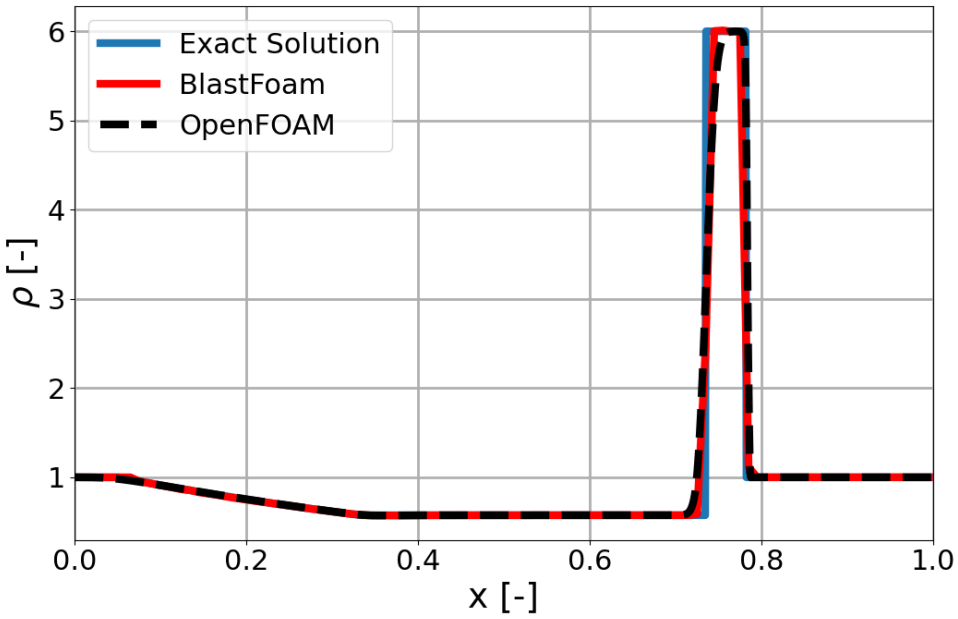


Figure 3.19: Density results for Toro test 3 at $t = 0.12$. The comparison includes simulation results with BlastFOAM (solid red line) and OpenFOAM (dash-dot black line) using the second-order numerical scheme SFCD, and the exact solution (solid blue line) of the Riemann problem with a 1000-cell mesh and ideal gas equation of state.

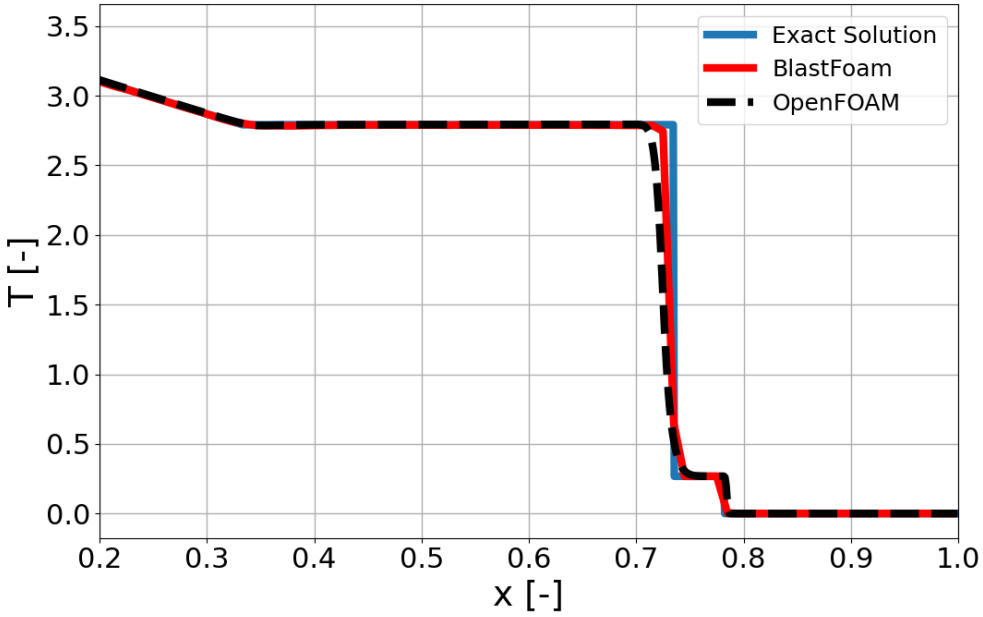


Figure 3.20: Temperature results for Toro test 3 at $t = 0.12$. The comparison includes simulation results with BlastFOAM (solid red line) and OpenFOAM (dash-dot black line) using the second-order numerical scheme SFCD, and the exact solution (solid blue line) of the Riemann problem with a 1000-cell mesh and ideal gas equation of state.

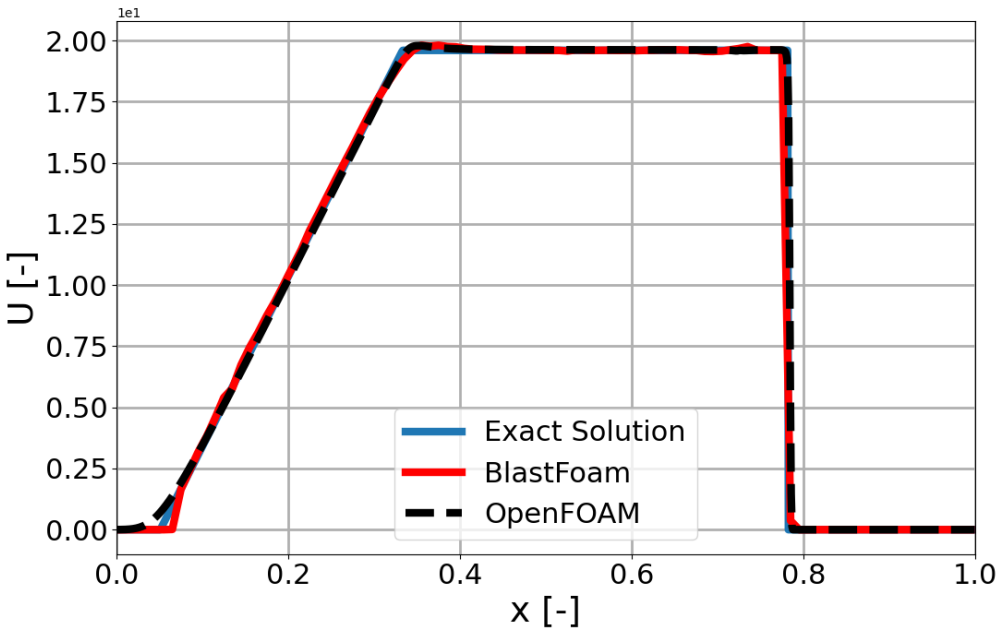


Figure 3.21: Velocity results for Toro test 3 at $t = 0.12$. The comparison includes simulation results with BlastFOAM (solid red line) and OpenFOAM (dash-dot black line) using the second-order numerical scheme SFCD, and the exact solution (solid blue line) of the Riemann problem with a 1000-cell mesh and ideal gas equation of state.

Test 4

Test 4 is designed to assess the robustness of the numerical code, similar to test 3. In this Riemann problem, two very strong shock waves propagate towards each other. If the numerical code is not robust enough, this test case can lead to several issues such as smearing of the shock or numerical instabilities. OpenFOAM produces oscillations at the discontinuity in density, velocity, and pressure, whereas BlastFOAM's results for density, velocity, and temperature are very stable and very close to the exact solution. Some oscillations are generated in the pressure prediction in BlastFOAM as well.

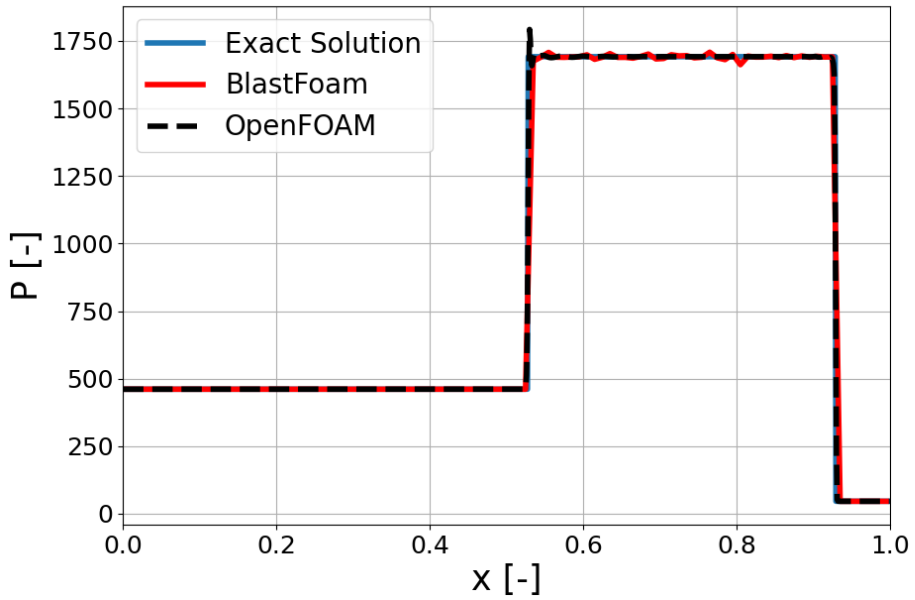


Figure 3.22: Pressure results for Toro test 4 at $t = 0.35$. The comparison includes simulation results with BlastFOAM (solid red line) and OpenFOAM (dash-dot black line) using the second-order numerical scheme SFCD, and the exact solution (solid blue line) of the Riemann problem with a 1000-cell mesh and ideal gas equation of state.

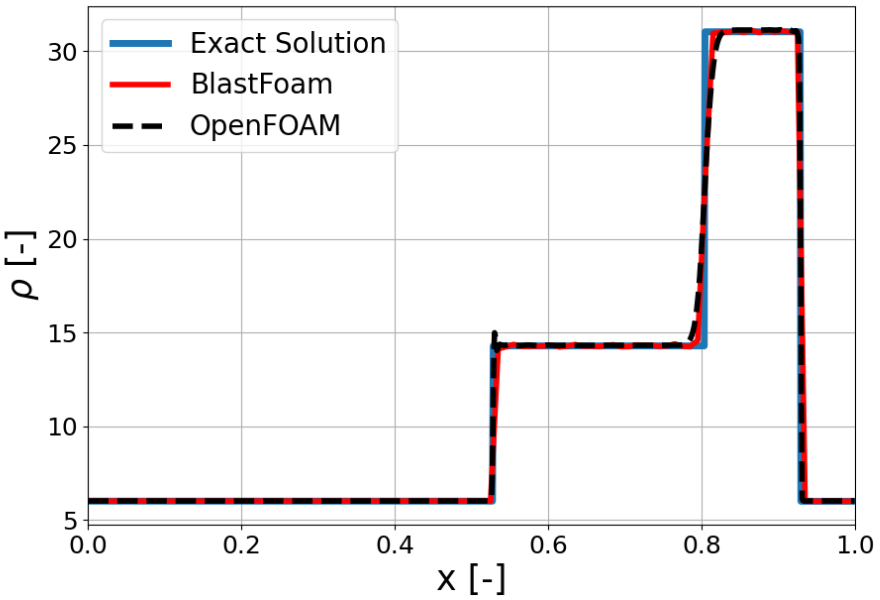


Figure 3.23: Density results for Toro test 4 at $t = 0.35$. The comparison includes simulation results with BlastFOAM (solid red line) and OpenFOAM (dash-dot black line) using the second-order numerical scheme SFCD, and the exact solution (solid blue line) of the Riemann problem with a 1000-cell mesh and ideal gas equation of state.

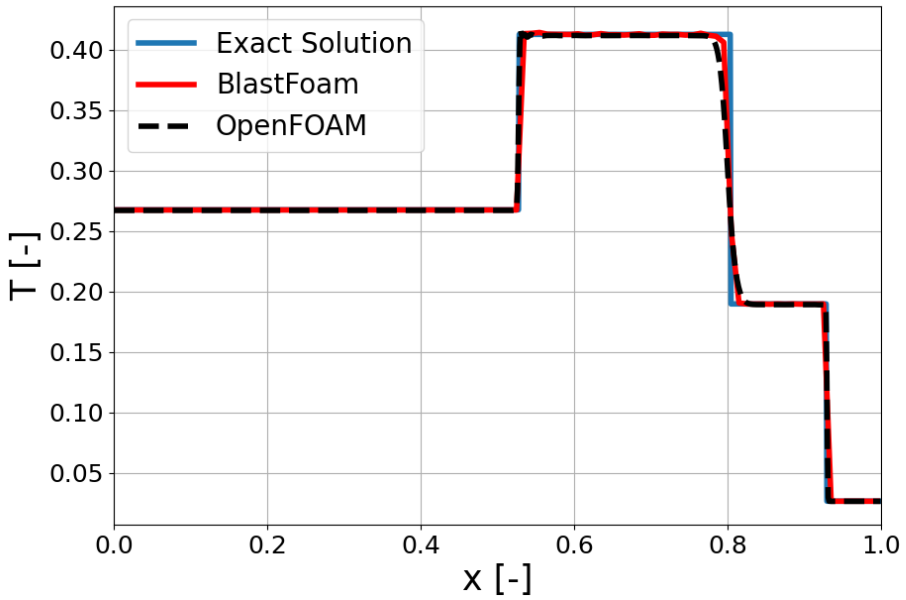


Figure 3.24: Temperature results for Toro test 4 at $t = 0.35$. The comparison includes simulation results with BlastFOAM (solid red line) and OpenFOAM (dash-dot black line) using the second-order numerical scheme SFCD, and the exact solution (solid blue line) of the Riemann problem with a 1000-cell mesh and ideal gas equation of state.

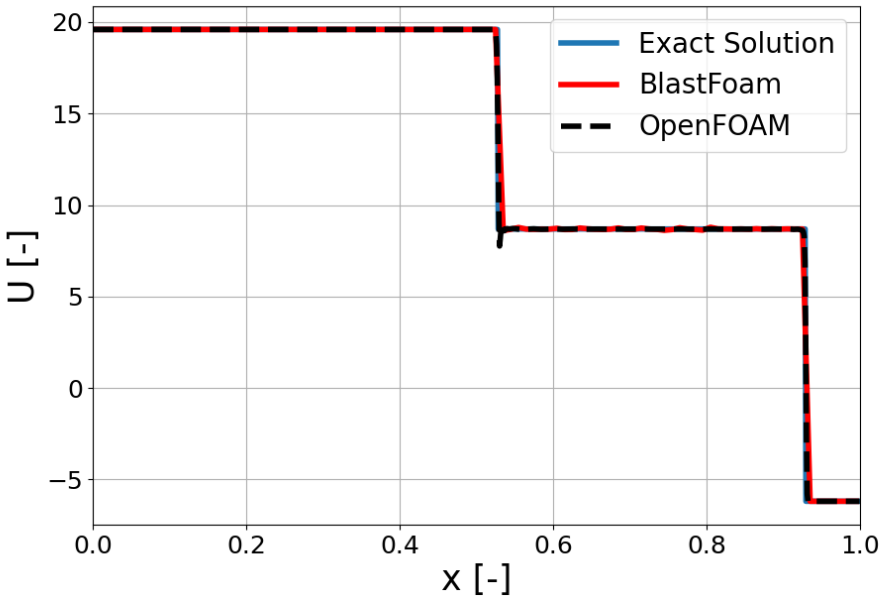


Figure 3.25: Velocity results for Toro test 4 at $t = 0.35$. The comparison includes simulation results with BlastFOAM (solid red line) and OpenFOAM (dash-dot black line) using the second-order numerical scheme SFCD, and the exact solution (solid blue line) of the Riemann problem with a 1000-cell mesh and ideal gas equation of state.

Test 5

This test is designed to assess the robustness of a numerical code under extreme conditions, similar to test 3. The focus of this Riemann problem is to evaluate the capability of a numerical code to accurately capture a slowly moving contact discontinuity. The test comprises a left rarefaction wave, a rightward slow-moving shock wave, and a stationary contact discontinuity. OpenFOAM could not simulate this test successfully. Several modifications, such as changing the numerical schemes, adjusting the time steps, and tweaking other numerical parameters, did not result in a successful simulation. On the other hand, BlastFOAM was able to successfully simulate this test. The results obtained from BlastFOAM were consistent with the expected outcomes as shown in figure 3.26, 3.27, 3.28 and 3.29. The results show BlastFoam's capability of handling highly compressible flows.

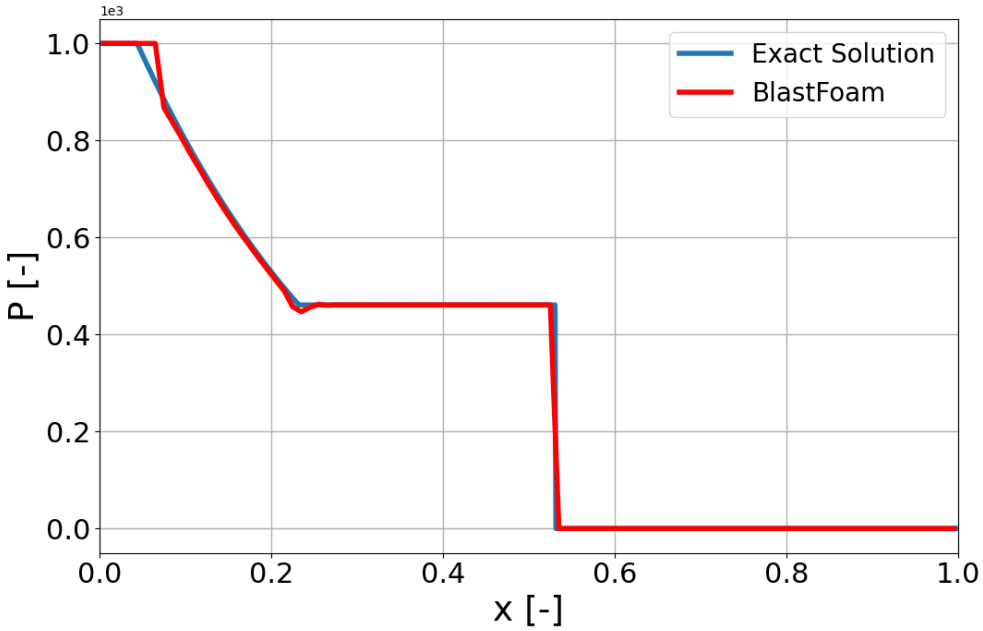


Figure 3.26: Pressure results for Toro test 5 at $t = 0.08$. The comparison includes simulation results with BlastFOAM (solid red line) using the second-order numerical scheme SFCD, and the exact solution (solid blue line) of the Riemann problem with a 1000-cell mesh and ideal gas equation of state.

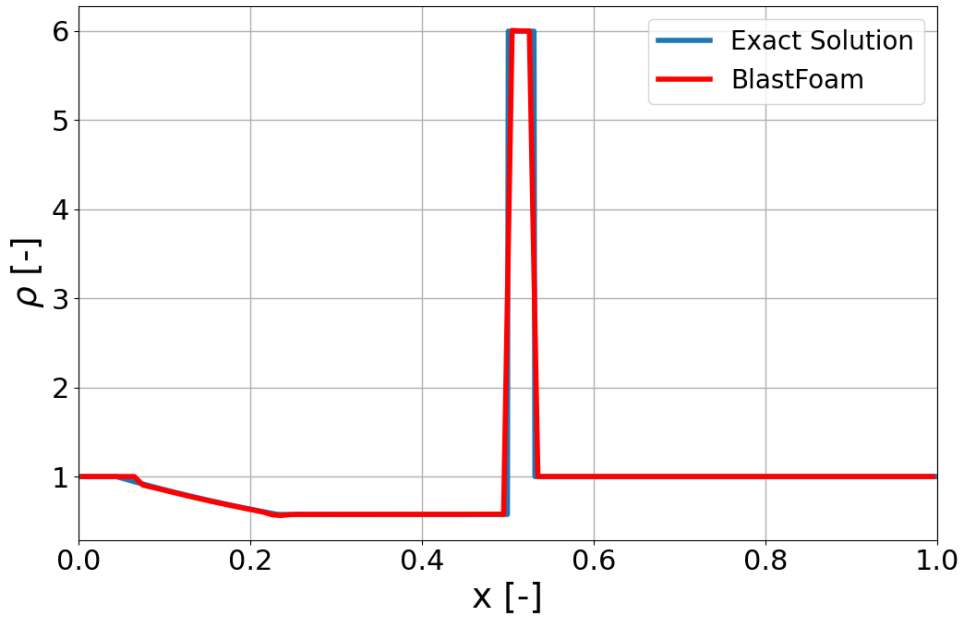


Figure 3.27: Density results for Toro test 5 at $t = 0.08$. The comparison includes simulation results with BlastFOAM (solid red line) using the second-order numerical scheme SFCD, and the exact solution (solid blue line) of the Riemann problem with a 1000-cell mesh and ideal gas equation of state.

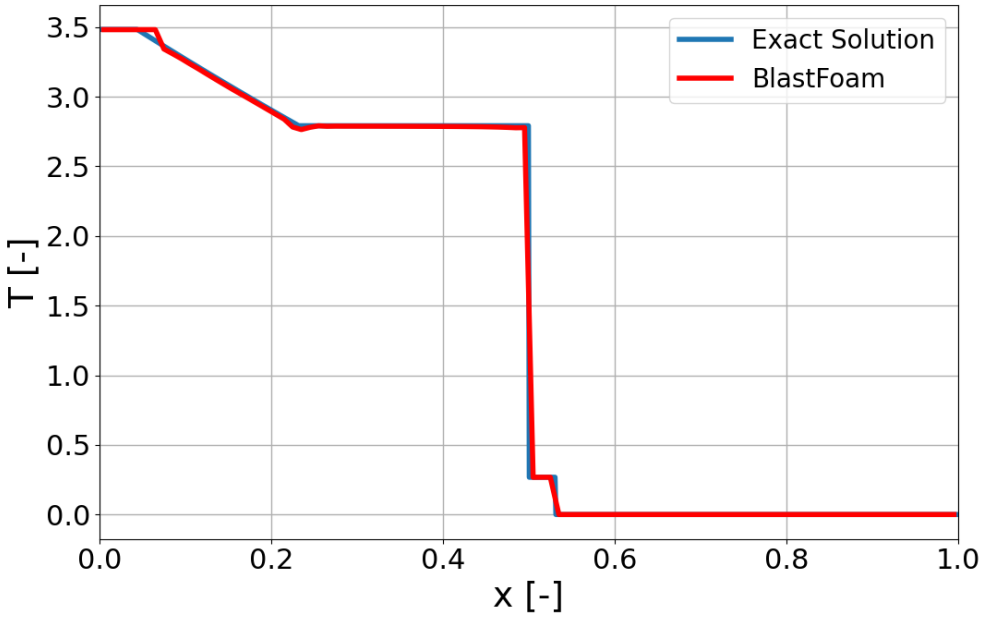


Figure 3.28: Temperature results for Toro test 5 at $t = 0.08$. The comparison includes simulation results with BlastFOAM (solid red line) using the second-order numerical scheme SFCD, and the exact solution (solid blue line) of the Riemann problem with a 1000-cell mesh and ideal gas equation of state.

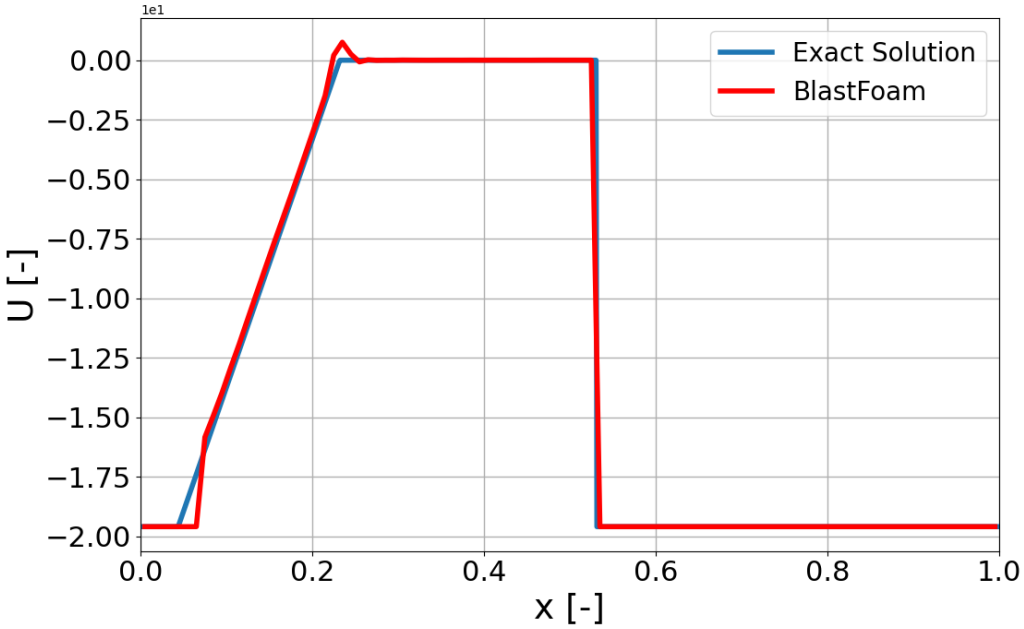


Figure 3.29: Velocity results for Toro test 5 at $t = 0.08$. The comparison includes simulation results with BlastFOAM (solid red line) using the second-order numerical scheme SFCD, and the exact solution (solid blue line) of the Riemann problem with a 1000-cell mesh and ideal gas equation of state.

BlastFOAM passes all the five Toro tests successfully. These tests establish confidence in BlastFOAM capability of handling highly compressible flows, whereas OpenFoam fails test 2 and test 5. The fact that OpenFOAM fails to produce satisfactory results in test 2 and test 5 indicates that the OpenFOAM could have inherent limitations when simulating highly compressible flows with certain types of physical phenomena. Specifically, test 2's pronounced shock wave and test 5's complex intermingling of shock waves and contact discontinuities expose potential weaknesses in OpenFOAM's computational capabilities.

Table 3.2: Comparison of BlastFOAM and OpenFOAM for various tests

Tests	BlastFOAM	OpenFOAM
1	Passed	Passed
2	Passed	Failed
3	Passed	Passed
4	Passed	Passed
5	Passed	Failed

3.1.2 Shock-Induced Bubble Collapse

In the shock-tube tests, it was investigated whether the algebraic volume-of-fluid method as implemented in OpenFOAM and BlastFOAM can capture extremely strong shocks. BlastFOAM passed all five tests, whereas OpenFOAM failed test 2 and test 5. A further investigation is needed to assess the ability of OpenFOAM and BlastFOAM to capture the interface. Therefore, a shock-induced bubble collapse simulation is carried out. The simulation results are validated against the experimental results from Haas et al. [42]. In this experiment Haas et al. used helium confined within a cylindrical domain. One end of the cylinder is sealed by a Pyrex window with 5 cm diameter and 3 mm thickness. Helium is filled inside a 0.5 μm thick nitrocellulose membrane wrapped around the Pyrex window. A detailed description of the experimental setup can be found in [42].

A schematic of the simulation domain to replicate Haas et al.'s experiment is shown in figure 3.30. A 2D domain with a specified area of 1m $\times$ 1m is used. A helium bubble of 5 cm in diameter is used. The fluids involved in this simulation are air and helium. To ensure accuracy and precision, a resolution of 2 million cells is implemented. The initial conditions are set with both air and helium at a pre-shock state of 1 bar and 290 K. Furthermore, a shock wave with a magnitude of 1.22 Mach is introduced. The numerical scheme SFCD is applied in OpenFOAM and BlastFOAM.

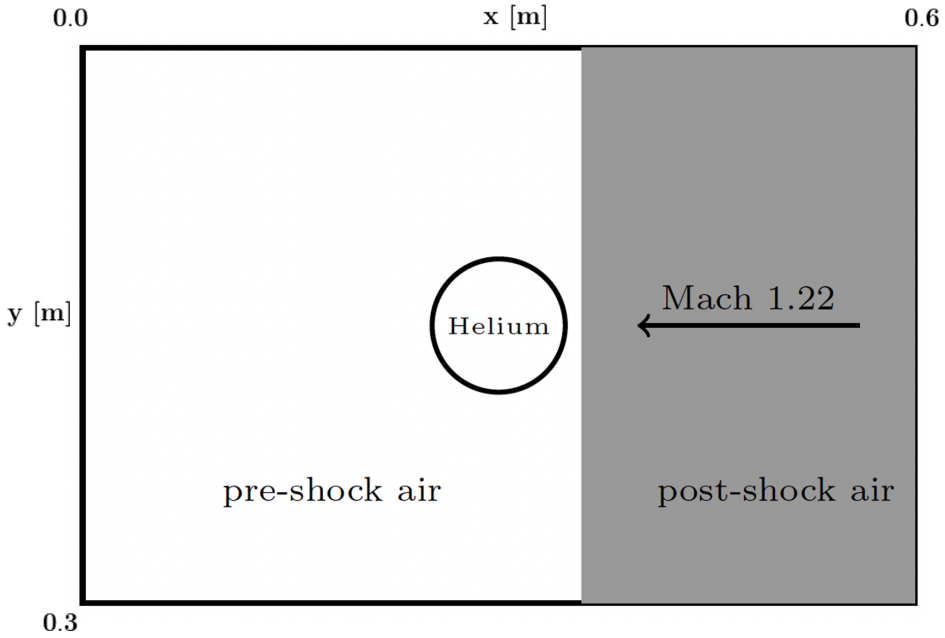


Figure 3.30: A schematic of the shock-induced bubble collapse simulation domain as used in OpenFoam and BlastFOAM.

The shock-induced bubble collapse experiment of Haas et al. can lead to Kelvin-Helmholtz and Richtmyer-Meshkov instabilities. Therefore, it serves a good validation case for assessing the interface-capturing capabilities of BlastFOAM and OpenFOAM. Numerous authors [43, 44] have used this shock-induced bubble collapse experiment as a benchmark for validating compressible CFD codes. A side-by-side comparison between the simulation results and the experiment is shown in figure 3.31. The shock wave compresses the gas contained inside the cylinder and leads to vorticity development as a result of misalignment of the pressure gradient to the density. Clockwise vorticity is generated at the top and anticlockwise vorticity is generated at the bottom. The vorticity resulting from misalignment of the pressure and density gradients is referred to as the baroclinic vorticity. A detailed description of the baroclinic vorticity will be given in the following chapter. In figure 3.31 (a), the impact of the Mach 1.22 shock wave, travelling from the right and impinging on the helium gas in the experiment and the simulations is illustrated. The circular shape in the experiment (Haas et al.) represents the Pyrex window located at the cylinder's ends. The T-shaped object at the bottom serves as structural support for the window. The incoming shock wave converges on the cylinder and results in a shock, transmitted and refracted wave. BlastFOAM and OpenFOAM capture the compression and the shock dynamics: shock, transmitted, and refracted wave. In figure 3.31 (b) displays the progressing compression and the propagation of the refracted, transmitted, and shock wave. The simulations from BlastFOAM and OpenFOAM are in good agreement with the experiment.

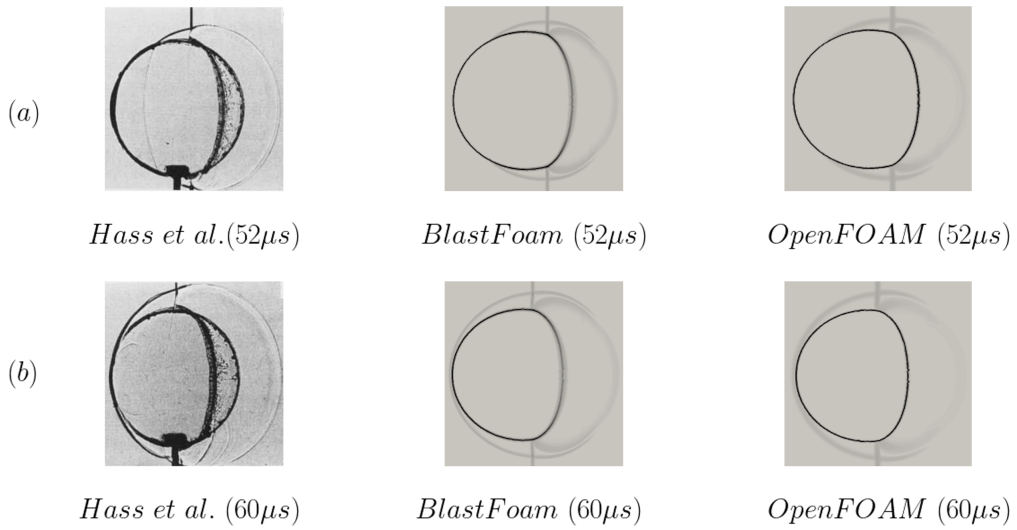


Figure 3.31: Comparison of BlastFOAM and OpenFOAM shock-induced bubble collapse density plots with the experimental schlieren images of Haas et al. using ideal gas for air and helium and a Mach 1.22 shock wave. at $52\mu s$ (a) and $60\mu s$ (b) after the impact of the shock wave upon helium.

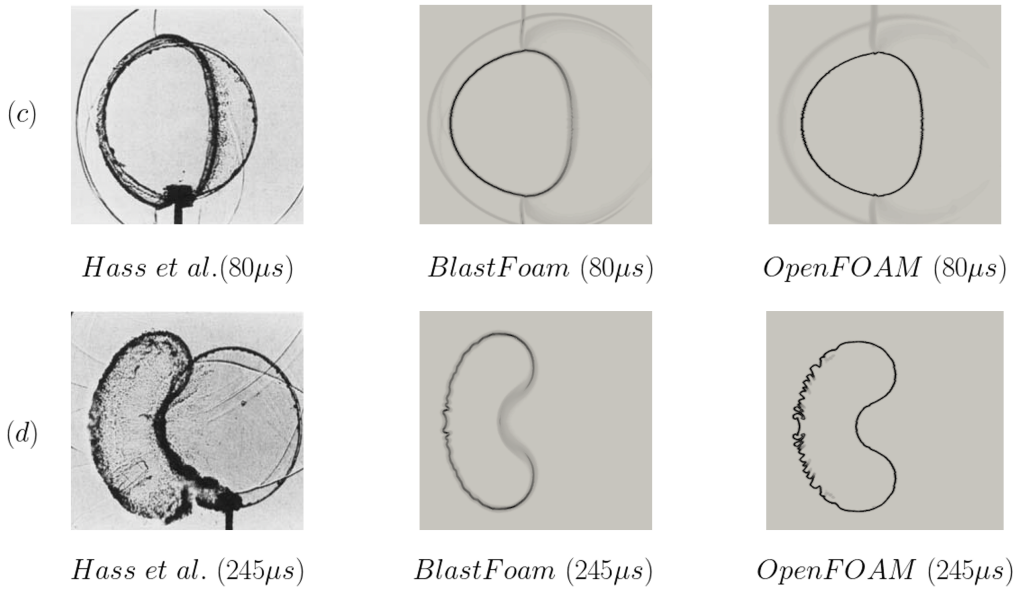


Figure 3.32: Comparison of BlastFOAM and OpenFOAM shock-induced bubble collapse density plots with the experimental schlieren images of Haas et al. using ideal gas for air and helium and a Mach 1.22 shock wave. at $80\mu s$ (c) and $245\mu s$ (d) after the impact of the shock wave upon helium.

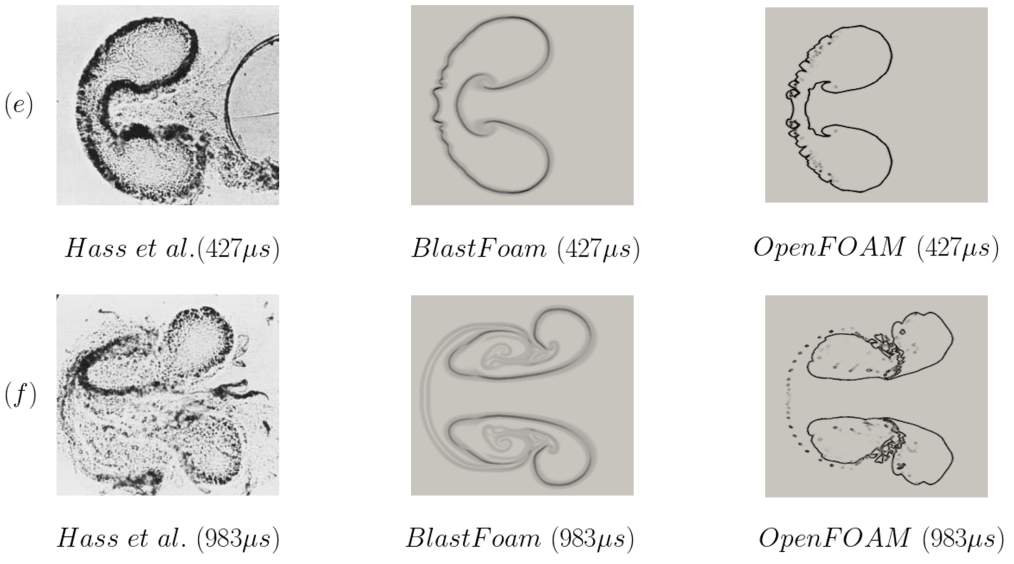


Figure 3.33: Comparison of BlastFOAM and OpenFOAM shock-induced bubble collapse density plots with the experimental schlieren images of Haas et al. using ideal gas for air and helium and a Mach 1.22 shock wave. at $427\mu s$ (e) and $983\mu s$ (f) after the impact of the shock wave upon helium.

In figure 3.32 (d), the initially circular helium gas begins its transformation into a kidney-like shape. As previously mentioned, the shock wave induces clockwise vorticity at the top and anticlockwise vorticity at the bottom of the circular shape. This differential rotational motion exerts shear forces on the helium circular shape, leading to the deformation from its original form to a kidney-like shape. Both numerical codes BlastFOAM and OpenFoam capture this complex phenomenon well. However, OpenFoam generates more small-scale structure instabilities compared to BlastFOAM or the experiment. BlastFOAM's interface is smoother which dampen the development of the small-scale structures. As the deformation progresses, Rayleigh-Taylor and Kelvin-Helmholtz instabilities start developing. These instabilities form a mushroom-like structure as shown in 3.33 (e)-(f). BlastFOAM captures both instabilities, Rayleigh-Taylor and Kelvin-Helmholtz, effectively. This demonstrates BlastFOAM's ability to capture complex interfaces. OpenFOAM, on the other hand, seems to miss the roll-up associated with the Kelvin-Helmholtz instability. In addition to this, OpenFOAM shows a highly oscillatory interface when compared to the experiment and BlastFOAM. In figure 3.33 (e)-(f), the further evolution of the mushroom shape is illustrated. BlastFOAM shows a well-defined mushroom shape, while OpenFOAM lacks the ability to capture this structure accurately.

The shock-tube tests strengthen confidence in BlastFOAM's capability to capture extremely strong shocks. As discussed in the previous section, BlastFOAM passes all five Toro tests. OpenFOAM, on the other hand, failed test 2 and test 5. This shock-induced bubble collapse case is used to assess the interface capturing capability of both codes. BlastFOAM demonstrates its ability to capture complex fluid dynamics processes, such as Richtmyer-Meshkov and Kelvin-Helmholtz instabilities, whereas OpenFOAM captured the shock-dynamics in this bubble collapse case in good agreement with the experiment and BlastFOAM. OpenFOAM captured the shock, transmitted, and refracted waves. However, OpenFOAM does not capture the roll-ups associated with the mushroom shape. In addition to this, OpenFOAM produces a very oscillatory interface. As a result, BlastFOAM is chosen as the volume-of-fluid code. In the following section, BlastFOAM will be compared with the First Light Fusion's in-house code, Hytrac, which is based on the hybrid front-tracking method.

3.2 BlastFOAM vs Hytrac

BlastFOAM is chosen as the volume-of-fluid code due to its good results in Toro shock-tube study and the bubble collapse case. In this section, BlastFOAM is compared with the First Light Fusion in-house code Hytrac. Hytrac is based on the hybrid front-tracking method. In the first comparison, a 1-D multi-material shock-tube is simulated with Hytrac and BlastFOAM. This multi-material shock-tube consists of copper, plastic (PMMA) and deuterium. This is a 1-D version of the fusion-target case that will be investigated in the chapter 5. In the second case, it is investigated whether Hytrac and BlastFOAM can model Richtmyer-Meshkov instabilities.

3.2.1 Multi-material 1D Shock-Tube

A 1-D multi-material shock-tube simulation is conducted using Hytrac and BlastFOAM, incorporating materials such as copper, plastic, and deuterium. This simulation represents a simplified, 1-D version of the shock-driven fusion target, which will be explored in greater detail in chapter 5. In this 1-D shock-tube, the shock propagates from left to right, as shown in 3.34. The initial conditions of the simulation are given in table 3.3.

Table 3.3: Initial conditions of multi-material Shock-Tube.

u_s	ρ_{cs}	p_s	T_s	ρ_c	ρ_p	ρ_d
$-15830\ m/s$	$24551\ kg/m^3$	$1.8e14\ Pa$	$120630\ K$	$8950\ kg/m^3$	$1150\ kg/m^3$	0.16

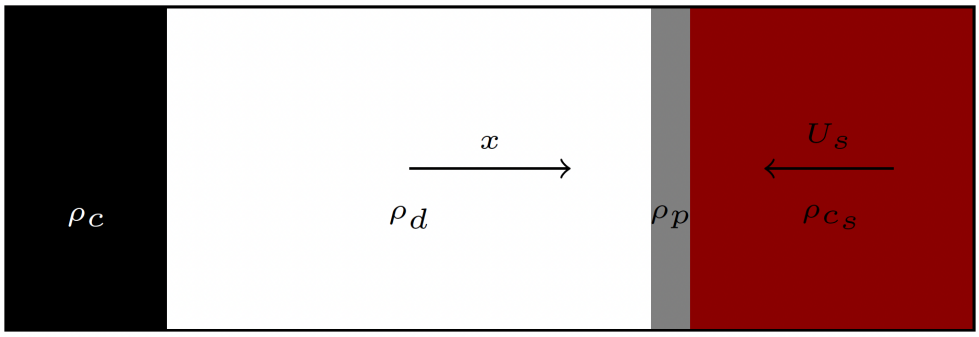


Figure 3.34: 1-D domain of the multi-material shock-tube.

Here, $\boldsymbol{u_s}$, ρ_{cs}, p_s, T_s, ρ_c, ρ_p, ρ_d are shock velocity, shocked cooper density, shock pressure, shock temperature, copper density, plastic density and deuterium density. A mesh consisting of 4000 cells along the x direction is employed in both Hytrac and BlastFOAM. The total length of the shock-tube is set to $x = 2.8$ mm. The shock is initiated in copper as represented by the red area in figure 3.34. As the simulation progresses, the shock wave transits from the copper into the plastic and subsequently compresses the deuterium.

The simulation results are shown in figure 3.35, 3.36, 3.37 and 3.38 BlastFOAM and Hytrac show a significant similarity in their predictions of temperature, pressure, density, and velocity. However, a notable distinction is observed in the shock discontinuity between BlastFOAM and Hytrac. This difference in shock discontinuity can be attributed to the interface modelling method used in BlastFOAM and Hytrac. BlastFOAM employs the volume-of-fluid (VOF) method. The volume-of-fluid method tends to exhibit a more diffusive interface, a characteristic already discussed in chapter 2. In contrast, Hytrac employs the front-tracking method.

The front-tracking method is known for its precision in modelling sharp interfaces. This characteristic of front-tracking method has also been discussed in chapter 2. After the shock discontinuity exits the domain, the results from both BlastFOAM and Hytrac overlap significantly as depicted in figure 3.39, 3.41, 3.40 and 3.42 that their predictions are essentially identical. In figure 3.35 a significant pressure drop is observed, reaching near-zero levels. This phenomenon is attributed to the formation of a strong rarefaction wave, which results from the interaction of the shock wave with the deuterium.

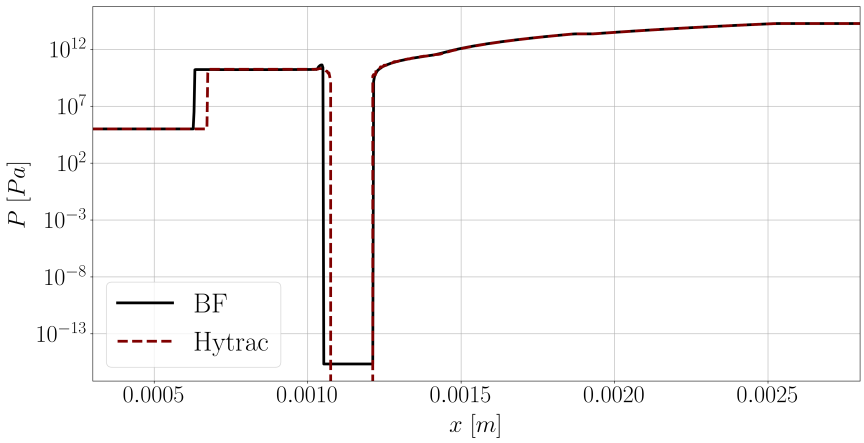


Figure 3.35: Pressure predictions by BlastFOAM and Hytrac at $4{\times}10^{-9}$ seconds, utilizing the stiffened gas equation of state for copper and plastic, and the ideal gas equation of state for deuterium ($\rho = 0.16$ kg/m^3).

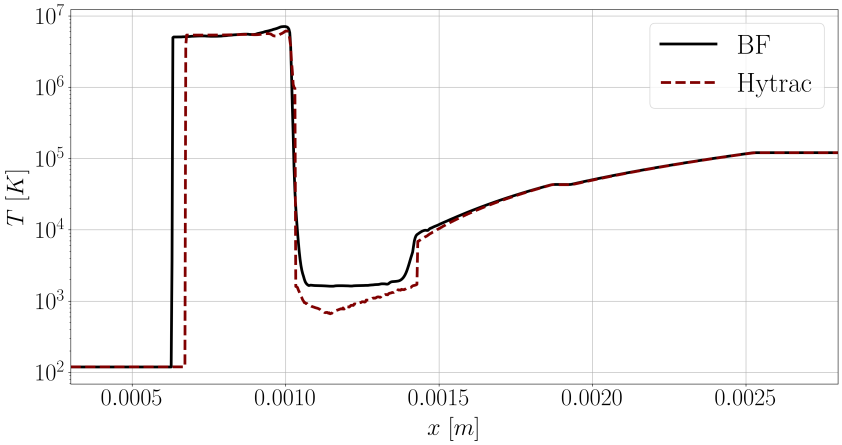


Figure 3.36: Temperature predictions by BlastFOAM and Hytrac at 4×10^{-9} seconds, utilizing the stiffened gas equation of state for copper and plastic, and the ideal gas equation of state for deuterium ($\rho = 0.16$ kg/m^3).

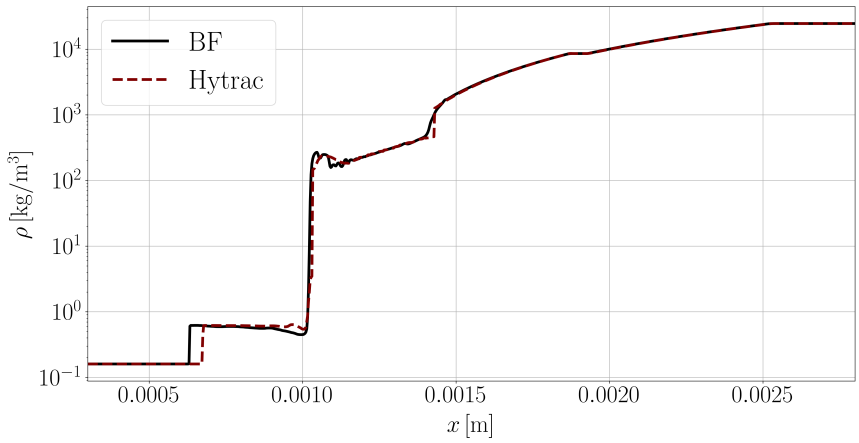


Figure 3.37: Density predictions by BlastFOAM and Hytrac at 4×10^{-9} seconds, utilizing the stiffened gas equation of state for copper and plastic, and the ideal gas equation of state for deuterium ($\rho = 0.16$ kg/m^3).

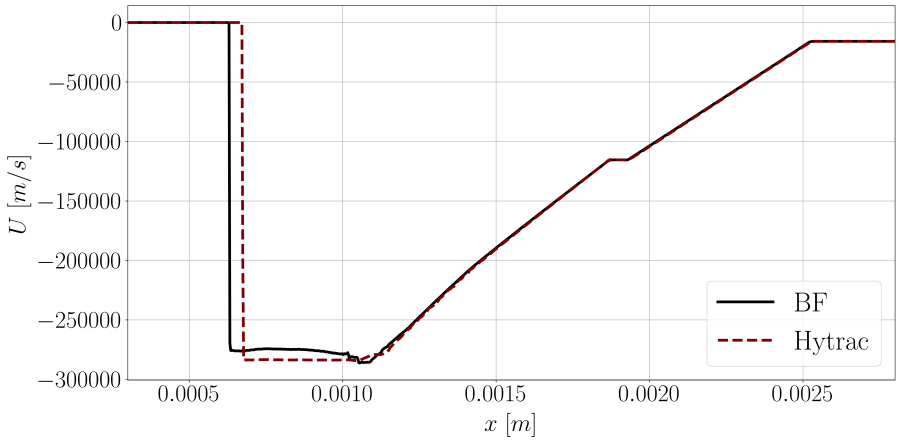


Figure 3.38: Velocity predictions by BlastFOAM and Hytrac at 4×10^{-9} seconds, utilizing the stiffened gas equation of state for copper and plastic, and the ideal gas equation of state for deuterium ($\rho = 0.16$ kg/m^3).

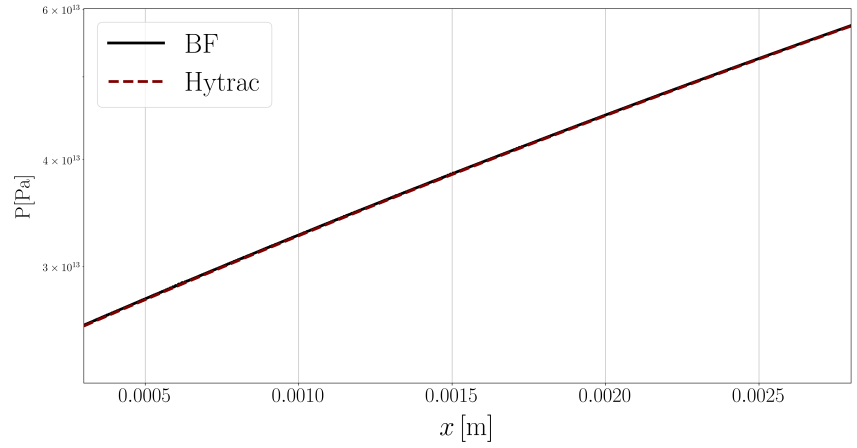


Figure 3.39: Pressure predictions by BlastFOAM and Hytrac at 5×10^{-8} seconds, using the stiffened gas equation of state for copper and plastic, and the ideal gas equation of state for deuterium ($\rho = 0.16$ kg/m^3).

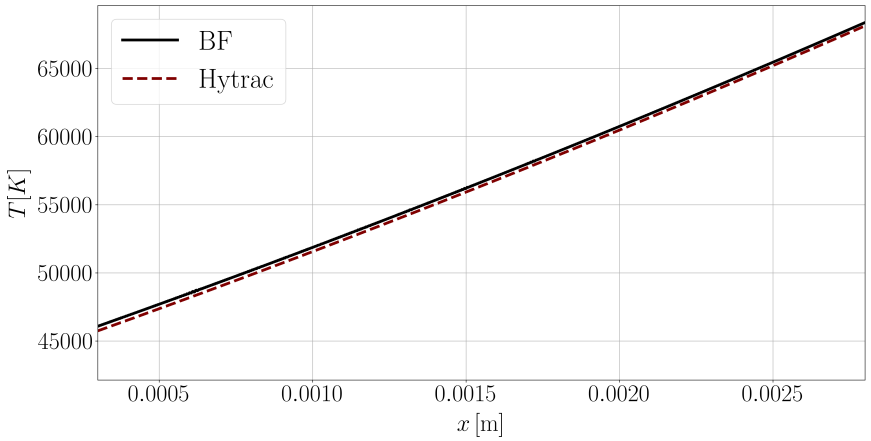


Figure 3.40: Temperature predictions by BlastFOAM and Hytrac at 5×10^{-8} seconds, using the stiffened gas equation of state for copper and plastic, and the ideal gas equation of state for deuterium ($\rho = 0.16$ kg/m^3).

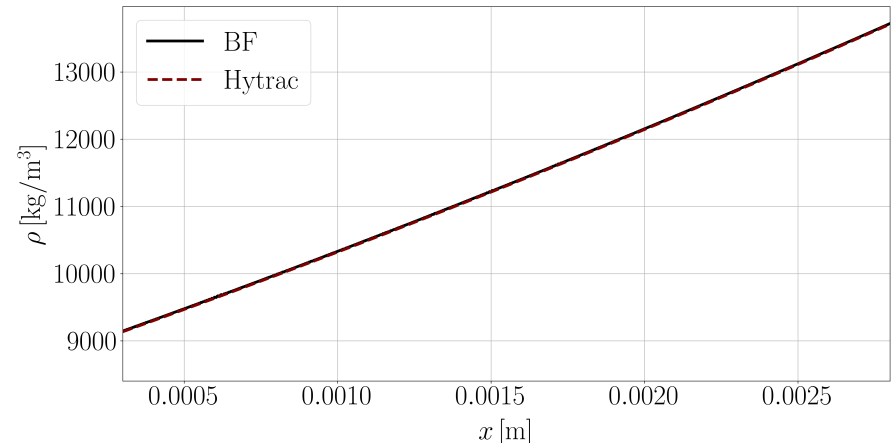


Figure 3.41: Density predictions by BlastFOAM and Hytrac at 5×10^{-8} seconds, using the stiffened gas equation of state for copper and plastic, and the ideal gas equation of state for deuterium ($\rho = 0.16$ kg/m^3).

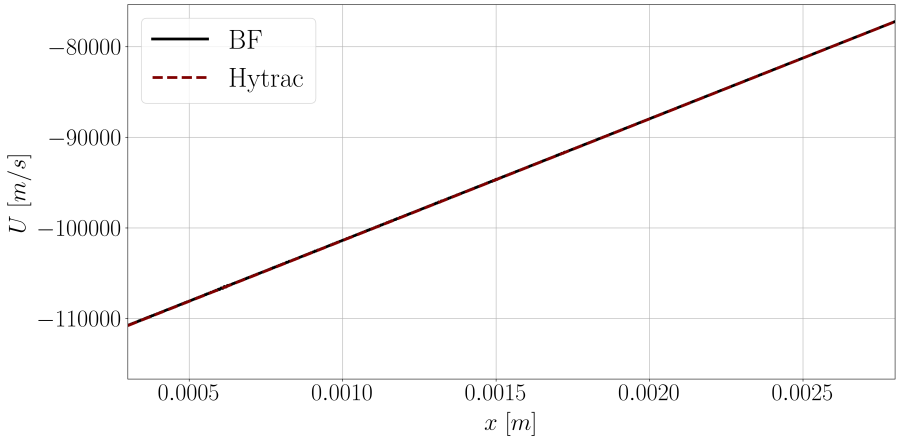


Figure 3.42: Velocity predictions by BlastFOAM and Hytrac at 5×10^{-8} seconds, using the stiffened gas equation of state for copper and plastic, and the ideal gas equation of state for deuterium ($\rho = 0.16$ kg/m^3).

Considering the substantial density difference between deuterium (0.16 kg/m^3) and plastic (1150 kg/m^3), the intensity of the rarefaction wave is significantly amplified. This leads to a strong expansion, resulting in a pressure drop nearly to vacuum condition, as shown in the figure 3.35. The rarefaction wave is identified as the primary source of thepressure drop. An effective strategy to mitigate this effect is to increase the density of deuterium from 0.16 kg/m^3 to 100 kg/m^3. This decreases the ratio of density between plastic and deuterium from 7187 to 11.5. By decreasing the density ratio between plastic and deuterium, a strong rarefaction wave, which leads to a substantial pressure drop, can be mitigated. This adjustment decreases the intensity of the rarefaction wave to stabilize the pressure profile within in the shock-tube. Such a stabilization is evident in the comparative analysis of the pressure profiles, particularly in the context of the modified deuterium density, as illustrated in figure 3.43.

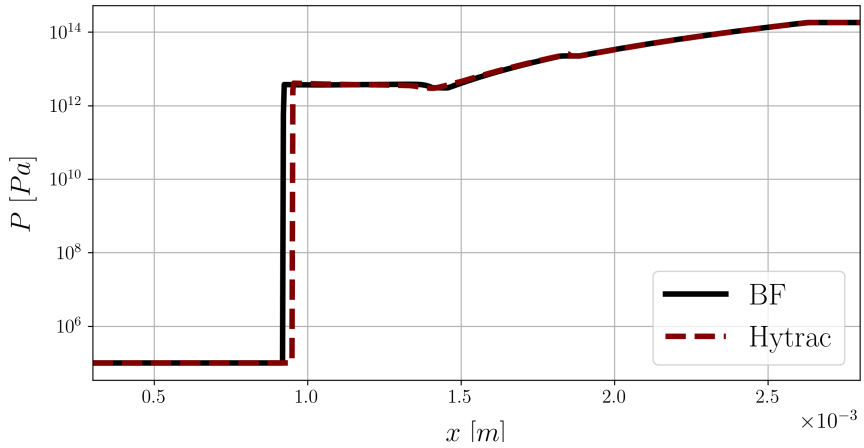


Figure 3.43: Pressure predictions by BlastFOAM and Hytrac at 5×10^{-9} seconds, using the stiffened gas equation of state for copper and plastic, and the ideal gas equation of state for deuterium ($\rho = 100.0$ kg/m^3).

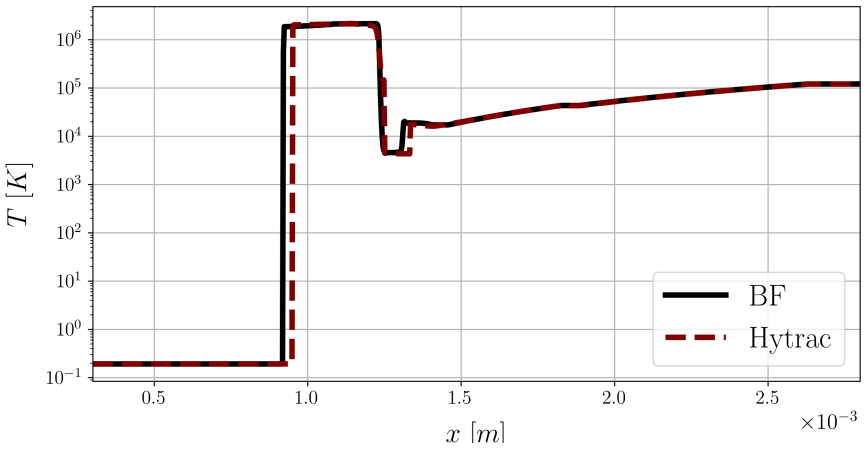


Figure 3.44: Temperature predictions by BlastFOAM and Hytrac at 5×10^{-9} seconds, using the stiffened gas equation of state for copper and plastic, and the ideal gas equation of state for deuterium ($\rho = 100.0$ kg/m^3).

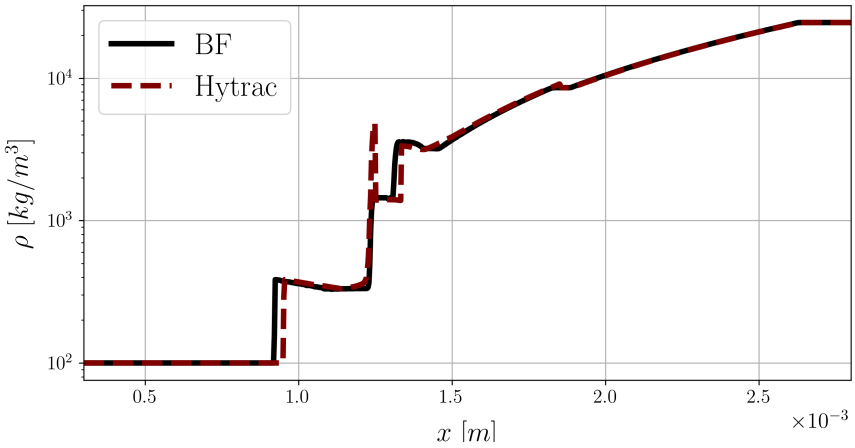


Figure 3.45: Density predictions by BlastFOAM and Hytrac at 5×10^{-9} seconds, using the stiffened gas equation of state for copper and plastic, and the ideal gas equation of state for deuterium ($\rho = 100.0$ kg/m^3).

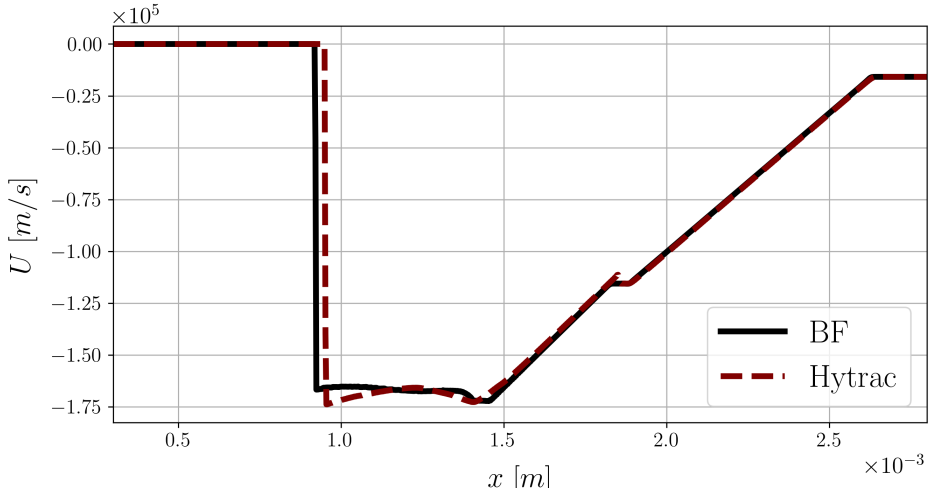


Figure 3.46: Velocity predictions by BlastFOAM and Hytrac at 5×10^{-9} seconds, using the stiffened gas equation of state for copper and plastic, and the ideal gas equation of state for deuterium ($\rho = 100.0$ kg/m^3).

3.2.2 RMI Trilab

The RMI Trilab case tests the codes' proficiency in modeling multiple fluid interactions under shock conditions, and their capacity to capture the large- and fine-scale dynamics of the mixing layer, e.g., mixing layer amplitude, displacement, and secondary instabilities such as the Kelvin-Helmholtz instability. The initial conditions are given in table 3.4.

Table 3.4: Initial conditions of Trilab RMI case.

u_s	$\rho_{air,s}$	$p_{air,s}$	ρ_{air}	p_0	ρ_{SF6}
142 m/s	2.08 kg/m^3	1.65e5 Pa	1.32 kg/m^3	9.3e4 Pa	5.6 kg/m^3

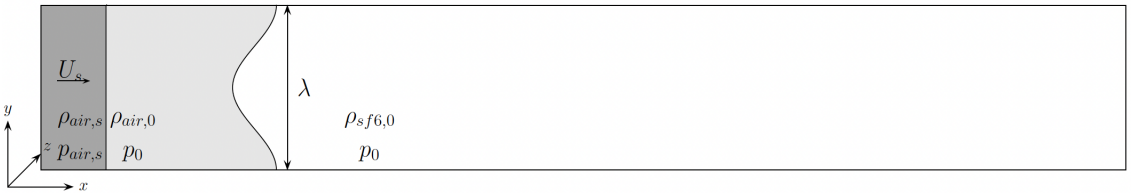


Figure 3.47: Schematic of the flow configuration in which a perturbation of wavelength λ is applied to an interface separating two phases at pressure p_0 of initial densities $\rho_{air,0}$ and $\rho_{SF6,0}$ shown by the light grey and white regions, respectively, where $\rho_{air,0} > \rho_{SF6,0}$. A shock is initiated in the air phase (dark grey region) with density $\rho_{air,s}$ and pressure $p_{air,s}$, which travels in the direction of the lighter phase at constant speed U_s

In figure 3.48 simulation results of BlastFOAM and Hytrac are compared with the theoretical models of Richtmyer [30] and Dimonte and Schneider [14], where h, h_0, k, and At are amplitude, initial amplitude after shock, wavenumber, and Atwood number, respectively, and $\Delta\mathbf{u}$ is the velocity jump in the direction of travel of the shock following its propagation through the interface at which stage this model assumes that the flow becomes incompressible. This assumption is not valid for high Ma at which strong shocks are formed; for this range of Ma, the transmitted shock recedes slowly and represents an effectively impenetrable boundary, which reduces the growth of the RMI. The Nova laser experiments of Dimonte et al. [45, 46] and Farley et al. [47] showed lower growth rate at large Ma as compared to the predictions by the Richtmyer (1960) incompressbile model; the latter is only valid for the early, linear stage of the RMI prior to the development of secondary KHI whose vortices decelerate the RMI growth. It is therefore unsurprising that the agreement with the Richtmyer (1960) model deteriorates after early times giving way to significantly larger growth rate estimates.

$$\frac{dh}{dt} = k \cdot A_t \cdot h_0 \cdot \Delta\mathbf{u} \tag{3.1}$$

An additional comparison is conducted with the numerical predictions for the perturbation amplitude with those obtained from the work of Dimonte Schneider (2000) who introduced a late-stage model 3.2 which accounts for the drag effects on the growth of RMI. The evolution of the amplitude h of the single-mode RMI is described in this model by the following equation. In 3.2 $c_d = 24$ Re represents a drag coefficient for simple laminar flow around a sphere. The predictions for the perturbation growth made by BlastFOAM and Hytrac are close to each other as shown in 3.48, strengthening the credibility of both codes for these kinds of projections.

$$\frac{d^2h}{d^2t} = -c_d \left(\frac{dh}{dt}\right) \left|\frac{dh}{dt}\right| \frac{1}{h} \tag{3.2}$$

In figure 3.49, the evolution of Richtmyer-Meshkov instability is shown, as simulated using BlastFOAM (BF) and Hytrac (HT). The initial base mesh applied in the simulations is 100x1011 cells. The resolution is increased by using the adaptive mesh refinement (AMR) up to level 3. Both codes BlastFOAM and Hytrac predict a similar growth rate for the Richtmyer-Meshkov instability. As BlastFOAM applies the VOF method, it is expected that BlastFOAM is more diffusive as compared to Hytrac, which uses the hytrid-front-tracking method. As the instability progresses the roll-ups associated with the Kelvin-Helmholtz Instabilty start developing. With increasing AMR level BlastFOAM captures the KHI more accurately, whereas Hytrac does not show a evolving roll-up.

As a next step, a further simulation with AMR level 4 is conducted in Hytrac as depicted in figure 3.50. However, this increase in resolution does not result in resolving the roll-ups associated with KHI. Increasing the resolution beyond AMR level 4 in Hytrac becomes prohibitively expensive in terms of computational cost. It is anticipated that even with resolutions beyond AMR level 4, Hytrac may still not successfully resolve the Kelvin-Helmholtz instability (KHI). For this reason, a preliminary parametric study is conducted to understand the underlying reason. This preliminary parametric study is based on variation of adaptive mesh refinement (AMR), smoothing factor (SF) and redistribution factor (RF). This preliminary study is given in the appendix of this PhD. thesis. To comprehensively understand the specific challenges and limitations associated with Hytrac's resolution capabilities, a more detailed investigation is recommended.

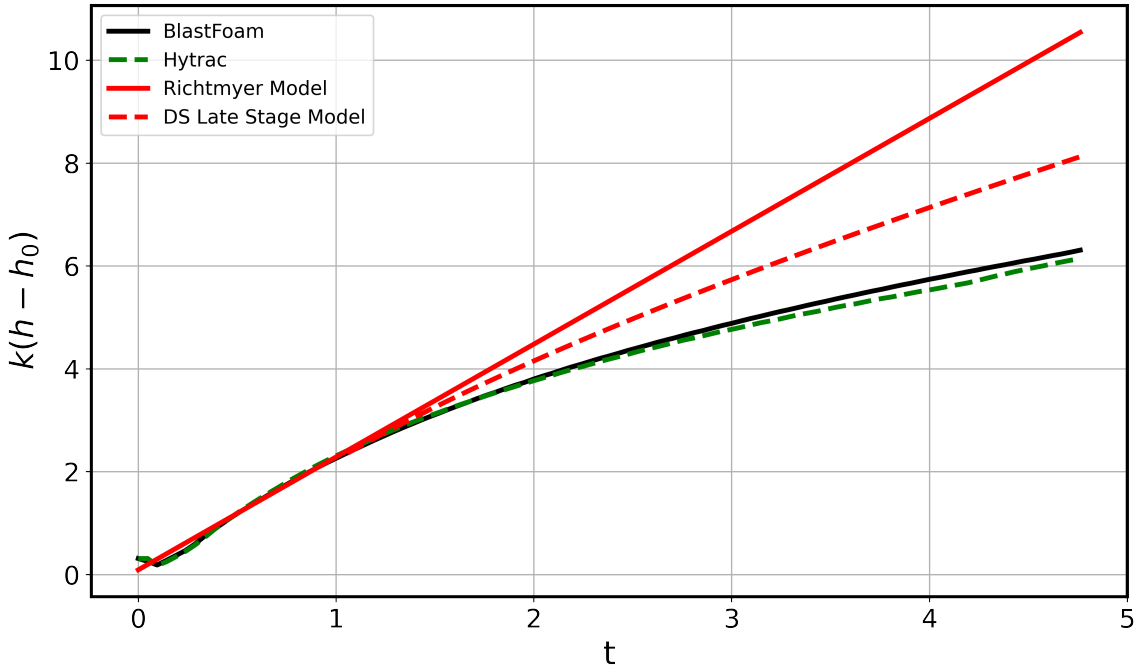


Figure 3.48: Temporal variation of the perturbation amplitude for At = 0.635 and Ma = 1.3, the red solid and dashed lines represent the predictions of the Richtmyer Model and Dimonte Schneider Model (DS Late Stage Model), and black solid and green dashed lines represent the numerical predictions obtained for the BlastFOAM and Hytrac using ideal gas equation of state.

In the volume-of-fluid method, the interface is defined at the volume fraction 0.5. As already discussed in chapter 2 volume-of-fluid method is inherently diffusive as compared to front-tracking, which is a sharp interface modelling method. The diffusion effect can play a significant role for the development of the small-scale structures of the roll-up in the simulations. Considering Hytrac uses a sharp interface modelling method. Hytrac is able to capture the thin ligaments but Hytrac struggles to capture the roll-ups.

The figure 3.51 shows BlastFOAM results at volume fraction 0.5 with AMR 1,2 and 3. figure 3.52 shows BlastFOAM results at AMR level 2 at volume fraction: 0.4, 0.5, 0.6 and 0.7. In the VOF method, increasing the volume fraction from 0.4 to 0.7 leads to better distinction between fluids in a cell. A clearer distinction makes the roll-ups more visible as shown in figure 3.52. BlastFOAM's results at volume fraction 0.5 are very similar to the results of Hytrac. At volume fraction 0.5 BlastFOAM does not capture the roll-up. BlastFOAM uses a diffusive interface method, whereas Hytrac applies a sharp interface modeling method. One potential reason for Hytrac's difficulty in capturing roll-ups may stem from the lack of diffusion phenomena within Hytrac. A detailed investigation into the fluid representation in Hytrac's interface modeling method is recommended. A detailed investigation could deliver valuable insights into the interplay between interface modeling and the diffusion phenomenon and its importance in successfully capturing roll-ups in KHI.

The simulations are conducted at various AMR levels with an initial base mesh of 100x1011 cells. adaptive mesh refinement (AMR) is a computational technique that increases the resolution of the mesh based on a selected criterion in regions where it is needed. In these simulations density gradient is used as the criterion for refinement. The resolution is increased using AMR up to level 3. figures 3.49 show the evolution of Richtmyer-Meshkov instability (RMI) and Kelvin-Helmholtz instability (KHI) as simulated using BlastFOAM and Hytrac at different AMR levels. With increasing AMR levels, BlastFOAM captures the Kelvin-Helmholtz instability (KHI) more accurately, whereas Hytrac does not show evolving roll-ups even at higher AMR levels. The inability of Hytrac to resolve KHI at higher AMR levels suggests a need for further detailed investigation into its numerical methods. The volume-of-fluid (VOF) method in BlastFOAM, which is inherently diffusive compared to Hytrac's front-tracking method, shows that increasing the AMR level improves the resolution of small-scale structures like roll-ups associated with KHI.

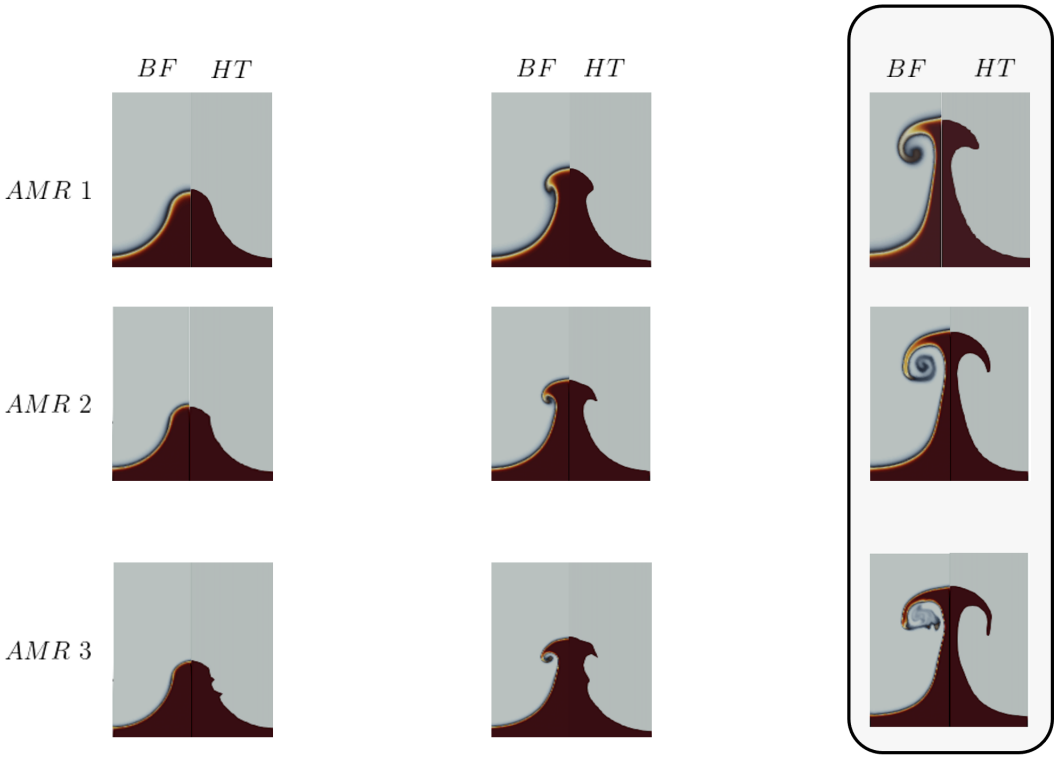


Figure 3.49: Evolution of the Richtmyer-Meshkov instability at $AT = 0.635$, $Ma = 1.3$, using the ideal gas equation of state for air and SF6. This showcases different AMR levels (1-3) in BlastFOAM (BF) and Hytrac (HT) at three time intervals: $t = 1 \times 10^{-3}$ s, 1.8×10^{-3} s, and 3×10^{-3} s.

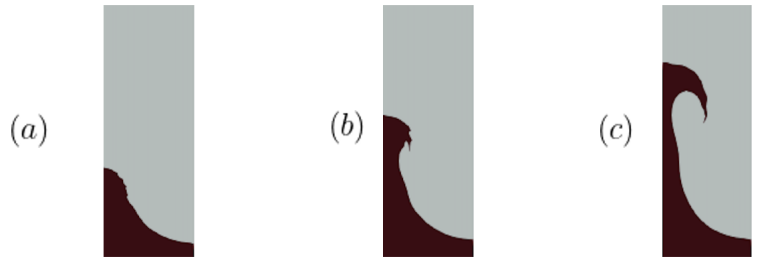


Figure 3.50: Evolution of the Richtmyer-Meshkov instability at $AT = 0.635$, $Ma = 1.3$, using the ideal gas equation of state for air and SF6, AMR 4 in Hytrac (HT) at three time intervals: $t = 8 \times 10^{-4}$ s, 1.8×10^{-3} s, and 3×10^{-3} s.

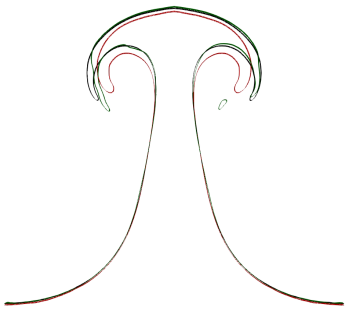


Figure 3.51: Evolution of the Richtmyer-Meshkov instability in BlastFOAM: The red line represents the volume fraction 0.5 using AMR level 1, the black line corresponds to AMR level 2, and the green line indicates AMR level 3 at $AT = 0.635$ and $Ma = 1.3$, employing the ideal gas equation of state at 3×10^{-3} s.

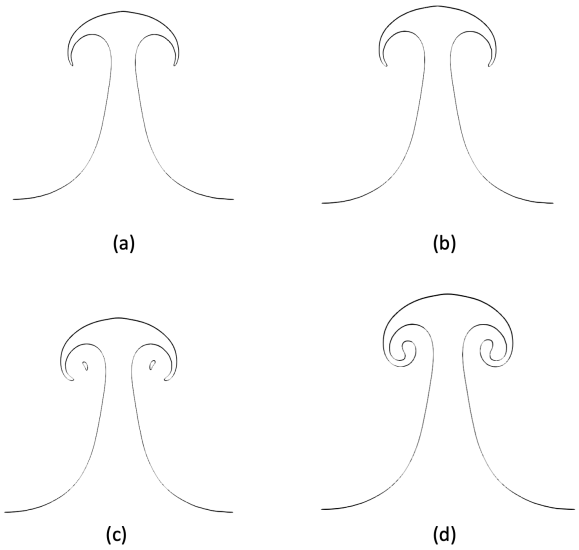


Figure 3.52: Evolution of the Richtmyer-Meshkov instability in BlastFOAM: a, b , c and represent the volume fraction 0.4, 0.5 , 0.6 and 0.7 using adaptive mesh refinement (AMR) level 2 at $AT = 0.635$ and $Ma = 1.3$, employing the ideal gas equation of state at 3×10^{-3} s.

3.2.3 Kelvin-Helmholtz Instabilities

In the Trilab simulations, Hytrac and BlastFOAM demonstrated their capability to capture the dynamics of the Richtmyer-Meshkov instability (RMI). Hytrac and BlastFOAM, predict a similar growth rate for the RMI. However, Hytrac struggles to resolve the roll-ups associated with the Kelvin-Helmholtz instability (KHI). These roll-ups in KHI typically develop due to shear forces resulting from the velocity gradient. An isolated KHI simulation is conducted to study whether Hytrac can accurately resolve these shear forces, which drive the KHI. The initial conditions are given in table 3.5, air with a density of 1.2 kg/m^3 and SF6 with a density of 5.4 kg/m^3 are used. The base mesh is 25x125 cells. A section of the air (darkgray in figure 3.53) is initialised with a velocity of u_1= 400 m/s and a section of SF6 is initialised with the velocity of u_2 = 700 m/s (gray in figure 3.53), while the result of the domain is at rest i.e. adaptive mesh refinement up to level 5 is used to increase the resolution of the simulation. This setup creates a significant velocity gradient at the interface between air and SF6. This velocity gradient is the driving factor for the development of the Kelvin Helmholtz instability. An initial perturbation in induced by the velocity gradient.

Table 3.5: Initial condition of KHI case.

U_1	U_2	ρ_{air}	ρ_{SF6}	p_0
4×10^2 m/s	7×10^2 m/s	1.2 kg/m^3	5.4 kg/m^3	1×10^5 Pa

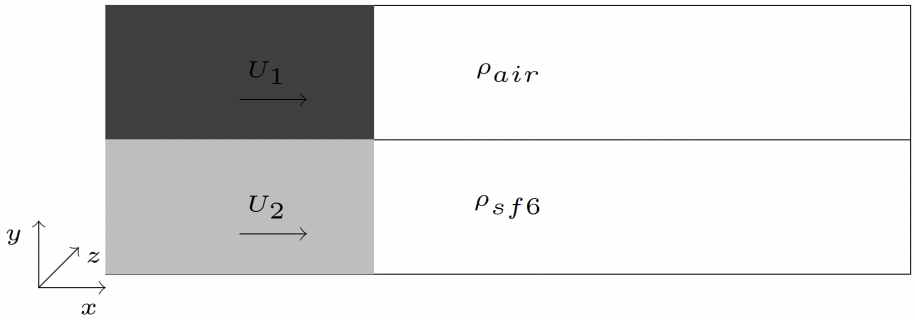


Figure 3.53: Schematic of a flow configuration, where the upper flow region containing air and the lower flow region containing SF6 are separated by an interface. the dark gray area is initialized with a velocity of $U_1 = 400$ m/s, while the light gray area is initialized with a velocity of $U_2 = 700$ m/s.

The simulation results using adaptive mesh refinement (AMR) 4 and 5 are shown in figure 3.54. Both codes BlastFOAM and Hytrac can capture the roll-ups associated with the KHI. BlastFOAM's results are more diffusive compared to Hytrac, especially notable at AMR 4. BlastFOAM uses the volume-of-fluid method, which is very diffusive, whereas Hytrac uses a sharp interface modeling method, the front-tracking method. These results affirm Hytrac's proficiency in accurately capturing the shear forces integral to KHI phenomena.

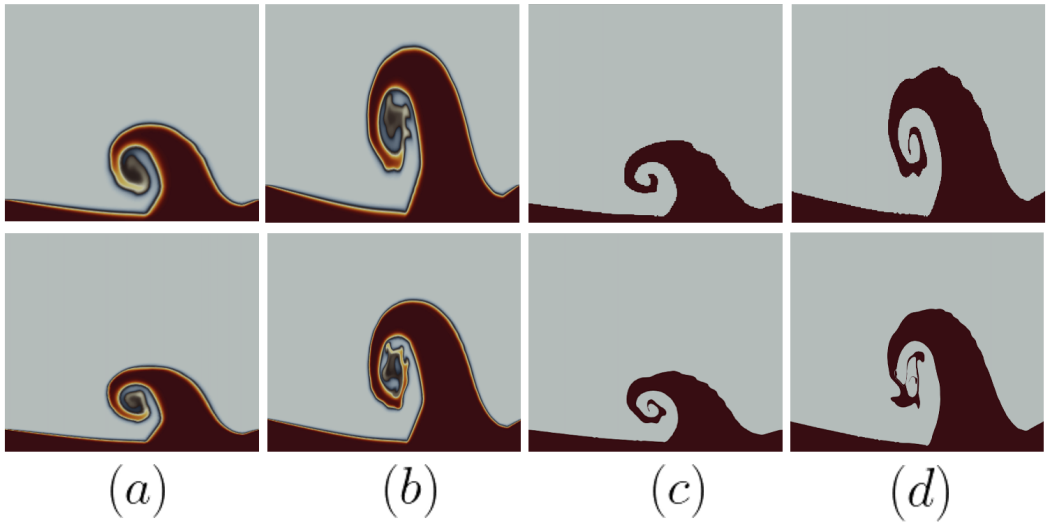


Figure 3.54: Temporal Evolution of Kelvin-Helmholtz instability in air and SF6 fluids using the ideal gas equation of state: a comparative analysis with BlastFOAM and Hytrac simulations. Panel (a) displays BlastFOAM simulations at $t = 5.2\times10^{-3}$, where the upper part is generated with adaptive mesh refinement (AMR) level 4 and the lower part with AMR level 5. Panel (b) presents BlastFOAM simulations at $t = 1 \times 10^{-2}$, with the upper part employing AMR level 4 and the lower part AMR level 5. Panel (c) showcases Hytrac simulations at $t = 5.2 \times 10^{-3}$, with the upper and lower parts generated with AMR levels 4 and 5, respectively. Panel (d) illustrates Hytrac results at $t = 1 \times 10^{-2}$, also utilizing AMR level 4 for the upper part and AMR level 5 for the lower part.

3.2.4 RMI: Jacobs-Krivets Case and Mesh Independence

The simulation results of the Trilab case indicate that both Hytrac and BlastFOAM are able to predict the perturbation amplitude with good accuracy. BlastFOAM is proficient in capturing the roll-ups associated with Kelvin-Helmholtz instability (KHI) as well, while Hytrac successfully models KHI in isolated scenario as discussed in section 3.2.3. However, when addressing the combined effects of KHI and Richtmyer-Meshkov instability (RMI), Hytrac's capability to accurately replicate the associated roll-ups is constrained.. As previously mentioned, a detailed parametric study is recommended to investigate the factors that could influence the model's performance in fully resolving the roll-up structures. Since the experimental data for the span, stream, and neck is not provided for the Trilab case. The RMI experiment from the Jacobs and Krivets is utilized to investigate the accuracy of BlastFOAM in capturing the amplitude, stream, span and neck as shown in figure 4.7. The initial conditions are given in the table 3.6.

Table 3.6: Initial condition of Jacobs and Krivets case.

u_s	Ma	ρ_{air}	ρ_{SF6}
94 m/s	1.3	1.32 (kg/m^3)	5.6(kg/m^3)

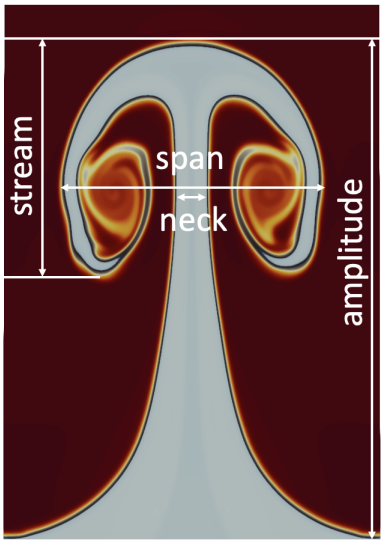


Figure 3.55: Schematic of a fully-developed mushroom-like structure formed following the passage of a shock. The features that characterise the structure are shown together with their defined dimensions.

In figure 3.56, the evolution of Richtmyer-Meshkov instability is illustrated, as simulated using BlastFOAM. The simulation results are validated with the experimental data from Jacobs and Krivets using a 100x1000 base mesh. With increasing AMR level BlastFOAM captures the KHI more accurately. There is a very good agreement between the BlastFOAM results and the experiment of Jacobs and Krivets.

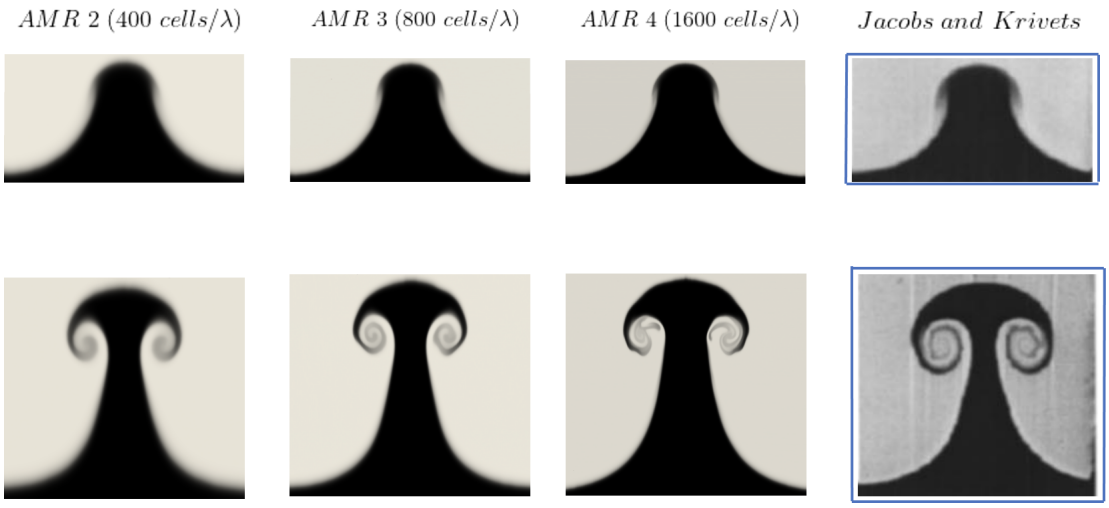


Figure 3.56: Temporal variation of the perturbation amplitude for $At = 0.635$ and $Ma = 1.3$, (a), where the red solid and dashed lines represent the predictions of the Richtmyer (1960) and Dimonte Schneider (2000) models, and black solid and red dashed lines represent to the numerical predictions obtained for the BlastFOAM and Jacobs and Krivets.

In figure 3.57, 3.58, 3.59 and 3.60 BlastFOAM's predictions for amplitude, stream, span and neck are compared with the experiment of Jacobs and Krivets. In figure 3.57 the red solid line represents the combination of Richtmyer's impulsive model and the late-stage model by Dimonte and Schneider. Richtmyer's model is applied until the early time, i.e., $t/tm = 0.5$, after which the late-stage model by Dimonte and Schneider takes over. The BlastFOAM predictions for amplitude for all AMR levels closely match the theoretical predictions, as well as the experimental results In figure 3.60 the BlastFOAM prediction for the neck is shown. As expected, the simulation results closely match the experimental data. The span and stream are characteristics associated with the Kelvin-Helmholtz instability (KHI). Accurately resolving KHI is essential for improving predictions of both span and stream. At AMR level 4, BlastFOAM predictions for span and stream are very close to the experiment However, at a very late stage, the simulation prediction and the experimental result diverge. This divergence can be attributed to the fact that, in the experiment, the Richtmyer-Meshkov instability (RMI) does not remain symmetrical at very late stages, while in the simulation, the results remain symmetric. The divergence in the experiment leads to bigger span and stream.

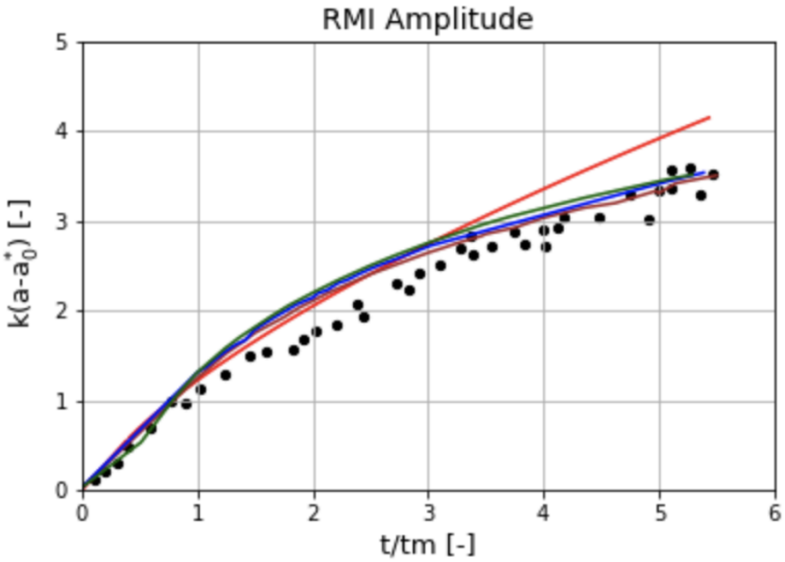


Figure 3.57: Comparison of experimental results for amplitude (black dots) from Jacobs and Krievets [12], theoretical models by Richtmyer [13] and the Late Stage model [14] (red line), with BlastFOAM simulations using the ideal gas equation of state for air and SF_6, where purple line represents AMR level 2, blue AMR level 3, and green AMR level 4 respectively.

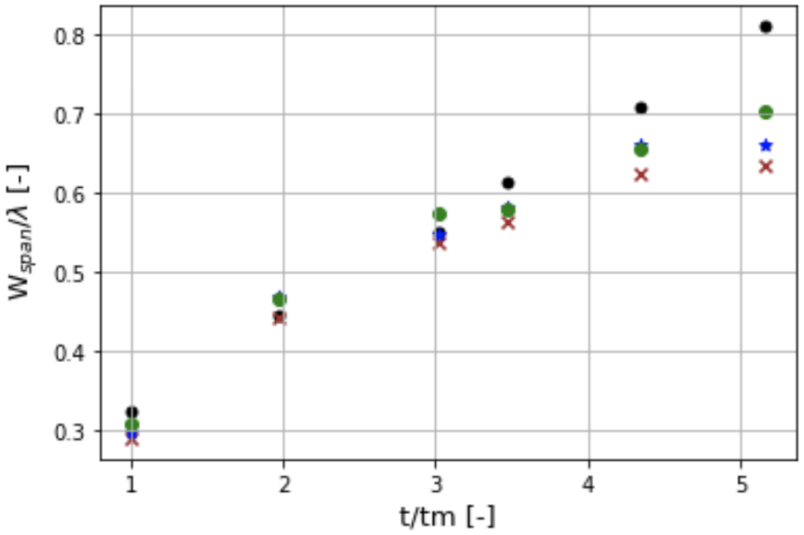


Figure 3.58: Comparison of experimental results for span (black dots) from Jacobs and Krivets [12], with BlastFOAM simulations using the ideal gas equation of state for air and SF_6, where red represents AMR level 2, blue AMR level 3, and green AMR level 4 respectively.

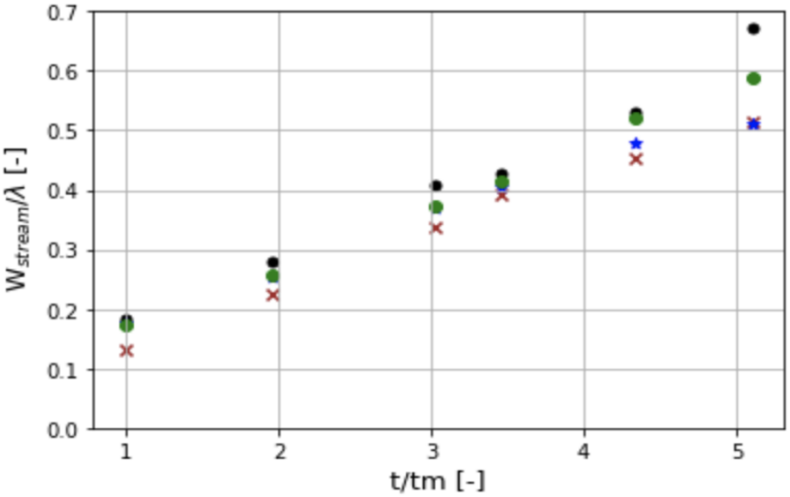


Figure 3.59: Comparison of experimental results for stream (black dots) from Jacobs and Krivets [12], with BlastFOAM simulations using the ideal gas equation of state for air and SF_6, where red represents AMR level 2, blue AMR level 3, and green AMR level 4 respectively.

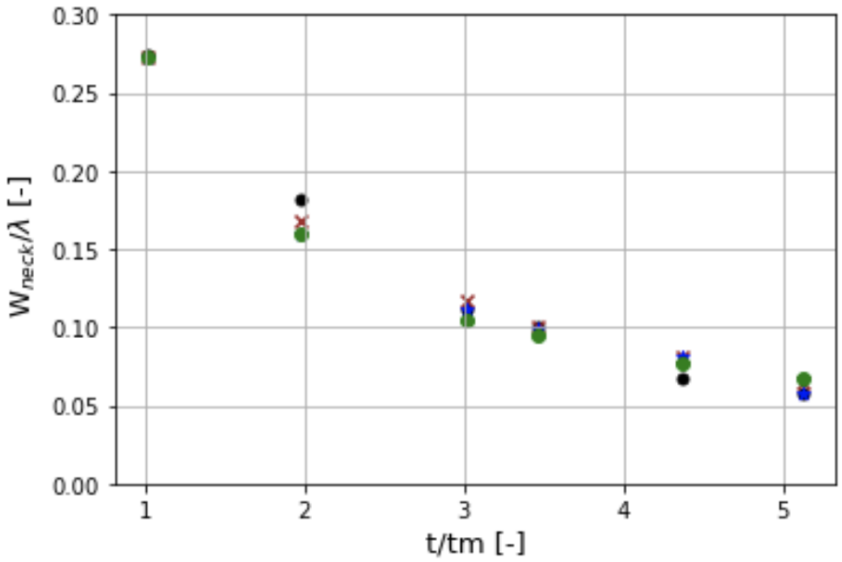


Figure 3.60: Comparison of experimental results for neck (black dots) from Jacobs and Krivets [12], with BlastFOAM simulations using the ideal gas equation of state for air and SF_6, where red represents AMR level 2, blue AMR level 3, and green AMR level 4 respectively.

In these simulations, adaptive mesh refinement (AMR) uses the density gradient as the criterion for refinement. It refines the mesh regions, where significant density gradients occur. As shown in figures 3.57 to 3.60, increasing the AMR level from 2 to 4 leads to results that are closer to experimental results of Jacobs and Krivets [48]. At higher AMR levels, particularly at AMR level 4 as shown in figure 3.56, the shape of the RMI matches the experimental results closely. BlastFOAM's predictions at AMR 4 for amplitude, span, stream and neck are very close to the experimental data. This shows that higher mesh refinement levels lead to better resolution of small-scale structures, such as the roll-ups associated with the Kelvin-Helmholtz instability (KHI) as shown in figure 3.57. However, going beyond AMR 4 becomes computationally expensive, so it is not viable. This trend confirms that while higher refinement levels improve accuracy, there is a trade-off with computational cost. This mesh configuration will be used for all RMI cases in the following chapters.

3.3 Impact of Initial Wavelength

In this section, the impact of initial wavelength on the development of Richtmyer-Meshkov instability (RMI) is investigated while keeping other parameters constant, such as the initial amplitude h_0, the Atwood number A_t, and the shock constant. The initial conditions for the simulations are summarized in table 3.7. The wavelength λ is varied from 1.5 mm to 4.5 mm to investigate how the wavelength impacts the development of RMI.

Table 3.7: Initial conditions

u_s	Ma	ρ_{air}	ρ_{SF6}	λ_a	λ_b	λ_c	h_0
94 m/s	1.3	1.32 (kg/m^3)	5.6 (kg/m^3)	1.5 mm	3 mm	4.5 mm	0.008 mm

Richtmyer-Meshkov instability grows according to the Richtmyer model, as shown in equation 3.3.

$$\frac{dh}{dt} = k \cdot A_t \cdot h_0 \cdot \Delta \mathbf{u} \tag{3.3}$$

where k is the wavenumber, A_t is the Atwood number, h_0 is the initial amplitude, and $\Delta \mathbf{u}$ is the velocity difference across the interface. The wavenumber k is related to the wavelength λ by the equation $k = \frac{2\pi}{\lambda}$. The comparison of the RMI development for different initial wavelengths, as shown in figure 3.61, reveals that the initial wavelength has a significant impact on the overall development of the RMI. With shorter wavelengths, the disturbances occur more frequently, leading to quicker destabilization of the interface.The growth of the RMI varies significantly with different initial wavelengths. For shorter wavelengths, the instability grows more rapidly compared to longer wavelengths, as shown in figure 3.61. This is due to the higher ratio of initial perturbation amplitudes to their wavelengths, leading to rapid growth. This rapid growth can be quantified using the Richtmyer model equation 3.3.

A smaller initial wavelength results in a larger wavenumber. A larger wave number leads to a higher growth rate. Simulations demonstrate that shorter wavelengths result in more pronounced perturbations at earlier times. For instance, at t_1, the RMI for $\lambda_a = 1.5$ mm is significantly more developed compared to the cases with wavelength of $\lambda_c = 3.0$ mm or $\lambda_c = 4.5$ mm . By t_2, these differences become even more evident, indicating that initial wavelength is a crucial factor in the evolution of RMI as shown in figure 3.61. Shorter wavelengths correspond to higher frequencies of the initial perturbation, resulting in faster energy transfer and more rapid destabilization of the interface.

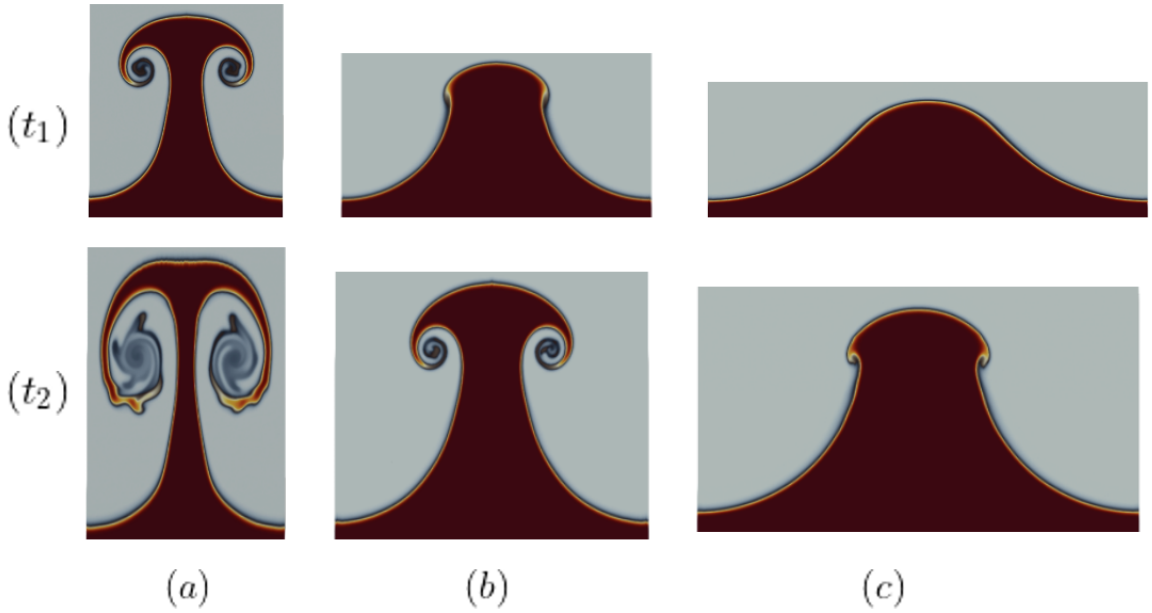


Figure 3.61: Comparison of the development of Richtmyer-Meshkov instability (RMI) using different initial wavelengths: (a) corresponds to 1.5 mm, (b) to 3 mm, and (c) to 4.5 mm at $t_1 = 0.00045$ s and $t_2 = 0.0009$ s. Simulations are performed using BlastFOAM with the ideal gas equation of state for air and SF_6 an intial shock at Mach 1.3.

3.4 Limitations of Models

The volume-of-fluid method as implemented in BlastFOAM is very robust in capturing interfaces between fluids. However, one of its major limitations is diffusivity. This limitation can lead to smearing of the interface, particularly in regions, where high resolution of small-scale structures like the roll-ups in KHI is required. This smearing can diminish such important details of the fluid interface, lowering the overall accuracy of the results. This inherent feature (diffusivity) of the volume-of-fluid method can lead to less accurate predictions of the growth and evolution of instabilities. These inaccuracies are particularly problematic in scenarios where precise interface modelling is crucial for capturing the correct physics of the problem. A high mesh resolution is needed to counteract the diffusion in BlastFOAM. High resolution meshes can capture finer details of the interface. However, increasing the resolution requires significantly higher computational costs. This requirement of higher mesh resolution makes simulations computationally prohibitive, limiting their practical applicability. Although higher AMR levels can provide better accuracy, but they are often not feasible due to their resource-intensive nature.

Hyrac is based on the hybrid front-tracking method. This method provides an alternative approach to the volume-of-fluid method. Hybrid front-tracking can model the interface very accurately even at lower mesh resolutions compared to volume-of-fluid method as implemented in BlastFOAM. BlastFOAM requires a higher resolution to counteract diffusion. However, Hytrac has its own limitations. It cannot capture the roll-ups associated with KHI. Preliminary studies conducted in the appendix could not determine the underlying cause of this limitation. Therefore, a detailed investigation into the code is needed to understand the underlying problem.

In the multi-material 1D shock-tube case, stiffened gas equation of state model is used for copper and plastic, while an ideal gas equation of state is used for deuterium. Using the ideal gas equation of state and stiffened gas equation of state simplifies the behavior of materials under extreme conditions. While these simplifications can make the simulations more manageable, they also introduce inaccuracies, such as the pressure drop to vacuum conditions due to the rarefaction wave induced by a high gradient between deuterium and plastic. A tabulated equation of state derived from empirical data of the materials is needed to increase the accuracy of the results.

In addition to this, multi-physics interactions are neglected. These simulations do not fully account for multi-physics interactions such as turbulence, heat and mass transfer, phase changes, and conduction. These interactions can significantly impact the overall fluid behavior. For example, turbulence can enhance mixing and influence the growth and structure of instabilities, while heat and mass transfer can affect phase distribution and fluid properties. The absence of these interactions means that the simulations provide a limited view of the actual physical processes, potentially overlooking important dynamics. Incorporating multi-physics interactions would provide a more comprehensive understanding.

Chapter 4

RMI:Non-Newtonian Effects

This chapter presents a distinct contribution to the field of fluid dynamics by extending the capabilities of the BlastFOAM code to model the non-Newtonian shear-thinning flows, enabling more accurate simulations of complex scenarios relevant to inertial confinement fusion (ICF). Additionally, a vorticity equation for non-Newtonian fluids is formulated to investigate the influence of non-Newtonian viscosity on the evolution of vorticity with a detailed breakdown of each term to identify their roles in generating and damping vorticity. This chapter further studies the effects of non-Newtonian viscosity on the development of hydrodynamic instabilities, such as RMI and KHI, which are relevant to ICF due to their role in mixing hot and cold fluids and potentially reducing the temperature and pressure necessary for ignition under high Mach number conditions.

4.1 Code Development

BlastFOAM 3.5 [49] is an open-source numerical code based on the OpenFOAM framework. BlastFOAM is developed for highly compressible multiphase flows. It uses the algebraic volume-of-fluid method to model multiphase flows. A detailed explanation of the algebraic volume-of-fluid method can be found in chapter 2. BlastFOAM uses a density-based solution algorithm. Density-based solution codes are suitable for highly compressible flows. These codes solve the conservation equations in a fully coupled manner. This approach is essential for accurately capturing the density variations and the dynamics of the flow especially at high speeds. The density is calculated from the continuity equation, and the pressure is determined by the equation of state. In contrast, pressure-based methods such as compressibleInterFOAM in OpenFOAM use a segregated solution algorithm. They calculate the pressure from a correction loop derived from combining the momentum and continuity equations, and the density is calculated from the equation of state. They are more suitable for incompressible, low Mach number flows.

Implementation of non-Newtonian Model

This study aims to investigate the impact of non-Newtonian effects on the development of the Richtmyer-Meshkov instability. Richtmyer-Meshkov instability plays a crucial role in nuclear fusion research, as already described in chapter 2 RMI leads to mixing of colder and hotter fluids, potentially reducing the temperature necessary to sustain a fusion reaction. As a result, RMI is typically not a desirable phenomenon in fusion research. This study investigates how a non-Newtonian material can impact the growth of the RMI and KHI. Currently, BlastFOAM models viscosity as a constant value. However, non-Newtonian fluids' viscosity varies with strain rate and temperature. Therefore, to accurately simulate such fluids, further development of BlastFOAM is necessary to model non-Newtonian fluids. Shear rate is implemented as a primitive variable, similar to pressure, density, and velocity in the code.

By implementing the shear rate in BlastFOAM, any viscosity model where the viscosity varies with temperature or shear rate can be used. The complete further development of BlastFOAM including scripts developed within this PhD project for calculating vorticity based on the derived vorticity equation 4.32 for non-Newtonian fluids and scripts that solve the Richtmyer [30] and Dimonte and Schneider [31] model will be published on Github. The vorticity equation for non-Newtonian fluids is derived in this chapter. Further scripts used but not developed within this PhD thesis, such as the Riemann solver used in Toro and Kaliski's shock-tube to find the theoretical solution (developed by Wolfdynamics Ltd. [50]), will also be provided on GitHub. The further developed version of BlastFOAM 3.5 is named non-Newtonian BlastFOAM 3.5. By implementing the shear rate in BlastFOAM, any viscosity model where the viscosity varies with temperature or shear rate can be used.. The shear-rate $\dot{\gamma}$ is calculated with the equation 4.1. The following libraries have been modified to implement the shear-rate.

- compressibleSystem
  - multiphaseCompressibleSystem
  - phaseCompressibleSystem
  - singlePhaseCompressibleSystem
  - twoPhaseCompressibleSystem
- fluxSchemes
  - fluxScheme
- thermodynamicModels/basic
  - basicThermo
  - blendedThermo
  - eThermo
  - fluidThermo

  - solidThermo

- thermodynamicModels/derived
  - basicFluidThermo
  - basicSolidThermo
  - detonatingFluidThermo
  - multiphaseFluidThermo
  - TwoPhaseFluidThermo

After modifying the above-mentioned libraries, any non-Newtonian viscosity model can be implemented in the transport model library. Now, any viscosity model that depends on the shear rate, temperature, or density can be used.

$$\dot{\gamma} = \sqrt{2} \cdot \|\text{symm}(\nabla \mathbf{U})\| \tag{4.1}$$

where $\dot{\gamma}$ is the shear rate, $\nabla \mathbf{U}$ is the velocity gradient tensor, and $\text{symm}(\nabla \mathbf{U})$ denotes the symmetric part of the velocity gradient tensor.

4.1.1 Code Validation

A non-Newtonian fluid with a density of $1000\ kg/m^3$ based on a power-law model is chosen to validate the further development of BlastFOAM 3.5. The theoretical results [15] are compared with the predicted simulation results of the further developed version of BlastFOAM. The power-law fluid is described by equation 4.2, where μ, K, $\dot{\gamma}$, and n are dynamic viscosity, consistency index, shear rate, and flow index, respectively. The flow index is set to 0.75, and the consistency index to 1.47 $Pa\ s^n$. The computational domain is a wedge-shaped segment of a cylindrical pipe, representing an axisymmetric section to model the full pipe as shown in figure 4.1. A pressure difference of 58.6 Pa between the inlet and the outlet is used to drive the flow. A comparison of the predicted velocity profile for a shear-thinning fluid by BlastFOAM against the theoretical solution is shown in figure 4.2. BlastFOAM's results are very close to the theoretical solution. This validates the further development of BlastFOAM to capture shear-thinning fluids.

$$\mu = K\dot{\gamma}^{n-1} \tag{4.2}$$

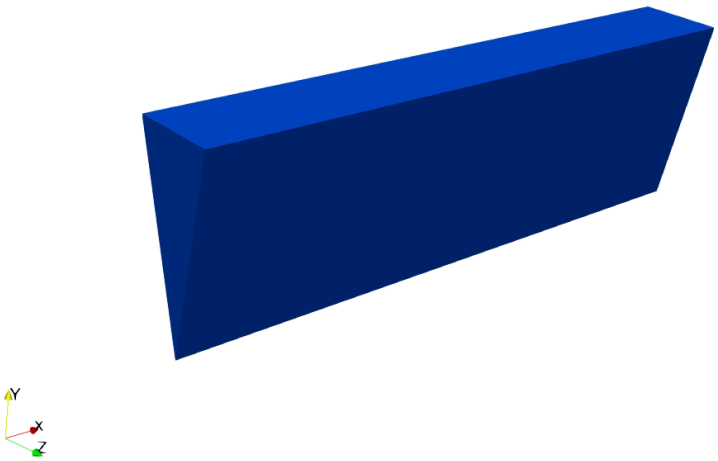


Figure 4.1: A sketch of the domain as used in BlastFOAM for the shear-thinning flow simulation in a pipe.

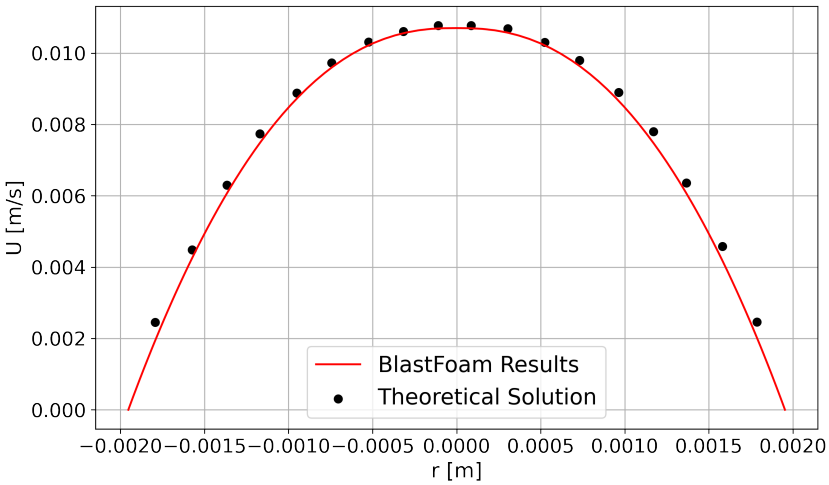


Figure 4.2: Comparison of BlastFOAM predicted using stiffened gas equation of state and theoretical velocity [15] profile for a shear-thinning power-law fluid in a pipe with n = 0.75, K=1.47 $Pa\ s^n$, ρ=1000 kg/m^3

4.2 Evolution of RMI

The Richtmyer-Meshkov instability (RMI) results from the misalignment of pressure and density gradients at the interface of two materials with different densities when a shock wave passes through. This instability generates vorticity that leads to the growth of perturbations at the interface, eventually leading to a transition to a turbulent regime. The RMI was first proposed by Richtmyer [30], and the theory was later

confirmed by the shock-tube experiments conducted by Meshkov [31]. This instability has important implications for a wide range of natural and engineering problems, including supersonic combustion, supernovae, and inertial confinement fusion. For example, the occurrence of RMIs in supersonic combustion triggers better mixing and thus enhanced combustion efficiency. In supernova explosions, RMIs break the spherical symmetry of the progenitor star and create conditions for the synthesis of heavy elements. In inertial confinement fusion, RMIs initiate mixing between the hotter and colder layers, resulting in a reduction of temperature that inhibits the thermonuclear burn. Despite the extensive research that has been conducted on RMI and associated phenomena, there are still many unresolved questions, particularly regarding the non-Newtonian effects on the instability. The impulsive model proposed by Richtmyer [30] only analyzed the 'light-to-heavy' flow configuration, where the shock travels in the direction of the denser fluid. However, Meshkov [31] ran shock tube experiments with both flow configurations, suggesting that the impulsive model could be applied for both light-to-heavy and heavy-to-light flow configurations. The Richtmyer impulsive model is based on a linear framework and is therefore valid for early times when the perturbation amplitude is considerably smaller than its wavelength. As the amplitude exceeds the wavelength, nonlinear effects become significant, rendering the impulsive model invalid. In response to these limitations, Yang et al. [51] introduced a refined version of Richtmyer's model to incorporate compressibility effects, which provides a more comprehensive description of perturbation evolution under shock compression.

Additionally, the Zhang and Sohn [52] model offers an alternative approach to simulate the late-time behaviour of the perturbation, distinguished by its utilization of Padé approximants. However, this model has its limitations as well, notably its tendency to underestimate the late-time average growth rate of the perturbation. To address this issue, Sadot et al. [53] introduced a model developed using data from shock-tube experiments with air and sulfur hexafluoride. Another significant model for the late-time stage is the Dimonte and Schneider [14] model, which, unlike that of Richtmyer [30], uses a drag coefficient to account for the reduced growth rate at the late-time stage. The predictions obtained from both these models will be compared to those provided by the numerical computations in this study. Building upon the foundational work in this field, Thornber et al. [54] studied the critical influence of three-dimensional multi-mode initial conditions on the growth of turbulent mixing layers in RMI. Their use of high-resolution large-eddy simulations underscored the significant impact of initial conditions on the evolution of these layers. Further advancing our understanding of RMI, Thornber et al. also explored the reshock phase [55]. Through high-order accurate Implicit Large-Eddy-Simulations, they extended theoretical models to accurately predict the behavior of reshocked mixing layers, offering invaluable insights for scenarios involving broadband initial perturbations.

Numerical simulations have also been used to study the effects of viscosity on the RMI. Mikaelian [56] proposed a theoretical model in which viscosity dampens the growth of the instability, while Carles and Popinet [57] used direct numerical simulations as a benchmark to derive a theoretical model for the RMI of viscous flows. Movahed and Johnsen [58] performed numerical simulations using a solution-adaptive method, which revealed that viscosity dampens the growth of the instability in agreement with the work of Mikaelian [56]. The study of vorticity evolution within RMI has also undergone considerable progress. Kotelnikov, Ray and Zabusky [59] shed light on the dynamics of secondary baroclinic vorticity deposition. Building upon this work Peng, Zabusky and Zhang [12] studied vortex-accelerated secondary baroclinic vorticity generation and its effects on the intermediate and late-time flow evolution and RMI features such as amplitude, neck, span, and stream (all of which will feature in the validation studies presented below), at different stages of its evolution. Baroclinic vorticity has traditionally been viewed as the exclusive source of vorticity evolution, often overlooking the impact of viscosity.

To investigate the viscosity effects Wang et al. [60] studied a shock-bubble-interaction problem. They introduced a dimensionless number for the baroclinic to viscous source ratio in the vorticity evolution. Liu et al. [61] demonstrated that viscosity gradients, which emerge due to temperature variations within strong shock waves, make a positive contribution to the generation of vorticity particularly at high Mach numbers.

While previous studies have mainly focused on the effects of viscosity on the instability, non-Newtonian fluids exhibit additional complexities, such as shear-thinning and elasticity, which could have a significant impact on the instability growth. This gap in the literature will be addressed in the present study. This study investigates the influence of non-Newtonian effects on the generation and damping of vorticity that influence the dynamics of the RMI. By incorporating these effects into the numerical simulations. The aim is to provide insights into the dynamics associated with shock impact wherein at least one of the fluids is a non-Newtonian material; this is relevant to nuclear fusion-type applications such as in the shock-driven fusion application of Derentowicz et al. [17]. In this study, numerical simulations are used to investigate the effects of shear-thinning and temperature dependent viscosity behaviour in the denser phase, with the lighter one remaining Newtonian, and demonstrate that these effects promote the RMI. The non-Newtonian fluid will be modelled as a Bird-Carreau-Yasuda fluid; elasto/plastic effects will be neglected in this study. A parametric study is carried out to examine the effect of the Mach and Atwood numbers on the emergent dynamics and provide a breakdown of all the terms that contribute to vorticity production and damping to pinpoint the destabilising mechanisms unambiguously over the various stages of the flow; these will include the dynamics following the passage of the initial shock as well as subsequent reflected shocks. The results will be compared with those obtained when both fluids are either inviscid or Newtonian.

Simulation Setup

An interface perturbation of wavelength λ, separating two fluids of different densities, corresponding to a denser and a less dense phase is applied. The denser and lighter will loosely referred in this study as 'heavy' and 'light', respectively. The initial densities and viscosities of the light and heavy fluids are $\rho_{l,0}$ and $\rho_{h,0}$, and $\mu_{l,0}$ and $\mu_{h,0}$, respectively, and both fluids are at a pressure p_0. As shown in figure 4.3, a shock wave resulting from a jump in pressure and density within the heavy phase, propagates towards the lighter phase and impacts the interface, leading to the development of a Richtmyer-Meshkov instability. The pressure and density ratios associated with the shock are denoted by $p_{h,s}/p_0$ and $\rho_{h,s}/\rho_{h,0}$, where the subscripts s and 0 designate the shocked left state (away from the interface) and the right state (close to the interface), respectively; interfacial tension effects are neglected. It is considered in this study that the heavy phase can be either inviscid or viscous, with a non-Newtonian rheology featuring a shear rate dependent and temperature dependent apparent viscosity.

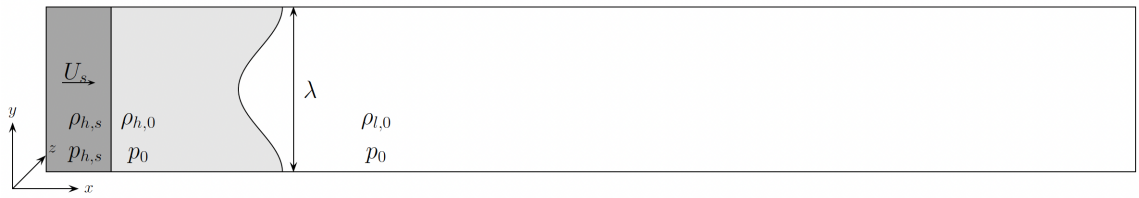


Figure 4.3: Schematic of the flow configuration in which a perturbation of wavelength λ is applied to an interface separating two phases at pressure p_0 of initial densities $\rho_{h,0}$ and $\rho_{l,0}$ shown by the light grey and white regions, respectively, where $\rho_{h,0} > \rho_{l,0}$. A shock is initiated in the heavier phase (dark grey region) with density $\rho_{h,s}$ and pressure $p_{h,s}$, which travels in the direction of the lighter phase at constant speed U_s.

In contrast, the lighter phase is either considered to be inviscid or Newtonian, with a constant viscosity. The shock and interface dynamics are governed by the mass conservation of each phase and the one-fluid formulation of the compressible momentum, and energy equations, respectively expressed by

$$\frac{\partial \rho_h}{\partial t} + \boldsymbol{\nabla} \cdot (\rho_h \mathbf{u}) = 0, \tag{4.3}$$

$$\frac{\partial \rho_l}{\partial t} + \boldsymbol{\nabla} \cdot (\rho_l \mathbf{u}) = 0, \tag{4.4}$$

$$\begin{aligned}\frac{\partial \rho \mathbf{u}}{\partial t} + \boldsymbol{\nabla} \cdot (\rho \mathbf{u}\mathbf{u}) = & - \boldsymbol{\nabla} p + \rho \mathbf{g} \\ & + \boldsymbol{\nabla} \cdot \left(\mu \left[\boldsymbol{\nabla} \mathbf{u} + (\boldsymbol{\nabla} \mathbf{u})^T \right] \right) \\ & - \frac{2}{3} \boldsymbol{\nabla} \cdot \left(\mu \left[(\boldsymbol{\nabla} \cdot \mathbf{u}) \mathbf{I} \right] \right), \end{aligned} \tag{4.5}$$

$$\frac{\partial (\rho e)}{\partial t} + \boldsymbol{\nabla} \cdot [(\rho e + p)\mathbf{u}] = \boldsymbol{\nabla} \cdot (\mu \boldsymbol{\nabla} \cdot \mathbf{u}\mathbf{u}) + \boldsymbol{\nabla} \cdot (\kappa \boldsymbol{\nabla} T) - \rho \mathbf{g} \cdot \mathbf{u}, \tag{4.6}$$

where t, ρ_h, ρ_l, ρ, μ, $\mathbf{u}$, p, $\mathbf{g}$, e, T, and κ correspond to the time, heavy fluid density, light fluid density, local mixture density and viscosity, mixture velocity, mixture pressure, acceleration due to gravity, mixture total energy per unit mass, temperature, and thermal conductivity, respectively. Using the wavelength of the interface perturbation λ as the length scale and the shock speed U_S as the velocity scale, the corresponding time scale is $t_S = \lambda / U_S$; in addition, the dynamic pressure scale is $\rho_{h,0} U_S^2$, the energy per unit mass scale U_S^2, and the density and viscosity scales as $\rho_{h,0}$ and $\mu_{h,0}$, respectively, the above governing equations are written in dimensionless form as follows:

$$\tilde{\boldsymbol{\nabla}} \cdot \tilde{\mathbf{u}} = -\frac{1}{\tilde{\rho_h}} \frac{D\tilde{\rho_h}}{D\tilde{t}} = -\frac{Ma^2}{\tilde{\rho_h}} \frac{D\tilde{p_h}}{D\tilde{t}}, \tag{4.7}$$

$$\tilde{\boldsymbol{\nabla}} \cdot \tilde{\mathbf{u}} = -\frac{1}{\tilde{\rho_l}} \frac{D\tilde{\rho_l}}{D\tilde{t}} = -\frac{C_h^2}{C_l^2} \frac{Ma^2}{\tilde{\rho_l}} \frac{D\tilde{p_l}}{D\tilde{t}}, \tag{4.8}$$

$$\begin{aligned}\frac{\partial \tilde{\rho} \tilde{\mathbf{u}}}{\partial \tilde{t}} + \tilde{\boldsymbol{\nabla}} \cdot (\tilde{\rho} \tilde{\mathbf{u}} \tilde{\mathbf{u}}) = & - \tilde{\boldsymbol{\nabla}} \tilde{p} + \frac{1}{Fr^2} \tilde{\rho} \tilde{\mathbf{g}} \\ & + \frac{1}{Re} \tilde{\boldsymbol{\nabla}} \cdot \left(\tilde{\mu} \left[\tilde{\boldsymbol{\nabla}} \tilde{\mathbf{u}} + \left(\tilde{\boldsymbol{\nabla}} \tilde{\mathbf{u}} \right)^T \right] \right) \\ & - \frac{2}{3} \tilde{\boldsymbol{\nabla}} \cdot \left(\tilde{\mu} \left[\left(\tilde{\boldsymbol{\nabla}} \cdot \tilde{\mathbf{u}} \right) \mathbf{I} \right] \right), \end{aligned} \tag{4.9}$$

$$\begin{aligned}\frac{\partial (\tilde{\rho} \tilde{e})}{\partial \tilde{t}} + \tilde{\boldsymbol{\nabla}} \cdot [(\tilde{\rho} \tilde{e} + \tilde{p}) \tilde{\mathbf{u}}] = & \frac{1}{Re} \tilde{\boldsymbol{\nabla}} \cdot (\tilde{\mu} \tilde{\boldsymbol{\nabla}} \cdot \tilde{\mathbf{u}} \tilde{\mathbf{u}}) + \frac{1}{Pe} \tilde{\boldsymbol{\nabla}} \cdot (\tilde{\kappa} \tilde{\boldsymbol{\nabla}} \tilde{T}) \\ & - \frac{1}{Fr^2} \tilde{\rho} \tilde{\mathbf{g}} \cdot \tilde{\mathbf{u}}. \end{aligned} \tag{4.10}$$

Using mass conservation, the momentum equation can also be re-written as

$$\begin{aligned}\frac{\partial\tilde{\rho}\tilde{\mathbf{u}}}{\partial\tilde{t}} + \tilde{\boldsymbol{\nabla}}\cdot(\tilde{\rho}\tilde{\mathbf{u}}\tilde{\mathbf{u}}) &= -\tilde{\boldsymbol{\nabla}}\tilde{p} \\ &+ \frac{1}{Re}\tilde{\boldsymbol{\nabla}}\cdot\left(\tilde{\mu}\left[\tilde{\boldsymbol{\nabla}}\tilde{\mathbf{u}} + \left(\tilde{\boldsymbol{\nabla}}\tilde{\mathbf{u}}\right)^{T}\right]\right) + \frac{Ma^2}{Re}\tilde{\boldsymbol{\nabla}}\cdot\left(\frac{2}{3}\frac{\tilde{\mu}}{\tilde{\rho}}\frac{D\tilde{p}}{D\tilde{t}}\,\mathbf{I}\right) \\ &+ \frac{1}{Fr^2}\tilde{\rho}\tilde{\mathbf{g}}.\end{aligned} \tag{4.11}$$

In the above equations, C_h and C_l are the speeds of sound in the heavy and light phases, and $Ma = U_S/C_h$, $Re = \rho_{h,0}\,U_S\,\lambda/\mu_{h,0}$, and $Fr = U_S/\sqrt{g\,\lambda}$ stand for the Mach, Reynolds, and Froude numbers, respectively. Furthermore, the Péclet number, $Pe = U_s\lambda/\mathcal{D}$, represents the ratio of advective to diffusive transport phenomena wherein $\mathcal{D}$ denotes the thermal diffusivity. In this study conduction is considered negligible, corresponding to scenarios where the Péclet number is large, i.e., the $Pe \to \infty$ limit.

Additionally, the Atwood number, At, is defined as the ratio of the difference in initial densities to their sum and expressed by:

$$At = \frac{\rho_{l,0} - \rho_{h,0}}{\rho_{l,0} + \rho_{h,0}}. \tag{4.12}$$

According to this definition, a negative (positive) At suggests the propagation of the shock from the heavier (lighter) to the lighter (heavier) fluid. This study focuses on flows parameterised by negative At. equations (4.7)-(4.10) are solved using the open-source software BlastFOAM [49], which has been further developed to model non-Newtonian multiphase flows in this study. BlastFOAM also employs the volume-of-fluid method to capture the interface by advecting the volume fraction of the heavy fluid, α, according to

$$\frac{\partial\alpha}{\partial t} + \tilde{\boldsymbol{\nabla}}\cdot(\alpha\tilde{\mathbf{u}}) = \alpha\tilde{\boldsymbol{\nabla}}\cdot\tilde{\mathbf{u}}, \tag{4.13}$$

where $\alpha = 0$ and $\alpha = 1$ for cells occupied by the light and heavy fluids, respectively; the interface resides in cells wherein $0 < \alpha < 1$. Within the VOF framework, α is used to calculate the local density and viscosity as follows:

$$\tilde{\rho} = \alpha\tilde{\rho}_h + (1-\alpha)\tilde{\rho}_l, \tag{4.14}$$

$$\tilde{\mu} = \alpha\tilde{\mu}_h + (1-\alpha)\tilde{\mu}_l. \tag{4.15}$$

The stiffened gas equation of state is employed to calculate the pressure in each phase $\tilde{p}_i$ and the mixture pressure $\tilde{p}$ in Mie-Gruneisen form [62],

$$\tilde{p}_i = (\gamma_i - 1)\tilde{\rho}_i\tilde{e} - \gamma_i\tilde{a}_i, \tag{4.16}$$

$$\tilde{p} = \frac{\tilde{\rho}\tilde{e} - \left(\frac{\alpha\gamma_h\tilde{a}_h}{\gamma_h - 1} + \frac{(1-\alpha)\gamma_l\tilde{a}_l}{\gamma_l - 1}\right)}{\frac{\alpha}{\gamma_h - 1} + \frac{1-\alpha}{\gamma_l - 1}}, \tag{4.17}$$

where γ_i and $\tilde{a}_i$ are the compressibility and the reference pressures, respectively, which are (constant) material properties in each phase. The non-Newtonian behavior of the heavier fluid is modeled using the Bird-Carreau-Yasuda (BCY) model in which both the shear-thinning and temperature dependency of the viscosity are taken into account:

$$\tilde{\mu}_h(\tilde{\dot{\gamma}}, T) = \tilde{\mu}_{h,\infty} + \frac{\tilde{\mu}_{h,0}\tilde{E_T} - \tilde{\mu}_{h,\infty}}{[1 + (\tilde{\tau}\tilde{\dot{\gamma}}\tilde{E_T})^2]^{(1-n)/2}}; \tag{4.18}$$

$$\tilde{E_T} = \exp\left[\alpha_{\mathrm{T}}\left(\frac{\tilde{\mathrm{T}}^*}{\tilde{\mathrm{T}}} - 1\right)\right] \tag{4.19}$$

Here, $\tilde{\mu}_{h,\infty}$ and $\tilde{\mu}_{h,0}$ represent the dimensionless infinite and zero-shear rate viscosities, respectively, $\tilde{\dot{\gamma}}$ is the dimensionless shear rate, the flow index is denoted by n, while $\tilde{\tau}$ represents the ratio of the relaxation time, τ, to the flow time scale, t_S. $\tilde{T^*}$ and $\tilde{T}$ are dimensionless initial temperature and current temperature and α_T is the temperature constant. If the viscosity is considered to be only shear-rate dependent α_T is set to 0.0, otherwise in case of shear-rate and temperature dependency α_T is set to 16.0. The equation of state parameters are given in table 4.1 as are the rheological properties used for the two phases. BlastFOAM's explicit solution approach for conservative variables is applied. This offers both high accuracy and computational efficiency. The third-order accurate Runge-Kutta time integration method along with the SFCD interpolation scheme and HLLC flux scheme are used. The simulations of the RMI are conducted within a rectangular domain of size 10×1, where unity is the initial wavelength of RMI that is equal to the width of the domain. The shock is initiated in the heavier fluid, on the left side of the interface, as shown in figure 4.3, and propagates towards the interface. In scenarios similar to inertial confinement fusion (ICF), the shock travels from the heavier to the lighter fluid [63, 17]. Given this, the simulations are designed to emulate conditions relevant to ICF, thereby closely reflecting the RMI phenomena that are the aim of the study. The top and bottom boundaries are set to be symmetric to the shock axis. A zero-gradient boundary condition is used for density, volume fraction, and pressure at both the left and right

boundaries. Moreover, a zero-gradient boundary condition is employed for velocity at the left boundary, while zero velocity is imposed at the right boundary to simulate a reflected shock. The interface at the start of the simulations is modeled as a cosine function $f(y) = \alpha \cos\left(\frac{2\pi y}{\lambda}\right)$, where y is the vertical coordinate, as shown in figure 4.3. Furthermore, to mitigate the influence of small-scale perturbations originating from the volume-of-fluid method and the mesh, a diffusion-type layer is introduced [12]. This layer has an initial thickness-to-wavelength ratio of less than 5% and diminishes after the shock impinges on the interface.

In this study, non-Newtonian effects on the RMI are investigated for Mach and Atwood numbers in the ranges $Ma = [2.5, 10]$ and $At = -[0.048, 0.66]$, respectively. The negative At values reflect the flow situations, which are associated with shock propagation from the heavier to the lighter phase, typical of ICF applications. The results of these simulations will be compared with those generated for cases wherein both fluids are either inviscid or Newtonian to highlight the role played by the shear-thinning and shear-thinning/temperature-dependent viscosity behavior in the development of instabilities. In the first study, the viscosity of the non-Newtonian heavier fluid is only varied with the shear rate. The temperature dependency of viscosity is neglected, i.e. α_T is set to 0.0 in equation 4.19. The figure 4.4 shows RMI at different stages for a situation wherein a shock propagates from the heavier to the lighter fluid (see figure 4.4 (a)) characterised by $At = -0.66$ and $Ma = 5$. The shock impacts the interface, as depicted in figure 4.4 (b) which leads to the development of counter-clockwise vorticity and, in turn, the protrusion of the heavier phase into the lighter one (see figure 4.4(c)). The mechanisms for vorticity generation, and the role of non-Newtonian effects, will be discussed later in this chapter.

Following the propagation of the shock past the interface, the protrusion becomes elongated and the development of roll-up driven by a Kelvin-Helmholtz instability is clearly evident giving rise to a mushroom-like structure at the protrusion leading edge, as shown in figure 4.4(d). The shock is reflected by the right boundary and propagates towards the interface from the lighter fluid side of the domain (see figure 4.4(d)). As shown in figure 4.4 (e), upon impact, the reflected shock is repelled by the interface due to the higher density of the heavier fluid which induces the formation of shock waves that travel towards the upper, lower, and right boundaries. These waves are then reflected from these boundaries and interact once again with the interface only to be reflected back, and the process is then repeated. As shown in figure 4.4(f), the mushroom-like structure becomes larger, with a flattened leading edge; highly pronounced KHI-driven roll-up phenomena are also clearly evident in this figure 4.4.

Table 4.1: Dimensionless stiffened gas equation of state parameters which appear in equation (4.16). The initial densities are scaled on $\rho_{h,0}$. Rheological parameters for the light and heavy phases which appear in equations (4.18).

Phase	γ_i	$\tilde{a}_i$	μ_0	μ_∞	$\tilde{\tau}$	n	α_T
Light	4.0	0.74	6.2×10^{-9}	0.0	0.0	1.0	0.0
Heavy	4.0	0.75	1.0	2.5×10^{-3}	8505	0.55	16.0/0.0

4.2.1 Shear-Thinning Effects

As aforementioned, in the first study, the viscosity of the non-Newtonian heavier fluid is only varied with the shear rate, i.e., the temperature effects on the viscosity are neglected. In figure 4.5(a), the temporal variation of the perturbation amplitude for three situations is plotted: one in which both phases are inviscid; the second in which both phases are Newtonian; and the third which involves a Newtonian light fluid and a heavier non-Newtonian fluid, the properties of which are given in table 4.1; the rest of the parameters remain unchanged from those used to generate figure 4.4. In the Newtonian-Newtonian case, the impact time between the shock and the interface is denoted by T_1 and is followed in the other cases by the protrusion of the heavier phase into the lighter one at T_2. The results presented in figure 4.5(a) are compared to predictions obtained from the Richtmyer model [13] given by

$$\frac{d\tilde{h}}{d\tilde{t}} = At\,\tilde{h_0}\,\tilde{k}\,\Delta\tilde{u}, \tag{4.20}$$

where $\tilde{h_0}$ is the initial amplitude of the perturbation, $\tilde{k}$ is its wavenumber, and $\Delta\tilde{u}$ is the velocity jump in the direction of travel of the shock following its propagation through the interface at which stage this model assumes that the flow becomes incompressible. This assumption is not valid for high Ma at which strong shocks are formed; for this range of Ma, the transmitted shock recedes slowly and represents an effectively impenetrable boundary, which reduces the growth of the RMI. The Nova laser experiments [64, 65, 66] showed a lower growth rate at large Ma as compared to the predictions by the Richtmyer incompressible model [13]; the latter is only valid for the early, linear stage of the RMI, prior to the development of secondary KHI whose vortices decelerate the RMI growth. It is therefore unsurprising that the agreement with the Richtmyer model [13] deteriorates after early times, giving way to significantly larger growth rate estimates than those generated numerically for both the inviscid and viscous cases. The numerical predictions for the perturbation amplitude are also compared with those obtained from the work of Dimonte and Schneider [16] who introduced a late-stage model that accounts for the drag effects on the growth of RMI. The evolution of the amplitude $\tilde{h}$ of the single-mode RMI is

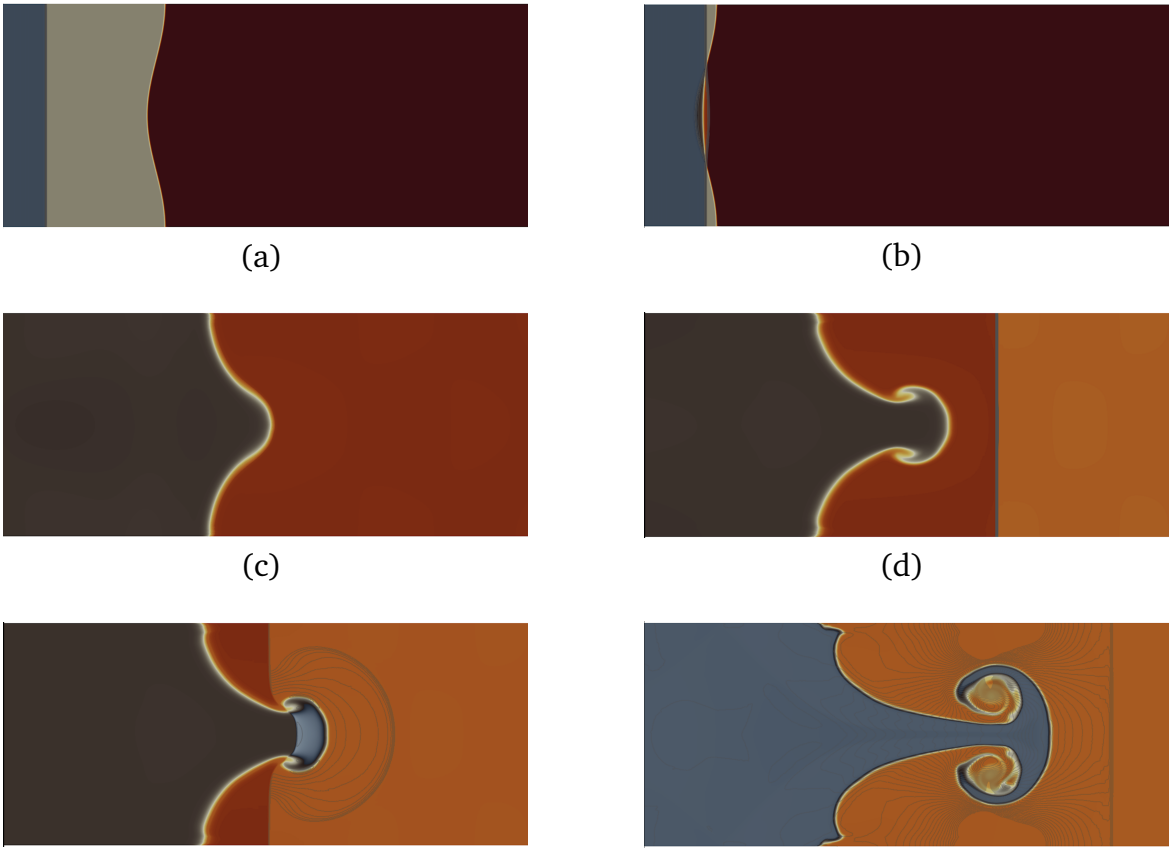


Figure 4.4: Projections of the density field in the $x-y$ plane depicting the development of a RMI in inviscid case, and a subsequent KHI, driven by the left-to-right propagation of a shock wave from the heavier towards the lighter phase for $t = 0$, 0.06, 0.67,1.35,1.43,1.89 shown in (a)-(f), respectively. The parameter values are $At = -0.66$, $Ma = 5$, and $Fr = 48571$; the remaining parameters are in table 4.1.

described in this model by the following equation:

$$\frac{d^2\tilde{h}}{d\tilde{t}^2} = -c_d \left(\frac{d\tilde{h}}{d\tilde{t}}\right) \left|\frac{d\tilde{h}}{d\tilde{t}}\right| \frac{1}{\tilde{h}}. \tag{4.21}$$

In Eq. (4.21), $c_d = \frac{24}{Re}$ represents a drag coefficient for simple laminar flow around a sphere. A comparison of the Dimonte and Schneider model [16] predictions and those from the inviscid and viscous numerical models demonstrates an improvement over those obtained from the work of Richtmyer [13]. The $x-y$ projections of the interphase superimposed on vorticity contour plots in figure 4.5(b)-(e) for $t = 0.075, 0.18, 1.41, 1.48$, respectively, for the inviscid and viscous cases; the variation of the z-component of the vorticity, w_z, along the arc length is also shown for the same times. It is seen clearly that vorticity is generated in the regions immediately adjacent to the interface, and this is closely correlated to the interfacial deformation associated with the RMI and the KHI-related roll-up phenomena; the development of the latter, whose onset is at T_3, leads to a deceleration of the perturbation amplitude.

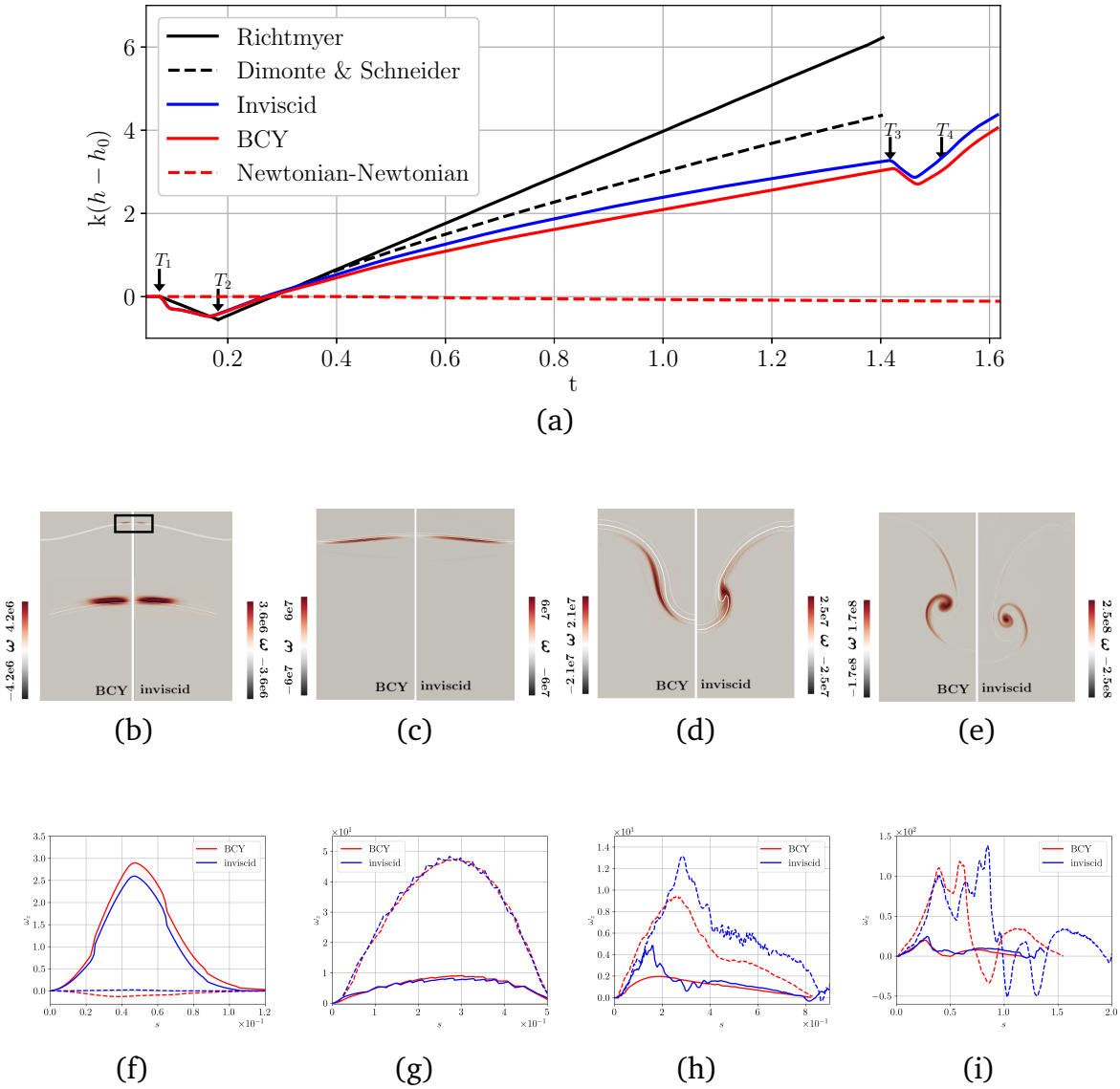


Figure 4.5: Temporal variation of the perturbation amplitude for $At = -0.66$ and $Ma = 5$, (a), where the black solid and dashed curves represent the predictions of the Richtmyer [13] and Dimonte and Schneider [16] models, the blue curves represent the inviscid case, while the red dashed and solid lines represent the numerical predictions obtained for the Newtonian-Newtonian and BCY cases, respectively; in the latter case, the light and heavy fluids correspond to Newtonian and BCY fluids, respectively; here, $T_1 - T_4$ correspond to $t = 0.075$, 0.18,1.41, and 1.48, respectively. Snapshots of the $x-y$ projections of the density field at $t = T_1 - T_4$ depicting the interface shape superimposed on vorticity contours shown in (b)-(e), respectively; in each panel the predictions associated with the BCY and inviscid cases are shown on the left and right, respectively. Variation of the z-component of the vorticity with arc length for the inviscid and viscous cases represented by blue and red lines for $t = T_1 - T_4$ shown in (f)-(i), respectively, plotted on the heavy- (with $\alpha = 0.9$) and light-side (with $\alpha = 0.1$) of the interface using solid and dashed lines, respectively. The rest of the parameters remain unchanged from the previous figure.

Furthermore, the dominant contribution is due to the heavier phase during the earliest stages of the flow; following the crossing of the shock into the lighter phase, the latter becomes the dominant contributor to vorticity generation. The divergence in the evolving dynamics between the inviscid and viscous cases becomes more accentuated with increasing time as can be confirmed upon inspection of figures 4.5(d), (e), (h) and (i); it is also seen that the vortical structures are more pronounced for the inviscid case for which the interface becomes more stretched as revealed by the expanded arc length range associated with this case (see figure 4.5(i)). Lastly, the impact of the reflected shock on the interface at $t = T_4$ leads to further development of the RMI and KHI and acceleration of perturbation growth. In figure 4.6, the analogous variables to those shown in figure 4.5 except $Ma = 10$ are plotted, and the rest of the parameters remain unchanged. A comparison of the results presented in these figures reveals similar trends in terms of perturbation amplitude growth and the close association between the vorticity in the vicinity of the interface and the development of the RMI and KHI roll-up phenomena. An exception is provided by the Newtonian-Newtonian case where the strong influence of viscosity prevents any increase in perturbation amplitude, as can be seen from figures 4.5(a) and 4.6(a).

At the higher Ma, it is seen clearly that not only are these phenomena significantly more pronounced, the difference in vorticity generated between the inviscid and BCY cases is lower than that associated with the $Ma = 5$ case. This is due to the higher shear rates at $Ma = 10$ and therefore lower viscosity in the heavy phase in comparison to that at $Ma = 5$. In contrast, the Newtonian-Newtonian cases exhibit comparatively very little perturbation growth even at the elevated Ma. Following the passage of the incident shock, viscous damping associated with the residual viscosity becomes dominant and acts to suppress the RMI and KHI roll-up. This is more effective for the lower Ma studied due to the comparatively smaller shear rates and therefore larger residual viscosity.. There is also evidence for perturbation amplitude deceleration due to the development of KHI roll-up in the $Ma = 10$ case, as can be seen in figure 4.6(a). Furthermore, the impact of the first reflected shock at $t = T_3$ on the KHI and RMI growth rate is similar in both the viscous and inviscid cases, as shown in figure 4.6(d). The impact of the second reflected shock at $t = T_4$ leads to the development of small-scale roll-up structures.

These small-scale structures lead to additional vorticity generation, the so-called vortex-accelerated secondary baroclinic vorticity, which has been investigated in detail by Peng et al. [12]. This mechanism involves the interaction of vortices generated by RMI and KHI, causing a further enhancement of baroclinic vorticity deposition, which contributes to an increase in the growth rate of RMI and a more developed KHI. In this study, the effects of vortex-accelerated secondary baroclinic vorticity on the RMI and KHI are visible: the RMI growth rate is higher, and KHI is further developed in the inviscid case. In the BCY case, however, the span of the RMI, which is a low shear rate region, is characterised by a relatively high viscosity, which leads to a lower growth rate of the RMI after the second reflected shock. As

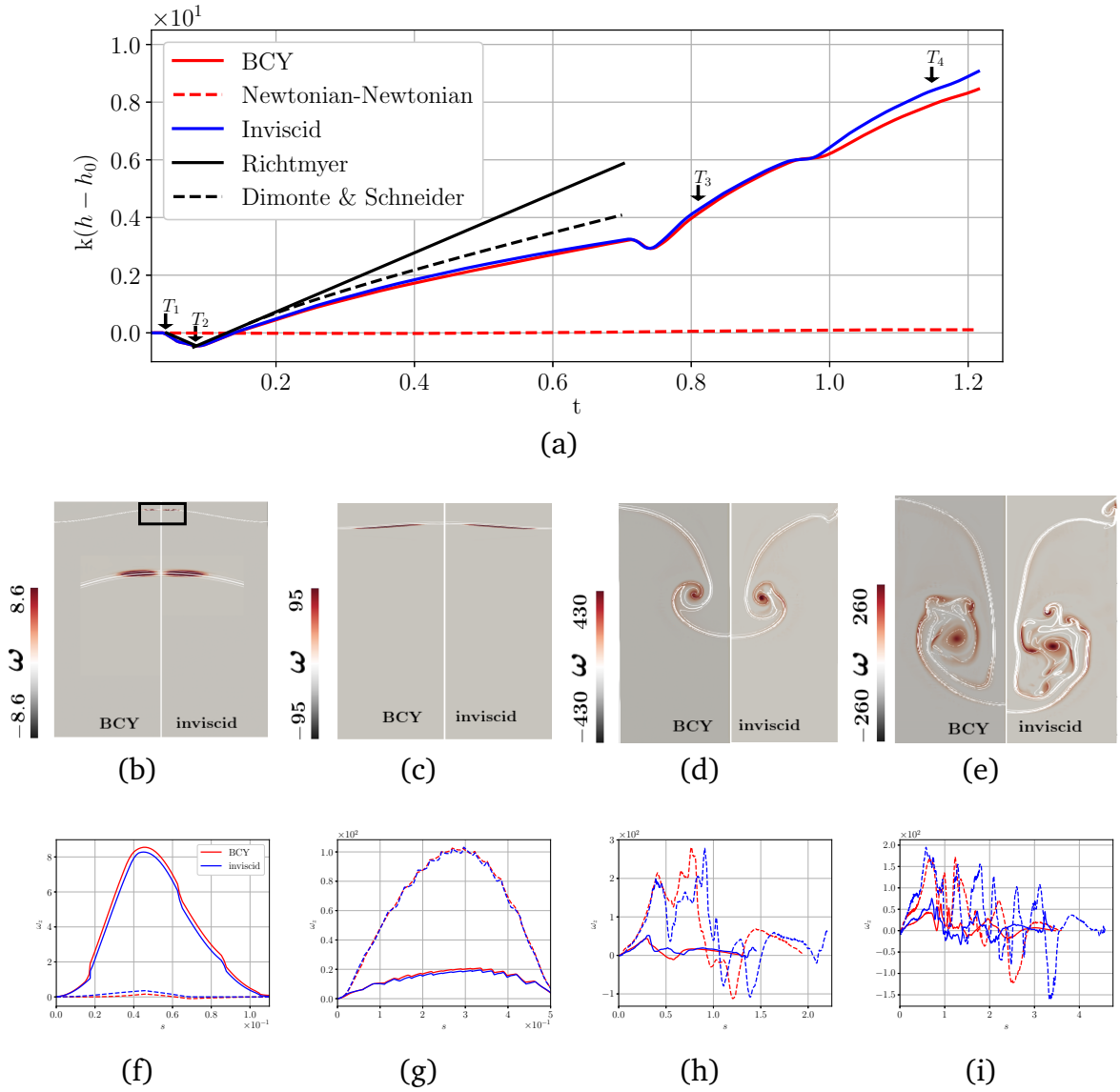


Figure 4.6: Temporal variation of the perturbation amplitude for $At = -0.66$ and $Ma = 10$, (a), where the black solid and dashed lines represent the predictions of the [13] and Dimonte and Schneider [16] models, the blue curves represent the inviscid case, while the red dashed and solid lines represent the numerical predictions obtained for the Newtonian-Newtonian and BCY cases, respectively; in the latter case, the light and heavy fluids correspond to Newtonian and BCY fluids, respectively; here, $T_1 - T_4$ correspond to $t = 0.037$, 0.085, 0.815, and 1.175, respectively. Snapshots of the $x - y$ projections of the density field at $t = T_1 - T_4$ depicting the interface shape superimposed on vorticity contours shown in (b)-(e), respectively; in each panel the predictions associated with the BCY and inviscid cases are shown on the left and right, respectively. Variation of the z-component of the vorticity with arc length for the inviscid and viscous cases represented by blue and red lines for $t = T_1 - T_4$ shown in (f)-(i), respectively, plotted on the heavy- (with $\alpha = 0.9$) and light-side (with $\alpha = 0.1$) of the interface using solid and dashed lines, respectively. The rest of the parameters remain unchanged from the previous figure.

a next step this study explores the effects of system parameters on the features of the mushroom-like structure discussed above, and show in figure 4.7 an annotated schematic of a fully-developed such structure; this figure highlights the dimensions of the various features: the 'span', 'stream', and 'neck'. In figure 4.7 the influence of the non-Newtonian effects on these features is demonstrated. As shown in figure 4.7(a), there is very little difference in stream development between the inviscid and BCY cases after the first reflected shock for $Ma = 10$. The second reflected shock leads to the development of small-scale structures, and the occurrence of these structures induces vortex-accelerated vorticity. This additional vorticity in the inviscid case results in a higher stream compared to the BCY case, where the higher viscosity due to the comparatively lower shear rates damps the small-scale structures, leading to a lower stream. For $Ma = 5$, the stream does not develop until the first reflected shock for the BCY case, in contrast to the inviscid case. The second reflected shock leads to the development of small-scale structures and vortex-accelerated vorticity, resulting in elevation of the BCY stream, which remains below that of the inviscid case due to larger viscous damping in the BCY case. Similar behavior is observed in the development of the span and neck for both $Ma = 5$ and $Ma = 10$, as shown in figures 4.7(b) and (c), respectively.

A parametric study is carried out to investigate the effects of At and Ma on the development of RMI and associated phenomena. In figures 4.8 and 4.9, show the fully-developed $x - y$ projections of the density field for the inviscid and BCY cases, respectively, generated for $At = (-0.048, -0.230, -0.66)$ and $Ma = (5, 7.5, 10)$. Inspection of the results presented in figure 4.8 demonstrates that an increase in Ma and/or At is destabilising. At $Ma = 5$ and low At, characterised by $At = (-0.048, -0.23)$, the generation of vorticity is insufficient for the formation of the characteristic mushroom-like structure associated with the RMI. Furthermore, at $At = -0.048$, i.e., when the fluid densities are similar in magnitude, and $Ma = (5, 7.5, 10)$, minimal vorticity generation and a relatively flat interface are observed with no RMI development. figure 4.9 highlights the combined effects of At, Ma, and the non-Newtonian rheology in the heavy phase on RMI development. Inspection of this figure reveals that viscous damping decelerates the development of the RMI compared to the inviscid case shown in figure 4.8 for all At and Ma investigated. Notably, however, the flow features exhibited by both cases are qualitatively similar due to the shear-induced viscosity reduction in the BCY fluid. This is in marked contrast to the Newtonian-Newtonian case (not shown) which is significantly more stable and is accompanied by virtually no perturbation growth.

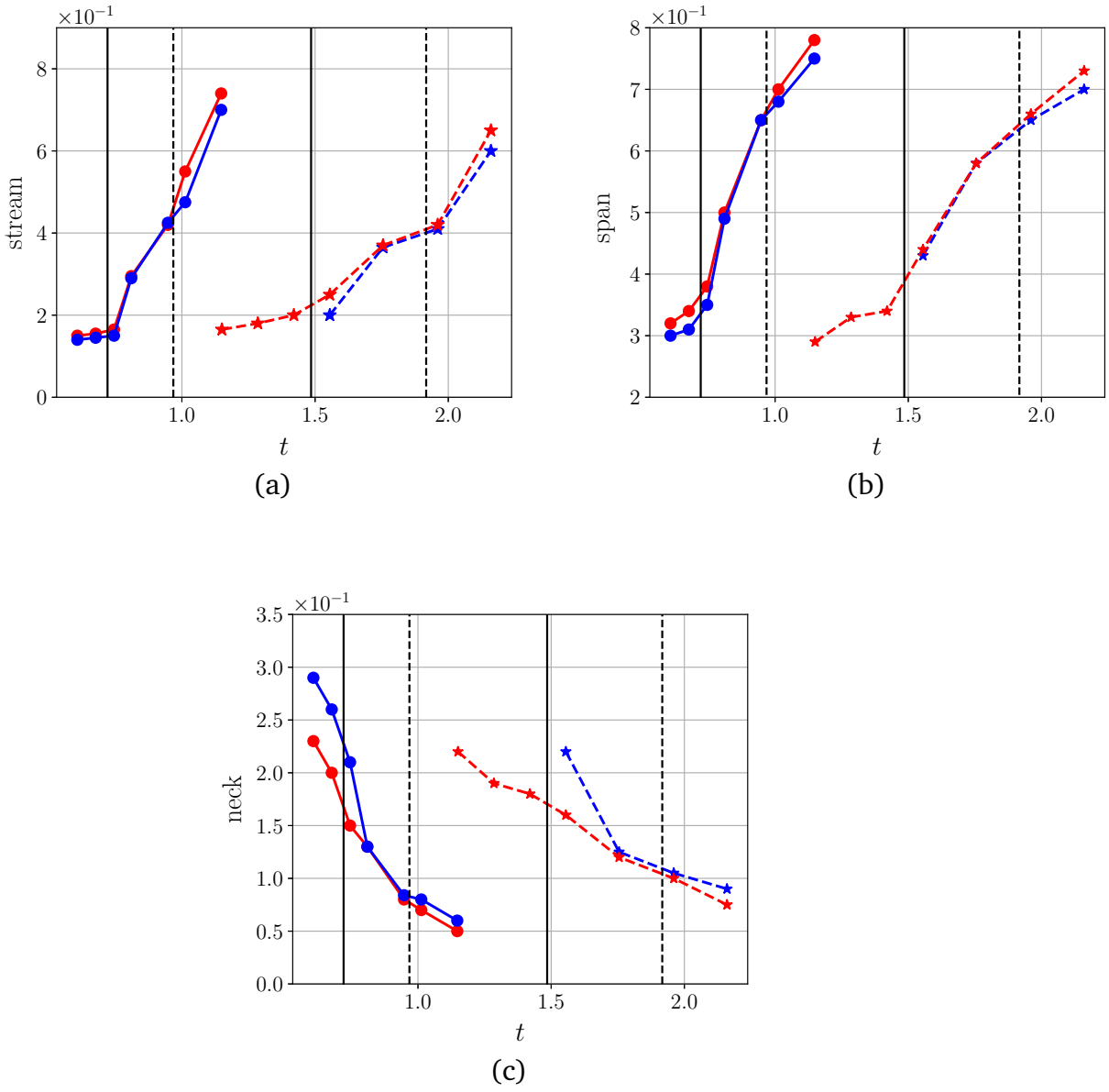


Figure 4.7: Temporal evolution of the length of the stream, span, and neck (see figure 4.7 for the definitions of these features) $At = -0.66$ shown in (a)-(c), respectively. In each panel, the red and blue solid lines designate the inviscid and BCY cases for $Ma = 10$, and their dashed counterparts the $Ma = 5$ case, respectively. The solid and dashed vertical lines at $t = 0.71$ and $t = 0.95$, and $t = 1.41$ and $t = 1.89$ highlight the times at which the interface is impacted by the first and second reflected shocks for $Ma = 10$ and $Ma = 5$, respectively. The rest of the parameters are unchanged from previous figures.

The Dynamics of Vorticity Generation and Damping

In the previous sections, the role of vorticity in the dynamics associated with the RMI and KHI roll-up was highlighted. In particular, it was shown that vorticity generation is enhanced with increasing At and Ma. In this section, the mechanisms are identified that lead to vorticity generation and damping, paying particular attention to the role of non-Newtonian rheology. In the vicinity of an interface between two immiscible fluids of different densities, it is well known that the presence of a pressure gradient due to hydrostatic pressure or a shock leads to vorticity generation in Rayleigh-Taylor and RMIs, respectively. However, when considering generalised Newtonian fluids, not only should the viscous dissipation be taken into account in the vorticity balance, but also the viscosity gradients.

The vorticity equation for compressible non-Newtonian fluid is derived as follows. Starting from the momentum equation, which may be expressed by

$$\frac{\partial \mathbf{u}}{\partial t} + (\mathbf{u}\cdot\nabla)\,\mathbf{u} = -\frac{1}{\rho}\nabla p + \frac{1}{\rho}\nabla\cdot\left(\mu\left[\nabla\mathbf{u} + (\nabla\mathbf{u})^T - \frac{2}{3}(\nabla\cdot\mathbf{u})\,\mathbf{I}\right]\right), \tag{4.22}$$

The viscous term can be rewritten as follows:

$$\begin{aligned}\nabla\cdot\left(\mu\left[\nabla\mathbf{u} + (\nabla\mathbf{u})^T - \frac{2}{3}(\nabla\cdot\mathbf{u})\,\mathbf{I}\right]\right) &= \mu\nabla\cdot\left(\left[\nabla\mathbf{u} + (\nabla\mathbf{u})^T\right]\right)\\ -\frac{2}{3}\mu\nabla\cdot([(\nabla\cdot\mathbf{u})\,\mathbf{I}]) + \nabla\mu\cdot&\left(\left[\nabla\mathbf{u} + (\nabla\mathbf{u})^T - \frac{2}{3}(\nabla\cdot\mathbf{u})\,\mathbf{I}\right]\right).\end{aligned} \tag{4.23}$$

The following identities are used

$$\nabla\cdot(\nabla\mathbf{u}) = \nabla(\nabla\cdot\mathbf{u}) - \nabla\times(\nabla\times\mathbf{u}), \tag{4.24}$$

$$\nabla\cdot(\nabla\mathbf{u})^T = \nabla(\nabla\cdot\mathbf{u}), \tag{4.25}$$

$$\nabla\cdot((\nabla\cdot\mathbf{u})\,\mathbf{I}) = \nabla(\nabla\cdot\mathbf{u}), \tag{4.26}$$

to write the first two terms on the right-hand-side of Eq. 4.22 as

$$\mu\nabla\cdot\left(\left[\nabla\mathbf{u} + (\nabla\mathbf{u})^T - \frac{2}{3}(\nabla\cdot\mathbf{u})\,\mathbf{I}\right]\right) = \mu\left(\frac{4}{3}\nabla(\nabla\cdot\mathbf{u}) - \nabla\times\boldsymbol{\omega}\right), \tag{4.27}$$

where $\boldsymbol{\omega} = \nabla\times\mathbf{u}$ is the vorticity. In addition, the following relation can be written.

$$\nabla\mu\cdot\nabla\mathbf{u}^T = \nabla\mu\cdot\nabla\mathbf{u} + \nabla\mu\times(\nabla\times\mathbf{u}), \tag{4.28}$$

so that the third term on the right-hand-side of equation 4.22 can be written as follows:

$$\nabla\mu \cdot \left(\left[\nabla\mathbf{u} + (\nabla\mathbf{u})^T - \frac{2}{3}(\nabla \cdot \mathbf{u})\mathbf{I} \right] \right) = 2\nabla\mu \cdot \nabla\mathbf{u} + \nabla\mu \times \boldsymbol{\omega} - \frac{2}{3}(\nabla \cdot \mathbf{u})\nabla\mu. \tag{4.29}$$

Taking the curl of the resultant equation, leads to the following equation for the vorticity:

$$\begin{aligned} \frac{D\boldsymbol{\omega}}{Dt} = {} & \boldsymbol{\omega} \cdot \nabla\mathbf{u} - \boldsymbol{\omega}(\nabla \cdot \mathbf{u}) - \frac{1}{\rho^2}(\nabla\rho \times \nabla p) \\ & + \nabla \times \left[\frac{\mu}{\rho} \left(\frac{4}{3}\nabla(\nabla \cdot \mathbf{u}) - \nabla \times \boldsymbol{\omega} \right) \right] \\ & + \nabla \times \left[\frac{1}{\rho} \left(2\nabla\mu \cdot \nabla\mathbf{u} + \nabla\mu \times \boldsymbol{\omega} - \frac{2}{3}(\nabla \cdot \mathbf{u})\nabla\mu \right) \right]. \end{aligned} \tag{4.30}$$

For two-dimensional (2D) flows, $\boldsymbol{\omega} \cdot \nabla\mathbf{u} = 0$, and the vorticity equation can be expressed as follows:

$$\begin{aligned} \frac{D\boldsymbol{\omega}}{Dt} = {} & -\boldsymbol{\omega}(\nabla \cdot \mathbf{u}) - \frac{1}{\rho^2}(\nabla\rho \times \nabla p) + \frac{\mu}{\rho}\nabla^2\boldsymbol{\omega} \\ & + \frac{1}{\rho}\nabla\mu \times \left[\left(\frac{4}{3}\nabla(\nabla \cdot \mathbf{u}) - \nabla \times \boldsymbol{\omega} \right) \right] \\ & - \frac{\mu}{\rho^2}\nabla\rho \times \left[\left(\frac{4}{3}\nabla(\nabla \cdot \mathbf{u}) - \nabla \times \boldsymbol{\omega} \right) \right] \\ & + \frac{1}{\rho}\nabla \times \left[\left(2\nabla\mu \cdot \nabla\mathbf{u} + \nabla\mu \times \boldsymbol{\omega} - \frac{2}{3}(\nabla \cdot \mathbf{u})\nabla\mu \right) \right] \\ & - \frac{1}{\rho^2}\nabla\rho \times \left[\left(2\nabla\mu \cdot \nabla\mathbf{u} + \nabla\mu \times \boldsymbol{\omega} - \frac{2}{3}(\nabla \cdot \mathbf{u})\nabla\mu \right) \right]. \end{aligned} \tag{4.31}$$

Using $\nabla \times [(\nabla \cdot \mathbf{u})\nabla\mu] = \nabla\mu \times \nabla(\nabla \cdot \mathbf{u})$ and $\boldsymbol{\omega} \cdot \nabla = 0$ (valid in 2D), this equation can be slightly rearranged as follows:

$$\begin{aligned} \frac{D\boldsymbol{\omega}}{Dt} = {} & -\boldsymbol{\omega}(\nabla \cdot \mathbf{u}) + \frac{\mu}{\rho}\nabla^2\boldsymbol{\omega} + \frac{1}{\rho^2}\boldsymbol{\omega}\nabla\rho \cdot \nabla\mu \\ & + \frac{1}{\rho^2}\nabla\rho \times \left[\nabla p - \mu\frac{4}{3}\nabla(\nabla \cdot \mathbf{u}) + \mu\nabla \times \boldsymbol{\omega} \right] \end{aligned}$$

$$
\begin{aligned}
&- \frac{1}{\rho^2}\nabla\rho \times \left[2\nabla\mu \cdot \nabla\mathbf{u} + \frac{2}{3}\left(\nabla \cdot \mathbf{u}\right)\nabla\mu\right] \\
&+ \frac{1}{\rho}\nabla\mu \times \left[\frac{2}{3}\nabla\left(\nabla \cdot \mathbf{u}\right) - \nabla \times \boldsymbol{\omega}\right] \\
&+ \frac{1}{\rho}\nabla \times \left[2\nabla\mu \cdot \nabla\mathbf{u} + \nabla\mu \times \boldsymbol{\omega}\right].
\end{aligned} \tag{4.32}
$$

Finally, using the scalings as described in simulation setup in this chapter, the dimensionless form of the 2D vorticity equation is expressed by:

$$
\begin{aligned}
\frac{D\boldsymbol{\omega}}{Dt} = \boldsymbol{\omega}&\frac{Ma^2}{\rho}\frac{Dp}{Dt} + \frac{1}{Re}\nabla^2\boldsymbol{\omega} + \frac{1}{Re}\frac{1}{\rho^2}\boldsymbol{\omega}\nabla\rho \cdot \nabla\mu \\
&+ \frac{1}{\rho^2}\nabla\rho \times \left[\nabla p + \frac{4\,Ma^2}{3\,Re}\mu\nabla\left(\frac{1}{\rho}\frac{Dp}{Dt}\right) + \frac{1}{Re}\mu\nabla \times \boldsymbol{\omega}\right] \\
&- \frac{1}{\rho^2}\nabla\rho \times \left[\frac{2}{Re}\nabla\mu \cdot \nabla\mathbf{u} + \frac{2\,Ma^2}{3\,\rho\,Re}\frac{Dp}{Dt}\nabla\mu\right] \\
&- \frac{1}{Re}\frac{1}{\rho}\nabla\mu \times \left[\frac{2\,Ma^2}{3}\nabla\left(\frac{1}{\rho}\frac{Dp}{Dt}\right) + \nabla \times \boldsymbol{\omega}\right] \\
&+ \frac{1}{Re}\frac{1}{\rho}\nabla \times \left[2\nabla\mu \cdot \nabla\mathbf{u} + \nabla\mu \times \boldsymbol{\omega}\right].
\end{aligned} \tag{4.33}
$$

Note that in the simultaneous limits $Ma \to 0$ and $Re \to \infty$, this equation reduces to

$$
\frac{D\boldsymbol{\omega}}{Dt} = \frac{1}{\rho^2}\nabla\rho \times \nabla p, \tag{4.34}
$$

which implies that the baroclinic term on the right-hand-side of this equation is responsible for vorticity generation resulting from misalignments of density and pressure at the interface. The figure 4.10 illustrates how the major gradients such as $\nabla\rho$, $\nabla\mu$, and ∇p are oriented after the passage of the shock and the creation of the protrusion of the heavier phase into the lighter one. This protrusion leads to large gradients in pressure, density, and viscosity across the interface, transitioning from high values in the heavier fluid to lower ones in the lighter fluid. The misalignment of ∇p and $\nabla\rho$ leads to a destabilising baroclinic mechanism, which is present in the inviscid case, that drives a RMI. For finite Re, other effects compete with this mechanism. The presence of non-Newtonian rheology in one of the phases gives rise to additional mechanisms related to $\nabla\mu$.

Table 4.2: A breakdown of the rate of change of vorticity into the terms that appear on the right-hand-side of equation 4.33. The terms are characterised as 'Stabilising' or 'Destabilising' depending on their time-averaged contribution to this equation, and are ranked according to the magnitude of their respective contributions, e.g, 'S1' and 'D1' correspond to the terms with the largest stabilising and destabilising contributions, respectively.

Term 1	$\omega \frac{Ma^2}{\rho} \frac{Dp}{Dt}$	Stabilising (S5)
Term 2	$\frac{1}{Re} \nabla^2 \omega$	Stabilising (S3)
Term 3	$\frac{1}{Re} \frac{1}{\rho^2} \omega \nabla \rho \cdot \nabla \mu$	Destabilising (D3)
Term 4	$\frac{1}{\rho^2} \nabla \rho \times \nabla p$	Destabilising (D2)
Term 5	$\frac{1}{\rho^2} \nabla \rho \times \frac{4\,Ma^2}{3\,Re} \mu \nabla \left(\frac{1}{\rho} \frac{Dp}{Dt} \right)$	Destabilising (D5)
Term 6	$\frac{1}{\rho^2} \nabla \rho \times \frac{1}{Re} \mu \nabla \times \omega$	Destabilising (D4)
Term 7	$-\frac{1}{\rho^2} \nabla \rho \times \frac{2}{Re} \nabla \mu \cdot \nabla \mathbf{u}$	Stabilising (S2)
Term 8	$-\frac{1}{\rho^2} \nabla \rho \times \frac{2\,Ma^2}{3\,\rho\,Re} \frac{Dp}{Dt} \nabla \mu$	Destabilising (D6)
Term 9	$-\frac{1}{Re} \frac{1}{\rho} \nabla \mu \times \frac{2\,Ma^2}{3} \nabla \left(\frac{1}{\rho} \frac{Dp}{Dt} \right)$	Stabilising (S6)
Term 10	$\frac{1}{Re} \frac{1}{\rho} \nabla \times 2 \nabla \mu \cdot \nabla \mathbf{u}$	Stabilising (S4)
Term 11	$-\frac{1}{Re} \frac{1}{\rho} \nabla \mu \times \nabla \times \omega$	Destabilising (D1)
Term 12	$\frac{1}{Re} \frac{1}{\rho} \nabla \times 2 \nabla \mu \cdot \nabla \mathbf{u}$	Stabilising (S1)

Various terms are listed, Terms 1-12 that appear in equation 4.33 in table 4.2, the terms are integrated over half the wavelength for volume fractions $\alpha = 0.1$ and $\alpha = 0.9$ yielding integrals $I_1 - I_{12}$, respectively, and the temporal evolution of these integrals is plotted in figures 4.11, 4.12, and 4.13. These figures provide an indication of the instantaneous contributions of $I_1 - I_{12}$, and their associated Terms and mechanisms, to the stability of the flow following impact by the primary shock and reflected shocks during the the early and latter stages of the flow, as shown in panels (a) and (b) of figures 4.11-4.13, respectively. The time-averages of $I_1 - I_{12}$ are obtained, which highlight the overall contributions of Terms 1-12 to the system stability over the duration of the flow investigated, and this is also indicated in table 4.2. This study now examines the contribution of each term. Inspection of figure 4.11 (a) reveals that the primary shock impact leads to a rapid rise in I_3, I_4, and I_{11} which exhibit positive values highlighting the destabilising contributions of Terms 3, 4, and 11; in contrast, I_8 is comparatively smaller in magnitude though it is also destabilising albeit marginally. It is also seen that I_4 associated with the inviscid case

is virtually indistinguishable from that of the BCY case. The largest instantaneous contributor to instability is Term 4, which is related to the baroclinic mechanism discussed above, and this is followed by Term 11, represented by $-\frac{1}{Re}\frac{1}{\rho}\nabla\mu\times\nabla\times\omega$, a distinct source of vorticity generation specifically driven by the gradient in viscosity. This, in turn, is followed by the contribution from Term 3, which is represented by $\frac{1}{Re}\frac{1}{\rho^2}\boldsymbol{\omega}\nabla\rho\cdot\nabla\mu$, and emerges when the vorticity interacts with regions of sharp density and viscosity variations. Lastly, Term 8, represented by $-\frac{1}{\rho^2}\nabla\rho\times\frac{2Ma^2}{3\rho Re}\frac{Dp}{Dt}\nabla\mu$, is marginally destabilising and signifies the interactions between the density and viscosity gradients, the temporal variation in pressure, and the Mach number, which provides a measure of the flow compressibility. The ordering of the terms remains unchanged following the impact of the reflected shock, though, as shown in figure 4.11(b), the magnitudes of I_3, I_4, I_8, and I_8 are smaller than their early-times counterparts. It is observed that whereas the contribution of the baroclinic term is short-lived, as can be discerned from figure 4.11(a), that of Term 11 is relatively longer-lasting, and the time-averages of I_3, I_4, I_8, and I_{11} indicate that the largest contributor to instability is associated with Term 11 (see table 4.2), which exceeds Term 4 and further highlights the role of viscosity gradients, related to the non-Newtonian rheology of the heavier fluid, in driving instability. Lastly, in the insets in Fig. 4.11 show $x-y$ projections of the density field associated with the inviscid and BCY cases following the impact of the reflected shock; inspection of these figures reveals that the interface is unstable due to the shock impact in the BCY case, albeit not to the extent of instability observed in the absence of viscous effects. In a similar vain to figure 4.11, the figure 4.12 show the temporal evolution of the spatial integrals of Terms 5, 6, 9, and 10, I_5, I_6, I_9, and I_{10}, respectively, over the same time duration and parameter values. It is clearly seen that Terms 5 and 6, which are represented by $\frac{1}{\rho^2}\times\frac{4Ma^2}{3Re}\mu\nabla(\frac{1}{\rho}\frac{Dp}{Dt})$ and $\frac{1}{\rho^2}\nabla\rho\times\frac{1}{Re}\mu\nabla\times\omega$, are destabilising and stabilising, respectively, following the impact of the primary shock, as shown in figure 4.12(a); the impact of the reflected shock appears to have virtually no effect on I_5, while I_6 is slightly negative suggesting that Terms 5 and 6 have a weakly stabilising influence on the late-stage dynamics. Although Term 9, represented by $-\frac{1}{Re}\frac{1}{\rho}\nabla\mu\times\frac{2Ma^2}{3}\nabla(\frac{1}{\rho}\frac{Dp}{Dt})$, makes a relatively modest, and mostly stabilising, contribution to the dynamics, Term 10, represented by $\dfrac{1}{Re}\dfrac{1}{\rho}\nabla\times2\nabla\mu\cdot\nabla\mathbf{u}$ is destabilising immediately following primary shock impact and strongly stabilising thereafter as manifested by the rise in I_{10}. This is because the shock impact gives rise to sharp velocity and viscosity gradients whose coupling through the Term 10 mechanism induces vorticity generation. The reflected shock impact also leads to an increase in I_{10}. The overall contribution to the flow, however, is destabilising due to Term 5, and stabilising due to Terms 6, 9, and 10. In the case of the latter, it appears that its stabilising long-time influence outweighs its destabilising effect during the shock impact episodes at the early- and late-stage dynamics. In figure 4.13, the contributions due to Terms 1, 2, 7, and 12 is assessed.

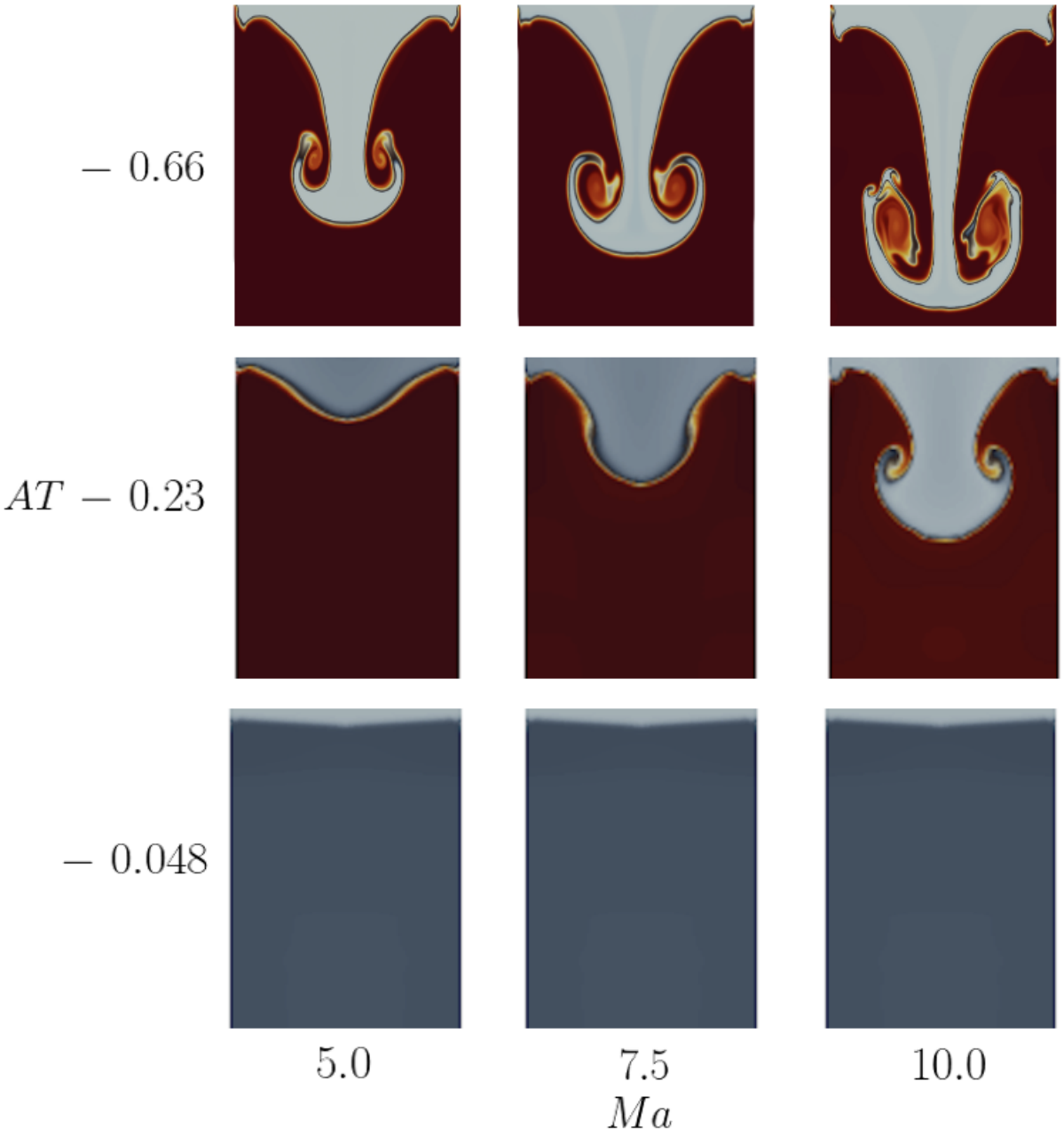


Figure 4.8: Fully-developed $x - y$ projections of the density field for the inviscid case in the (At, Ma) space for $At = (-0.048, -0.230, -0.66)$ and $Ma = (5, 7.5, 10)$; the rest of the parameters remain unchanged from previous figures.

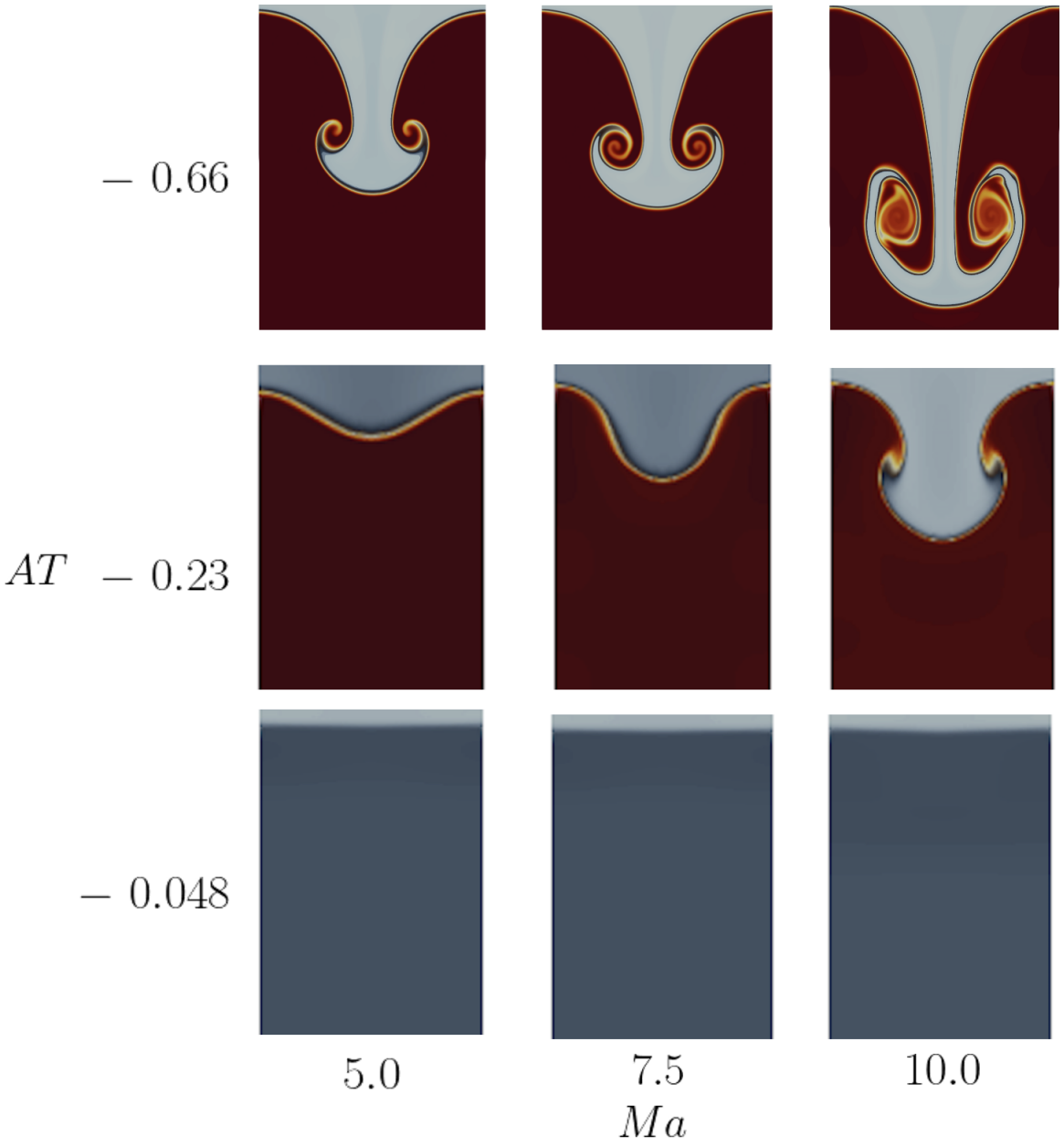


Figure 4.9: Fully-developed $x - y$ projections of the density field for the case wherein the lighter and heavier phases correspond to Newtonian and BCY fluids, respectively, in the (At, Ma) space for $At = (-0.048, -0.230, -0.66)$ and $Ma = (5, 7.5, 10)$; the rest of the parameters remain unchanged from previous figures.

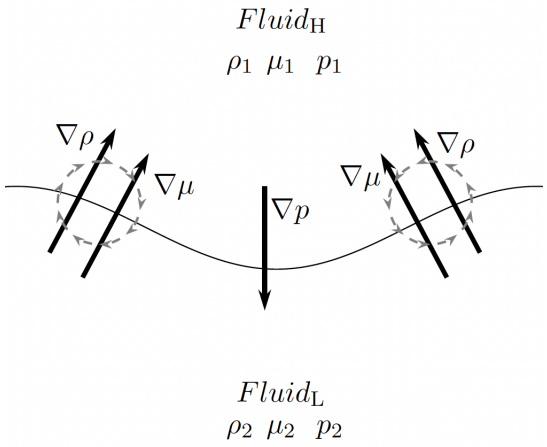


Figure 4.10: Orientation of the pressure, density, and viscosity gradients following shock impact and protrusion of the heavier phase into the lighter one.

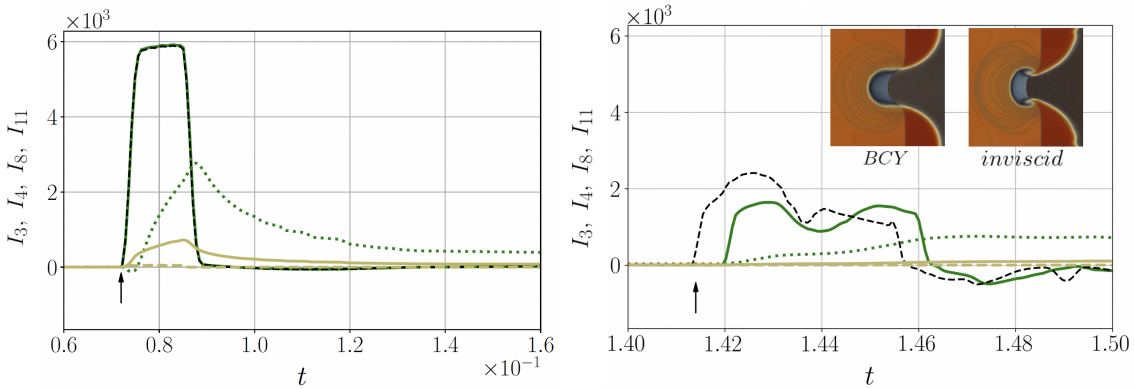


Figure 4.11: Temporal evolution of the spatial integrals of Terms 3, 4, 8, and 11, I_3, I_4, I_8, and I_{11} shown between $t = 0.06 - 0.16$ and $t = 1.4 - 1.5$ in (a) and (b), respectively, highlighting the effect of impact by the primary shock at $t \approx 0.7$ in (a), and reflected shock at $t \approx 1.415$ in (b), for $At = -0.66$ and $Ma = 5$. The green solid and dotted lines represent I_4 and I_{11}, the solid and dashed khaki lines represent I_3 and I_8 for there case wherein the heavier and lighter phases correspond to BCY and Newtonian fluids, respectively. The dashed black line represents I_4 for the case wherein both fluids are treated as inviscid. The insets in panel (b) represent $x - y$ projections of the density field for the inviscid and BCY cases following the impact of the reflected shock. All other parameters mirror those from preceding figures.

Term 1, represented by $\boldsymbol{\omega}\frac{Ma^2}{\rho}\frac{Dp}{Dt}$, is associated with stretching and tilting of vorticity in a flow field, while Term 2, $\frac{1}{Re}\nabla^2\boldsymbol{\omega}$, reflects the damping effect of viscosity on vorticity by converting the kinetic energy of the vortical motion into internal energy. When the vorticity and velocity divergences are aligned, the stretching can lead to damping. Damping is also provided by Term 7, $\frac{1}{\rho^2}\nabla\rho\times\frac{2}{Re}\nabla\mu\cdot\nabla\mathbf{u}$, and Term 12, $\frac{1}{Re}\frac{1}{\rho}\nabla\times\nabla\mu\times\boldsymbol{\omega}$, which are related to retardation of the secondary, Kelvin-Helmholtz instability that can arise in the nonlinear phase of RMI evolution. By hindering the development of these secondary instabilities, viscosity can indirectly damp the overall vorticity in the flow by damping the small-scale structures that form due to the interaction of multiple reflected shocks with the interface in the nonlinear stages of the flow. Confirmation of the damping, vorticity-attenuating effect of Terms 1, 2, 7, and 12 is provided by the temporal evolution of the spatial integrals of these terms, which are shown in figure 4.13 as well as their respective time-averages.

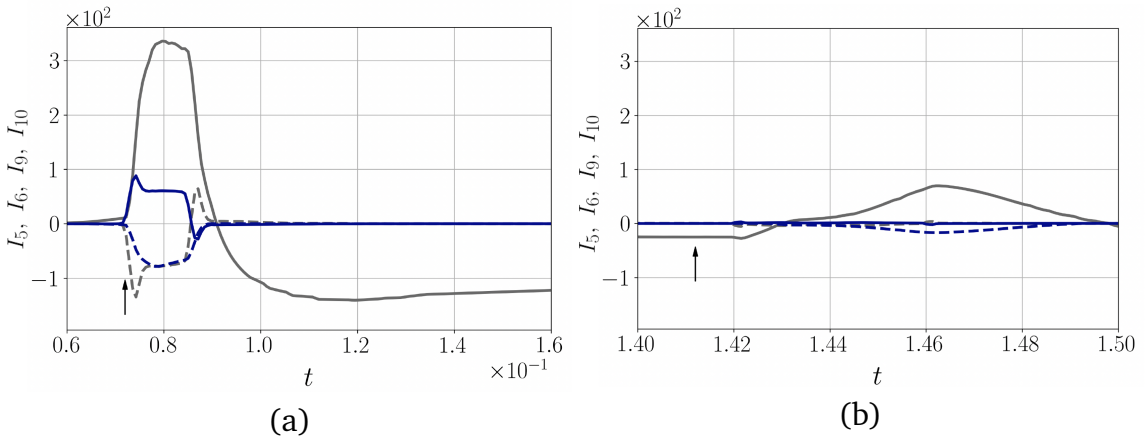
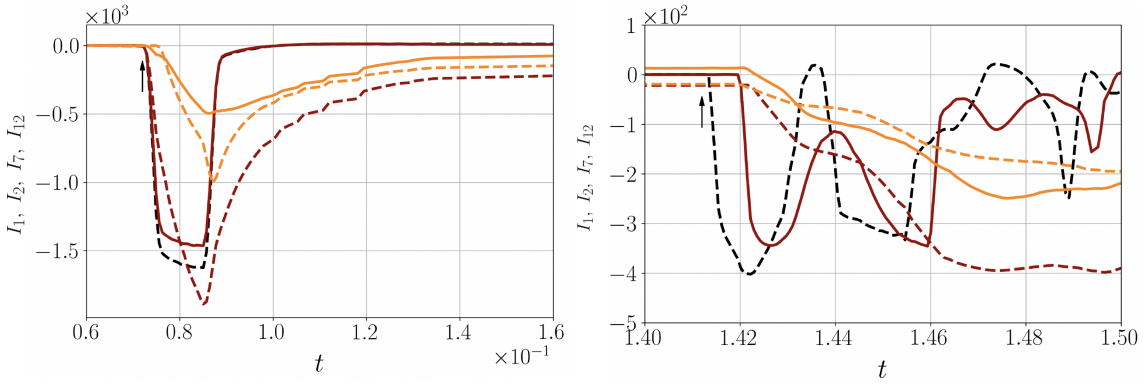


Figure 4.12: Temporal evolution of the spatial integrals of Terms 5, 6, 9, and 10, I_5, I_6, I_9, and I_{10} shown between $t = 0.06 - 0.16$ and $t = 1.4 - 1.5$ in (a) and (b), respectively, highlighting the effect of impact by the primary shock at $t \approx 0.7$ in (a), and reflected shock at $t \approx 1.415$ in (b), for $At = -0.66$ and $Ma = 5$. The blue solid and dashed lines represent I_5 and I_6, and the gray solid and dashed lines represent I_{10} and I_9, respectively. All other parameters mirror those from preceding figures.

The figure 4.14 shows the temporal variation of the major vorticity-generating terms, Terms 4 and 11, integrated along half of the arc length, $I_4^{(s)}$ and $I_{11}^{(s)}$, respectively, when the shock impacts the interface at Mach 2.5, 5, and 10 for the inviscid case and for that wherein the heavier and lighter phases correspond to BCY and Newtonian fluids, respectively. Results were generated for $\alpha = 0.1$ and $\alpha = 0.9$. It is seen that the magnitude of Term 4 associated with inviscid flow is larger than that for the viscous case, as expected, for all Ma considered, and higher in the heavier than the lighter fluid. It can be observed that although both $I_4^{(s)}$ and $I_{11}^{(s)}$ increase with Ma, the ratio of $I_4^{(s)}$ to $I_{11}^{(s)}$ increases. This indicates that the baroclinic mechanism gains in significance with rising Ma relative to the one associated with viscosity gradients.



(a) (b)

Figure 4.13: Temporal evolution of the spatial integrals of Terms 1, 2, 7, and 12, I_1, I_2, I_7, and I_{12} shown between $t = 0.06 - 0.16$ and $t = 1.4 - 1.5$ in (a) and (b), respectively, highlighting the effect of impact by the primary shock at $t \approx 0.7$ in (a), and reflected shock at $t \approx 1.415$ in (b), for $At = -0.66$ and $Ma = 5$. The red solid and dashed lines represent I_1 and I_{12}, and the orange solid and dashed lines represent I_2 and I_7, respectively. The black dashed lines represent I_1 for the inviscid case. All other parameters mirror those from preceding figures.

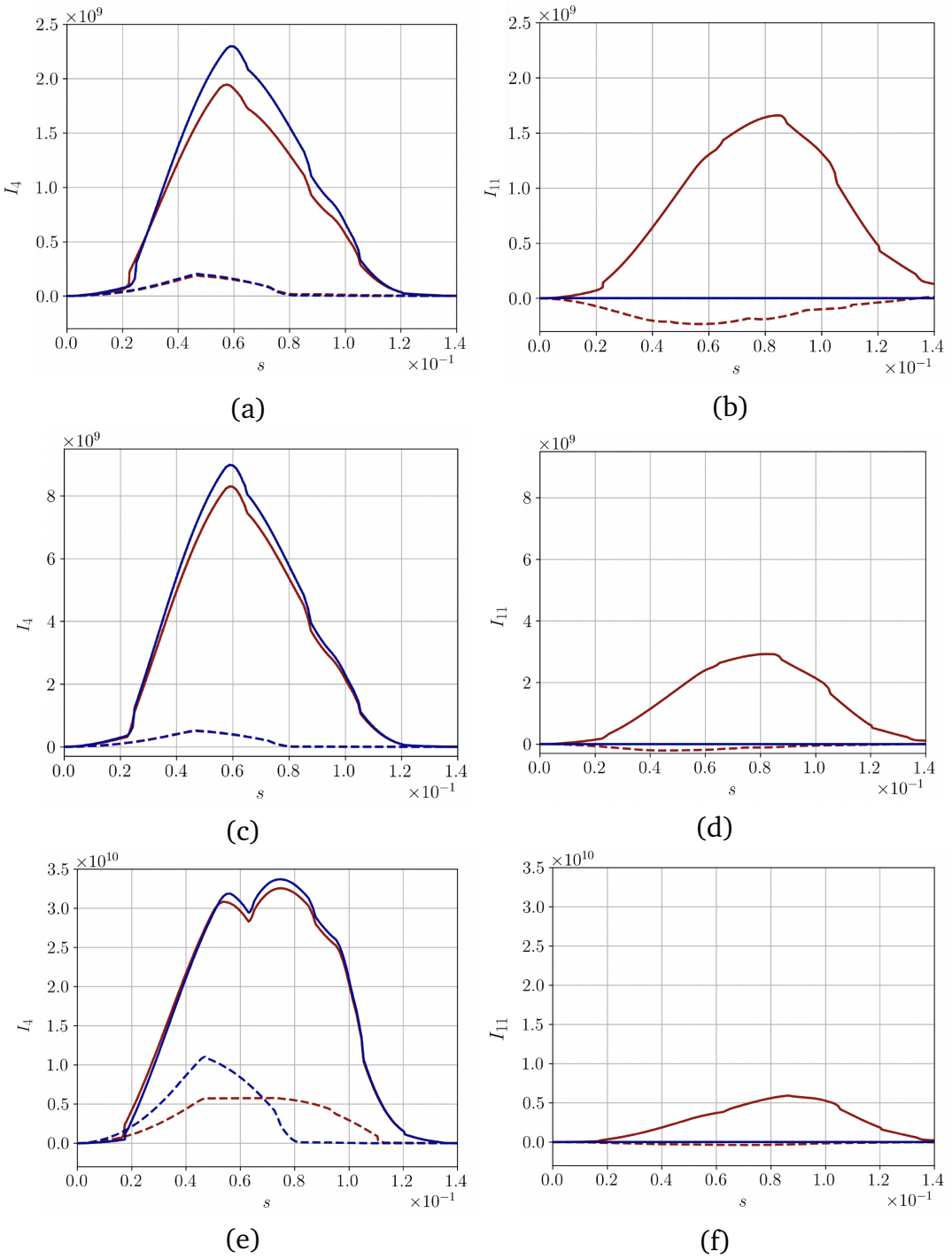


Figure 4.14: Variation of the arc length integrals of Terms 4 and 11 of equation 4.33, $I_4^{(s)}$ and $I_{11}^{(s)}$, respectively, when the primary shock impacts the interface with $AT = 0.66$ for $Ma = 2.5$, $Ma = 5$, and $Ma = 10$ shown in (a) and (b), (c) and (d), and (e) and (f), respectively. The blue and red lines represent the inviscid case and that wherein the heavier and lighter phases correspond to BCY and Newtonian fluids, respectively. The solid and dashed lines represent the results associated with $\alpha = 0.9$ and $\alpha = 0.1$, respectively.

4.2.2 Shear Thinning Effects with lower flow index

This section studies the effect of varying the flow index, which characterises the shear-thinning behaviour of the heavier fluid. The temperature effects on the viscosity are neglected by setting $\alpha_T = 0$ in equation 4.19. figure 4.15 shows the amplitude prediction for $Ma = 5$ and $At = -0.66$ by the theoretical model of Richtmyer [13], and Dimonte and Schneider [16], as well by BlastFOAM simulations for different cases that include the inviscid case, the BCY fluid in the heavier phase with flow indices of $n = 0.25$ and $n = 0.55$, as well as the case wherein both phases are modeled as Newtonian fluids. It is seen clearly that the perturbation amplitude associated with the $n = 0.25$ is even closer to that of the inviscid case than when $n = 0.55$; this suggests that lowering the flow index, and thus promoting the shear-thinning behaviour of the heavier phase, is destabilising.

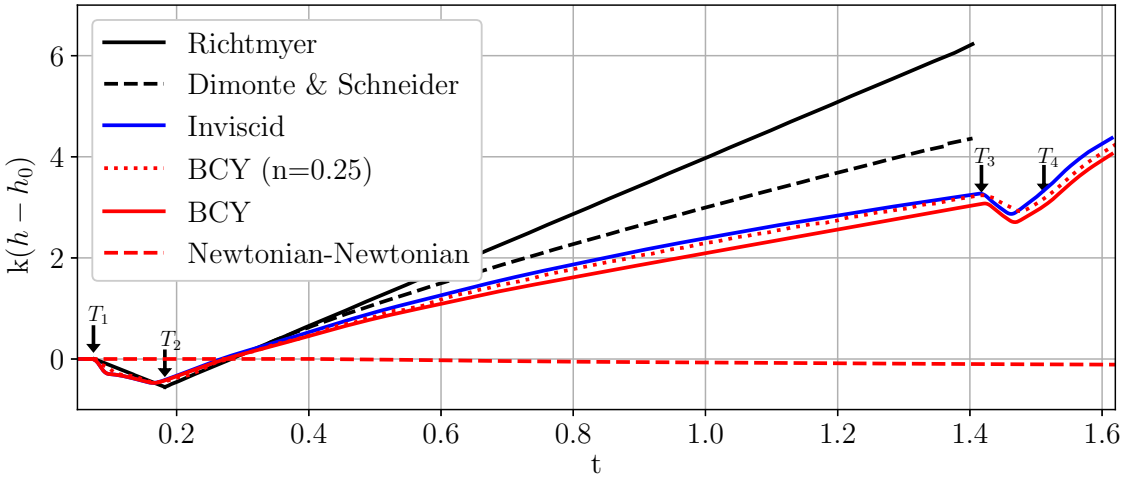


Figure 4.15: Temporal variation of the perturbation amplitude for $At = -0.66$ and $Ma = 5$, (a), where the black solid and dashed curves represent the predictions of the Richtmyer [13] and Dimonte and Schneider [16] models, the blue curves represent the inviscid case, while the red dotted, solid and dashed lines represent the numerical predictions obtained for the BCY with $n = 0.55$, BCY (n=0.25) and Newtonian-Newtonian cases, respectively; in the latter case, the light and heavy fluids correspond to Newtonian and BCY fluids, respectively; here, $T_1 - T_4$ correspond to t = 0.075, 0.18,1.41, and 1.48, respectively.

In figure 4.16, the fully-developed $x-y$ projections of the density field for the inviscid case in (a), BCY with a lower flow index of $n = 0.25$ in (b), and BCY with a higher flow index of $n = 0.55$ in (c) are displayed. The inviscid case is the most unstable case as compared to the other two cases. A important observation can be made in figure 4.16 (b) and (c): in figure 4.16 (b), which shows that in the $n = 0.25$ case, the roll-ups associated with the KHI are more advanced as compared to the $n = 0.55$ case. This stems from the higher resulting viscosity with higher flow index which dampens the development of the RMI amplitude and the development of roll-ups

and associated small scale structures.

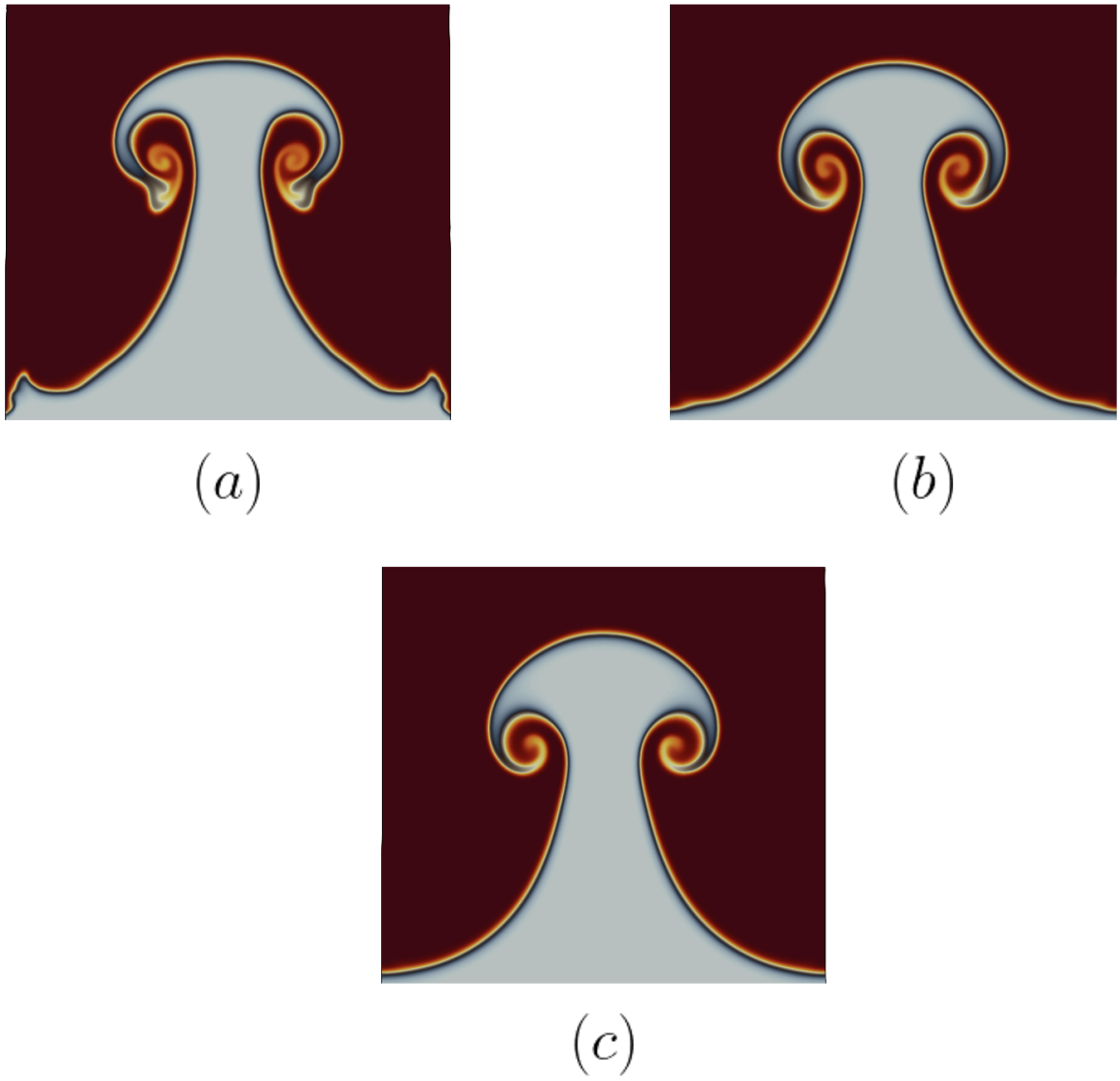


Figure 4.16: Fully-developed $x-y$ projections of the density field at $Ma = 6$, $At = 0.66$ for the cases inviscid in (a), BCY ($n = 0.25$) in (b) and BCY ($n = 0.55$) in (c), wherein the lighter and heavier phases correspond to Newtonian and BCY fluids, respectively, the rest of the parameters remain unchanged from previous figures.

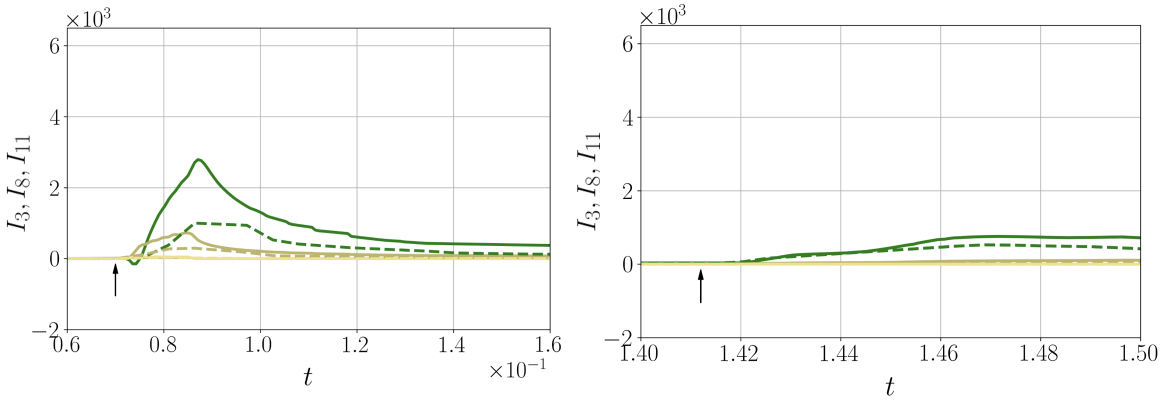


Figure 4.17: Temporal evolution of the spatial integrals of Terms 3, 8, and 11, I_3, I_8, and I_{11}, showcased between $t = 0.06 - 0.16$ and $t = 1.4 - 1.5$ in panels (a) and (b), respectively. These segments highlight the impacts of the primary shock at $t \approx 0.7$ in (a), and the reflected shock at $t \approx 1.415$ in (b), for $At = -0.66$ and $Ma = 5$. The green lines (solid for $n = 0.55$, dashed for $n = 0.25$) illustrate I_{11} within the BCY model, while I_3 and I_8 are depicted by khaki (solid for $n = 0.55$, dashed for $n = 0.25$) and yellow lines (solid for $n = 0.55$, dashed for $n = 0.25$), respectively. This convention allows for a direct comparison between different flow indices. Consistency with previous figures is maintained for all other parameters.

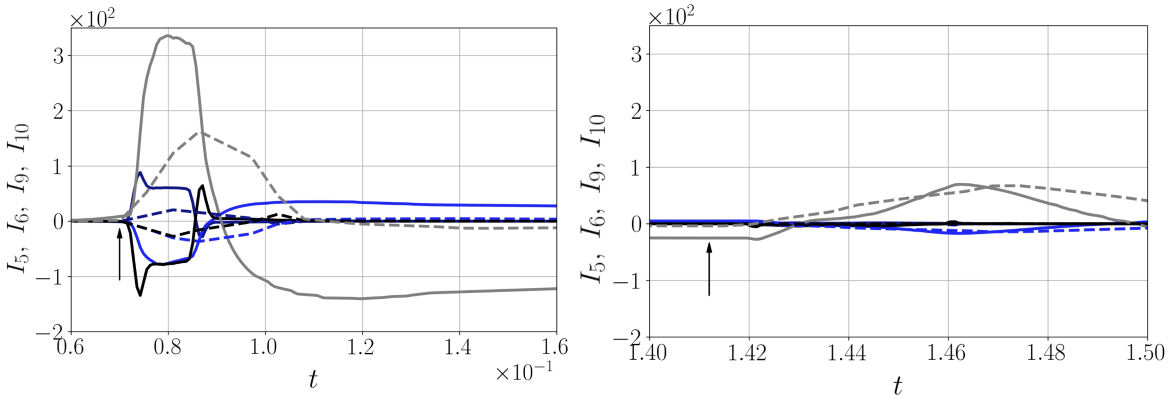


Figure 4.18: Temporal evolution of the spatial integrals of Terms 5, 6, 9, and 10, I_5, I_6, I_9, and I_{10} shown between $t = 0.06 - 0.16$ and $t = 1.4 - 1.5$ in (a) and (b), respectively, highlighting the effect of impact by the primary shock at $t \approx 0.7$ in (a), and reflected shock at $t \approx 1.415$ in (b), for $At = -0.66$ and $Ma = 5$.The dark blue lines (solid for $n = 0.55$, dashed for $n = 0.25$) illustrate I_5. The light blue lines (solid for $n = 0.55$, dashed for $n = 0.25$) illustrate I_6. The gray lines (solid for $n = 0.55$, dashed for $n = 0.25$) illustrate I_{10}. The black lines (solid for $n = 0.55$, dashed for $n = 0.25$) illustrate I_9. This convention allows for a direct comparison between different flow indices. Consistency with previous figures is maintained for all other parameters.

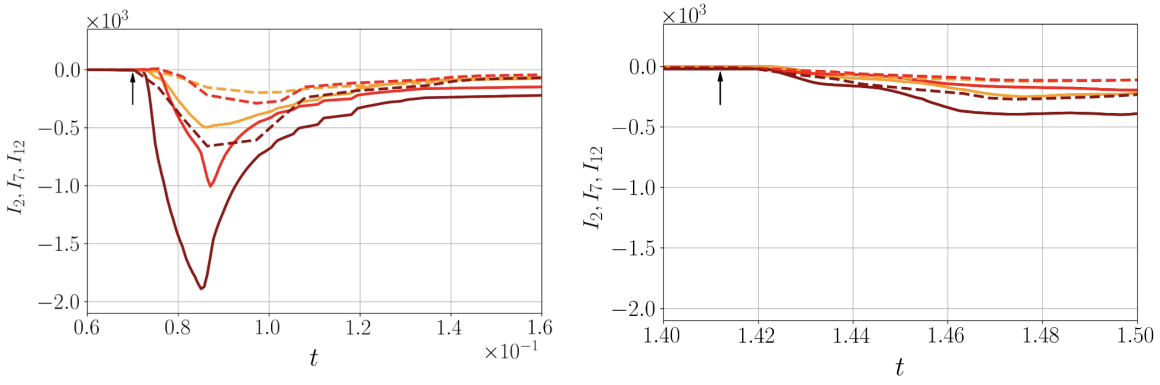


Figure 4.19: Temporal evolution of the spatial integrals of Terms 2, 7, and 12, I_2, I_7, and I_{12} shown between $t = 0.06 - 0.16$ and $t = 1.4 - 1.5$ in (a) and (b), respectively, highlighting the effect of impact by the primary shock at $t \approx 0.7$ in (a), and reflected shock at $t \approx 1.415$ in (b), for $At = -0.66$ and $Ma = 5$. The dark red lines (solid for $n = 0.55$, dashed for $n = 0.25$) illustrate I_{12}.The light red lines (solid for $n = 0.55$, dashed for $n = 0.25$) illustrate I_7. The orange lines (solid for $n = 0.55$, dashed for $n = 0.25$) illustrate I_2. This convention allows for a direct comparison between different flow indices. Consistency with previous figures is maintained for all other parameters

figures 4.17, 4.18, and 4.19 illustrate a comparison of destabilising, destabilising-stabilising, and stabilising terms that stems from the viscosity. The terms from the BCY case with flow index of $n = 0.55$ are displayed with solid lines, and the terms when using a flow index of $n = 0.25$ are displayed with dashed lines. It is seen that both destabilizing and stabilizing factors are diminished compared to those observed with a higher flow index in the BCY model; this is related to the comparatively lower viscosity associated with the reduction in the value of the flow index. This diminished influence of viscosity on the evolution of vorticity results in the BCY model with a lower flow index exhibiting more advanced roll-ups (see figure 4.16 (b)) as compared to the BCY case with a higher flow index (see figure 4.16 (c)), and the amplitude of the RMI is closer to the inviscid case, as shown in figure 4.16.

4.2.3 Shear Thinning Effects and Temperature Effects

In the previous sections, a flow index of $n = 0.55$ and $n = 0.25$ is used in equation 4.18 to model the rheological behavior of the heavier fluid. Here, it the combined effects of shear rate- and temperature-dependent viscosity are examined. The flow index is set to $n = 0.55$ and $\alpha_T = 16$ within the same rheological model given by equation 4.19. figure 4.15 shows the amplitude prediction for $Ma = 5$ and $At = -0.66$ by the theoretical models [13, 16] and our numerical simulation using BlastFOAM. It is clearly seen that the growth associated with the combined effects of temperature and shear rate dependence of the viscosity is closest to that obtained from the inviscid case, which represents the most unstable case. This demonstrates the destabilising nature of including thermal effects which act to lower the viscosity, in addition to similar effects brought about by the shear-thinning nature of the ma-

terial. This leads to reduced damping of the vortical structures and increased level of mixing.

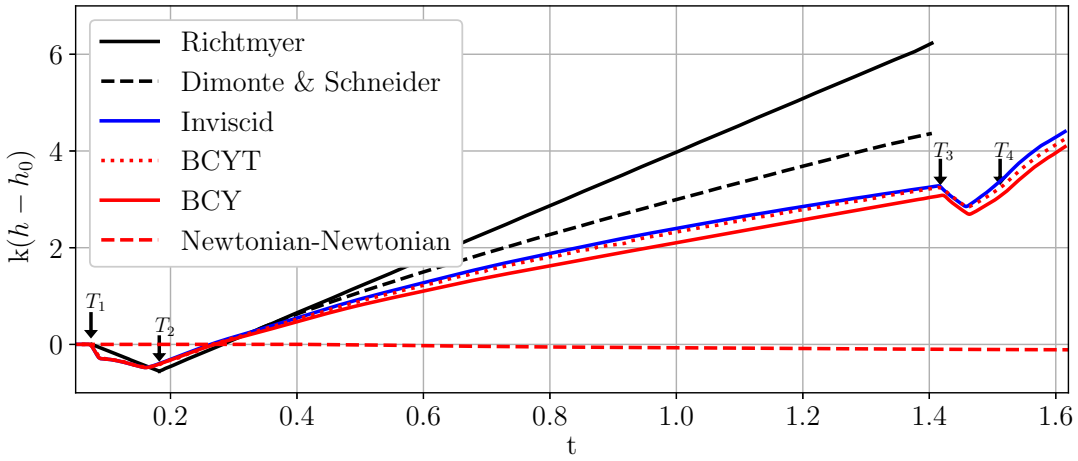


Figure 4.20: Temporal variation of the perturbation amplitude for $At = -0.66$ and $Ma = 5$, (a), where the black solid and dashed curves represent the predictions of th e Richtmyer [13] and Dimonte and Schneider [16] models, the blue curves represent the inviscid case, while the red dotted, solid and dashed lines represent the numerical predictions obtained for the BCY with $n = 0.55$, BCYT and Newtonian-Newtonian cases, respectively; in the latter case, the light and heavy fluids correspond to Newtonian and BCY fluids, respectively; here, $T_1 - T_4$ correspond to t = 0.075, 0.18,1.41, and 1.48, respectively.

In figure 4.21, the fully-developed $x-y$ projections of the density field for the inviscid case in (a), BCYT with a flow index of $n = 0.55$ and $\alpha_T = 16.0$ in (b), and BCY with a flow index of $n = 0.55$ in (c) are displayed. A important observation can be made in figure 4.21. The inviscid case (a) in figure 4.21 is the most unstable case with the most further developed KHI. The BCY case that only considers the shear-thinning effects is the most stable case with the least developed KIH as compared to inviscid case and BCYT, which shows that in the BCYT case, the roll-ups associated with the KHI are more advanced as compared to the BCY case. This stems from the lower viscosity that decreases with the combined effects of shear-thinning and temperature in the BCYT case.

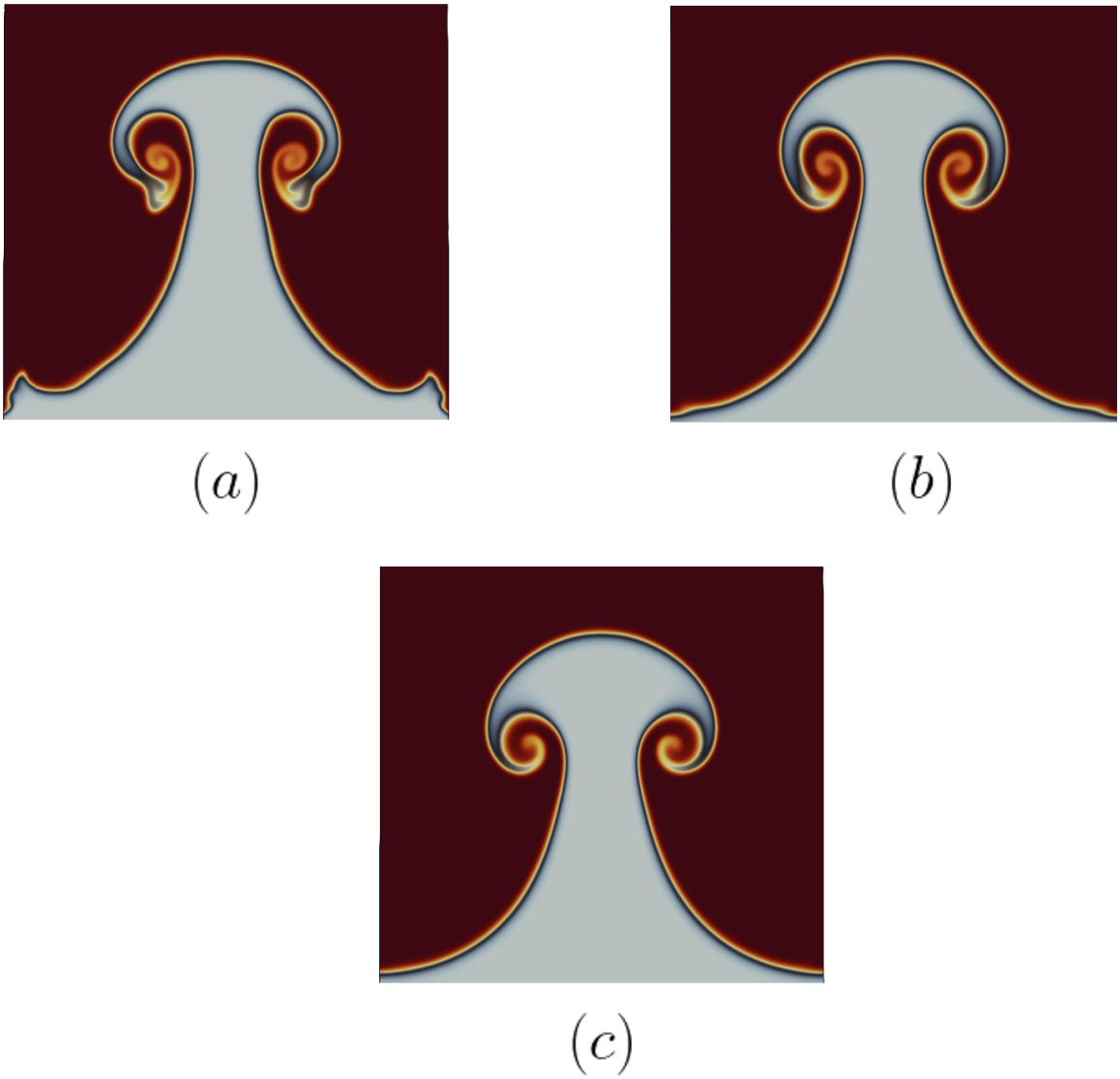
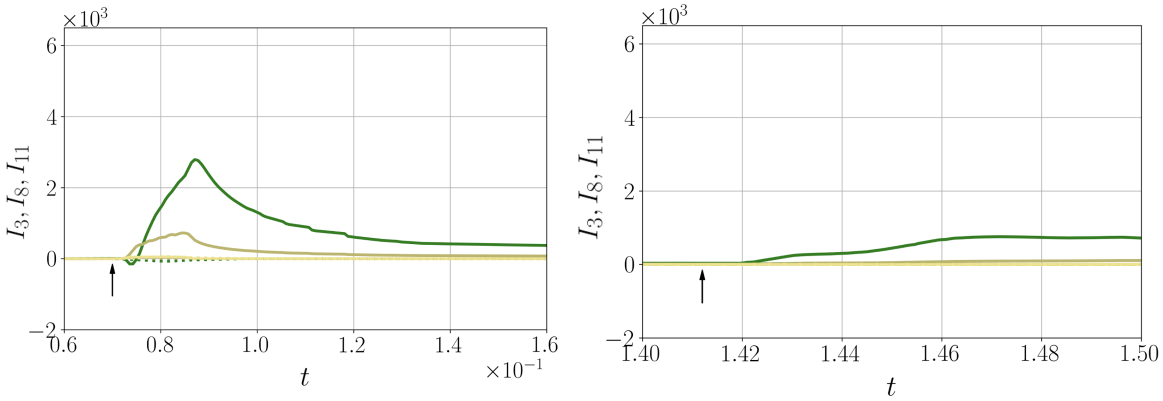
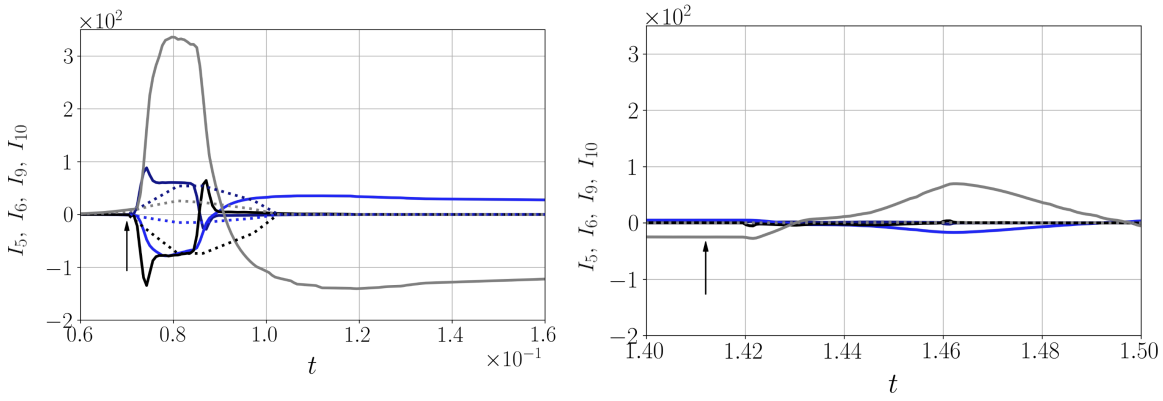


Figure 4.21: Fully-developed $x-y$ projections of the density field at $Ma = 6$, $At = 0.66$ for the cases inviscid in (a), BCYT in (b) and BCY ($n = 0.55$) in (c), wherein the lighter and heavier phases correspond to Newtonian and BCY fluids, respectively, the rest of the parameters remain unchanged from previous figures.



(a) (b)

Figure 4.22: Temporal evolution of the spatial integrals of Terms 3, 8, and 11, I_3, I_8, and I_{11}, showcased between $t = 0.06 - 0.16$ and $t = 1.4 - 1.5$ in panels (a) and (b), respectively. These segments highlight the impacts of the primary shock at $t \approx 0.7$ in (a), and the reflected shock at $t \approx 1.415$ in (b), for $At = -0.66$ and $Ma = 5$. The green lines (solid for BCY $n = 0.55$, dotted for BCYT) illustrate I_{11} within the BCY model, while I_3 and I_8 are depicted by khaki (solid for BCY $n = 0.55$, dotted for BCYT) and yellow lines (solid for BCY $n = 0.55$, dotted for BCYT), respectively. This convention allows for a direct comparison between different flow indices. Consistency with previous figures is maintained for all other parameters.



(a) (b)

Figure 4.23: Temporal evolution of the spatial integrals of Terms 5, 6, 9, and 10, I_5, I_6, I_9, and I_{10} shown between $t = 0.06 - 0.16$ and $t = 1.4 - 1.5$ in (a) and (b), respectively, highlighting the effect of impact by the primary shock at $t \approx 0.7$ in (a), and reflected shock at $t \approx 1.415$ in (b), for $At = -0.66$ and $Ma = 5$.The dark blue lines (solid for $n = 0.55$, dotted for $n = 0.25$) illustrate I_5. The light blue lines (solid for BCY $n = 0.55$, dotted for BCYT) illustrate I_6. The gray lines (solid for BCY $n = 0.55$, dotted for BCYT) illustrate I_{10}. The black lines (solid for BCY $n = 0.55$, dotted for BCYT) illustrate I_9. This convention allows for a direct comparison between different flow indices. Consistency with previous figures is maintained for all other parameters.

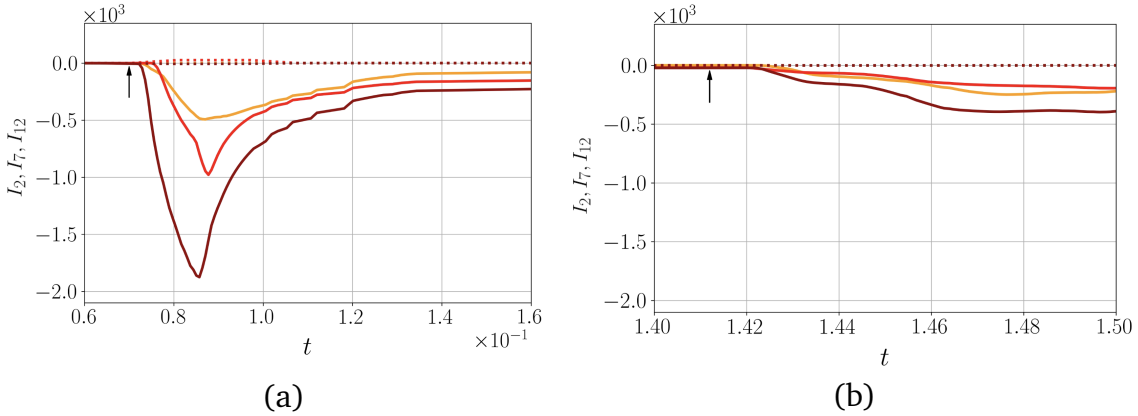


Figure 4.24: Temporal evolution of the spatial integrals of Terms 2, 7, and 12, I_2, I_7, and I_{12} shown between $t = 0.06 - 0.16$ and $t = 1.4 - 1.5$ in (a) and (b), respectively, highlighting the effect of impact by the primary shock at $t \approx 0.7$ in (a), and reflected shock at $t \approx 1.415$ in (b), for $At = -0.66$ and $Ma = 5$. The dark red lines (solid for $n = 0.55$, dashed for $n = 0.25$) illustrate I_{12}.The light red lines (solid for BCY $n = 0.55$, dotted for BCYT) illustrate I_7. The orange lines (solid for BCY $n = 0.55$, dashed for BCYT) illustrate I_2. This convention allows for a direct comparison between different flow indices. Consistency with previous figures is maintained for all other parameters

The Figures 4.22, 4.23 and 4.24 illustrate a comparison of destabilising, stabilising-destabilising, and stabilising terms that stem from the non-Newtonian rheology. The terms from the BCY case with flow index of $n = 0.55$ are displayed with solid lines, and the terms for BCYT are displayed with dotted lines. Inspection of these figures further demonstrates the destabilising nature of combining the effects of shear thinning and temperature on the non-Newtonian rheology of the heavier phase. This leads to higher amplitude and more developed KHI in the BCYT case as compared to the BCY case.

4.2.4 Summary and Implications

This chapter investigates the effects of non-Newtonian rheology on the development of Richtmyer-Meshkov instabilities (RMI) in flows characterised by negative Atwood numbers wherein a shock is initiated in the heavier, non-Newtonian fluid and travels towards the lighter, Newtonian one. In order to resolve the shock and interfacial dynamics, a one-fluid formulation for the mass, momentum, and energy equations for a compressible flow is used. A shear-thinning rheology is considered for the heavier phase, and a stiffened gas equation of state is used to relate the pressure to the density. A volume-of-fluid approach is utilised to capture the interface, and the open-source software BlastFOAM is employed to obtain numerical solutions of the governing equations for a range of Atwood and Mach numbers and a fixed set of rheological parameters for the heavier phase. A two-dimensional vorticity transport equation is derived. Terms that generate and dampen vorticity are identified. This provides valuable insights into the interplay between non-Newtonian effects, vorticity generation, and RMI growth in various regimes.

The results demonstrated that the incident shock creates a viscosity gradient along the interface, which generates additional vorticity due to non-Newtonian effects compared to the inviscid case, which is used as a benchmark. This additional vorticity generation is more pronounced at moderate Mach numbers Ma ($< Ma = 5$) than at high Mach numbers ($Ma = 10$) because lower shear rates in the former Ma range result in a higher residual viscosity gradient. After the passage of the shock, the damping effects of viscosity become dominant, leading to a reduction in the vorticity. The reflected shock then generates additional vorticity due to the non-Newtonian viscosity gradient.

For the low-to-moderate Ma range, the damping effects of viscosity hinder the development of secondary instabilities, such as the Kelvin-Helmholtz instability, leading to lower RMI growth. At high Ma, the residual viscosity is low due to the very high shear rates associated with high-Ma flows, resulting in low rates of vorticity generation associated with non-Newtonian effects. Furthermore, viscous effects in these situations damp out the small-scale structures which could have given rise to vortex-accelerated vorticity deposition that would have enhanced the RMI and associated mixing.

This study also examines the influence of a reduced flow index and temperature variations on the evolution of vorticity, and consequently, on the development of the RMI and KHI. The findings reveal that a lower flow index intensifies shear-thinning effects, leading to decreased viscosity. This reduction in viscosity diminishes both the generation and damping effects, which, on balance, facilitates greater growth of both RMI and KHI.

Furthermore, temperature effects are observed to reduce the impact of viscosity on the destabilizing and stabilizing factors associated with it. As a result, the amplitude of RMI approaches that of the inviscid scenario, although the influence of viscosity remains evident in the small-scale structures within KHI rolls. Even with reduced viscosity, these small-scale structures are damped and the associated roll-up is less developed as compared to the inviscid case but more developed as compared to the case with a higher flow index in the BCY model.

4.3 Limitations of Models

The non-Newtonian rheological model studied in this thesis is a Carreau-type, power-law model. Viscoelastic effects are not implemented in this model. It is recommended to incorporate viscoelasticity in the model by choosing a suitable constitutive relation for the rheology, such as the FENE-P or Oldroyd-B models, and coupling an evolution equation for the conformation tensor of the polymeric chains to the other equations of motion. Therefore, BlastFOAM must be further developed to implement viscoelastic effects.

The impact of temperature on the viscosity of non-Newtonian fluids is only partially considered in these simulations. Therefore, further investigations of coupling between the non-Newtonian effects and heat transfer are needed as it could significantly influence the generation of small-scale vortical structures, which promote mixing. The mixing of hot and cold fluids could reduce the temperature that is required for ignition in inertial confinement fusion. In addition to this, The coupling between non-Newtonian effects and heat transfer can impact the stability and evolution of fluid interfaces, which can result in more complex flow dynamics and instabilities. A detailed understanding of coupling between non-Newtonian effects, including the shear-thinning and viscoelastic effects with heat transfer would be essential to understand the flow dynamics under extreme conditions such as the high Mach numbers.

Several multi-physics interactions, such as turbulence, heat and mass transfer, phase changes, and conduction, are neglected as well. It is recommended to study multi-physics interactions for a better understanding of this problem. The effects of conduction and heat transfer on the mixing and small-scale structures within the roll-up of Kelvin-Helmholtz instability (KHI) would be particularly interesting. Additionally, turbulence can enhance mixing and affect the growth and structure of instabilities. Neglecting turbulence could lead to an incomplete understanding of the fluid dynamics, especially within the roll-ups, where the small-scale structures develop.

Chapter 5

Fusion Target

This chapter explores how viscosity impacts the shock dynamics and post-compression properties such as average pressure, temperature, and density. Additionally, this study examines the impact of coverslip material and configuration on hydrodynamic instabilities, particularly the Richtmyer-Meshkov Instability (RMI), and how the coverslip material and configuration influence subsequent mixing processes. This mixing process leads to the undesirable mixing of hot and cold fluids, reducing temperature and pressure and preventing ignition. The findings provide valuable insights into optimizing coverslip material choices to enhance the efficiency and effectiveness of ICF processes.

5.1 Viscosity Effects on Shock Dynamics

5.1.1 1-D shock-tube

A one-dimensional (1-D) shock-tube is used to investigate the viscosity effects on the shock dynamics before delving into the detailed analysis of non-Newtonian viscosity effects on shock dynamics, as well as the Richtmyer Meshkov and Kelvin Helmholtz instabilities in the Fusion Target case of Derentowicz et al. [17]. A 1-D shock-tube such as the one shown in figure 5.1 is used in this study, which consists of polyethylene (PMMA) and deuterium. This simulation study is designed with the shock being initiated within the PMMA and subsequently moving towards and compressing the deuterium. The computational grid consists of 5000 cells along the streamwise direction, represented by the x-axis.

The dark-gray section of the shock-tube in figure 5.1 is shocked and the white section is at ambient conditions. The shock is initialised with a density of $4345\,\text{kg/m}^3$, a velocity of $46755\,\text{m/s}$, a pressure of $3.5 \times 10^{12}\,\text{Pa}$, and a temperature of $1371\,\text{K}$. At ambient conditions (white section in figure 5.1), the temperature is $1371\,\text{K}$, the pressure $10^5\,\text{Pa}$, the density of deuterium $0.16\,\text{kg/m}^3$, and the density of PMMA $1150\,\text{kg/m}^3$. The velocity, pressure, temperature, and density are non-dimensionalised by the the shocked velocity, pressure, temperature, and density of copper. This study is conducted with BlastFOAM. A constant dynamic viscosity of 2.5×10^{-4} mPa $\cdot$ s is employed for deuterium, while constant dynamic viscosities of 5, 10 and 20 mPa $\cdot$ s are used for PMMA. The viscosity is non-dimensionalised by the viscosity of PMMA. The ideal gas equation of state is used for deuterium and a stiffened gas one, expressed by Eq. (4.16), is used for PMMA.

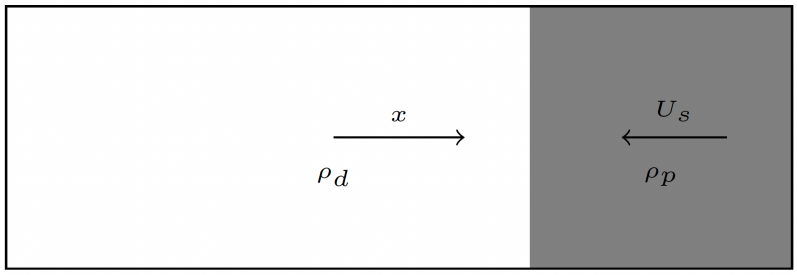


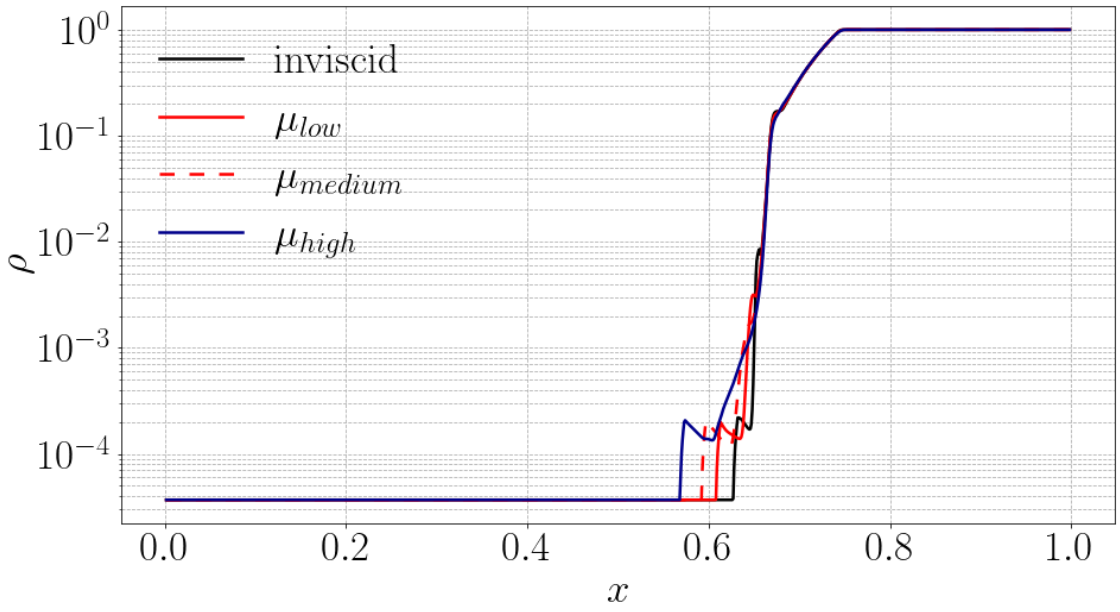
Figure 5.1: Schematic of a flow configuration, where the right gray region contains PMMA (of density ρ_p) and the white region contains deuterium (of density ρ_d). The dark gray area is initialized with a shock, which travels towards the deuterium.

In figures 5.2 and 5.3, the viscous cases are compared with the inviscid case to investigate the impact of viscosity on the shock dynamics, and the velocity, density, temperature, and pressure. The results indicate that the viscosity has a significant influence on the velocity and temperature. A notable trend observed is that an increase in viscosity results in a significant rise in both the velocity and temperature of the shock front, while the density of the shock front also shows an increase. The pressure drops to near-zero level in viscous and inviscid cases, which stems from the formation of a strong rarefaction wave that leads to a strong expansion. This expansion results in a pressure drop close to vacuum conditions. The sudden pressure drop has been studied in section 3.2.1 and shown in figure 3.35.

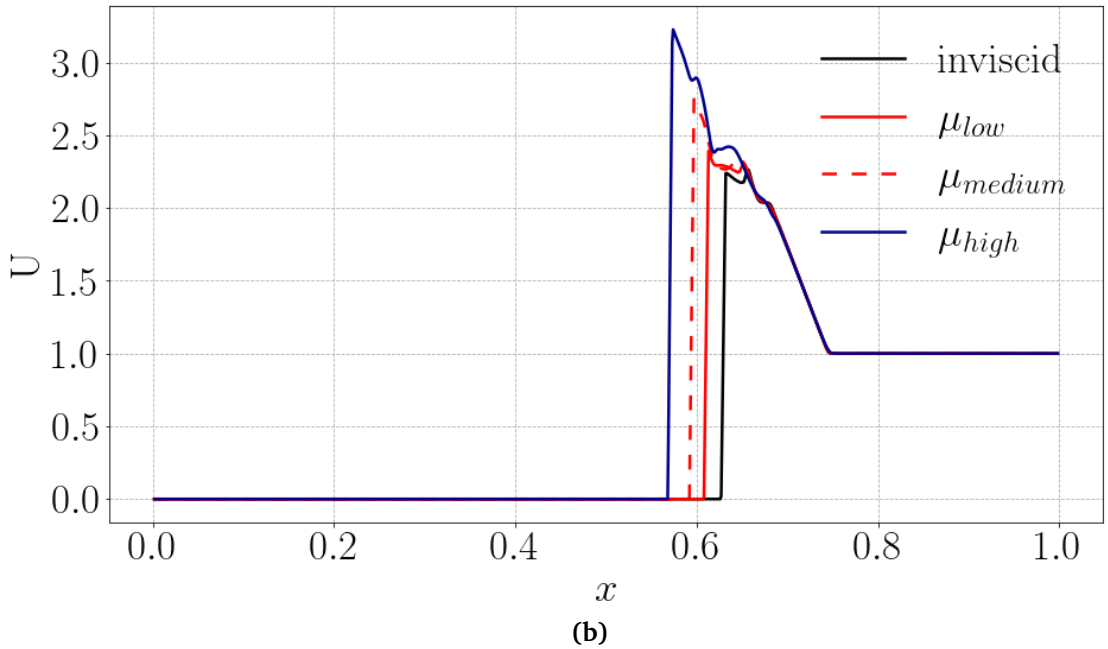
In the study presented in section 3.2.1, both BlastFOAM and Hytrac show a pressure drop resulting from a strong rarefaction wave initiated due to a large density jump between the gaseous deuterium and the PMMA. The ratio of density between PMMA and gaseous deuterium is 7187, as already discussed in section 3.2.1. Due to the substantial density difference between deuterium and PMMA, the intensity of the rarefaction wave is significantly amplified, which leads to a strong expansion, resulting into a sudden pressure drop nearly to vacuum condition as shown in section 3.35. An effective strategy to mitigate this effect is to increase the density of deuterium in order to decrease the intensity of the rarefaction wave and stabilise the pressure profile in the shock-tube. In figure 5.5, results of a similar case are shown,

where the non-dimensionalised density of deuterium is increased by factors of 6.25 and 625; it is clear that the latter increase eliminates the sudden pressure drop by mitigating the formation of strong rarefaction that could have led to the strong expansion. As shown in figures 5.2 and 5.3, shock in a viscous fluid propagates faster as compared to the inviscid case. The higher the viscosity the faster and hotter the shock. One of the reasons behind this mechanism could be that the shock front is diffusive due to the presence of the second-order viscous term in the momentum and energy equation. The momentum and heat diffusion lead to less steep gradient in velocity and temperature. The other reason could be that the viscosity impacts the shock properties. The viscous dissipation term in the energy equation converts the kinetic energy of the fluid into heat which leads to higher pressure and temperature behind the shock front, and results in faster shock propagation as compared to the inviscid case. A similar shock behaviour was observed in a study conducted by Vold et al. [67] who investigated how the viscosity influences the shock dynamics in ICF implosions. The results of that study agree with the observations in the present thesis. Vold et al. [67] also attributed the shock speed acceleration to the viscous dissipation mechanism. The findings of this PhD project and of Vold et al. [67] could be significant for the field of ICF.

Figures 5.4 - 5.5 present the scenario where the density is increased by a factor of 6.25 as compared to the baseline case shown in 5.2 and 5.3. The aim is to investigate, how an increase in density affects the impact of viscosity on shock dynamics. The results show that increasing the density leads to a decrease in the impact of viscosity on hydrodynamic parameters such as density, velocity, pressure, and temperature. In figures 5.6 and 5.7, the density of deuterium is increased by a factor of 625 as compared to the baseline case shown in figures 5.2 and 5.3. It is found that this significant increase in density by a factor of 625 further diminishes the impact of viscosity on the shock dynamics. The inviscid and viscous cases predict almost identical pressure, temperature, velocity, and density. Therefore, increasing the density decreases the impact of viscosity on the shock dynamics. In less dense flows, as shown in figures 5.2 and 5.3, the influence of viscosity on the shock properties is substantial, whereas for denser fluids, as shown in figures 5.6 and 5.7, the impact of viscosity on the shock properties is negligible.

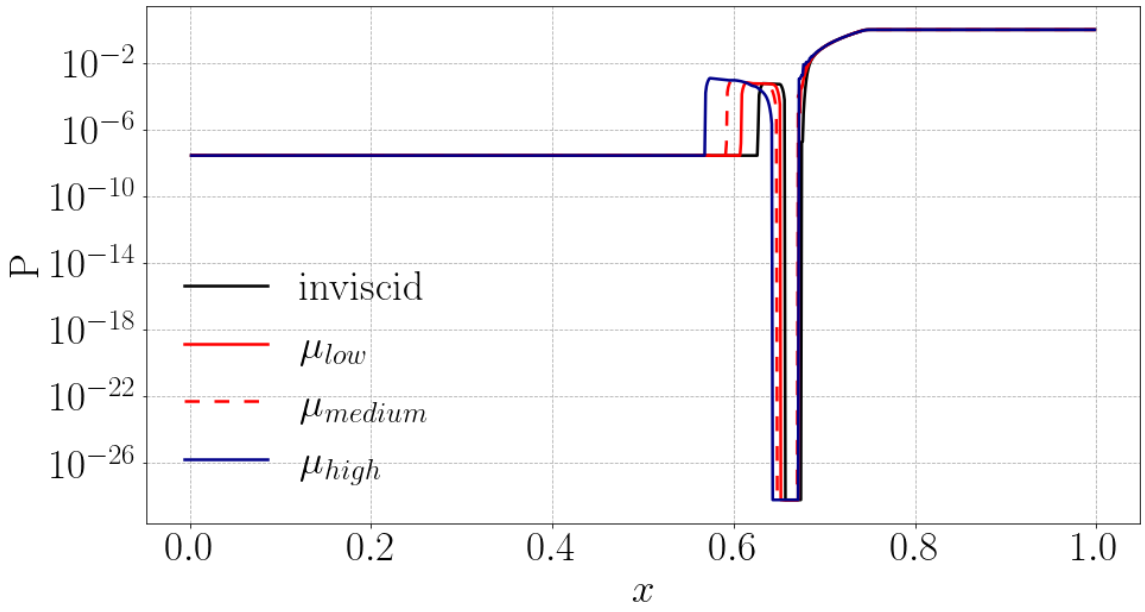


(a)

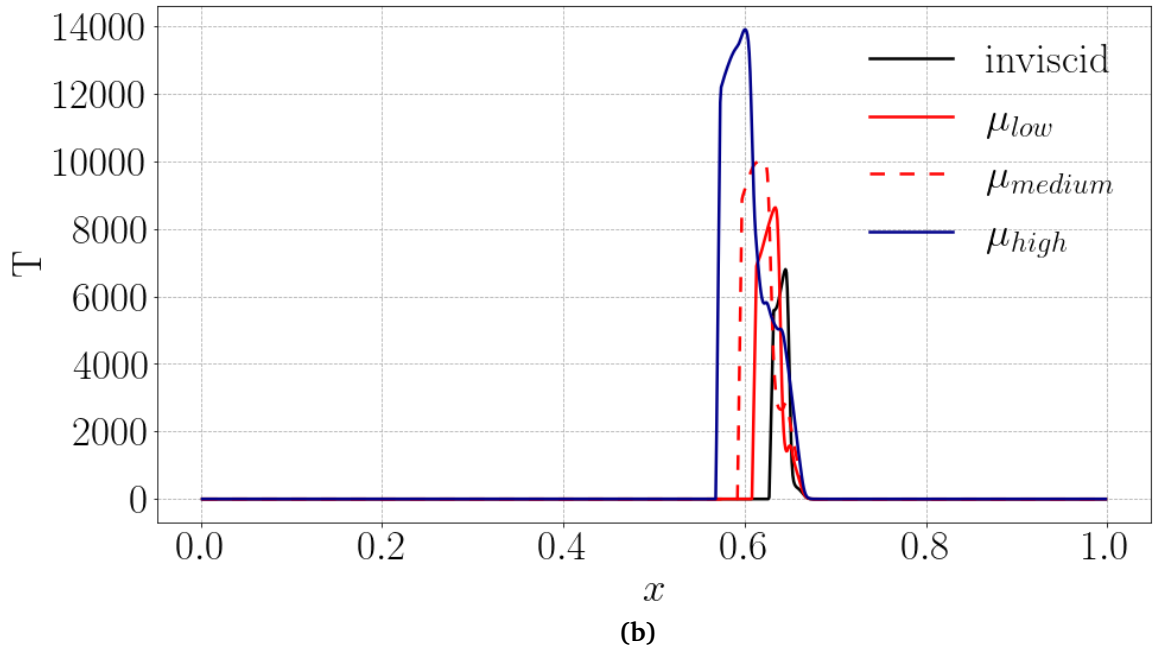


(b)

Figure 5.2: Density (a) and velocity (b) predictions at $t = 0.03$ using the BlastFOAM solver, with the ideal gas equation of state for deuterium and the stiffened gas equation of state for PMMA, under inviscid and viscous conditions. The study evaluates three viscous scenarios based on non-dimensionalised viscosity values: μ_{low} with deuterium at a viscosity of 5×10^{-5} and PMMA at 1, μ_{medium} with deuterium's viscosity unchanged and PMMA's increased to 2, and μ_{high}, where deuterium remains at 5×10^{-5} but PMMA's viscosity is raised to 4.

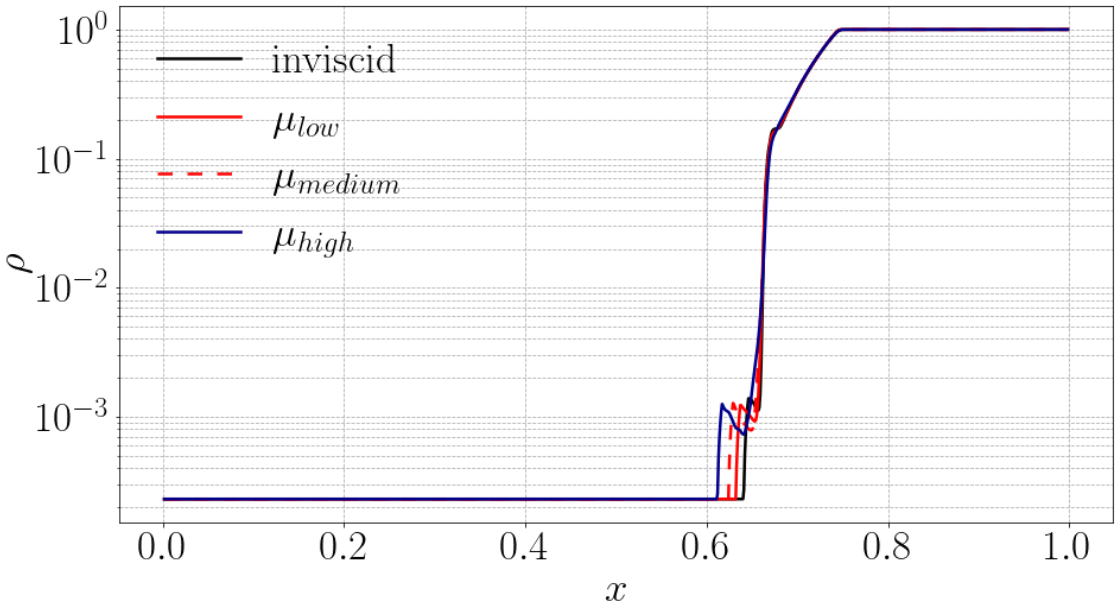


(a)

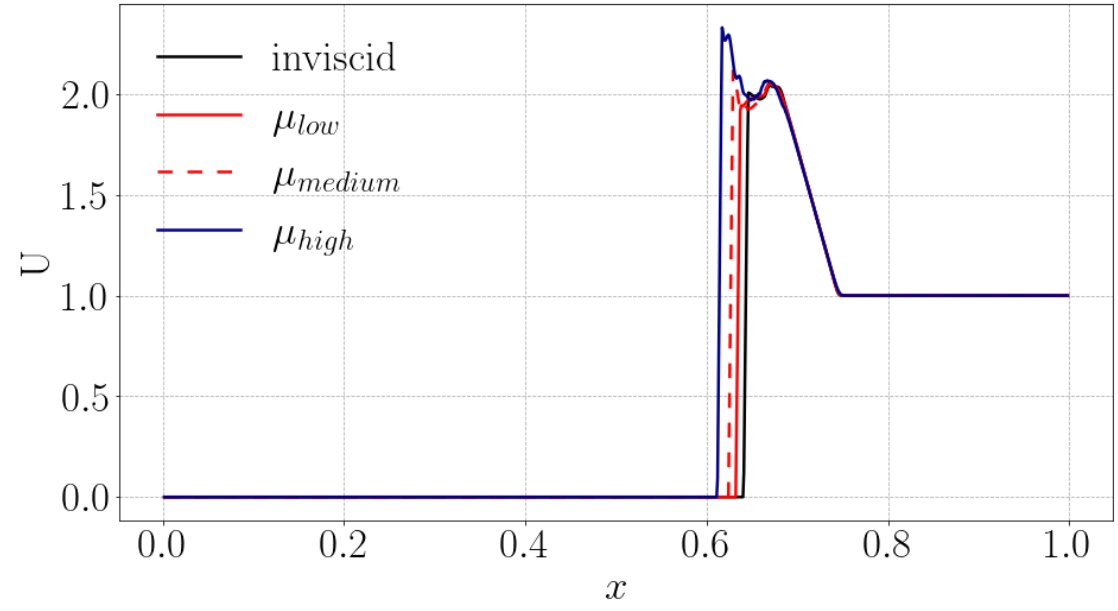


(b)

Figure 5.3: Pressure (a) and temperature (b) predictions at $t = 0.03$ using the BlastFOAM solver, with the ideal gas equation of state for deuterium and the stiffened gas equation of state for PMMA, under inviscid and viscous conditions. The study evaluates three viscous scenarios based on non-dimensionalised viscosity values: μ_{low} with deuterium at a viscosity of 5×10^{-5} and PMMA at 1, μ_{medium} with deuterium's viscosity unchanged and PMMA's increased to 2, and μ_{high}, where deuterium remains at 5×10^{-5} but PMMA's viscosity is raised to 4.

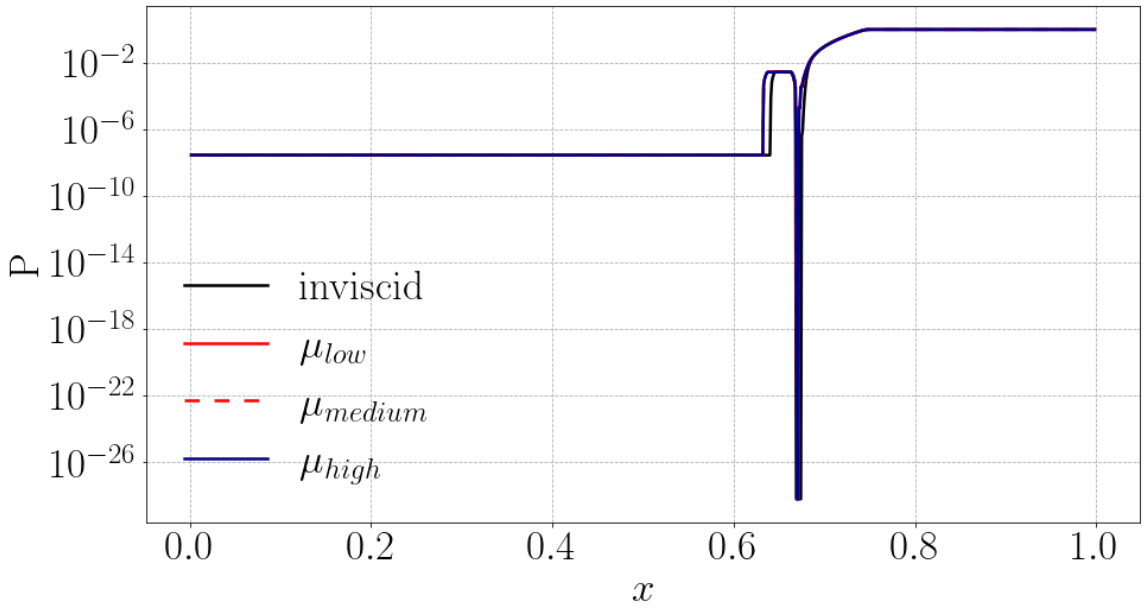


(a)

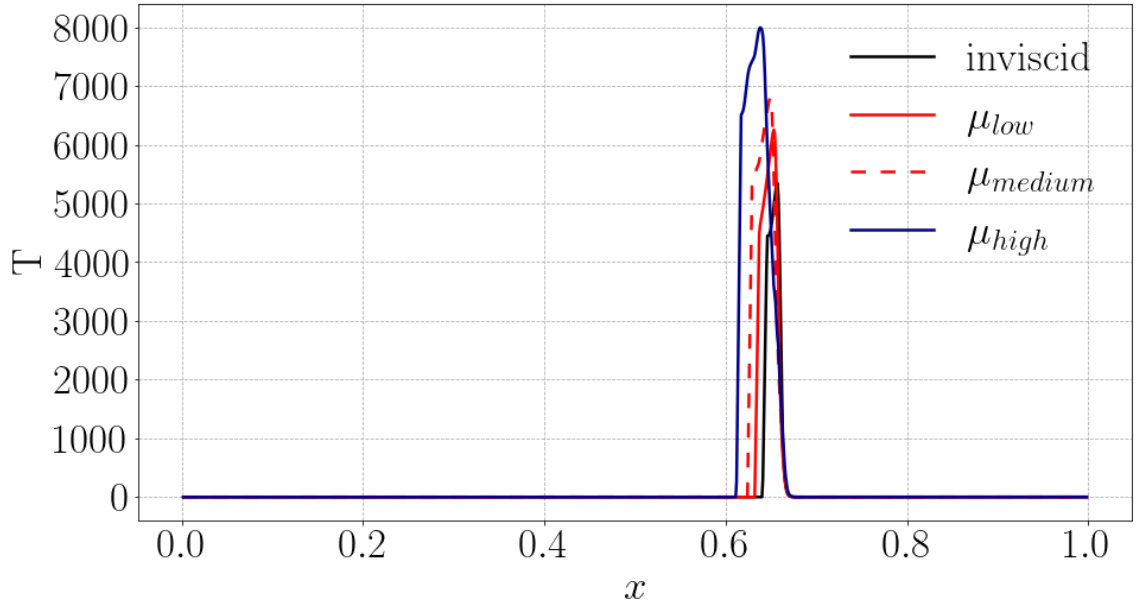


(b)

Figure 5.4: Density (a) and velocity (b) predictions at $t = 0.03$ using the BlastFOAM solver, with the ideal gas equation of state for deuterium and the stiffened gas equation of state for PMMA, under inviscid and viscous conditions. The study evaluates three viscous scenarios based on non-dimensionalised viscosity values: μ_{low} with deuterium at a viscosity of 5×10^{-5} and PMMA at 1, μ_{medium} with deuterium's viscosity unchanged and PMMA's increased to 2, and μ_{high}, where deuterium remains at 5×10^{-5} but PMMA's viscosity is raised to 4. The density of deuterium is increased by a factor of 6.25 as compared to the base case shown in figures 5.2 and 5.3.

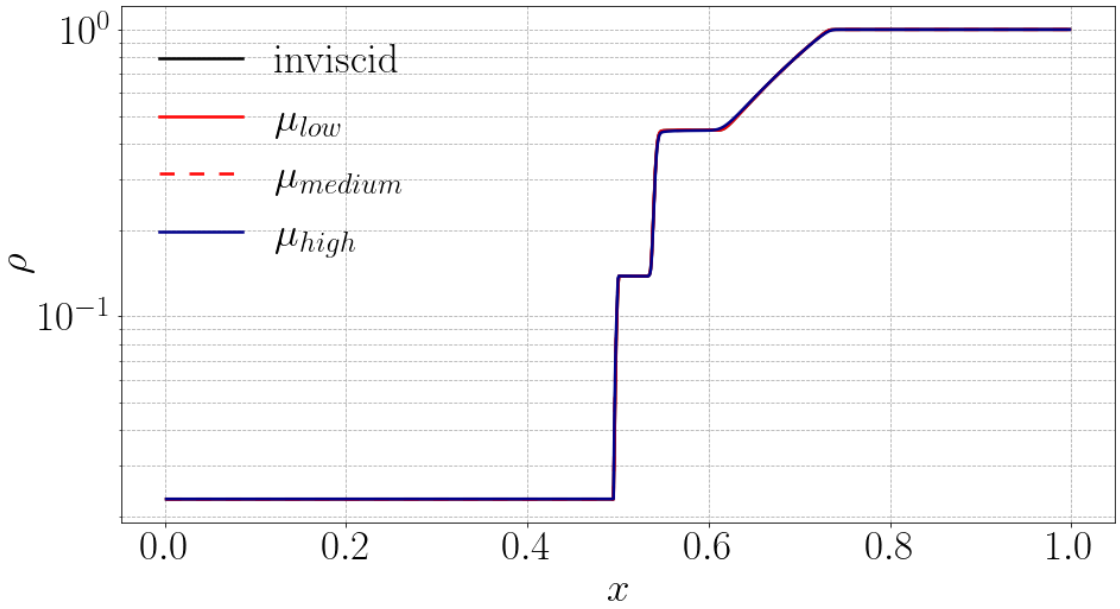


(a)

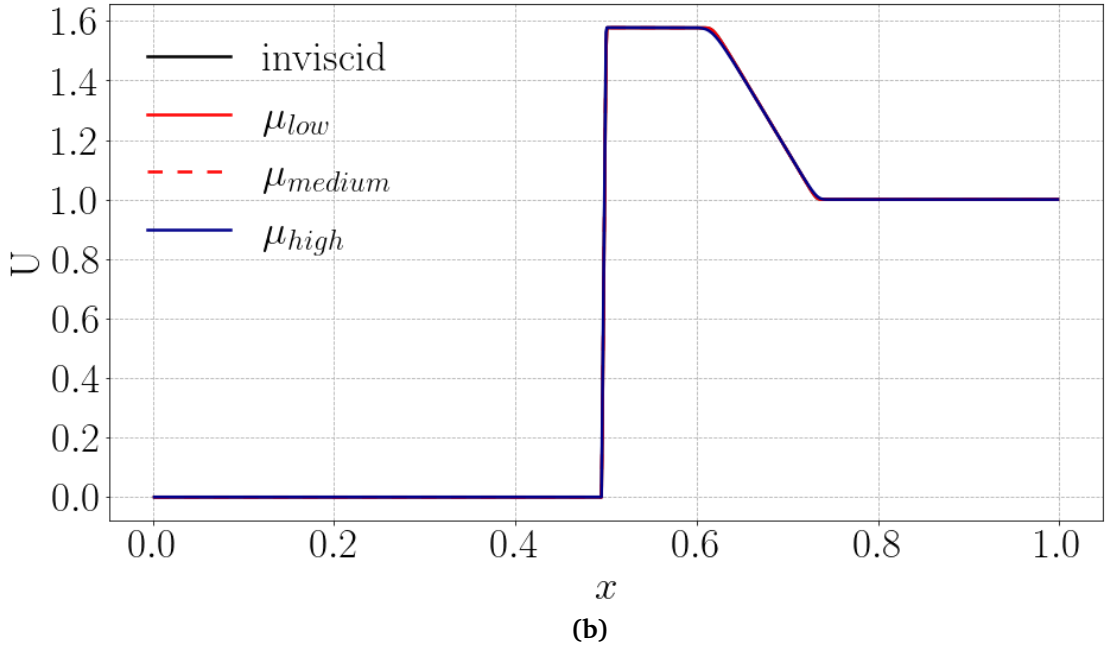


(b)

Figure 5.5: Pressure (a) and temperature (b) predictions at $t = 0.03$ using the BlastFOAM solver, with the ideal gas equation of state for deuterium and the stiffened gas equation of state for PMMA, under inviscid and viscous conditions. The study evaluates three viscous scenarios based on non-dimensionalised viscosity values: μ_{low} with deuterium at a viscosity of 5×10^{-5} and PMMA at 1, μ_{medium} with deuterium's viscosity unchanged and PMMA's increased to 2, and μ_{high}, where deuterium remains at 5×10^{-5} but PMMA's viscosity is raised to 4. The density of deuterium is increased by a factor of 6.25 as compared to the base case shown in figures 5.2 and 5.3.

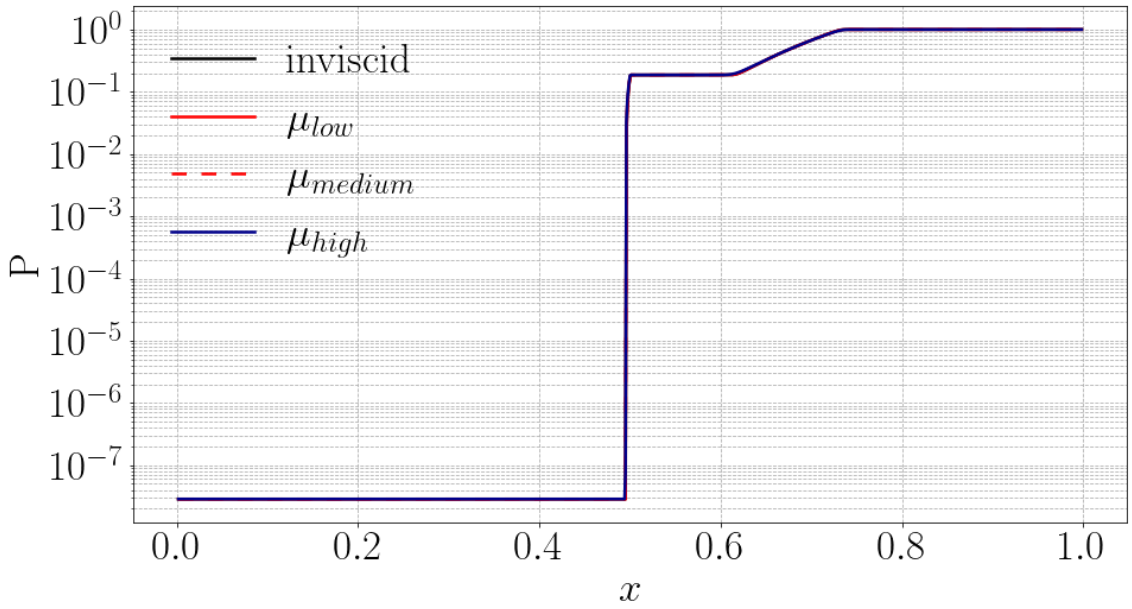


(a)

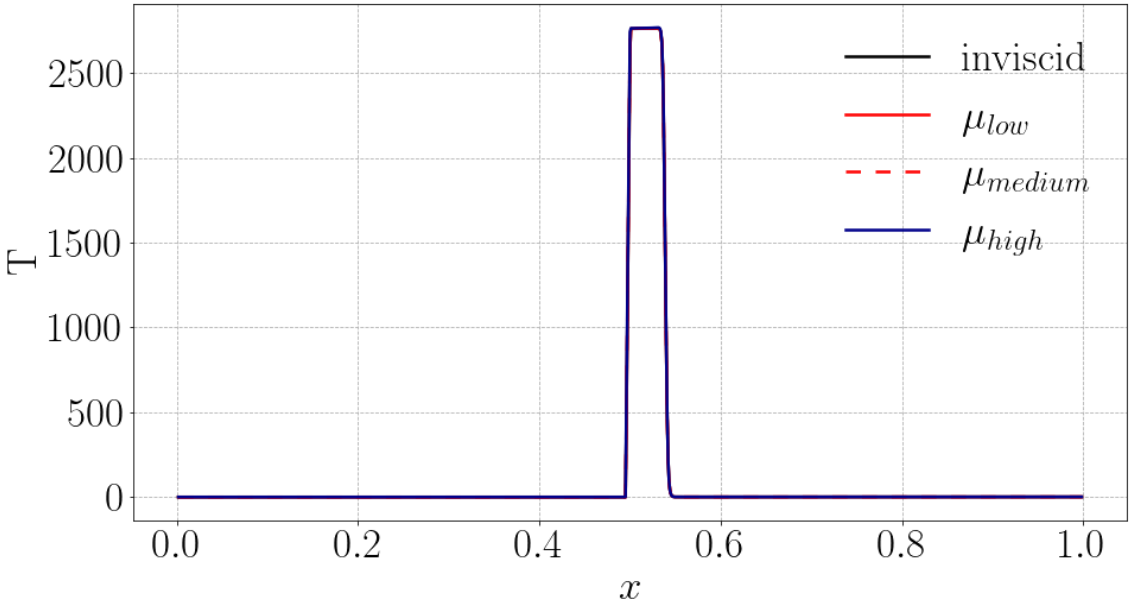


(b)

Figure 5.6: Density (a) and velocity (b) predictions $t = 1.21$using the BlastFOAM solver, with the ideal gas equation of state for deuterium and the stiffened gas equation of state for PMMA, under inviscid and viscous conditions. The study evaluates three viscous scenarios based on non-dimensionalised viscosity values: μ_{low} with deuterium at a viscosity of 5×10^{-5} and PMMA at 1, μ_{medium} with deuterium's viscosity unchanged and PMMA's increased to 2, and μ_{high}, where deuterium remains at 5×10^{-5} but PMMA's viscosity is raised to 4. The density of deuterium is increased by a factor of 625 as compared to the base case shown in Figures 5.2 and 5.3.



(a)



(b)

Figure 5.7: Pressure (a) and temperature (b) predictions at $t = 1.21$ using the BlastFOAM solver, with the ideal gas equation of state for deuterium and the stiffened gas equation of state for PMMA, under inviscid and viscous conditions. The study evaluates three viscous scenarios based on non-dimensionalised viscosity values: μ_{low} with deuterium at a viscosity of 5×10^{-5} and PMMA at 1, μ_{medium} with deuterium's viscosity unchanged and PMMA's increased to 2, and μ_{high}, where deuterium remains at 5×10^{-5} but PMMA's viscosity is raised to 4. The density of deuterium is increased by a factor of 625 as compared to the base case shown in Figures 5.2 and 5.3.

5.1.2 Shock-driven nuclear fusion

Derentowicz et al. [17] studied the generation of thermonuclear fusion neutrons through a shock-wave. The aim of this research was to explore non-traditional methods of neutron generation. The traditional methods typically utilize strong lasers to compress the fuel. Such laser systems are very expensive and complicated as discussed in chapter 2. The idea behind this is that the fusion fuel is heated rapidly by the lasers, and the created plasma is compressed so immensely that it will not have enough time to escape. The plasma is trapped by its own inertial forces before it is burnt in a fusion reaction. The National Ignition Facility (NIF) in Lawrence Livermore National Laboratory is an example of a facility conducting research using laser systems. A schematic illustration of ICF (at NIF) is given in figure 2.2.

Derentowicz et al. [17] explored whether a strong shock can be used to compress the fuel to initiate fusion reaction. Using a shock instead of laser systems could simplify the technology and reduce the costs associated with traditional method such as laser systems. The experiment setup, described in [17], comprises a PMMA layer and a hollow conical region filled with deuterium gas. The system uses a conic liner, where a strong shock wave is generated. This shock wave propagates along the axis to the polyethylene layer, made of PMMA. The PMMA layer is shot into the conical region, where the deuterium gas is compressed. This compression leads to generation of neutrons through thermonuclear fusion. The experimental setup is shown in figure 5.8. The experiment conducted by Derentowicz et al. [17] was the first significant alternative method of ICF. In this experiment, neutrons were obtained by using a pure shock-wave for compressing the fuel generated by an explosion. The authors reported obtaining a neutron emission of the order of 3×10^7 from a mass of 10×10^{-7} g. A detailed description of the experiment can be found in [17].

In their study, Derentowicz et al. [17] did not provide any data on the hydrodynamic parameters such as pressure, temperature, velocity, or density. For this reason, a direct comparison of their experimental results with BlastFOAM's simulations is not possible. BlastFOAM is a pure hydrodynamic simulation tool without any plasma physics libraries. However, considering that the coverslip is made out of PMMA which is a non-Newtonian and visco-elastic material, this chapter studies how the non-Newtonian properties of the coverslip effects the hydrodynamics of the flow. As described in chapter 4.1, BlastFOAM has been further developed in this PhD project to model non-Newtonian though not visco-elastic flows. Therefore this chapter exclusively presents results of a study of the non-Newtonian effects, neglecting the visco-elastic effects under the assumption that visco-elastic effects may be negligible, especially in scenarios involving high temperatures.

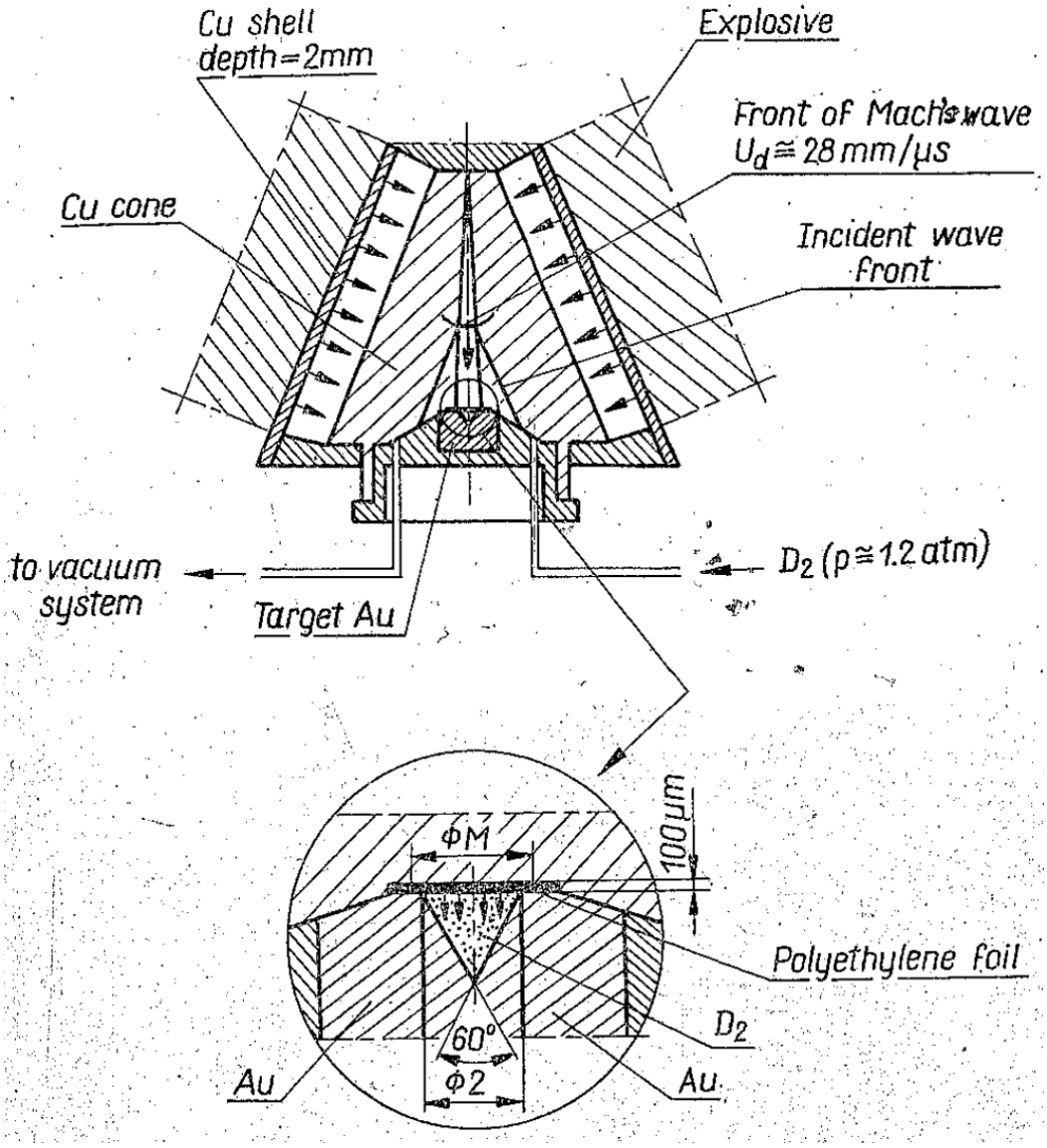


Figure 5.8: Experimental setup as used in explosion-driven thermonuclear fusion experiment by Derentowicz et al. [17]. A Mach wave is generated through explosion. This Mach wave shots the polyethylene foil into the conical region filled with deuterium. The deuterium gas is compressed to achieve neutrons through thermonuclear fusion.

The geometry of the Fusion Target is assumed to be axisymmetrical, as shown in figure 5.8. Based on this assumption, 2-D axisymmetric simulations are performed and the simulation domain is shown in figure 5.9. The simulation domain consists of copper, PMMA, and deuterium but due to the unavailability of an equation of state for gold (Au), the exterior of the Fusion Target is considered to be made of copper instead. It is also assumed that the influence of the exterior of the Fusion Target is negligible. The stiffened gas equation of state, as defined in Eq. 4.16, is used for PMMA and copper, and the ideal gas equation of state is used for deuterium. The shock wave propagates from the copper through the PMMA layer, eventually compressing the deuterium. A density of $0.16\,\text{kg/m}^3$ is used for deuterium, $1150\,\text{kg/m}^3$ for PMMA, and $8950\,\text{kg/m}^3$ for copper. The ambient temperature is $293\,\text{K}$. Copper is treated as an inviscid material, while constant viscosities of 2.5×10^{-4} mPa $\cdot$ s and 5 mPa $\cdot$ s are used for deuterium and PMMA, respectively. The viscosity is non-dimensionlized by the viscosity of the denser material, which is PMMA.

The key parameters of the shock wave are as follows:

- Velocity: $15689\,\text{m/s}$,
- Pressure: $3.536 \times 10^{12}\,\text{Pa}$,
- Density: $24551\,\text{kg/m}^3$,
- Temperature $2700\,\text{K}$.

The shock is initialised in the copper phase, denoted as copper$_s$ in figure 5.9, travels through PMMA, and compresses the deuterium. The dimension of the simulation domain are $1.3\,\text{mm}$ and $2.665\,\text{mm}$ in the radial and axial directions respectively, and a mesh of 800×1600 cells is used. The velocity, pressure, density, and temperature are non-dimensionalised by their respective shock wave values, while the dimensions of the domain are non-dimensionlized by its width.

The Fusion Target simulations are conducted with BlastFOAM using the same scheme numerical schemes as in chapter 4. In figure 5.10, a sudden pressure drop to near-zero values in the 2-D simulation is shown. This pressure drop can be attributed to the formation of a strong rarefaction wave resulting from the substantial density disparity between deuterium and PMMA. This phenomenon has been studied and discussed in a 1-D context within section 3.2.1 and 5.1.1. It is found that increasing the density of deuterium can mitigate this sudden pressure drop. In the 1-D shock-tube study in section 5.1.1, it is found that the viscosity has a substantial impact on the shock properties and the viscous shock propagates faster as compared to the inviscid case. This mechanism results from the shock front being diffusive due to the presence of second-order viscous terms in the momentum and energy equations. The viscous dissipation term in the energy equation converts the kinetic energy of the fluid into heat, which results in higher pressure and temperature behind the shock front, and, ultimately, in a faster shock as compared to the inviscid case.

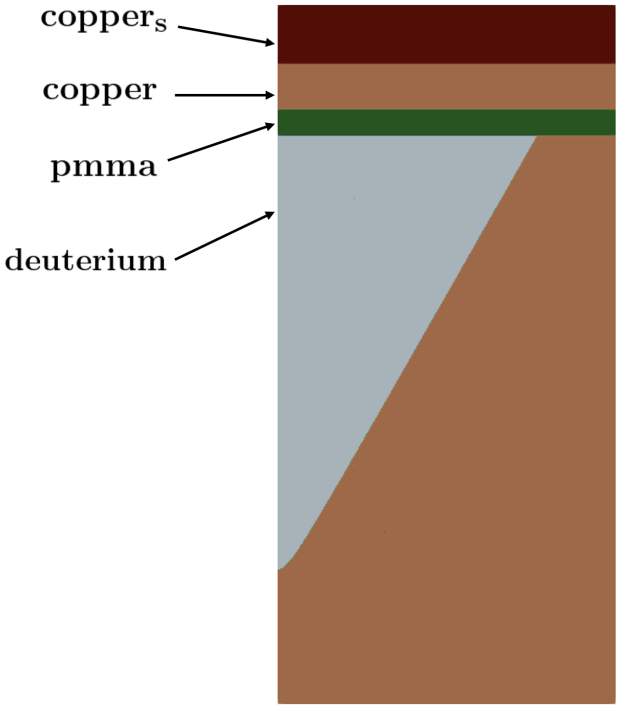


Figure 5.9: Simulation domain as used in BlastFOAM to simulate the Derentowicz et al. [17] experiment.

In figure 5.11, the viscosity of gaseous deuterium is modeled using

$$\mu = \mu_0 \cdot \left(\frac{T}{T_0}\right)^{0.5} \tag{5.1}$$

where μ is the viscosity of the fluid, μ_0 is a reference viscosity under standard conditions, T is the temperature of the fluid, and T_0 is the reference temperature. According to this relation, the viscosity of the gaseous medium clearly increases with temperature which has a substantial impact on the shock properties. An increase in temperature of the shock due to the viscosity of PMMA can lead to a rise in the viscosity of the gaseous deuterium; this, in turn, leads to an increase in viscous dissipation and a further rise in temperature that raises the deuterium viscosity, and so on. This mechanism is clearly evidenced by the widening gap between the inviscid and viscous shock wave profiles as shown in figure 5.11 and 5.12. Furthermore, it is observed that the jets and associated RMI in the inviscid case are further developed as compared to the viscous case.

In chapter 4, a detailed study is conducted to investigate how viscosity affects the development of the RMI and KHI. One of the key findings of this study is that the viscosity dampens the growth of the RMI and KHI. In figure 5.11, it can be observed that although the shock is faster in the viscous fluid compared to the inviscid case, the development of the RMI and KHI is more dampened in the viscous case. In figure 5.13 a constant viscosity model is used for PMMA and deuterium, unlike the scenario

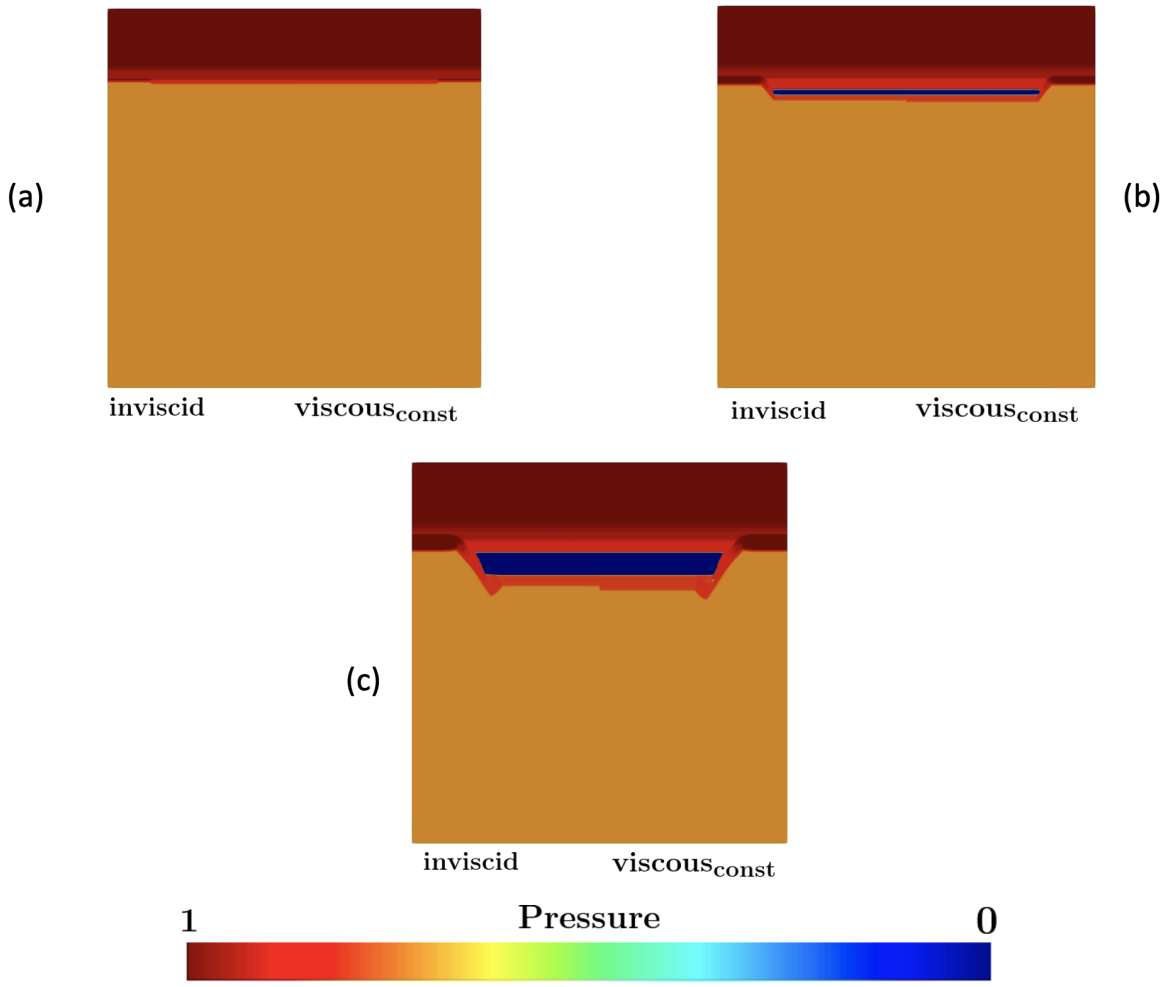


Figure 5.10: Comparison of inviscid and viscous cases, where a constant viscosity is applied to deuterium and PMMA. figures (a), (b), and (c) display pressure at 0.13, 0.152, and 0.19, respectively. This scenario is considered the base case; the densities for deuterium and PMMA align with the original base case, as demonstrated in figures 5.2 and 5.3.

shown in figure 5.11 and 5.12 where only the viscosity of PMMA is kept constant, but the viscosity of the deuterium increases with temperature using equation 5.1. It can be observed that in the case where the viscosity of deuterium does not increase with temperature (see figure 5.13), the viscous shock still propagates faster compared to the inviscid case. However, the difference between the inviscid and viscous cases is not as pronounced as in the scenario where the viscosity of deuterium increases with temperature, as shown in 5.11 and 5.12.

In figure 5.14 two cases are compared: one where the viscosity of deuterium is held constant, denoted as viscous$_{const}$, and the other where the viscosity of deuterium increases with temperature, denoted as viscous$_T$. It is clearly evident that in the case where the viscosity of deuterium increases with temperature, the shock propagates faster compared to the case where the viscosity of deuterium is held constant. Fur-

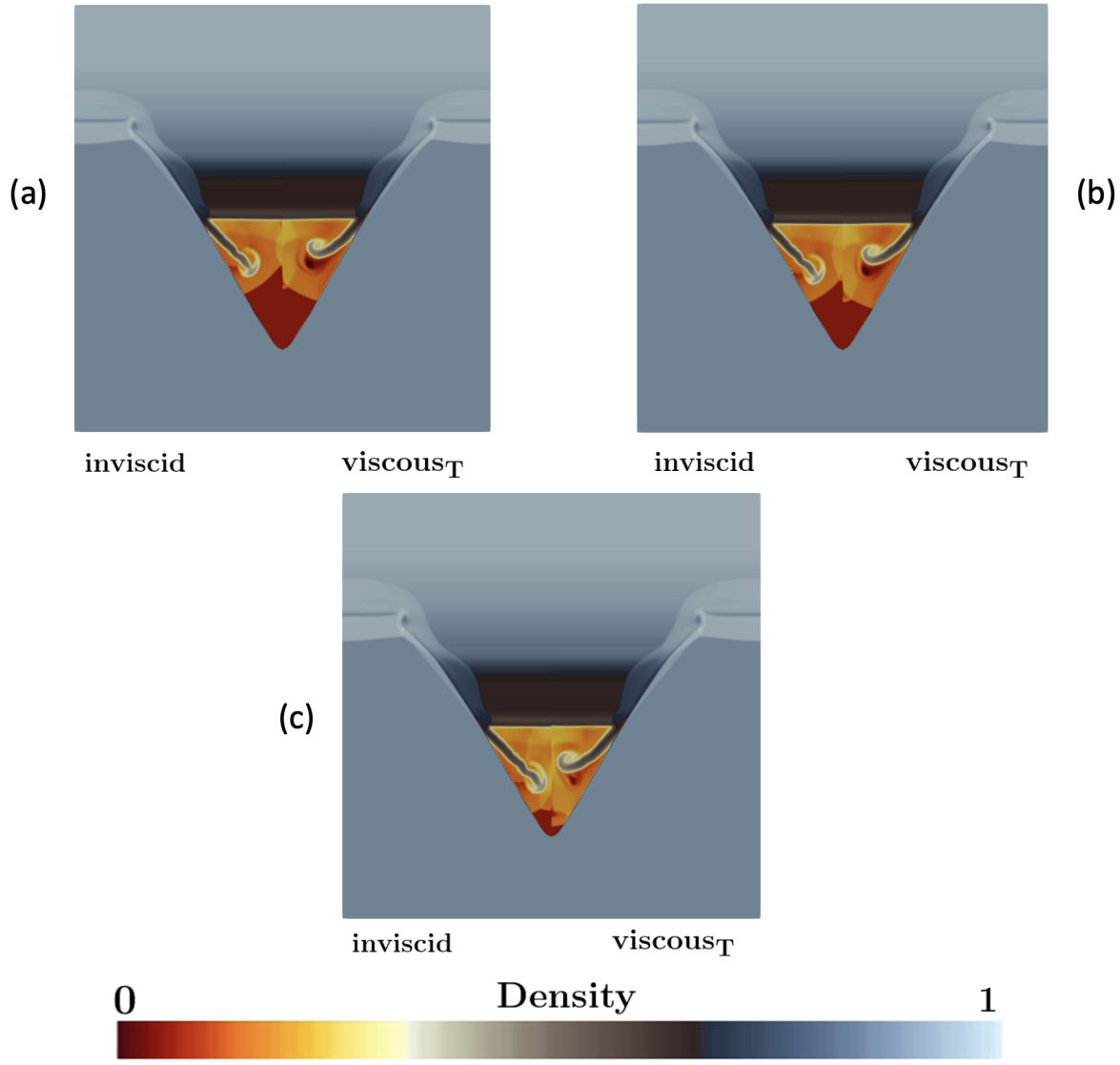


Figure 5.11: Comparison of inviscid and viscous cases, with a constant dynamic viscosity for PMMA and temperature-dependent viscosity for deuterium, as described by equation 5.1. figures (a), (b), and (c) display densities at 0.3, 0.32, and 0.34. This scenario is considered the base case; the densities for deuterium and PMMA align with the original base case, as shown in figures 5.2 and 5.3.

thermore, as a result of increasing viscosity with increasing temperature, the RMI and KHI are more damped in the case where the deuterium viscosity increases with temperature.

As already discussed in section 5.1.1, the large density disparity between deuterium and PMMA leads to a strong rarefaction wave, which leads to a sudden pressure drop. In the 2-D axisymmetric simulation, this abrupt pressure drop is shown in figure 5.10. The density of deuterium is increased by a factor of 625 to mitigate the sudden pressure drop to near-zero values, as done in the 1-D shock-tube simulation (section 5.1.1, figure 5.7). This increase of deuterium density also allows to mitigate the sudden pressure drop in the 2-D axisymmetric simulation, as shown in figure 5.15. In figure 5.16 the effect of viscosity on shock dynamics is investigated in a case where the density of deuterium is increased by a factor of 625. Although the shock in the viscous fluid propagates faster as compared to the inviscid case, the gap between the shock in the inviscid fluid and the viscous one is smaller as compared to the cases in figures 5.12, 5.13, and 5.14. As already discussed in the previous sections, increasing the deuterium density allows to mitigate the sudden pressure drop observed with large density jumps but it also weakens the effects of viscosity on shock dynamics as shown in figures 5.2-5.7 for the 1-D shock tubes. In figure 5.16, two cases are compared: one with a lower constant PMMA non-dimensionlized viscosity of 2, and the other with a higher viscosity of 4. It can be observed that the case with the higher viscosity has a wider gap between the inviscid and viscous scenarios compared to the case with the lower viscosity. This would result in a faster shock reaching the tip of the cone earlier as compard to the inviscid case. In adittion to this, higher viscosity will dampen the development of the RMI and KHI, resulting in less mixing.

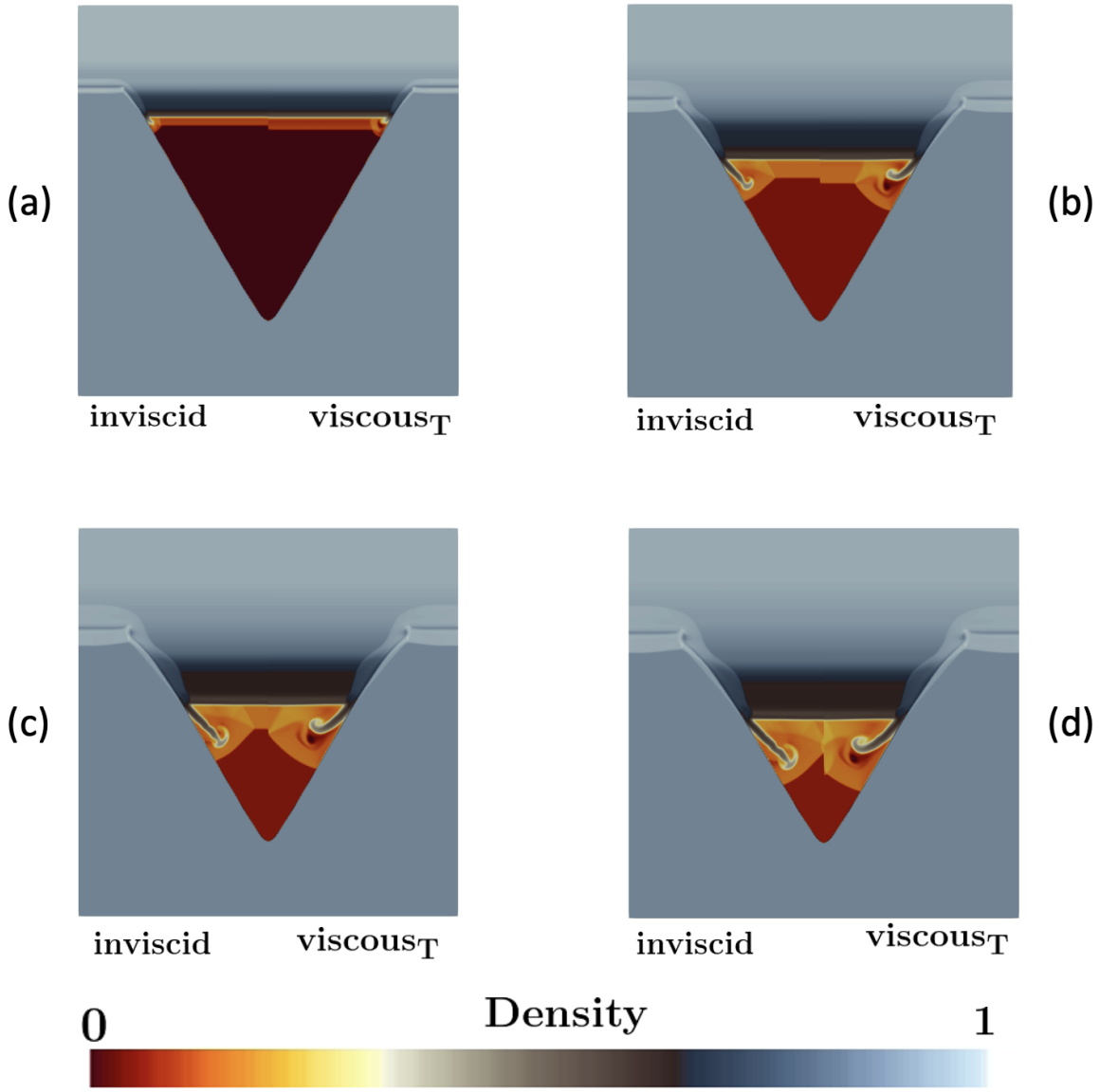


Figure 5.12: Comparison of inviscid and viscous case at, with a constant dynamic viscosity for PMMA and temperature-dependent viscosity for deuterium, as described by equation 5.1. figures (a), (b), (c) and (d) display densities at 0.2, 0.25, 0.28 and 0.3. This scenario is considered the base case; the densities for deuterium and PMMA align with the original base case, as shown in figures 5.2 and 5.3.

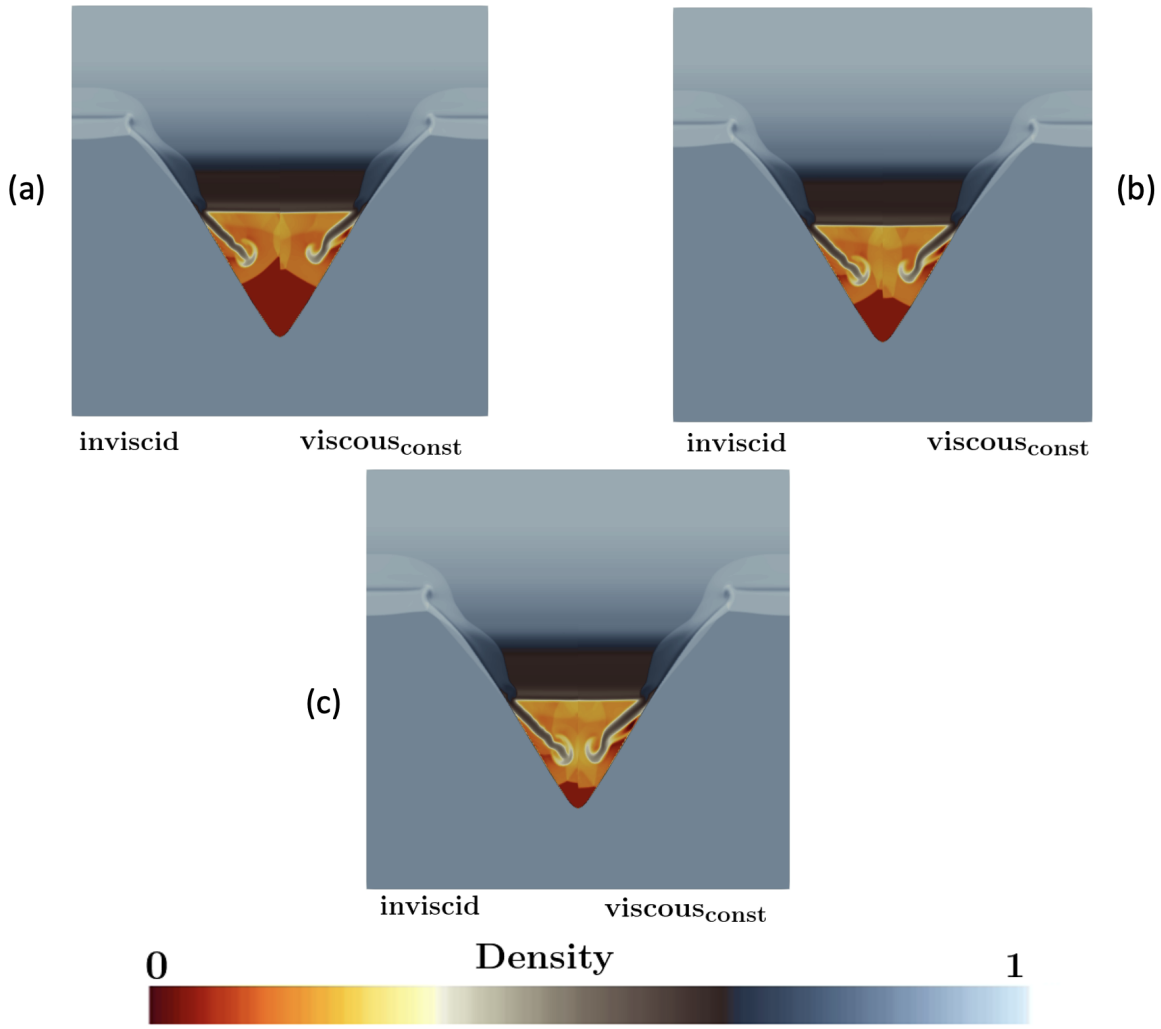


Figure 5.13: Comparison of inviscid and viscous cases, with a constant dynamic viscosity for deuterium and PMMA. figures (a), (b), and (c) display densities at 0.3, 0.32, and 0.34. This scenario is considered the base case; the densities for deuterium and PMMA align with the original base case, as shown in figures 5.2 and 5.3.

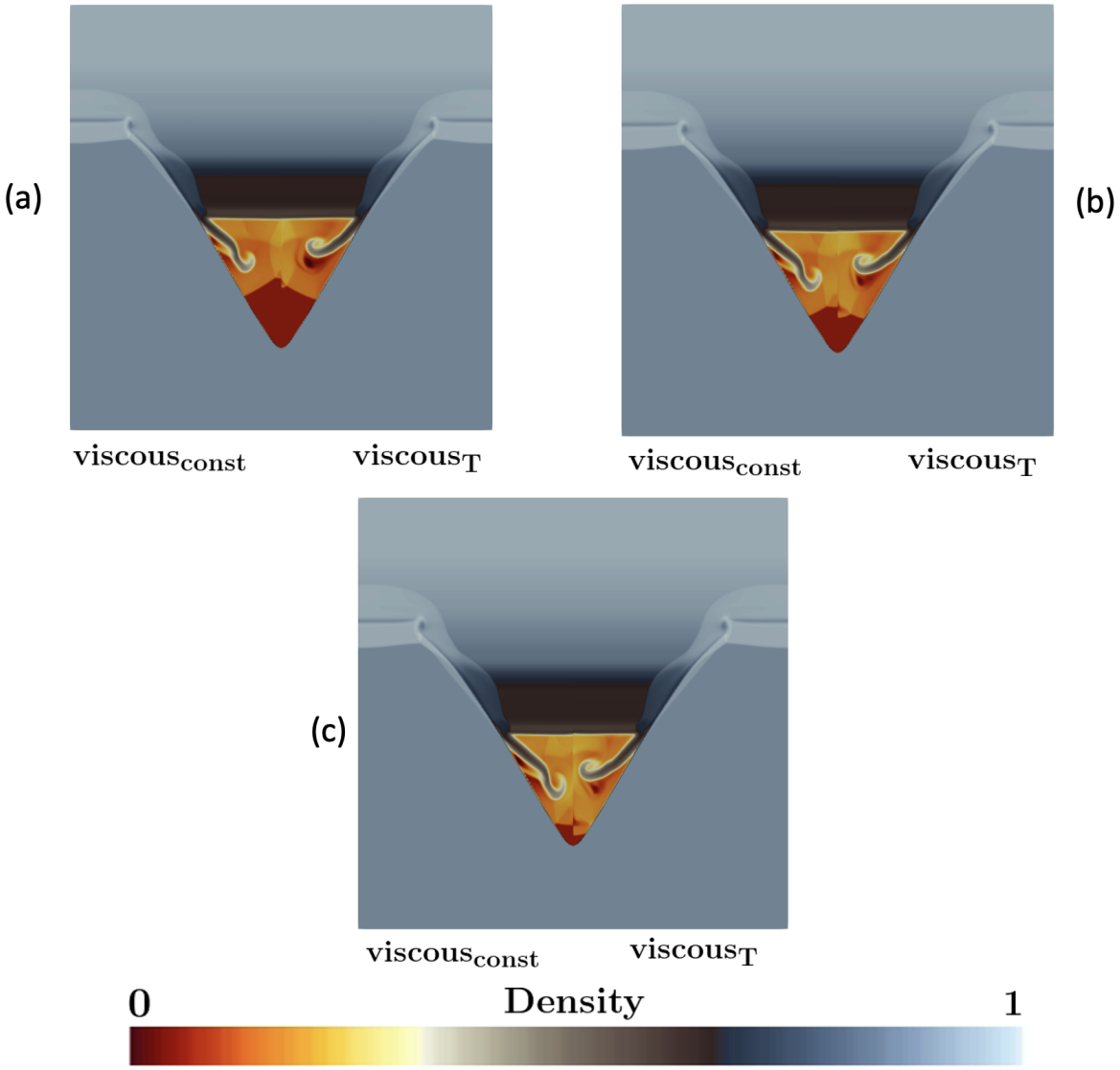


Figure 5.14: Comparison of two viscous scenarios: one with a constant dynamic viscosity for both deuterium and PMMA, denoted as *viscous_const*, and another where a constant dynamic viscosity is used for deuterium while a temperature-dependent viscosity is applied for PMMA. figures (a), (b), and (c) display densities at 0.3, 0.32, and 0.34, respectively. This scenario is considered the base case; the densities for deuterium and PMMA align with the original base case, as demonstrated in figures 5.2 and 5.3.

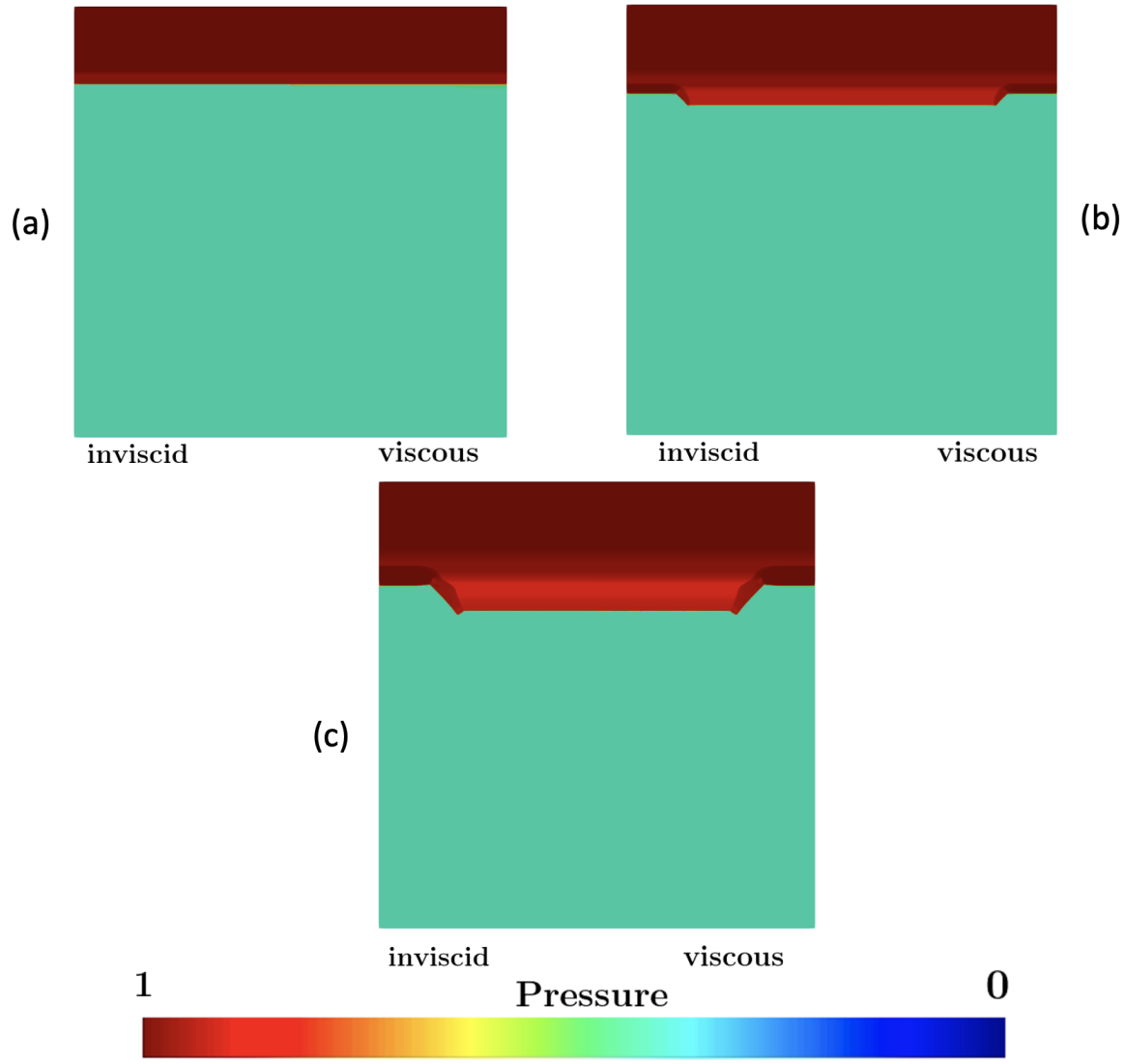


Figure 5.15: Comparison of inviscid and viscous cases at, where a constant viscosity is applied to deuterium and PMMA . figures (a), (b), and (c) display pressure at 0.13, 0.152, and 0.19, respectively. In this case the density of deuterium is increased by a factor of 625 compared to the base case as shown in the 1D simulation in figures 5.2 and 5.3 and 2-D simulation in 5.10.

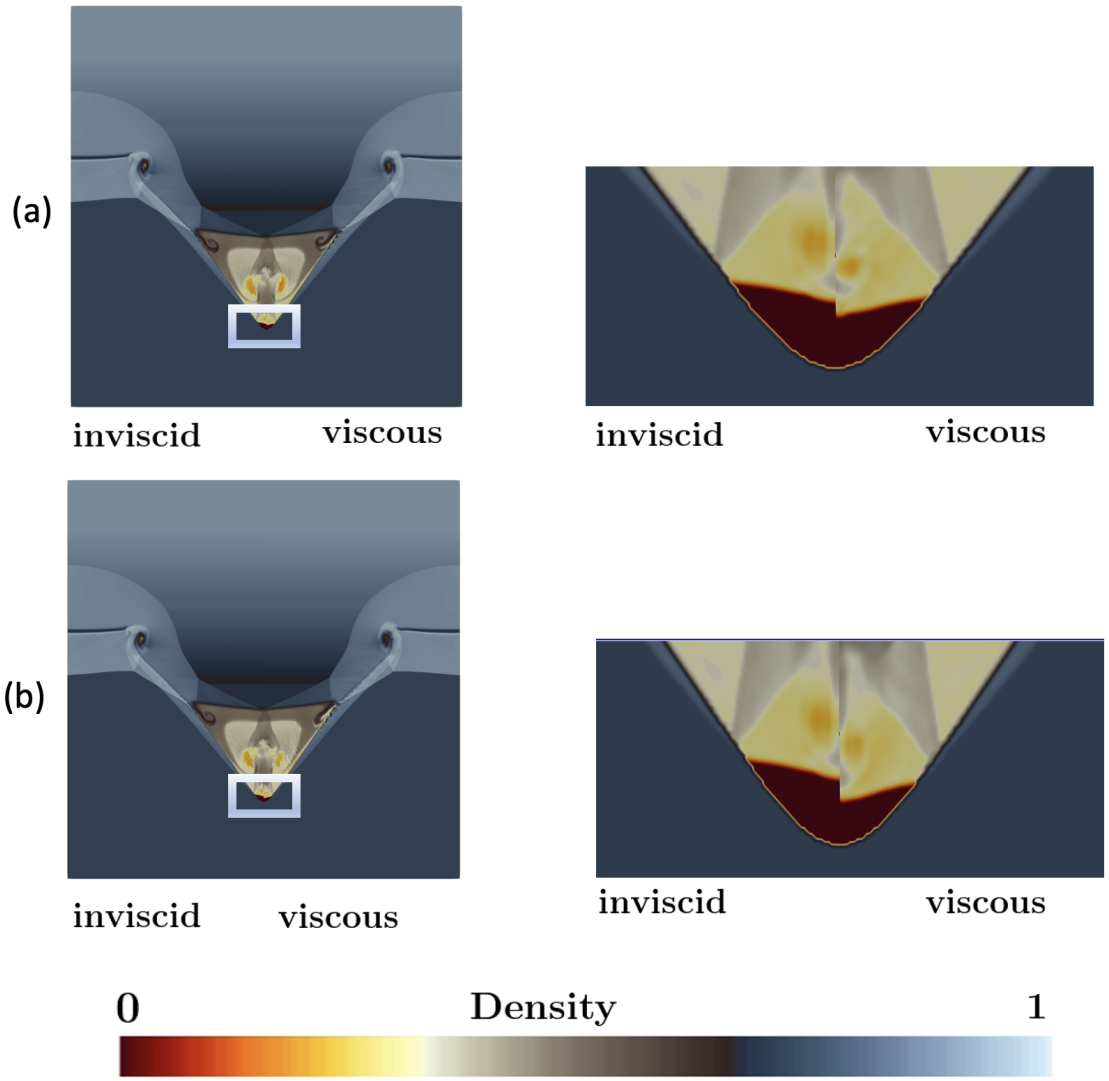


Figure 5.16: Comparison of the inviscid case with two viscous scenarios at $t = 0.5$: In (a), a constant non-dimensional dynamic viscosity of 5×10^{-6} is applied to deuterium, and a non-dimensional dynamic viscosity of 2 is applied to PMMA. In figure (b), a non-dimensional dynamic viscosity of 5×10^{-6} is used for deuterium, and a non-dimensional dynamic viscosity of 4 is used for PMMA.

5.2 Effect of material properties

This section examines the dependence of the patterns observed in the figures discussed in the foregoing, jet formation and roll-up phenomena in particular, on the properties of the materials involved in the setup shown in figure 5.9, which depicts the computational analogue of the experimental set up used by Derentowicz et al. [17]. This system was also studied by Chapman et al. [68] who used a front-tracking method and explored the impact of flux-limited thermal conduction on the fusion performance of uniaxially-driven targets. As shown in the previous sub-section, when the shock impacts the PMMA-deuterium interface, initial perturbations develop into RMI, followed by KHI. As discussed in chapter 4, the baroclinic voriticity growth mechanism plays a major role in driving disturbance growth, and there are additional mechanisms if non-Newtonian material properties are taken into account.

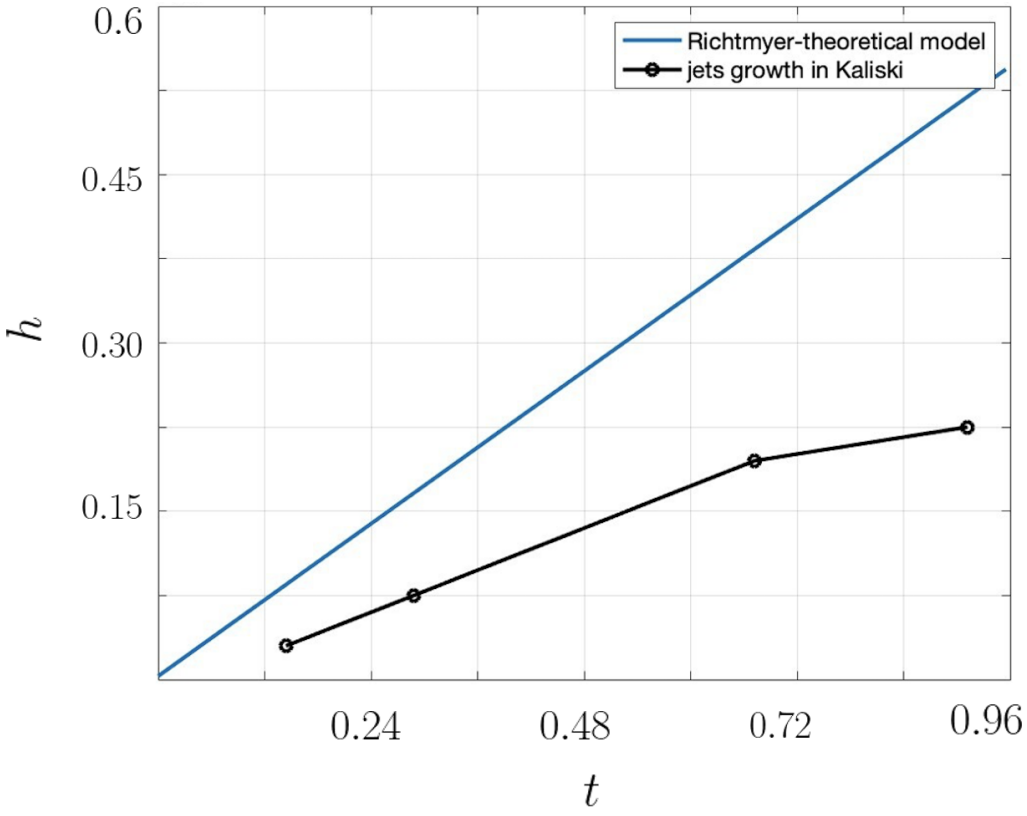


Figure 5.17: Comparison of amplitude predictins by Richtmyer model [13] and the RMI growth in BlastFOAM's simulation using ideal gas equation of state for deuterium and stiffened gas equation of state for copper and PMMA.

The figure 5.17 compares the numerical predictions with those obtained from the theory of Richtmyer, equation 4.20 [13], which demonstrates that the growth rates are of similar magnitudes (although it is well known that the Richtmyer theory over-predicts the growth rates at large Mach numbers). This provides reasonable confirmation that the flow dynamics discussed in the previous sub-section are driven by vorticity formation mechanisms; based on the results presented in chapter 4, it can also be assumed that the viscosity will act to damp out the instabilities. This is confirmed by inspection of Figures 5.18 - 5.21 wherein the RMI development is shown for flow situations in which copper is treated as inviscid, deuterium as a Newtonian fluid, and PMMA as a BCY fluid, described by equation 4.18 neglecting the temperature effects on the viscosity by setting $a_T = 0$. Three cases are discussed: the inviscid case, and two additional cases corresponding to two values of the large-shear rate viscosity limit. It is clear that the high viscosity case exhibits the smallest instability growth as is also shown in figures 5.20, 5.21, 5.22 and 5.23, which depict the flow characteristics at more advanced stages of the dynamics. This is in line with the findings presented in chapter 4 which highlighted the destabilising role of non-Newtonian rheology, and the stabilising influence of the residual viscosity.

Figures 5.26, 5.27, and 5.28 demonstrate that the viscous cases maintain stable temperature, pressure, and density for a longer period of time after the compression of deuterium, in contrast to the inviscid case. In the inviscid scenario, the mixing initiated by the development of the RMI and KHI lead to more rapid variations in the flow variables. The dynamics of RMI- (and KHI-) driven mixing and its impact on these variables can be significant for nuclear fusion as fusion reactions depend on keeping the pressures stable at high values. It is also very important in ICF to maintain a self-sustaining burn wave to achieve ignition. However, the development of RMI-induced mixing could lead to cooling of the fuel and disruption of the symmetry of the implosion. Reducing the growth of the RMI can therefore be beneficial for the fusion process. Insights gained from the present study suggest that using a coverslip material that has a higher viscosity can dampen the development of the RMI and reduce the mixing. This can help to sustain the pressure, temperature and density for a longer period of time as compared to the case where the coverslip material is considered to be inviscid. This will be discussed next.

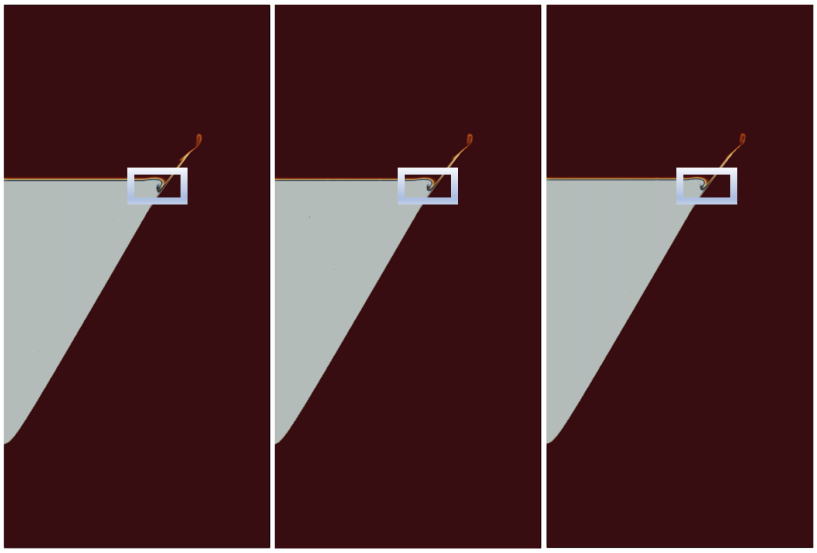


Figure 5.18: Comparison of an inviscid case with two viscous cases at $t = 0.241$ displaying the volume fraction of deuterium. figure (a) represents the inviscid case, (b) the low viscosity case, and (c) the high viscosity case. The ideal gas equation of state is used for deuterium, and the stiffened gas equation of state is used for PMMA and copper. Copper is treated as inviscid in all cases, and PMMA is modelled with the BCY model 4.18.

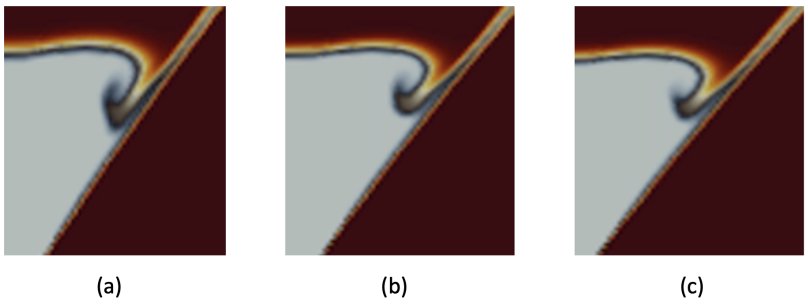


Figure 5.19: Zoomed-in comparison of an inviscid case with two viscous cases from figure 5.18.

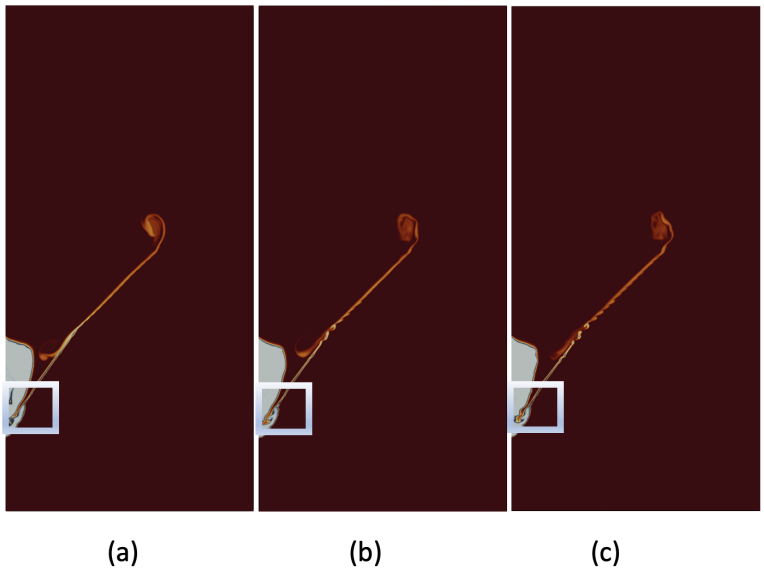


Figure 5.20: Comparison of an inviscid case with two viscous cases $t = 0.63$ displaying the volume fraction of deuterium. figure (a) represents the inviscid case, (b) the low viscosity case, and (c) the high viscosity case. The ideal gas equation of state is used for deuterium, and the stiffened gas equation of state is used for PMMA and copper. Copper is treated as inviscid in all cases, and PMMA is modelled with the BCY model 4.18.

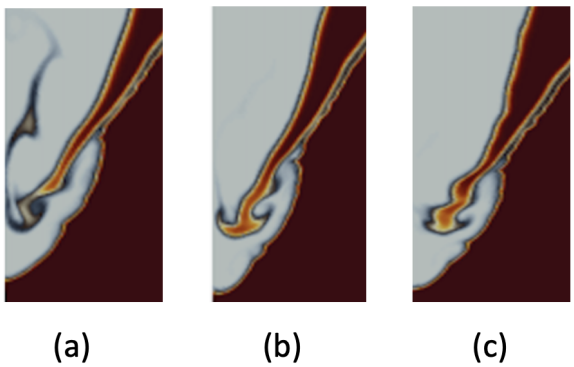


Figure 5.21: Zoomed-in comparison of an inviscid case with two viscous cases from figure 5.20

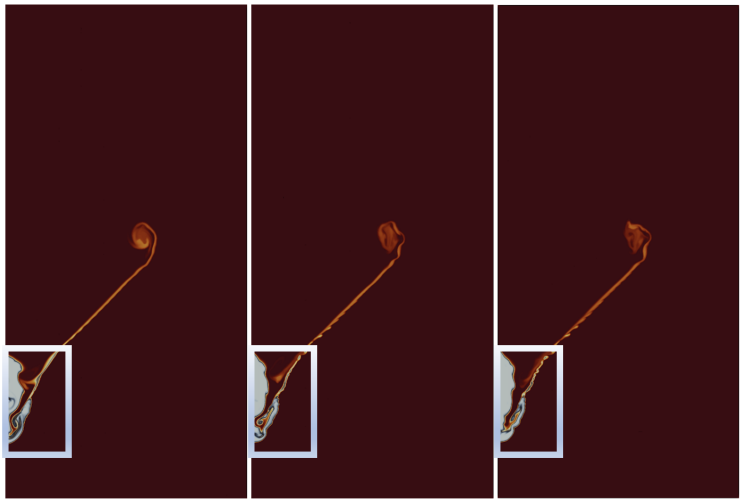


Figure 5.22: Comparison of an inviscid case with two viscous cases at $t = 0.664$ displaying the volume fraction of deuterium. figure (a) represents the inviscid case, (b) the low viscosity case, and (c) the high viscosity case. The ideal gas equation of state is used for deuterium, and the stiffened gas equation of state is used for PMMA and copper. Copper is treated as inviscid in all cases, and PMMA is modelled with the BCY model 4.18.

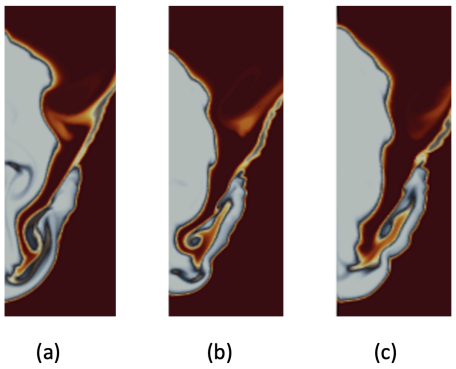


Figure 5.23: Zoomed-in comparison of an inviscid case with two viscous cases from figure 5.22

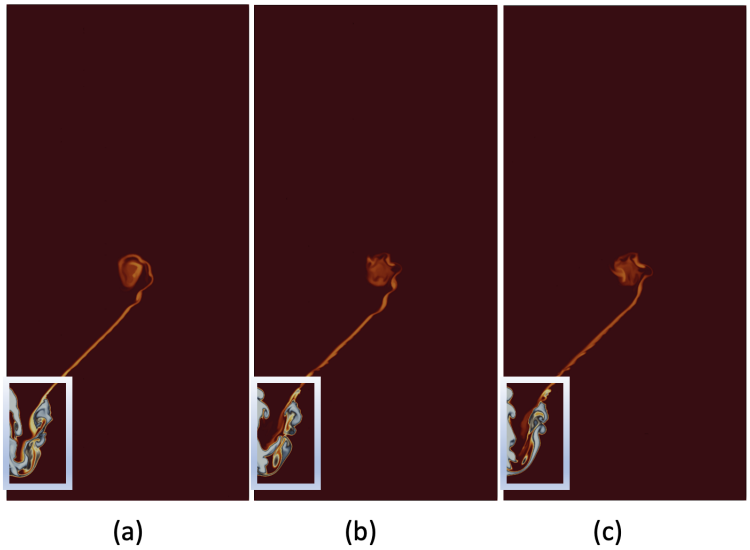


Figure 5.24: Comparison of an inviscid case with two viscous cases $t = 0.772$ displaying the volume fraction of deuterium. figure (a) represents the inviscid case, (b) the low viscosity case, and (c) the high viscosity case. The ideal gas equation of state is used for deuterium, and the stiffened gas equation of state is used for PMMA and copper. Copper is treated as inviscid in all cases, and PMMA is modelled with the BCY model 4.18.

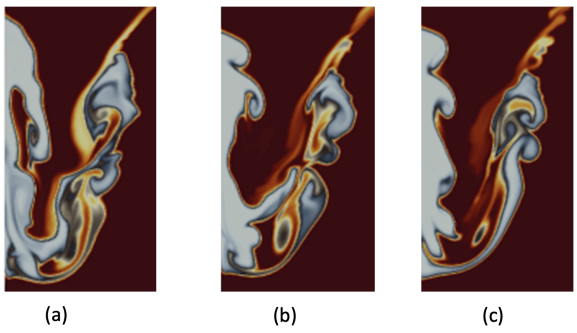


Figure 5.25: Zoomed-in comparison of an inviscid case with two viscous cases from figure

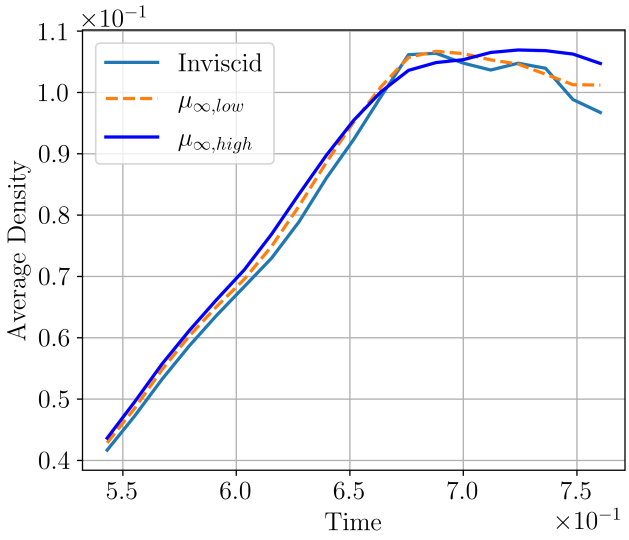


Figure 5.26: Comparison of area-averaged deuterium density predictions using the ideal gas equation of state for deuterium and the stiffened gas equation of state for copper and PMMA. Predictions are categorized by the viscosity models: inviscid, low viscosity (denoted as $\mu_{\infty,\text{low}}$), and high viscosity (denoted as $\mu_{\infty,\text{high}}$). Copper is treated as inviscid in all scenarios. For viscous cases, the BCY model (see equation 4.18) is applied to PMMA.

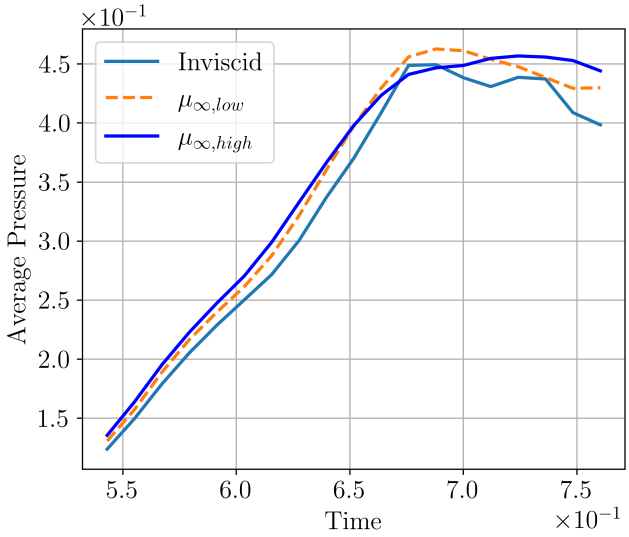


Figure 5.27: Comparison of area-averaged deuterium pressure predictions using the ideal gas equation of state for deuterium and the stiffened gas equation of state for copper and PMMA. Predictions are categorized by the viscosity models: inviscid, low viscosity (denoted as $\mu_{\infty,\text{low}}$), and high viscosity (denoted as $\mu_{\infty,\text{high}}$). Copper is treated as inviscid in all scenarios. For viscous cases, the BCY model (see equation 4.18) is applied to PMMA.

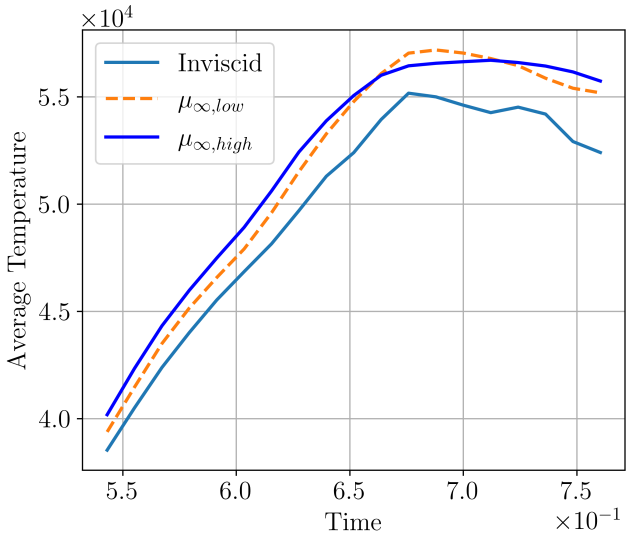


Figure 5.28: Comparison of area-averaged temperature pressure predictions using the ideal gas equation of state for deuterium and the stiffened gas equation of state for copper and PMMA. Predictions are categorized by the viscosity models: inviscid, low viscosity (denoted as $\mu_{\infty,\text{low}}$), and high viscosity (denoted as $\mu_{\infty,\text{high}}$). Copper is treated as inviscid in all scenarios. For viscous cases, the BCY model (see equation 4.18) is applied to PMMA.

5.3 Impact of Coverslip on RMI

In this section, the impact of different configurations of the coverslip on mixing and compression processes is studied; five different cases are studied, as shown in figure 5.29. In case a, the coverslip is made of PMMA and has the original thickness; in case b, there is no coverslip, instead, the coverslip is made of deuterium to investigate how the RMI will develop. In case c, the coverslip is made of PMMA, but its thickness is half of that considered in case a. In cases d and e, the coverslip is made up of two different materials, PMMA and PVC, but in two different configurations as shown in figure 5.29. This study aims to investigate the relationship between material properties and their impact on pressure, density, and temperature.

In case b (with no coverslip), the development of the RMI is observed at the boundary between the copper and deuterium interface, where a density gradient exists and grows into the copper phase, as shown in figures 5.30- 5.37. This growth is primarily driven by a baroclinic mechanism related to the misalignment between the density and pressure fields. In cases a and c, it is observed that due to the reduced thickness of the PMMA coverslip in case c, the shock wave travels slower compared to the original thickness in case a. A coverslip of greater thickness has higher rigidity due to its larger resistance to deformation, which leads to a more rapid transmission of waves through the material.

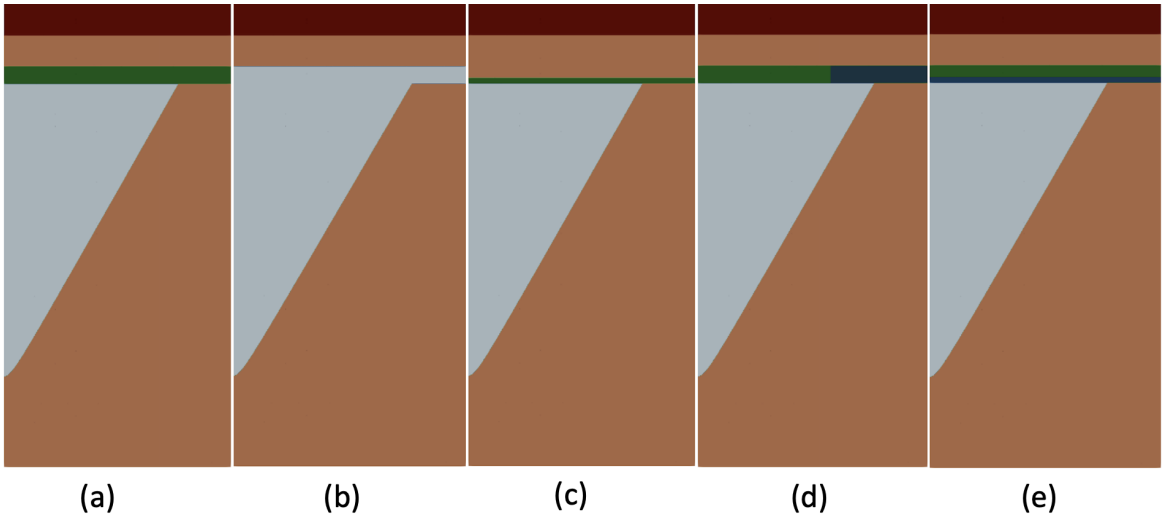


Figure 5.29: Domain of 5 different case with different configurations of coverslips as used in BlastFOAM

The initial development of two Richtmyer-Meshkov instabilities (RMIs) in case d, due to the shock wave's interaction with the coverslip made of PMMA and PVC, strongly indicates that the observed jets are vorticity-driven RMIs. figures 5.30 (d) and 5.31 (d) show that the two RMIs develop at the interface between PMMA/PVC and PMMA/deuterium. A gradient is present at the interface between PMMA/deuterium and PVC/PMMA. When the shock impacts these two interfaces, due to the present

gradient, vorticity is generated, resulting in the development of two RMIs. As the process progresses, these two RMIs merge, as can be seen in figures 5.32-5.35. Figures 5.38, 5.39 and 5.40 shows the area-averaged density, pressure, and temperature of deuteriumto investigate how the coverslip configuration impacts these flow variables, which can be critical for a fusion reaction. Inspection of these figures suggests that case c, with the thinner coverslip, results in the lowest predictions of pressure, density, and temperature, whereas in other instances, these variables maintain a similar range. A coverslip composed of two materials, such as PMMA and PVC, can pose manufacturing challenges. A thicker coverslip is preferable for achieving robust compression characterised by elevated and stable pressures. Moreover, as studied in the previous section, viscosity plays an important role in mitigating the development of vorticity, which in turn, suppresses the RMI. Reducing the growth of RMI can result in diminished mixing, thereby leading to stable flow variables after compression for a longer period of time. Thus, this work has provided the insights needed for the inclusion of a coverslip, and its design, to maintain high pressures and densities, and for the choice of material properties to suppress, as far as possible, the onset and development of the RMI (and KHI) to minimise mixing that can be detrimental to fusion.

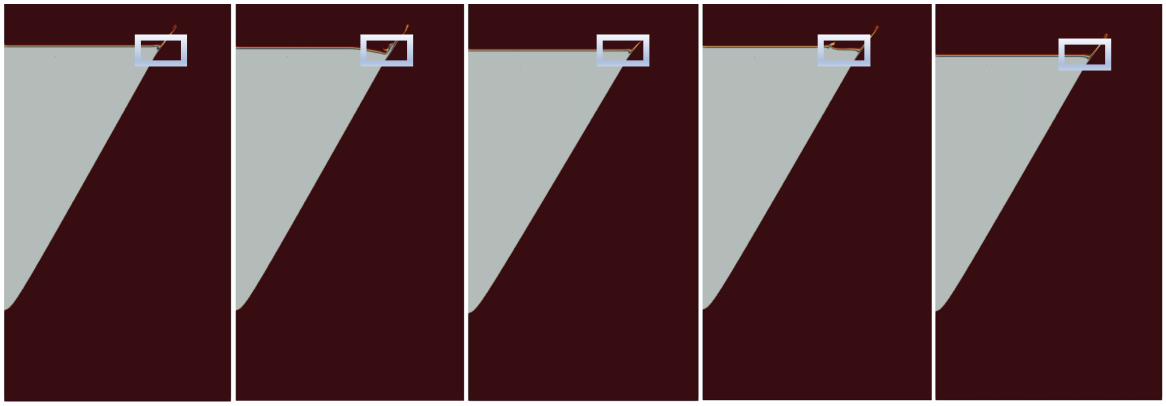


Figure 5.30: Comparison of cases a, b, c, d, and e at $t = 0.16$, displaying the volume fraction of deuterium. case a represents the original scenario. In case b, the coverslip is substituted with deuterium. In case c, the thickness of deuterium is reduced by half. In case d, the coverslip is composed of a different configuration, made up of PMMA/PVC. In case e, the coverslip is made from a different configuration, specifically PMMA/PVC. All cases are treated as inviscid, using the ideal gas equation of state for deuterium, and the stiffened gas equation of state is applied to PMMA, PVC, and copper.

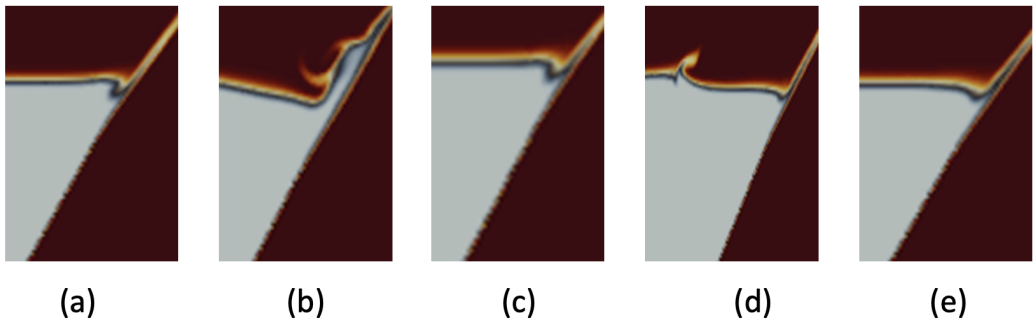


Figure 5.31: Zoomed-in comparison of cases a, b, c, and d at $t = 0.16$ from figure 5.30.

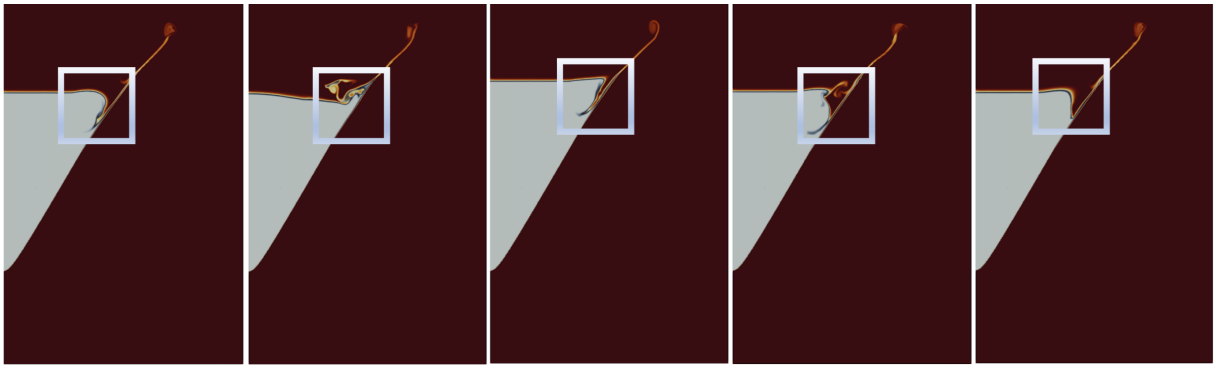


Figure 5.32: Comparison of cases a, b, c, d, and e at $t = 0.338$, displaying the volume fraction of deuterium. Case a represents the original scenario. In case b, the coverslip is substituted with deuterium. In case c, the thickness of deuterium is reduced by half. In case d, the coverslip is composed of a different configuration, made up of PMMA/PVC. In case e, the coverslip is made from a different configuration, specifically PMMA/PVC. All cases are treated as inviscid, using the ideal gas equation of state for deuterium, and the stiffened gas equation of state is applied to PMMA, PVC, and copper.

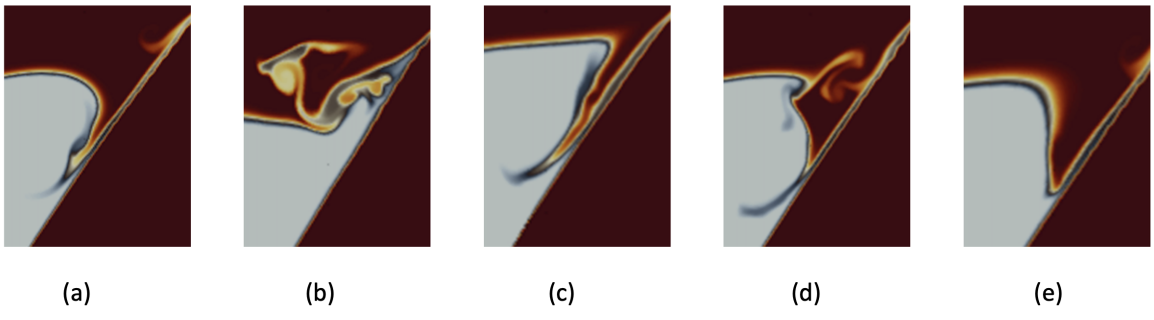


Figure 5.33: Zoomed-in comparison of cases a, b, c, and d at $t = 0.338$ from Figure 5.32.

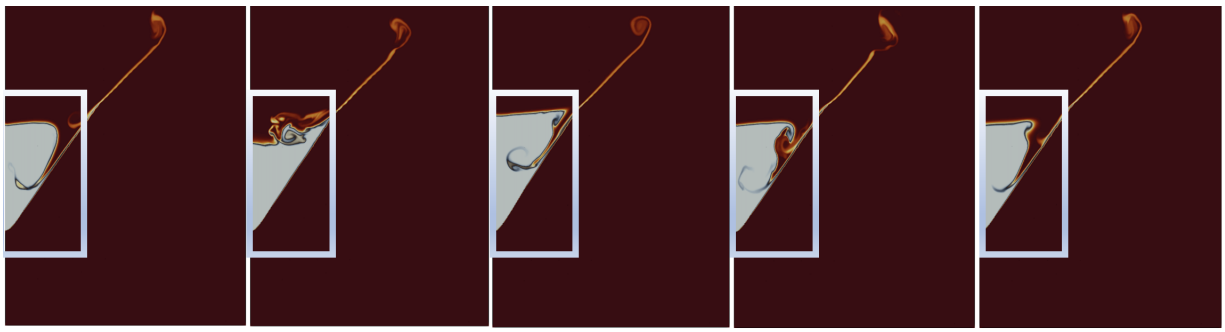


Figure 5.34: Comparison of cases a, b, c, d, and e at $t = 0.48$, displaying the volume fraction of deuterium. Case a represents the original scenario. In case b, the coverslip is substituted with deuterium. In sase c, the thickness of deuterium is reduced by half. In case d, the coverslip is composed of a different configuration, made up of PMMA/PVC. In case e, the coverslip is made from a different configuration, specifically PMMA/PVC. All cases are treated as inviscid, using the ideal gas equation of state for deuterium, and the stiffened gas equation of state is applied to PMMA, PVC, and copper.

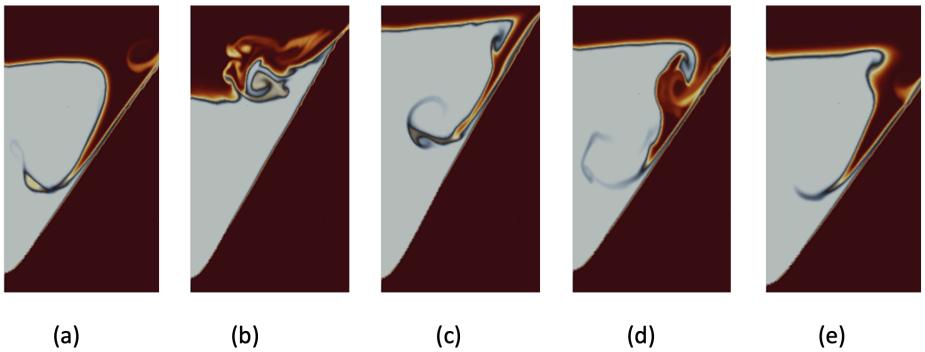


Figure 5.35: Zoomed-in comparison of cases a, b, c, and d at $t = 0.48$ from Figure 5.32.

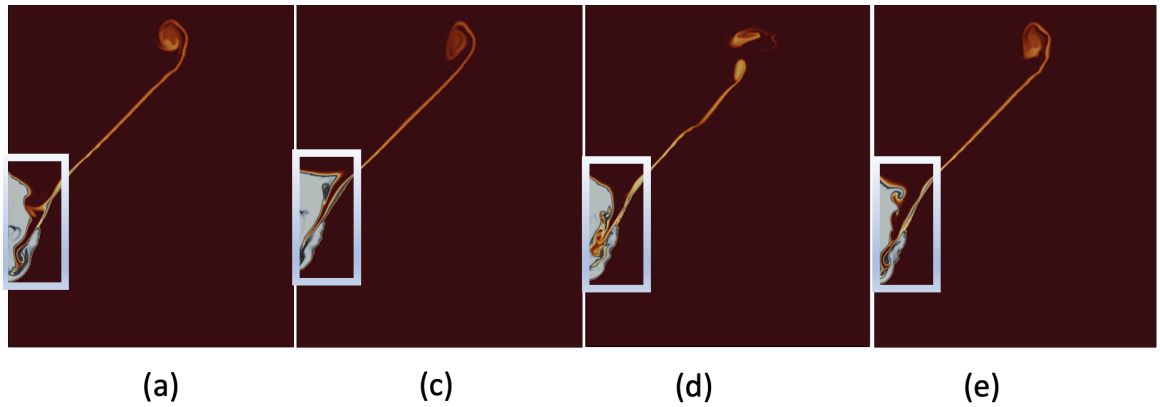


Figure 5.36: Comparison of cases a, c, d, and e at $t = 0.664$, displaying the volume fraction of deuterium. Case a represents the original scenario. In case c, the thickness of deuterium is reduced by half. In case d, the coverslip is composed of a different configuration, made up of PMMA/PVC. In case e, the coverslip is made from a different configuration, specifically PMMA/PVC. All cases are treated as inviscid, using the ideal gas equation of state for deuterium, and the stiffened gas equation of state is applied to PMMA, PVC, and copper.

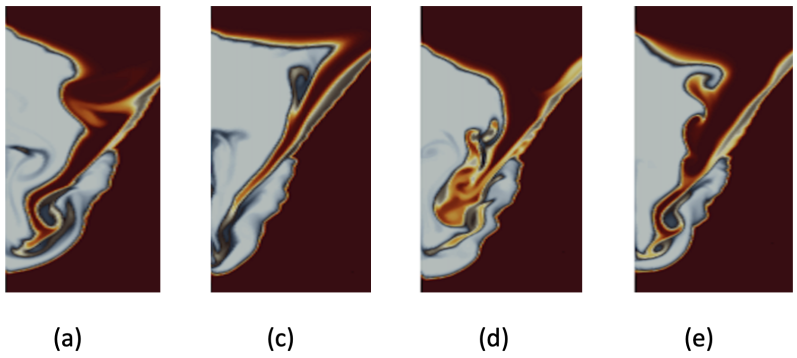


Figure 5.37: Zoomed-in comparison of cases a, c, and d at $t = 0.664$ from Figure 5.32.

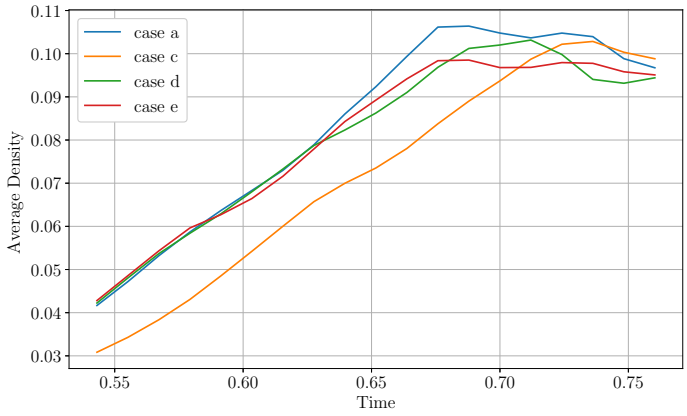


Figure 5.38: Comparison of predicted deuterium area-averaged density using BlastFOAM across different cases: a) original coverslip, c) halved-thickness coverslip, d and e) PMMA/PVC coverslips in various configurations (see figure 5.29). Ideal gas state equations used for deuterium; stiffened gas equations for PMMA, PVC, and copper.

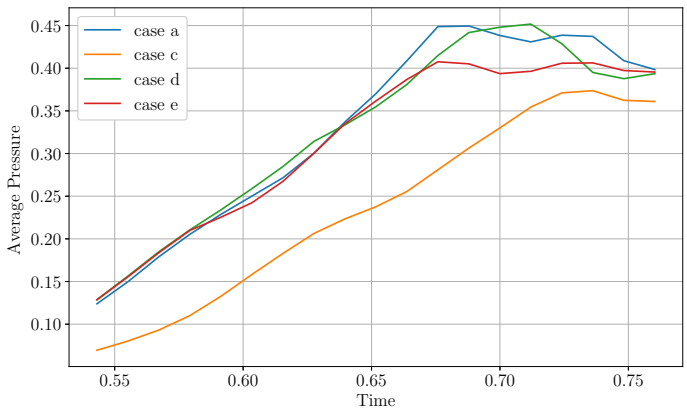


Figure 5.39: Comparison of predicted deuterium area-averaged pressure using BlastFOAM across different cases: a) original coverslip, c) halved-thickness coverslip, d and e) PMMA/PVC coverslips in various configurations (see figure 5.29). Ideal gas state equations used for deuterium; stiffened gas equations for PMMA, PVC, and copper.

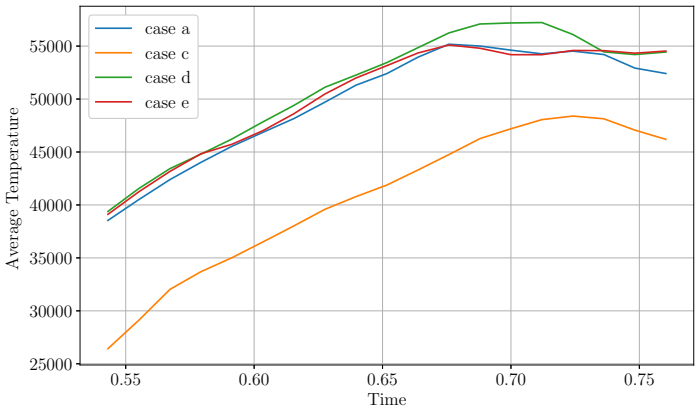


Figure 5.40: Comparison of predicted deuterium area-averaged temperature using BlastFOAM across different cases: a) original coverslip, c) halved-thickness coverslip, d and e) PMMA/PVC coverslips in various configurations (see figure 5.29). Ideal gas state equations used for deuterium; stiffened gas equations for PMMA, PVC, and copper.

5.4 Limitations of Models

There are several limitations of the models used in the shock-induced Fusion Target simulations. These limitations need to be addressed. The influence of temperature on the viscosity of non-Newtonian fluids is only partially considered in these simulations. While this work briefly examines the interaction between non-Newtonian effects and heat transfer, it remains largely unexplored. Further investigations are necessary, as these interactions could significantly impact the formation of small-scale vortical structures that can enhance mixing. The mixing of hot and cold fluids could potentially reduce the temperature required for ignition in inertial confinement fusion. Additionally, the coupling between non-Newtonian effects and heat transfer can affect the stability and evolution of fluid interfaces, potentially leading to more complex flow dynamics and instabilities.

Several multi-physics interactions, including turbulence, heat and mass transfer, phase change, and conduction, are also neglected. It is recommended to investigate these multi-physics interactions to gain a better understanding of this problem. The effects of conduction and heat transfer on the mixing and small-scale structures within the roll-up of Kelvin-Helmholtz instability (KHI) would be particularly insightful. Moreover, turbulence can enhance mixing and influence the growth and structure of instabilities. Ignoring turbulence could result in an incomplete understanding of the fluid dynamics, especially within the roll-ups where small-scale structures develop.

Stiffened gas equation of state is used for modelling copper and PMMA, while ideal gas equation of state is used for deuterium. While this approach simplifies the simulation, it does not account for the detailed thermodynamic behavior of these materials under extreme conditions. A tabulated equation of state, derived from empirical data, could provide more accurate predictions by capturing the specific phase transitions, heat capacities, and compressibility of the materials. The use of a simplified equation of state limits the accuracy of the simulations, particularly when dealing with the complex interactions and extreme conditions present in fusion target scenarios.

The bottom part of the Fusion Target case is made of gold, as shown in figure **??**. However, in the simulations, this gold is replaced with copper due to the unavailability of reliable data for the stiffened gas equation of state for gold. This substitution introduces some limitations, as the properties of copper and gold differ considerably, which can potentially affect the simulation results. Since these simulations focus on the hydrodynamics of the fluid, it is assumed that replacing the gold (outer area of the cone) with copper will not significantly impact the fluid's hydrodynamics.

These simulations focus on the hydrodynamics of the fluids, particularly the evolution of instabilities. However, they do not include plasma physics or neutron generation. This omission means that critical aspects of the fusion process are not modeled, potentially overlooking significant factors that influence the overall behavior and outcomes of the fusion target scenario. To provide a more accurate and complete representation of the physical processes involved, it is recommended to incorporate plasma physics models in BlastFOAM to simulate neutron generation and other relevant phenomena.

Chapter 6

Conclusion and Future Work

6.1 Conclusion and Summary

An extensive study into non-Newtonian effects on Richtmyer-Meshkov instabilities (RMI) and their implications for shock-driven nuclear fusion has been conducted in this thesis. In chapter 3, 5 Toro shock-tube tests were carried out with BlastFOAM and OpenFoam. Both codes apply the volume-of-fluid interface modeling method. The aim of this study was to assess the performance of these codes in simulating highly-compressible flows. The simulations of the codes were compared with the theoretical results: BlastFOAM passed all 5 Toro tests, whereas OpenFoam failed two of the them (tests 2 and 5). Next, a bubble collapse study was performed to assess whether OpenFoam and BlastFOAM accurately capture the interface. BlastFOAM's quantitative results of interface modeling are closer to the experimental results than those of OpenFoam. Given its superior performance in both the shock-tube studies and shock-induced bubble collapse tests, BlastFOAM was selected as the preferred volume-of-fluid code for the rest of the work presented in this thesis.

As a next step, BlastFOAM was compared with Hytrac, an in-house code from First Light Fusion based on the hydrid front-tracking method. A 1-D shock-tube test based on the work of [17] was used to compare Hytrac with BlastFOAM. Both codes provided similar predictions of the pressure, density, and temperature, and it was observed that due to the large density gradient between PMMA and deuterium, a strong rarefaction wave is initiated that leads to a significant drop in the pressure to near-zero values. To mitigate such a drop, the density gradient between PMMA and deuterium was reduced by increasing the density of deuterium by a factor of 625. This led to to weaker rarefaction, so a sudden pressure drop was avoided. The development of a Richtmyer-Meshkov instability (RMI) was also used to assess the codes' performances. The amplitude predictions of RMI by BlastFOAM and Hytrac were compared with the theoretical model by Richtmyer [13] and the late-stage model of

Dimonte and Schneider [14]. The simulation results agreed with the theoretical predictions. Furthermore, a quantitative comparison was made to study if BlastFOAM and Hytrac can effectively model the RMI. Hytrac struggled to model the roll-up associated with the Kelvin-Helmholtz instability (KHI) in contrast to BlastFOAM which demonstrated no such issues. The experiment by Jacobs and Krivets [12] was utilized to examine how accurately BlastFOAM can model roll-ups, span, neck, and stream features. The simulation results are compared with experimental data. Both the BlastFOAM simulation outcomes and the experimental results demonstrate good agreement.

In chapter 4, BlastFOAM is further developed to model non-Newtonian flows. Investigating the non-Newtonian effects on the RMI is one of the main topics of this PhD project. The study in chapter 4 investigated the effects of non-Newtonian rheology on RMI development in flows characterised by negative Atwood numbers wherein a shock was initiated in the heavier, non-Newtonian fluid, and travelled towards the lighter, Newtonian one. To resolve the shock and interfacial dynamics, a one-fluid formulation for the mass, momentum, and energy equations for a compressible flow was used. A shear-thinning and shear-thinning plus temperature dependent rheology was considered for the heavier phase, and a stiffened gas equation of state was used to relate the pressure to the density.

A volume-of-fluid approach is utilised to capture the interface, and BlastFOAM was employed to obtain numerical solutions of the governing equations for a range of Atwood and Mach numbers and a fixed set of rheological parameters for the heavier phase. A two-dimensional vorticity transport equation was derived using a budget analysis of this equation, This equation identified terms that generate and dampen vorticity, which provide valuable insights into the interplay between non-Newtonian effects, vorticity generation, and RMI growth in various regimes. The results demonstrate that the incident shock creates a viscosity gradient along the interface, generating additional vorticity due to non-Newtonian effects compared to the inviscid case, which was used as a benchmark. This additional vorticity generation is more pronounced at moderate Mach numbers Ma ($< Ma = 5$) than at high Mach numbers ($Ma = 10$) because lower shear rates in the former Ma range result in a higher residual viscosity gradient.

After the passage of the shock, the damping effects of viscosity become dominant, leading to a reduction in the vorticity. The reflected shock then generates additional vorticity due to the non-Newtonian viscosity gradient. For the low-to-moderate Ma range, the damping effects of viscosity hinder the development of secondary instabilities, such as the Kelvin-Helmholtz instability (KHI), leading to lower RMI growth. This observation might seem counterintuitive. One might intuitively assume that suppressing secondary instabilities would lead to enhanced growth of RMI, given that such instabilities act as a mechanism to limit or saturate growth. However the dampening effects of viscosity are not only present in nonlinear phase, where the viscosity effects dampen the onset of KHI at low-moderate Mach numbers. The

dampening effects of viscosity also play a crucial role in the linear phase. At high Ma, the residual viscosity is low due to the very high shear rates associated with high-Ma flows, resulting in low rates of vorticity generation associated with non-Newtonian effects. Furthermore, viscous effects in these situations damp out the small-scale structures, which could have given rise to vortex-accelerated vorticity deposition that would have enhanced the RMI and associated mixing.

Incorporating temperature dependence into the viscosity model aligns the growth rate more closely with the inviscid scenario, attributed to the substantial reduction of viscosity at elevated temperatures. The significance of viscosity becomes especially apparent within the regime marked by the presence of small-scale structures. These structures are instrumental in augmenting the generation of baroclinic vorticity through vortex acceleration, a phenomenon thoroughly investigated by Peng et al. [12]. A reduced occurrence of these small-scale structures could lead to reduced mixing, presenting a potential area for further exploration as an extension of the present work.

In chapter 5 a 1-D shock-tube consisting of PMMA and deuterium was used to investigate how the viscosity impacts the shock dynamics. It was found that viscosity has a substantial impact on the shock speed and temperature. Shock in viscous fluid travels faster compared to the inviscid fluid. Furthermore, a 2-d shock-driven fusion target case by [17] was investigated to study the development of the RMI and its impact on the averaged temperature, pressure and density. It was found that if the coverslip is made of a viscous fluid, it would lead to faster shocks and dampen the development of the RMI, reducing mixing and resulting in more stable pressure, temperature, and density. The mixing process can lead to cooling of the fuel and disruption of the symmetry of the implosion. Reducing the growth of the RMI can be beneficial for the fusion process. Insights gained from this study suggested that using a thicker coverslip leads to a stronger shock, and a coverslip made up of viscous material dampens the development of the RMI and reduces the mixing. This can help sustain pressure, temperature, and density for a longer period of time compared to the case where the coverslip material is considered to be inviscid.

6.2 Future Work

Here, ideas for future research avenues are outlined to answer questions that remained open following the completion of this thesis. In chapter 4, it is showed that non-Newtonian rheology can influence the growth and development of Richtmyer-Meshkov and Kelvin-Helmholtz instabilities, and identified the mechanisms for vorticity generation and damping. The detailed coupling between non-Newtonian effects and heat transfer was only briefly touched on in this work but remains largely unexplored and deserves further attention. This coupling could impact the generation of small-scale vortical structures, which will engender mixing and is likely to be detrimental to applications such as inertially confined fusion.

Moreover, the non-Newtonian rheological model studied in this thesis corresponded to a Carreau-type, power-law model. The properties of the materials one is likely to encounter in these applications are viscoelastic, yet elastic effects are neglected in this work. Future work could incorporate viscoelasticity in the model by choosing a suitable constitutive relation for the rheology, e.g. FENE-P or Oldroyd-B models, and coupling an evolution equation for the conformation tensor of the polymeric chains to the other equations of motion.

In terms of models for the thermophysical properties of the materials involved in the simulation of the Fusion Target case, a stiffened gas equation of state was used for copper and PMMA whereas a tabulated relation could have provided more accurate predictions. Furthermore, due to the unavailability of reliable data for gold, this material was replaced with copper. Future work will aim to remedy these shortcomings. It would also be of interest to optimise the geometry of the Fusion Target case according to suitable fusion energy metrics, e.g. the level of neutron generation, and to incorporate within the models an appropriate level of detail of fusion-related physics.

Chapter 7

Appendices

7.1 Tri-Lab case with Hytrac

7.1.1 AMR level Study



Figure 7.1: Evolution of the Richtmyer-Meshkov instability at $AT = 0.635$, $Ma = 1.3$, using the ideal gas equation of state for air and SF6. This showcases different AMR levels (0-3) in Hytrac (HT) at three time intervals: $t = 1 \times 10^{-3}$ s.



Figure 7.2: Evolution of the Richtmyer-Meshkov instability at $AT = 0.635$, $Ma = 1.3$, using the ideal gas equation of state for air and SF6. This showcases different AMR levels (0-3) in Hytrac (HT) at three time intervals: $t = 1.3 \times 1.0^{-3}$ s.



Figure 7.3: Evolution of the Richtmyer-Meshkov instability at $AT = 0.635$, $Ma = 1.3$, using the ideal gas equation of state for air and SF6. This showcases different AMR levels (0-3) in Hytrac (HT) at three time intervals: $t = 1.8 \times 10^{-3}$ s.



Figure 7.4: Evolution of the Richtmyer-Meshkov instability at $AT = 0.635$, $Ma = 1.3$, using the ideal gas equation of state for air and SF6. This showcases different AMR levels (0-3) in Hytrac (HT) at three time intervals: $t = 2.8 \times 10^{-3}$ s.



Figure 7.5: Evolution of the Richtmyer-Meshkov instability at $AT = 0.635$, $Ma = 1.3$, using the ideal gas equation of state for air and SF6. This showcases different AMR levels (0-3) in Hytrac (HT) at three time intervals: $t = 3.0 \times 10^{-3}$ s.

7.1.2 Smoothening Factor Study

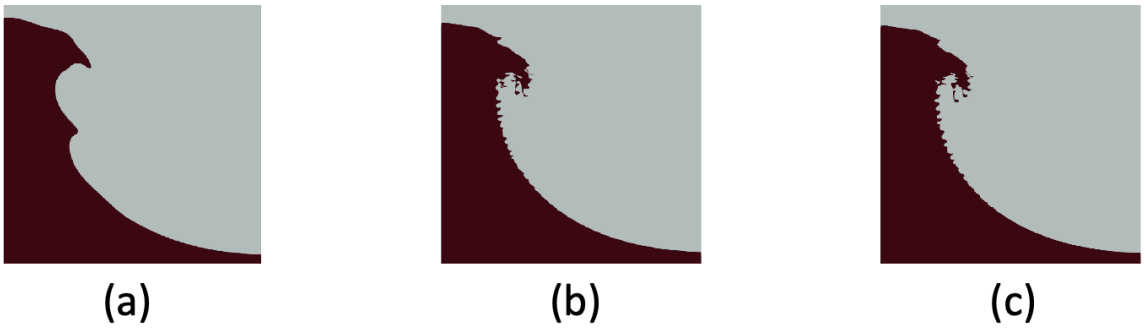


Figure 7.6: Evolution of the Richtmyer-Meshkov instability at $AT = 0.635$, $Ma = 1.3$, using the ideal gas equation of state for air and SF6. This showcases different smoothening factors (SF) $SF = 15$ in (a), $SF = 1000$ in (b), and $SF = 50000$ in (c) in Hytrac (HT) at three time intervals: $t = 1.3 \times 10^{-3}$ s.

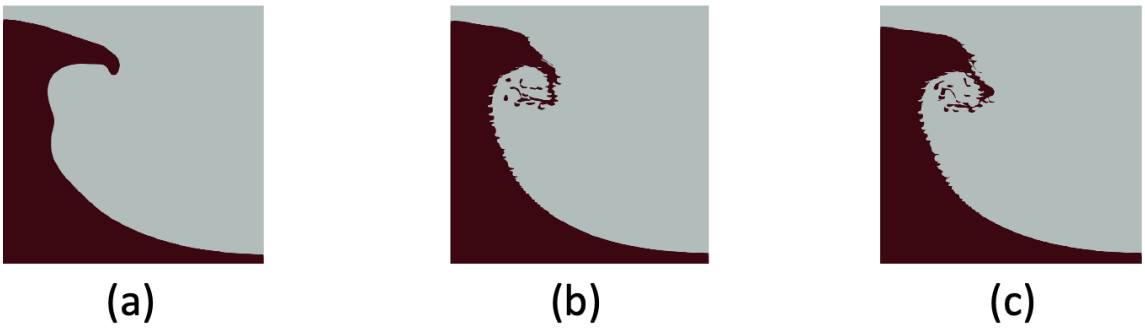


Figure 7.7: Evolution of the Richtmyer-Meshkov instability at $AT = 0.635$, $Ma = 1.3$, using the ideal gas equation of state for air and SF6. This showcases different smoothening factors (SF) $SF = 15$ in (a), $SF = 1000$ in (b), and $SF = 50000$ in (c) in Hytrac (HT) at three time intervals: $t = 1.8 \times 10^{-3}$ s.

7.1.3 Redistribuation Factor Study

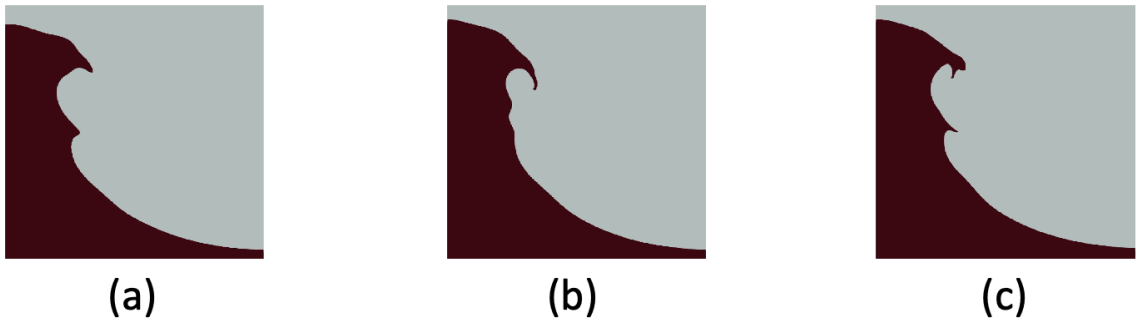


Figure 7.8: Evolution of the Richtmyer-Meshkov instability at $AT = 0.635$, $Ma = 1.3$, using the ideal gas equation of state for air and SF6. This showcases different redistribution factors (RF) $RF = 10$ in (a), $RF = 20$ in (b), and $RF = 200$ in (c) in Hytrac (HT) at three time intervals: $t = 1.3 \times 10^{-3}$ s.

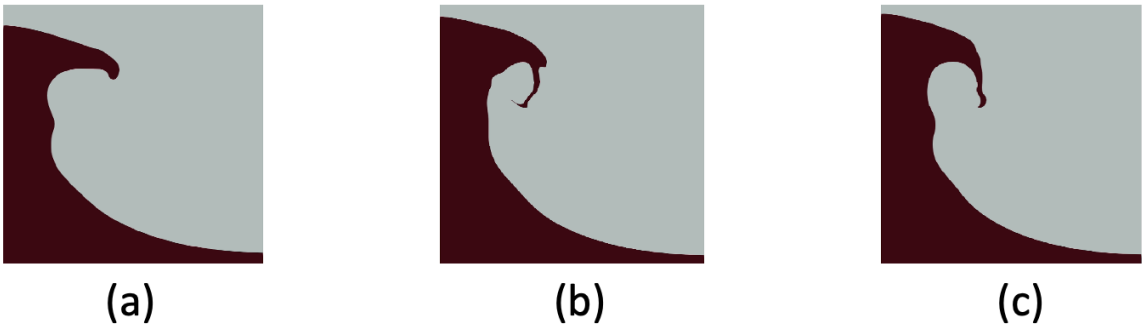


Figure 7.9: Evolution of the Richtmyer-Meshkov instability at $AT = 0.635$, $Ma = 1.3$, using the ideal gas equation of state for air and SF6. This showcases different redistribution factors (RF) $RF = 10$ in (a), $RF = 20$ in (b), and $RF = 200$ in (c) in Hytrac (HT) at three time intervals: $t = 1.8 \times 10^{-3}$ s.

Bibliography

[1] Y. Murtanu. Fission and Fusion. `https://chem.libretexts.org/` accessed: 05.08.2020. pages iii, 4

[2] National Ignition Facility. How ICF Works. `https://lasers.llnl.gov/science/icf/how-icf-works` accessed: 16.08.2020. pages iii, 6

[3] D. Lohse. Cavitation Hots Up. *Nature*, 434:33–34, 2005. pages iii, 7

[4] M. Brouillette. The Richtmyer-Meshkov Instability. *Annual Review of Fluid Mechanics*, 34:445–468, 2002. pages iii, 9

[5] L. Shengtai and H. Li. Parallel AMR Code for Compressible MHD or HD Equations. *Los Alamos National Laboratory*, 2006. pages iii, 10

[6] T. Yue, F. Pearce, A. Kruisbrink, and H. Morvan. Numerical Simulation of Two-Dimensional Kelvin-Helmholtz Instability using Weakly Compressible Smoothed Particle Hydrodynamics. *International Journal for Numerical Methods in Fluids*, 78:283–303, 2015. pages iii, 11

[7] E. F. Toro. Riemann Solvers and Numerical Methods for Fluid Dynamics: A Pratical Introduction. *Springer-Verlag*, third edition, 2009. pages iii, xxii, 15, 16, 19, 20, 33, 34

[8] S. Mirjalili, S. S. Jain, and M. S. Dood. Interface-Capturing Methods for Two-Phase Flows: An Overview and Recent Developments . *Center for Turbulence Research, Annual Research Briefs, Standford University*, 2017. pages iii, 24, 25, 27, 28, 29

[9] R. Scardovelli and S. Zaleski. Direct Numerical Simulation of Free-Surface and Interfacial Flow. *Annual Review of Fluid Mechanics*, 31:567–603, 1999. pages iii, 26, 27

[10] G. Tryggvason, R. Scardovelli, and S. Zaleski. Direct Nummerical Simulations of Gas-Liquid Multiphase Flows. *Cambridge University Press*, first edition, 2011. pages iii, 21, 24, 27, 28, 31

[11] S. Shin and D. Juric. Modeling Three-Dimensional Multiphase Flow using a Level Contour Reconstruction Method for Front-Tracking without Connectivity. *Journal of Computational Physics*, 180:427–470, 2002. pages iii, iv, 30, 31, 32

[12] Gaozhu Peng, Norman J. Zabusky, and Shuang Zhang. Vortex-accelerated secondary baroclinic vorticity deposition and late-intermediate time dynamics of a two-dimensional Richtmyer–Meshkov interface. *Phys. Fluids*, 15(12):3730–3744, December 2003. pages ix, x, 75, 76, 77, 86, 91, 95, 159, 160

[13] Robert D. Richtmyer. Taylor instability in shock acceleration of compressible fluids. *Comm. Pure App. Math.*, 13(2):297–319, May 1960. pages ix, x, xi, xii, xiv, xvii, 75, 92, 93, 94, 96, 110, 113, 114, 141, 142, 158

[14] G. Dimonte and M. Schneider. Density ratio dependence of Rayleigh-Taylor mixing for sustained and impulsive acceleration histories. *Physics of Fluids*, 12:304–321, 2000. pages ix, 67, 75, 85, 159

[15] Muhammad EESA. *CFD Studies of Complex Fluid Flows in Pipes*. PhD thesis, The University of Birmingham, 2009. pages x, 83, 84

[16] Guy Dimonte and Marilyn Schneider. Density ratio dependence of Rayleigh–Taylor mixing for sustained and impulsive acceleration histories. *Phys. Fluids*, 12(2):304–321, February 2000. pages x, xi, xii, xiv, 92, 93, 94, 96, 110, 113, 114

[17] H. Derentowicz, S. Kaliski, J. Wolski, and Z. Ziolkowski. Generation of thermonuclear fusion neutrons by means of a pure explosion part 2 experimental results. *Bulletin de l'Academie Polonaise des Sciences Serie des Sciences Techniques*, 25(10):897–910, 1977. pages xvi, 86, 90, 120, 129, 130, 132, 141, 158, 160

[18] M. Kikuchi, K. Lackner, and M. Q. Tran. Fusion Physics. *International Atomic Energy Agency*, 2012. pages 5

[19] H. Frenzel and H. Schultes. Luminescenz im ultraschallbeschickten Wasser. *Zeitschrift fuer Physikalische Chemie*, B27:421–424, 1934. pages 6

[20] J. Peter. Sonoluminescence: A Discussion. *The Journal of the Acoustical Society of America*, 32:1459–1462, 1960. pages 6

[21] C. C. Wu and P. H. Roberts. Shock-wave propagation in a sonoluminescing gas bubble. *Physical Review Letters*, 70:3424–3427, 1993. pages 6

[22] T. J. Matula, I. M. Hallaj, R. O. Cleveland, and L. A. Crumm. The Acoustic Emissions from Single-Bubble Sonoluminescence. *The Journal of the Acoustical Society of America*, 103:1377–1382, 1998. pages 6

[23] W. C. Moss, D. B. Clarke, and D. A. Young. Calculated Pulse Widths and Spectra of a Single Sonoluminescing Bubble. *Science*, 276:1398–1401, 1997. pages 6

[24] D. J. Flannigan and K. S. Suslick. Inertially confined plasma in an imploding bubble. *Nature*, 6:598–601, 2005. pages 7

[25] D. J. Flannigan and K. S. Suslick. Plasma Formation and Temperature Measurement during Single-Bubble Cavitation. *Nature*, 434:52–55, 2005. pages 7

[26] D. J. Flannigan, S. D. Hopkins, C. G. Camara, S. J. Putterman, and K. S. Suslick. Measurement of Pressure and Density inside a Single Sonoluminescing Bubble. *Physical Review Letters*, 96:204–301, 2006. pages 7

[27] N. A. Hawker and Y. Ventikos. Interaction of a Strong Shockwave with a Gas Bubble in a Liquid Medium: a Numerical Study. *Journal of Fluid Mechanics*, 701:59–97, 2012. pages 7

[28] N. Hawker, M. Betney, and Y. Ventikos. Single and Multiple Bubble Shock-Induced Collapse: A Computational Study. *The Journal of the Acoustical Society of America*, 129, 2011. pages 7

[29] N. Hawker and Y. Ventikos. Percussoluminescence. *The Journal of the Acoustical Society of America*, 133, 2013. pages 7

[30] R. D. Richtmyer. Taylor Instability in a Shock Acceleration of Compressible Fluids. *Communication on Pure and Applied Mathematics*, 13:297–319, 1960. pages 8, 67, 82, 84, 85

[31] E. E. Meshkov. Instabilty of the Interface of Two Gases Accelerated by a Shock Wave. *Soviet Fluid Dynamics*, 4:101–104, 1969. pages 8, 82, 85

[32] L. Rayleigh. Investigation of the Character of the Equilibrium of an Incompressible Heavy Fluid of Variable Density. *Proceedings of the London Mathematical Society*, 14:170–177, 1883. pages 9

[33] D. J. Lewis. The Instability of Liquid Surfaces When Accelerated in a Direction Perpendicular to their Planes 2. *Proceedings of the Royal Society of London: Series A, Mathematical, Physical and Engineering Sciences*, 202:81–96, 1950. pages 10

[34] S. W. Thomson. XLVI. Hydrokinetic Solutions and Observations. *The London, Endinburgh and Dublin Philosophical Magazine and Journal of Science*, 42:362–377, 1871. pages 10

[35] P. Helmholtz. On Discontinuous Movements of Fluids. *The London, Endinburgh and Dublin Philosophical Magazine and Journal of Science*, 36:337–346, 1868. pages 10

[36] G. H. Heng and J. Tu. Computational Techniques for Multi-Phase Flows. *Elsevier Ltd.*, first edition, 2009. pages 24, 25

[37] M. Sussmann and E. G. Puckett. A Coupled Level Set and Volume of Fluid Method for Computing 3D and Axisymmetric Incompressible Two-Phase Flows. *Journal of Computational Physics*, 162:301–337, 2000. pages 29

[38] G. Tryggvason, B. Bunner, A. Esmaeeli, D. Juric, N. Al-Rawahi, W. Tauber, J. Han, S. Nas, and Y. J. Jan. A Front-Tracking Method for the Computations of Multiphase Flow. *Journal of Computational Physics*, 169:708–759, 2001. pages 31

[39] J. Glimm, M. J. Graham, J. Grove, X. L. Li, T. M. Smith, D. Tan, F. Tangerman, and Q. Zhang. Front-Tracking in Two and Three Dimensions. *Computer Mathematics with Applications*, 35:1–11, 1998. pages 31

[40] J. Glimm, J. W. Groce, X. L. Li, K. Shyue, Y. Zeng, and Q. Zhang. Three-Dimensional Front-Tracking. *SIAM Journal on Scientific Computing*, 19:703–727, 1998. pages 31

[41] S. Shin and D. Juric. High Order Level Contour Reconstruction Method. *Journal of Mechanical Science and Technology*, 21:311–326, 2007. pages 32

[42] J. F. Haas and B. Sturtevant. Interaction of Weak Shock Wave with Cylindrical and Spherical Gas Inhomogeneities. *Journal of Fluid Mechanics*, 81:41–76, 1987. pages 54

[43] E. Johnson and T. Colonius. Implementation of WENO Schemes in Compressible Multicomponent Flow Problems. *Journal of Computational Physics*, 219:715–732, 2006. pages 55

[44] N. Apazidis. Numerical Investigation of Shock Induced Bubble Collapse in Water. *Physics of Fluids*, 28:046101–14, 2016. pages 55

[45] G. Dimonte, C. Frerking, M. Schneider, and B. Remington. Richtmyer-Meshkov instability with strong radiatively driven shocks. *Physics of Plasmas*, 3:614–630, 1996. pages 67

[46] G. Dimonte and B. Remington. Richtmyer-Meshkov experiments on the Nova at high compression. *Physical Review Letters*, 70:1806–1809, 1993. pages 67

[47] D. Farely, T. Peyser, L. Logory, S. Murray, and E. Burke. High Mach numbers mix instability experiments of an unstable density interface using a single-mode, nonlinear initial perturbation. *Physics of Plasmas*, 6:4304–4317, 1999. pages 67

[48] J. W. Jacobs and V. V. Krivets. Experiments on the late-time development of single-mode Richtmyer–Meshkov instability. *Phys. Fluids*, 17(3):034105, March 2005. Number: 3. pages 77

[49] blastFoam: A solver for compressible multi-fluid flow with application to high-explosive detonation, synthetik applied technologies, llc. 2019. pages 81, 89

[50] Wolfdynamics. http://www.wolfdynamics.com/tutorials.html. pages 82

[51] Y. Yang, Q. Zhang, and D. H. Sharp. Small amplitude theory of richtmyer-meshkov instability. *Phys. Fluids*, 6(5):1856, 1994. pages 85

[52] Q. Zhang and S.-I. Sohn. An analytic nonlinear theory of richtmyer-meshkov instability. *Phys. Lett. A*, 10(5):121–127, Sep 1996. pages 85

[53] O. Sadot, L. Erez, U. Alon, D. Oron, L. A. Levin, G. Erez, G. Ben-Dor, and D. Shvarts. Study of nonlinear evolution of single-mode and two-bubble interaction under richtmyer-meshkov instability. *Phys. Rev. Lett.*, 80:1654–1657, Feb 1998. pages 85

[54] B. Thornber, D. Drikakis, D. Youngs, and R. Williams. The influence of initial conditions on turbulent mixing due to richtmyer-meshkov instability. *Journal of Fluid Mechanics*, 654:99–139, 2010. pages 85

[55] B. Thornber, D. Drikakis, R. Youngs, and R. Williams. Growth of a richtmyer-meshkov turbulent layer after reshock. *Physics of Fluids*, 23:095107–1–095107–15, September 2011. pages 85

[56] Karnig O. Mikaelian. Effect of viscosity on Rayleigh-Taylor and Richtmyer-Meshkov instabilities. *Phys. Rev. E*, 47(1):375–383, January 1993. pages 86

[57] Pierre Carlès and Stéphane Popinet. Viscous nonlinear theory of Richtmyer–Meshkov instability. *Phys. Fluids*, 13(7):1833–1836, July 2001. pages 86

[58] Pooya Movahed and Eric Johnsen. A solution-adaptive method for efficient compressible multifluid simulations, with application to the Richtmyer–Meshkov instability. *J. Comp. Phys.*, 239:166–186, April 2013. pages 86

[59] A. D. Kotelnikov, J. Ray, and N. J. Zabusky. Vortex morphologies on reaccelerated interfaces: visualization, quantification and modeling of one- and two-mode compressible and incompressible environments. *Phys. Fluids*, 12(12):3245–3264, 2000. pages 86

[60] Z. Wang, B. Yu, H. Chen, B. Zhang, and H. Liu. Scaling vortex breakdown mechanism based on viscous effect in shock cylindrical bubble interaction. *Phys. Fluids*, 30(12):126103, 2018. pages 86

[61] Hao-Chen Liu, Bin Yu, Hao Chen, Bin Zhang, Hui Xu, and Hong Liu. Contribution of viscosity to the circulation deposition in the Richtmyer–Meshkov instability. *J. Fluid Mech.*, 895:A10, July 2020. pages 86

[62] H. W. Zheng, C. Shu, Y. T. Chew, and N. Qin. A solution adaptive simulation of compressible multi-fluid flows with general equation of state. *Int. J. Num. Meth. Fluids*, 67(5):616–637, 2011. pages 90

[63] D. Chapman, J. Pecover, N. Chaturvedi, N Niasse, M. Read, D. Vassilev, J. Chittenden, N. Hawker, and N. Joiner. A preliminary assessment of the sensitivity of uniaxially driven fusion target to flux-limited thermal conduction modelling. *Physics of Plasma*, 28:072702–1–072702–15, July 2021. pages 90

[64] Guy Dimonte, C. Eric Frerking, Marilyn Schneider, and Bruce Remington. Richtmyer–Meshkov instability with strong radiatively driven shocks. *Phys. Plasmas*, 3(2):614–630, February 1996. pages 92

[65] D. R. Farley, T. A. Peyser, L. M. Logory, S. D. Murray, and E. W. Burke. High Mach number mix instability experiments of an unstable density interface using a single-mode, nonlinear initial perturbation. *Phys. Plasmas*, 6(11):4304–4317, November 1999. pages 92

[66] Guy Dimonte and Bruce Remington. Richtmyer-Meshkov experiments on the Nova laser at high compression. *Phys. Rev. Lett.*, 70(12):1806–1809, March 1993. pages 92

[67] E. L. Vold, A. S. Joglekar, M. I. Ortega, R. Moll, D. Fenn, and K. Molvig. Plasma viscosity with mass transport in spherical inertial confinement fusion implosion simulations. *Physics of Plasmas*, 22(112708):1–11, 2015. pages 122

[68] D. A. Chapman, J. D. Pecover, N. Chaturvedi, N. Niasse, M. P. Read, D. H. Vassilev, J. P. Chittenden, N. Hawker, and N. Joiner. A preliminary assessment of the sensitivity of uniaxially driven fusion targets to flux-limited thermal conduction modeling. *Phys. Plasmas*, 28(7):072702, 2021. pages 141

[69] J. D. Anderson. Modern Compressible Flow with Historical Perspective. *McGraw-Hill Book Company*, pages 208–242, 1982. pages

[70] Z. Yang. Numerical Simulation of Incompressible and Compressible Flow. *Graduate Theses and Dissertations University of Sheffield*, 1989. pages

[71] M. Aslani. Numerical Simulation of Compressible Flows with Interfaces. *Graduate Theses and Dissertations Iowa State University*, 2017. pages

[72] S. Atzeni and J. Meyer-Ter-Vehn. The Physics of Inertial Fusion: Beam Plasma Interaction, Hydrodynamics, Hot Dense Matter. *Oxford University Press*, 2004. pages

[73] K. K. So. Uncertainty Analysis of Shock-Bubble Interaction. *Graduate Theses and Dissertations TU Munich*, 2013. pages

[74] S. A. Beig, B. Aboulhasanzadeh, and E. Johnsen. Temperatures Produced by Inertially Collapsing Bubbles near Rigid Surfaces. *Journal of Fluid Mechanics*, 852:105–125, 2018. pages

[75] M. Capuano, C. Bogey, and P.D.M. Spelt. Simulations of Viscous and Compressible Gas-Gas Flows Using High-Order Finite Difference Schemes. *Journal of Computational Physics*, 361:56–81, 2018. pages

[76] S. J. Shaw and P.D.M. Spelt. Shock Emission from Collapsing Gas Bubbles. *Journal of Fluid Mechanics*, 646:363–3731, 2010. pages

[77] S. Shin, J. Chergui, D. Juric, L. Kahouadji, O. K. Matar, and R. V. Craster. A Hybrid Interface Tracking - Level Set Technique for Multiphase Flow with Soluble Surfactant. *Journal of Computational Physics*, 359:409–435, 2018. pages

[78] T. Maric, H. Marschall, and D. Bothe. LentFOAM - A Hybrid Level Set/Front-Tracking Method on Unstructures Meshes. *Computers Fluids*, 113:20–31, 2015. pages

[79] M. Febres and D. Legendre. Enhancement of 2D Front-Tracking Algorithm with a Non-Uniform Distribution of Lagrangian Markers. *Journal of Computational Physics*, 358:173–200, 2018. pages

[80] H. Terashima and G. Tryggvason. A Front-Tracking/Ghost-Fluid Method for Fluid Interfaces in Compressible Flows. *Journal of Computational Physics*, 228:4012–4037, 2009. pages

[81] G. Allaire, S. Clerc, and S. Kokh. A Five-Equation Model for the Simulation of Interfaces between Compressible Fluids. *Journal of Computational Physics*, 181:575–616, 2002. pages

[82] M. Dianat, M. Skarysz, and A. Garmory. A Coupled Level Set and Volume of Fluid Method for Automotive Exterior Water Management Applications. *International Journal of Multiphase Flows*, 91:19–38, 2017. pages

[83] G. H. Yeoh and T. Barber. Assessment of Interface Capturing Methods in Computational Fluid Dynamics (CFD) Codes - A Case Study. *The Journal of Computational Multiphase Flows*, 2:201–215, 2009. pages

[84] G. Keshavarzi, G. H. Yeoh, and T. Barber. Comparison of the VOF and CLSVOF Methods in Interface Capturing of a Rising Bubble. *The Journal of Computational Multiphase Flows*, 5:43–55, 2013. pages

[85] J. W. Banks, D. W. Schwendeman, A. K. Kapila, and W. D. Henshaw. A High-Resolution Godunov Method for Compressible Multi-Material Flow on Overlapping Grids. *Journal of Computational Physics*, 223:262–297, 2007. pages

[86] S. S. Deshpande, L. Anumolu, and M. F. Trujillo. Evaluating the Performance of the Two-Phase Flow Solver InterFoam. *Computational Science Discovery*, 5:014016–36, 2012. pages

[87] D. Fuster and S. Popinet. An All-Mach Method for the Simulation of Bubble Dynamics Problems in the Presence of Surface Tension. *Journal of Computational Physics*, 374:752–768, 2018. pages

[88] P. Koukouvinis, M. Gavaises, O. Supponen, and M. Farhat. Simulation of Bubble Expansion and Collapse in the Vicinity of a Free Surface. *Physics of Fluids*, 28, 2016. pages

[89] M. Ozlem, D. W. Schwendeman, A.K. Kapila, and W. D. Henshaw. A Numerical Study of Shock-Induced Cavity Collapse. *Shock Waves*, 22:89–117, 2012. pages

[90] V. Coralic. Simulation of Shock-Induced Bubble Collapse with Application to Vascular Injury in Shockwace Lithotripsy. *Graduate Theses and Dissertations California Institute of Technology*, 2015. pages

[91] J. J. Qurk and S. Karni. On the Dynamics of a Shock-Bubble Interaction. *Journal of Fluid Mechanics*, 318:129–163, 1996. pages

[92] Y. Luan, M. Olzmann, and F. Magagnato. Simulation of a Shock-Tube with a Small Exit Nozzle. *Journal of Thermal Science*, 27:34–38, 2018. pages

[93] J. P. Cocchi, R. Saurel, and J. C. Loraud. Treatment of Interface Problems with Gudunov-Type Schemes. *Shock Waves*, 5:347–457, 1995. pages

[94] C. C. Chao, C. A. Brebbia, S. A. Orszag, and W. Shyy. Lecture Notes in Engineering: Recent Advances in Computational Fluid Dynamics. *Springer-Verlag*, 1989. pages

[95] R. P. Fedkiw, T. Aslam, B. Merriman, and S. Osher. A Non-Oscillatory Eulerian Approach to Interfaces in Multimaterial Flows (The Ghost Fluid Method). *Journal of Computational Physics*, 152:457–492, 1999. pages